Université de Strasbourg

Ecole Doctorale des Sciences de la Vie et de la Santé

Unité de Recherche : INCI – CNRS UPR3212

Thèse présentée par **Théo ROSSI**

Soutenue le **14 Décembre 2022**

En vue d'obtenir le grade de **Docteur de l'Université de Strasbourg**

Spécialité : **Neurosciences**

Functional diversity of glutamate release at individual cerebellar granule cell boutons

Diversité fonctionnelle de la libération du glutamate aux boutons individuels des cellules en grains du cervelet

Membres du jury

Dr. Cécile CHARRIER (IBENS, rapportrice externe)

Dr. Stéphane DIEUDONNE (IBENS, rapporteur externe)

Dr. Marie-France BADER (INCI, examinatrice interne)

Dr. David DIGREGORIO (Institut Pasteur, examinateur externe)

Dr. Frédéric LANORE (IINS, examinateur externe)

Dr. Philippe ISOPE (INCI, directeur de thèse)

_____

Dr. Frédéric DOUSSAU (INCI, invité)

« Dans la vie, rien n'est à craindre, tout est à comprendre »

Marie Sklodowska-Curie

Acknowledgements

Merci à **Didier**, pour ton côté franc-parler que j'admire et les nombreuses discussions sur les Etats-Unis. Je te tiendrai au courant sur l'avancée du postdoc à Chicago !

Merci à **Bernard**, pour ces nombreuses discussions diverses et variées. J'ai beaucoup appris au travers de nos échanges. Merci également pour les poivrons et le basilic de ton jardin ! Un vrai délice.

Merci à **Aline**, l'assistante ingénieure de l'équipe qui vient à l'instant de m'offrir un super calendrier de l'Avent contenant 24 thés. J'ai été très touché. Merci également pour le radiateur qui m'a évité de finir en mode Hibernatus pendant la rédaction de ce manuscrit.

Un très très très grand merci aux quatre anciens membres de l'équipe listés ci-après :
- **Ludo** : je dois admettre que je suis nostalgique du temps où tu me ligotais à ma chaise de bureau pour m'amener dans l'ascenseur et me faire défiler les 4 étages de l'institut. Prépare-toi à me voir débarquer à New-York à bord du 7-Turdy-7 pour te rendre une petite visite.
- Sa Divine Magnificence ou, comme tous les humains l'appellent, **Charlotte**. Que dire si ce n'est que tu es et resteras à jamais la femme de ma vie, ma moitié à travers tous les univers matériels et immatériels.
- **Fede** : grazie per questi momenti passati assieme ! Ricordo ancora quella volta a Sirmione che non dimentichero' mai. Spero riusciremo ad organizzare qualcos'altro assieme. Anzi ho coltivato la mia competenza di portinaia più informata del lab e gareggio al livello internazionale (ahahah).
- **Kevin** : merci pour toute cette aide que tu m'as apportée au cours de la thèse et de la rédaction du manuscrit. C'est toi qui m'as formé lorsque je suis arrivé dans l'équipe et tu n'as cessé de le faire depuis.

Many thanks to **Adriana**, a sweet former postdoc I had the pleasure to meet. You taught me some Slovakian words I still remember but I don't know how to write them… I really hope to meet again in the future and go drink some beers!

Merci à **Louise**, brillante et courageuse doctorante au mental d'acier qui sait faire face à n'importe quelle situation. J'ai adoré nos pauses à discuter de choses diverses et variées. J'espère de tout cœur qu'il y aura pleins d'autres moments semblables.

Merci à **Louis**, précieux ami que je côtoie depuis le master et qui va grandement me manquer lorsque je partirai à Chicago pour le postdoc. Je t'attendrai de pied ferme et je tacherai d'avoir assez de place dans l'appartement pour vous héberger Elsa et toi. Elsa je compte sur toi pour prendre bien soin de Louis comme tu le fais toujours et pour préparer les délicieux plats que tu sais faire lorsque vous viendrez me voir ☺.

Merci également à **Flo**, **Zélie** et **Guillaume** que je côtoie aussi depuis master et avec qui j'ai partagé de beaux moments. Nos chemins se séparent mais j'espère grandement que nous parviendrons à nous revoir. Zélie je tenais à te remercier également pour le délicieux thé dans la tasse « cagole » (ahahah).

Merci à **Nicolas**, **Déborah**, **Maxime**, **Léonard** et **Pauline**, des amis de longue date avec lesquels j'ai beaucoup partagé, malgré 3 années où nous nous sommes perdus de vue. Je vous attends aussi à Chicago avec impatience !

Un grand merci à **Maëlys** pour ses nombreux messages de soutien et son encouragement.

« Si bellezza ! » est attribué à mon amie **Solenn** que je connais depuis le lycée et qui est une vraie battante. Je t'admire pour ta persévérance et ta résilience. Hâte de refaire des parties à SmashBros !!!

Que serait la vie sans ma petite **Cécile**, également amie de longue date, qui apporte une fraîcheur d'Asie sans pareil et avec qui j'apprends le chinois. D'ailleurs, j'admire la patience que tu as à m'écouter sortir encore et encore des phrases et des mots que j'ai appris ! Je viendrai avec toi en Chine une fois, ça me rabattra le caquet ;)

Je tiens à remercier tout particulièrement mes proches pour leur soutien inconditionnel :
- A ma **maman**, qui a su faire face aux difficultés que la vie lui a imposées et sans laquelle je n'aurais à l'évidence jamais atteint ce stade. C'est toi qui m'as transmis la persévérance et la rigueur nécessaires à l'aboutissement de cette thèse. Bien qu'il n'existe ni parents ni enfants parfaits, tu es pour moi l'exemple que je continuerai de suivre.
- A **Laurent**, le beau-papa super héro Marvel que tout beau-fils rêverait d'avoir.
- A **Ysée**, une cousine unique que je considère comme ma sœur et qui deviendra une journaliste d'exception.
- A ma super **tante**, de laquelle je tiens mon esprit complètement perché que je me plais à extérioriser au quotidien. Hâte de retourner en randonnée en Forêt Noire !
- A **Manou**, une super grand-mère avec laquelle je rigole vraiment bien et qui a toujours cru en moi. Je me souviens de la fois, il y a plus d'une quinzaine d'année, où tu m'as dit que le métier de biologiste m'irait bien. Tu ne t'étais pas trompée !
- A **grand-papa**, mon grand-père d'exception qui m'a appris à marcher. J'espère que de là-haut tu es fier de ton petit-fils.
- A la **Tiole**, une super grande-tante qui m'a toujours aidé depuis tout petit.

Ringrazio mio **papa'**, **Roby**, **Jacopo** e **Emma** per avermi incoraggiato a fare la scelta giusta per quanto riguarda gli Stati Uniti. Grazie per avermi sempre accolto a casa e per tutte la camminate nelle Dolomiti. Ringrazio anche tutta la mia famiglia italiana : **Nonna** e **Nonno**, **Zia Manu**, **Alessio**, **Matteo**, **Zia Betty** e **Zio Sandro**.

Ringrazio particolarmente Nico, mio cugino acquisito che considero come mio fratello. Sono ormai 21 anni che spariamo cavolate a vicenda e non siamo mai a corto di idee (ahahah).

Enfin, le dernier remerciement est pour **Hugo**, avec qui je partage mon cœur depuis maintenant 2 ans et demi. Tu m'as encouragé tout du long malgré les sauts d'humeur et les longues semaines de travail qui m'ont souvent empêché de venir te voir. Même si une nouvelle distance s'impose bientôt, nous saurons la surmonter comme nous avons toujours fait. Merci pour tout.

Outline

List of abbreviations

AAV: Adeno-associated virus

AMPA: α-amino-3-hydroxy-5-methyl-4-isoxazolepropionic acid

BC: Basket cell

cAMP: Cyclic adenosine monophosphate

Cav: Voltage-gated calcium channel

CaMKII: Ca^{2+}/calmodulin-dependent protein kinase II

CB1: Cannabinoid receptor 1

CC: Candelabrum cell

CF : Climbing fibre

cpGFP: Circularly permutated green fluorescent protein

DAG: Diacylglycerol

DCN: Deep cerebellar nuclei

EAAT4: Excitatory amino acid transporter 4

eCFP: Enhanced cyan fluorescent protein

EOS: Glutamate (E) optical sensor

FLIP: Fluorescent indicator protein for glutamate

FWHM: Full width at half maximum

GABA: γ-aminobutyric acid

GC: Granule cell

GoC: Golgi cell

HCPC: Hierarchical clustering of principal components

iGluSnFR: Intensity-based glutamate-sensing fluorescent reporter

IO : Inferior olive

IP3: Inositol 1,4,5 trisphosphate

LTD: Long-term depression

LTP: Long-term potentiation

MF: Mossy fibre

mGluR1 : Metabotropic glutamate receptor 1

MLI: Molecular layer interneuron

NMDA: N-methyl-D-aspartate

PC: Purkinje cell

PCA: Principal component analysis

PDGFR: Platelet-derived growth factor receptor

PF: Parallel fibre

PKA: cAMP-dependent protein kinase A

PPR: Paired-pulse ratio

P_r: Probability of release

$P_{success}$: Synaptic probability of release success

PSF: Point-spread function

RRP: Ready-releasable pool

SC: Stellate cell

SF: Circularly-permuted superfolder GFP

SK: Small conductance calcium-activated potassium channel

SNARE: Soluble N-ethylmaleimide-sensitive-factor Attachment protein REceptor

STD : Short-term depression

STF : Short-term facilitation

STP : Short-term plasticity

TRPC3: Short transient receptor potential channel 3

VGLUT: Vesicular glutamate transporter

VOR: Vestibulo-ocular reflex

List of figures

RESULTS

DISCUSSION

ANNEXES

Preamble

The cerebellum plays a central role in learning and coordination of movement, balance maintaining, adaptation of reflexes, timing of actions and cognitive processes (*see Part I*). To do so, it receives contextual sensorimotor information from the body through a communication with many brain regions and the spinal cord (*see Part I* and *section II.2.1*). The topographical organization of inputs and outputs parcellates the cerebellar cortex into a series of modules and microzones processing specific sensorimotor information and overlapping with multiple molecular markers (*see section II.5*). Information is processed in multiple modules of the cerebellar cortex to encode accurate representation of a sensorimotor context (*see section II.2* and *II.3* and *II.4*). The main research axis established in the team is to understand *how cerebellar modules communicate each other to ensure proper motor output.*

Sensorimotor information from mossy fibres are conveyed to the cerebellar cortex at wide range of high frequencies, relayed by granule cells and distributed to Purkinje cells and inhibitory interneurons across multiple modules via the parallel fibres. Parallel fibre boutons contain mechanisms adapted for supporting high-frequencies (*see section III.1* and *III.2.1*) which trigger short-term synaptic plasticity (*see section III.2*). Short-term plasticity provides fast adaptation of glutamate release to shape the synaptic strength in the millisecond timescale and temporally filter sensorimotor information (*see section III.2.1*).This temporal coding is fundamental to shape the firing pattern of the postsynaptic cell and can be expanded through the diversity of short-term plasticity (*see section III.2.3*) to provide accurate representation of behaviours in Purkinje cells (*see section III.3*).

My thesis project aimed at understanding how sensorimotor information is temporally encoded across modules to shape the Purkinje cell output pattern. Anaïs Grangeray-Vilmint demonstrated that the diversity of short-term plasticity at excitatory and inhibitory synapses dynamically shapes the excitatory/inhibitory balance of Purkinje cells (*see section III.2.3.3*; Grangeray-Vilmint et al., 2018). In parallel, Kevin Dorgans reported that a single inhibitory interneuron receives granule cell inputs with heterogeneous short-term plasticity properties (*see section III.2.3.1*; Dorgans et al., 2019). Kevin also demonstrated that synapsin II, a presynaptic protein involved in regulation of synaptic vesicle pools, is heterogeneously expressed at these synapses. He noticed that deletion of synapsin II reduces the diversity of short-term plasticity and alters temporal coding of information in the inhibitory interneuron. This raised an appealing hypothesis: the diversity of short-term plasticity provides specific temporal coding of information across the modules.

Objectives of the study

Based on these works, my project aims at understanding the organization of short-term plasticity properties at granule cell boutons across the cerebellar modules. I addressed this problematic through the following questions:

Q1: Since granule cells communicate with multiple modules through the parallel fibre, are short-term plasticity properties heterogeneous from bouton to bouton along the same parallel fibre?

Q2: Since the diversity of short term plasticity modulates the excitatory/inhibitory balance in Purkinje cells, are short-term plasticity properties at unitary boutons target-dependent?

Q3: Since the synapsin II expands the diversity of short-term plasticity, what are the mechanisms in the bouton modulating the diversity of short-term plasticity?

Monitoring glutamate release and short-term plasticity at the level of a single bouton is extremely challenging with electrophysiological methods. New genetically-encoded fluorescent glutamate sensors (iGluSnFR; *see Part IV*) provide fast and reliable measurements of glutamate release from unitary boutons. I therefore set out to develop a two-photon microscopy method combined to expression of iGluSnFR in granule cells to monitor short-term plasticity at single granule cell boutons (*see section V.6*).

To answer the first question (Q1), I monitored glutamate release simultaneously from multiple boutons along the same parallel fibre to assess the diversity of short-term plasticity.

To answer the second question (Q2), I took advantage of a transgenic mouse line allowing real time visualization of Purkinje cells during iGluSnFR two-photon imaging of single boutons to discriminate these cells from other cell types.

To answer the third question (Q3), I investigated on the contribution of extracellular calcium and adenylyl cyclase to the diversity of short-term plasticity between single boutons.

Part I. General introduction on the cerebellum

I.1. The cerebellum through the ages

I.1.1. Recognition of the "little brain" and rise of a term

The core of thoughts and emotions is one of the greatest mystery the philosophers and scientists aim to resolve. It looks clear nowadays that our thinking, feelings, memory (in other words our consciousness) are established in the brain, not in the heart. However, this dogma has been the matter of long debates in ancient times.

In the Antiquity, Plato (428 B.C. – 347 B.C.) suggests that the brain is the seat of mental processes. Firmly opposed to such a hypothesis, Aristotle (384 B.C. – 322 B.C.), supporter of the cardiocentric theory, claims the heart as the seat of mental activities and feelings. Aristotle also described a particular structure beside the encephalon he called *paregkefalis* (*pareg-*, « close » and -*kefalis*, « head »), later referred as the cerebellum. Centuries later, the Greek physician Galen (129 – 201) made anatomical observations of the cerebellum in oxen and monkeys and recognized the apparent differences with the cerebrum in *De Usu Partium* (Voogd & De Zeeuw, 2020). The Latin term *puppi* - the stern - has been used by Constantine the African (1020 – 1087) in *Liber de oblivion* to pinpoint the posterior part of the brain in 1050. Niccolo' da Reggio (1280 – 1350) latinized the Greek version *paregkefalis* in *parencefalide* in 1307 and Mondino de' Luzzi (1275 – 1326) used the term *cerebri posterior* due to the posterior location of the cerebellum in 1310 (Voogd & De Zeeuw, 2020).

At dawn of the 16th century, golden age of the Renaissance, Magnus Hundt (1449 – 1519) publishes *Anthropologia* (1501) where the term *cerebellum* (little brain) probably appears for the first time (***Figure I1A***, Jan Voogd & De Zeeuw, 2020). Interestingly, *cerebellum* was already used by Celsus (25 B.C – 50) as a diminutive of *cerebrum* to describe the brain of small animals, not the cerebellum itself. The Flemish anatomist Andreas Vesalius (1514 – 1564), taking Celsus as a reference for the anatomical terms, used *cerebellum* in his famous *De humani corporis fabrica* (1543). With this work, Vesalius broke with Galen's tradition by using dissection of the human body to provide the first illustration (***Figure I1B***) and describe the surface of the cerebellum: « *The very highest part of the cerebellum extends only to the middle of the occiput although some, deluded by oxen and asses or by dreams, have written that the cerebellum ascends from the posterior site of the foramen, to the lambdoid suture […]* » (Glickstein et al., 2009). Hence, the name *cerebellum* sees the light of day at the time of the universal man.

A.

Magnus Hundt, *Anthrologia*, 1501
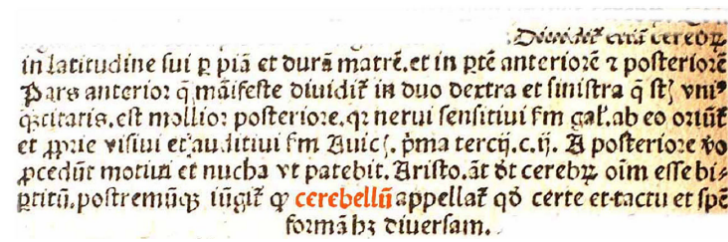
B.
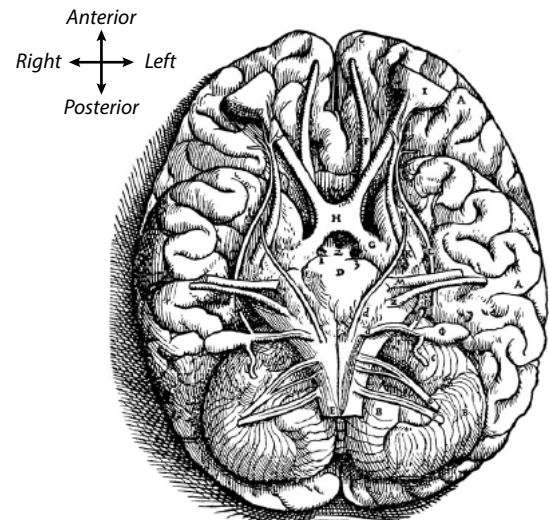
C.
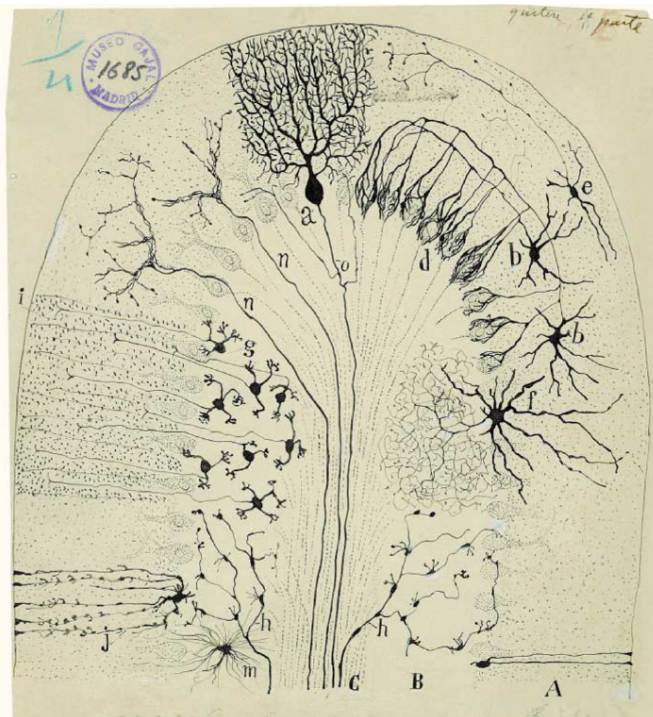
D.
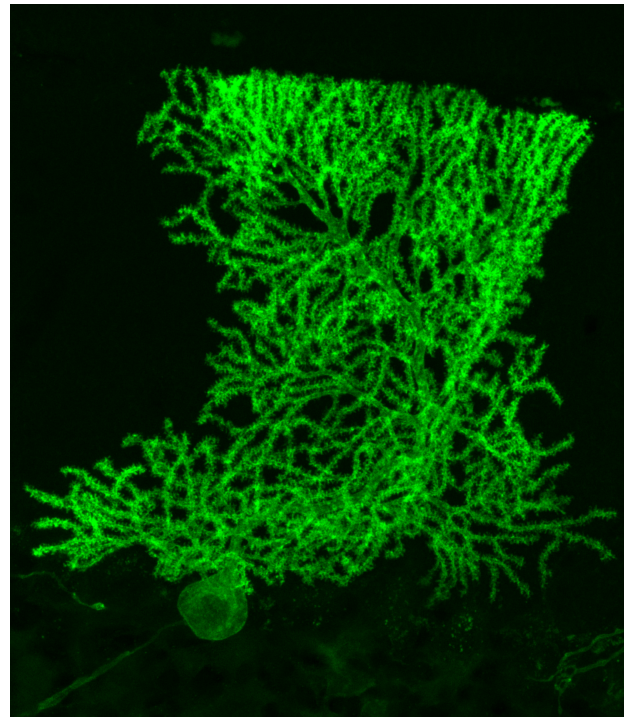
Figure I1 : From the name cerebellum to the network.

A) Text from *Anthropologia* by Magnus Hundt in 1501 using the modern term *cerebellum* highlighted in red. *From Voogd & De Zeeuw, 2020*.

B) First anatomical illustration of the ventral view of the cerebellum from *De humani corporis fabrica* by Vesalius. *From Scatfliff & Johnston, 2014*.

C) Diagram of the neuronal organization of the cerebellar cortex made by Santiago Ramon y Cajal in 1894. *A, molecular layer; a, Prkinje cell; B, granular layer; b, basket cell; C, white matter; d, pericellular basket of the basket cell; e, stellate cell; f, Golgi cell; g, granule cell; h, mossy fibre; i, ascending axon of granule cell; j, Bergmann glial cell; m, astroglial cell; n, climbing fibre; o, collateral branches of a Purkinje cell*. *From Sotelo, 2003*.

D) Confocal imaging of a Purkinje cell in the sagittal plane expressing the Channelrhodopsin 2 fused to the enhanced yellow fluorescent protein. *Image credit: Théo Rossi, Antoine Valera and Adriana Basnakova, INCI*.

I.1.2. Brief historical evolving views of cerebellar organization and function

In the next century, the Italian physician Marcello Malpighi (1628 – 1694) introduces the cerebellar cortex as a leaf delicately placed on the extremities of the extended fibres coming from the spinal cord. Thereafter, the French anatomist Raymond de Vieussens (1641 – 1716) reported the first identification of the cerebellar nuclei as the *corpus rhomboideum*. This latter has been renamed by Félix Vicq d'Azyr (1746 – 1794) as the *corps dentelé* (Glickstein et al., 2009). The German anatomist Benedict Stilling (1842 – 1915) labeled the other cerebellar nuclei as *emboliform*, *globose* and *fastigial* in 1864.

The study of the cerebellum gained considerable momentum in the eighteenth century. The Italian surgeon Vincenzo Malacarne (1744 – 1816) published *Nuova esposizione della vera struttura del cervelletto umano* (1776) (The new exposition of the real structure of the human cerebellum) entirely devoted to the cerebellum. In this masterpiece, Malacarne provides the name of the cerebellar lobules such as *lingula*, *uvula*, *laminate pyramid*, *tonsils* (Glickstein et al., 2009). After comparing the cerebellum from a man affected by cretinism to a normal one, he noticed a drastic reduction in the number of folia and suggested an involvement of the cerebellum in plastic changes.

More accurate understandings on cerebellar functions have been brought through the use of the animal experimentation in the 19th century. Luigi Rolando (1773 – 1831) demonstrated that cerebellar lesions impaired motor but not sensory or intellectual functions and suggested a role for the initiation of the movement. At that time, Pierre Flourens (1794 – 1867) made a striking discovery: after cerebellar ablation, movements are executed with a dramatic lack of fluidity. Flourens concluded that the cerebellum stands as the seat of coordination while the production of the movement originates in the spinal cord. In the monograph *Il cervelletto: nuovi studi di fisiologia normale e patologica*, Luigi Luciani (1840 – 1919) described a triad of symptoms after grossly localized cerebellar surgical lesions in dogs and monkeys: atonia – muscle weakness in postural tone –, asthenia – muscle weakness during voluntary movement – and astasia – head and trunk oscillations and tremor during movement (Glickstein et al., 2009). Thereafter, Luciani added a fourth symptom to his triad, dysmetria – error in the metric of movement – (Manni & Petrosini, 1997) later adding the new tetrad in the clinical picture of ataxia.

The hectic cerebellar experiments on animals profoundly influenced clinical observations. In 1902, Joseph Babinski (1857 – 1932), walking in the footsteps of Flourens, refined the panel of cerebellar symptoms and function. He noticed that patients affected by cerebellar lesions are unable to carry out rapid sequences of movements - *adiadokinesia* –

and to associate the components of a movement to create a fluid motion – *asynergia* (Babinsky, 1902). Gordon Holmes (1876 – 1965), following Luciani and unlike Babinsky, opted for more elementary deficits. He confirmed the symptoms described by Luciani in soldiers with cerebellar gunshot injuries during World War I and observed dyskinesia and tremor thus developing the concept of ataxia (Holmes, 1917). Despite the fact that neither highlighted precise locations of cerebellar lesions, the pioneers of the 19th century have strongly shed light on the involvement of the cerebellum in the coordinated execution of complex and voluntary movement.

I.1.3. A leap forward in the investigation of the cerebellum.

The very end of the 19th century and the 20th mark a fundamental need to investigate the neural basis underlying the confirmed involvement of the cerebellum in fine motor coordination. The development of microscopy and staining methods allowed Ramon y Cajal to highlight the crystalline architecture of the cerebellar network and its two major inputs (*Figure I1C*, Ramon y Cajal, 1894). Cajal provided drawings of the cerebellar cortex and its neurons including the Purkinje cells (PC, *Figure I1D*), sole output of the cerebellar cortex originally discovered in sheep by Jan Evangelista Purkinje in 1832. Anatomists such as Sanford Palay and Victoria Chan-Palay provided a detailed description of the cytoarchitecture of the cerebellar cortex (Palay & Chan-Palay, 1974). In parallel, Larsell, Janssen and Brodal made comparative anatomy of the cerebellum in mammalian species to shed light on cerebellar functional localization (e.g. the anterior lobe coordinates eyes muscles).

These pioneering studies kicked off important anatomo-functional works in the cerebellar cortex. Investigations on the connectivity with anatomical tracing and refinement of electrophysiology provided evidences on the functional somatotopy of modular information processing (Armstrong et al., 1974; Oscarsson, 1979; J. Voogd, 1967). From there, how does information flow and is processed in the cerebellar circuits became the central question on cerebellar physiology. Eccles, Ito and Szentagotai identified the excitatory and inhibitory nature of the cerebellar neurons (Eccles et al., 1967), of which the inhibitory nature of PCs (Ito et al., 1964), providing the functional architecture of the cerebellar cortex. This inspired David Marr and James Albus to model the cerebellar cortex as a perceptron algorithm for cerebellar function (Albus, 1971a; Marr, 1969a). Ito and Kano reported functional synaptic mechanisms through electrophysiological studies to validate this model (Ito & Kano, 1982) which is still a basic reference for investigating cerebellar computation.

Nowadays, a growing amount of studies highlight the heterogeneous functional and molecular compartmentalization of the cerebellar cortex and the associated functional synaptic rules governing cerebellar computation and functions (Apps et al., 2018; Cayco-Gajic & Silver, 2019; Cerminara et al., 2015; Spaeth et al., 2022).

I.2. Gross anatomy of the cerebellum

Formed by two hemispheres, the *Little brain* represents only 10% of the total volume of the brain and contains more than one-half of its neurons. It is localized in the posterior cranial fossa and is separated from the cerebrum by a thin layer of dura matter, the tentorium cerebelli. It overhangs the dorsal part of the metencephalon and connects to other structures through three cerebellar peduncles (superior, middle and inferior). The cerebellum is made up of the cerebellar cortex, the ramified white matter (the *arbor vitae*) and three deep cerebellar nuclei (DCN, *fastigial*, *emboliform/globose interposed* and *dentate* in humans; *medial*, *anterior/posterior interposed* and *lateral* in rodents). With the vestibular nuclei, the DCN constitute the output of the cerebellum projecting to different brain areas, the brainstem and the spinal cord. The gross anatomy is segmented in several compartments.

I.2.1. Anteroposterior and mediolateral axes

In the antero-posterior axis, two transverse fissures divide the cerebellum into three lobes (***Figure I2A-B***). The dorsal primary fissure delimits the anterior and the posterior lobes, the body of the cerebellum. The ventral posterolateral fissure separates the body of the cerebellum from the flocculonodular lobe. This latter is composed by two lateral flocculi connected to the midline structure, the nodulus.

The cerebellum is organized in 10 highly conserved lobules across species (***Figure I2B***; Apps & Hawkes, 2009) and many parallel thin folds called folia. The anterior lobe is composed of lobules I to V while the posterior lobe ranks from lobule VI to IX. Lobules IV and V are fused in mice while they are distinct in humans and rats. The lobule X is given by the flocculonodular lobe, also known as the vestibulo-cerebellum.

The mediolateral axis divides the cerebellum into three orthogonal areas from the midline to the hemispheres (***Figure I2C***): the medial vermis, the paravermis and the hemispheres. The combination of the vermis and the paravermis gives rise to the spino-cerebellum while the hemispheres are known as the cerebro-cerebellum (***Figure I2C***).
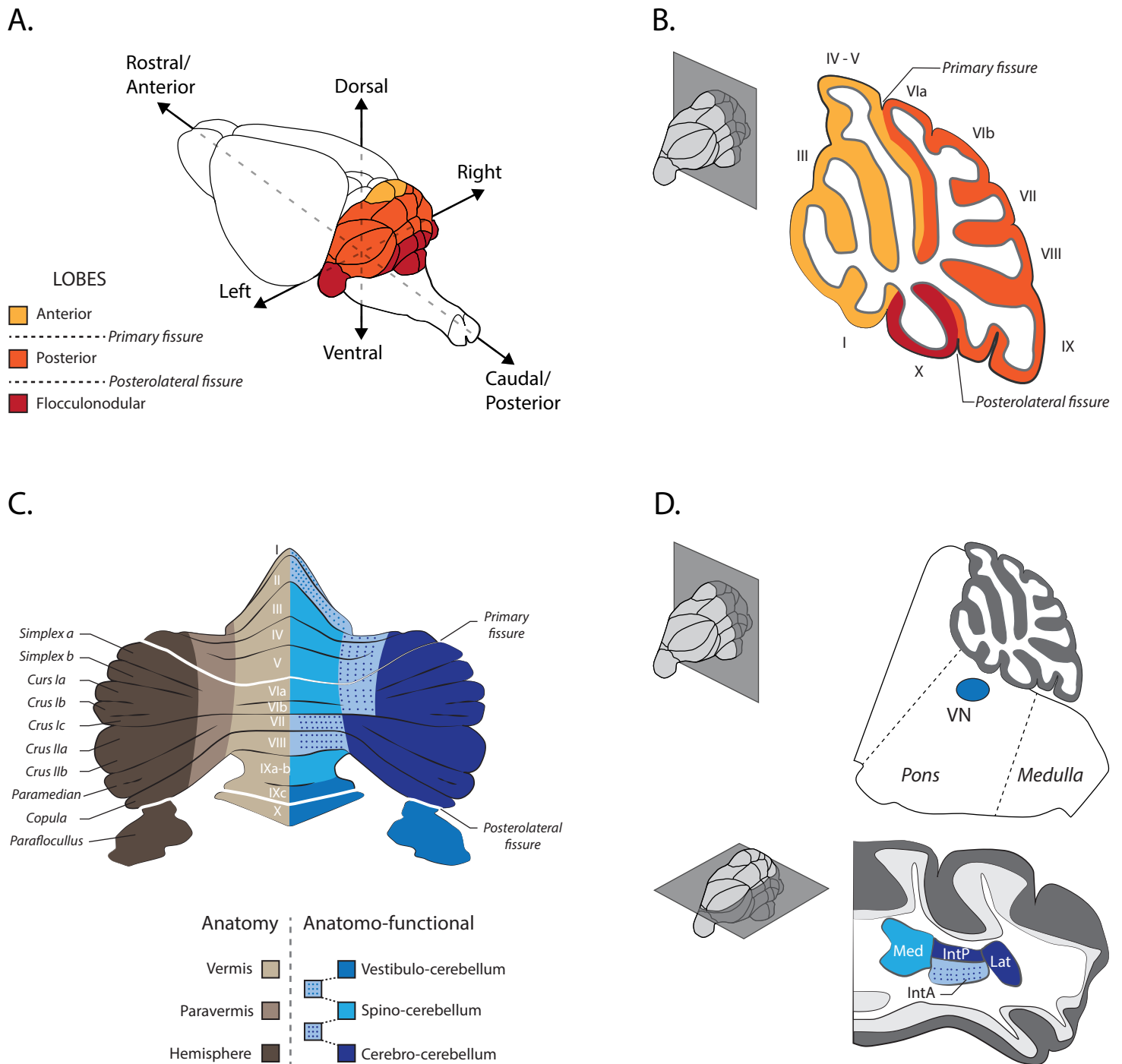
Figure I2 : Anatomo-functional cerebellar segmentation.

A) Isometric axes of the murine encephalon and cerebellar lobes.

B) Sagittal section of the murine cerebellum highlighting cerebellar lobes and lobules (I-X).

C) Anatomical and anatomo-functional segmentation on the unfolded view of the cerebellar cortex.

D) Anatomo-functional segmentation of the cerebellar output nuclei. Left, location of deep cerebellar nuclei. Right, location of vestibular nuclei. *IntA, interposed anterior; IntP, interposed posterior; Lat, lateral; Med, median; VN, vestibular nuclei.*

Adapted from Spaeth L. (2019) Modular information processing in the cerebellar cortex.

I.2.2. Evolutive segmentation

Usually smaller than the cerebrum, the cerebellum evolves parallel to the cerebrum. It appears in fishes as lampreys (Petromyzontidae Family) although only made up of the flocculonodular lobe – *archi-cerebellum* or *vestibulo-cerebellum*. This primitive appearance is associated to basic functions as control of axial muscles and position relative to gravity. However, the oversized cerebellum and the development of the vermis (*paleo-cerebellum* or *spino-cerebellum*) in Mormyrid fish is probably associated to the exquisitely developed electroreceptive system (Hodos, 2009).

Even though anatomical variations can be denoted between vertebrates, the cerebellum remains well conserved on the evolutionary line. The corpus cerebelli (the vermis) as well as the vestibulo-cerebellum are also present in amphibians, reptiles, birds and mammals. Fishes, amphibians and reptiles have a smooth cerebellum while it becomes foliated in birds and mammals. In mammals, the corpus cerebelli transversely narrows with regard to the development and the expansion of the lateral hemispheres (*neo-cerebellum* or *cerebro-cerebellum*) for more complex functions as infrasonic vocalizations in elephants (Jacobs et al., 2014).

The terminology vestibulo–, spino– and cerebro-cerebellum comes from the anatomical and functional evolutionary description and is based on the cerebellar inputs and outputs.

I.2.2.1. The vestibulo-cerebellum

The most primitive part is the vestibulo-cerebellum which participates in balance and adaptive eye movements (***Figure I2C***). For example, the vestibulo-cerebellum regulates the gain of the vestibulo ocular reflex (VOR, Lisberger et al., 1984). This reflex consists in moving the eyes in the opposite direction of the head rotation to stabilize the gaze on a target. To do this, the vestibulo-cerebellum receives inputs from the vestibular nuclei beneath the dorsal surface of the medullary brainstem through the inferior cerebellar peduncle (***Figure I3A***). Vestibular nuclei relay information from the three semicircular canals and the two otolith organs, which detect the head's motion and its position relative to the gravity (Kushiro et al., 2000; Ono et al., 2000). Moreover, visual information from the striate cortex relayed in the pretectal nuclei and the pontine nuclei project to the vestibulo-cerebellum (***Figure I3A***). In turn, the vestibulo-cerebellum projects directly on vestibular nuclei (***Figure I2D*** and ***I3C***) to modulate ascending and descending vestibular pathways. This modulation influences the activity of reflexive eye movements as well as axial muscles and limb extensors to adapt balance during posture and gait.
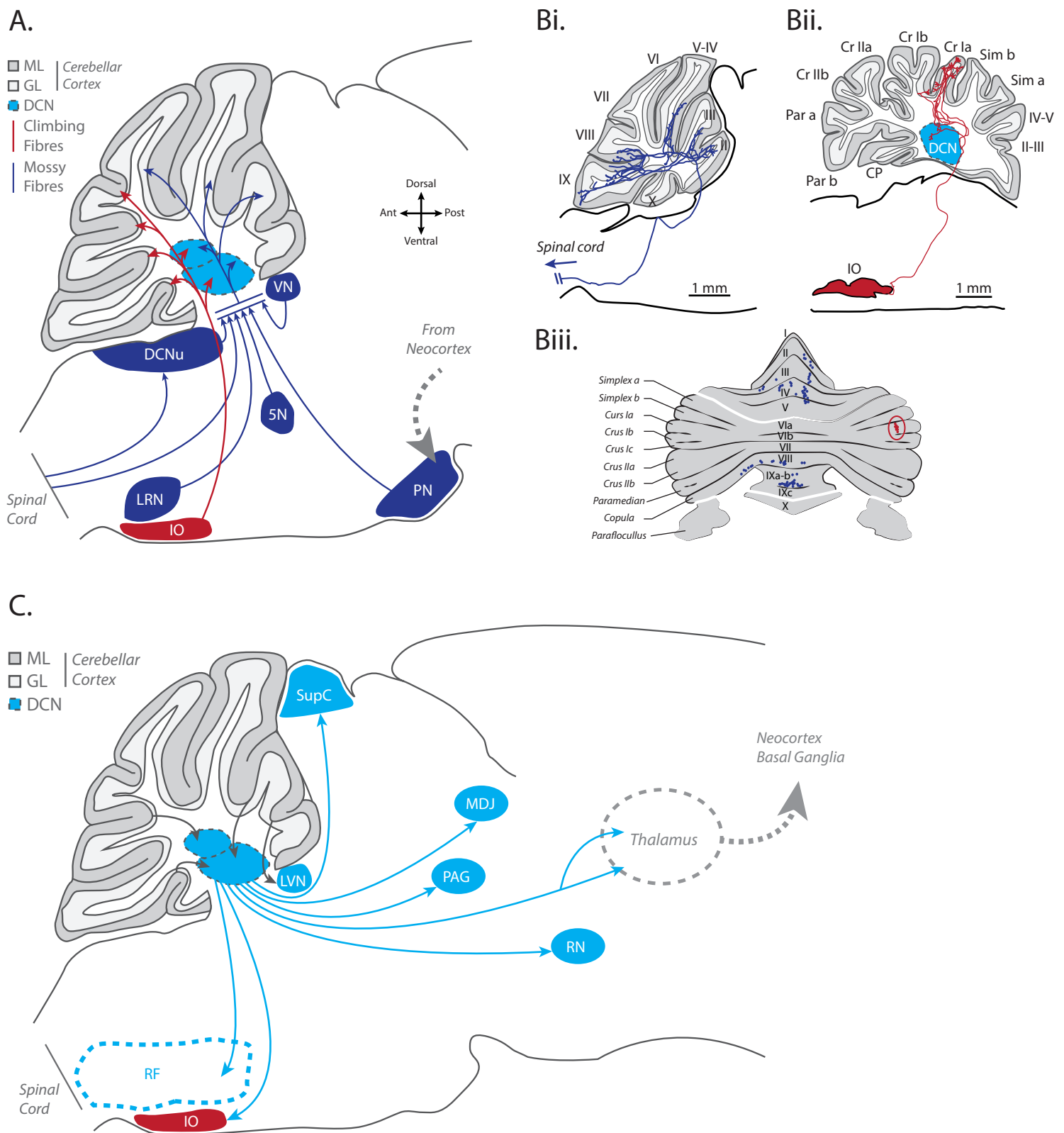
Figure I3 : Cerebellar inputs and outputs.

A) Two major inputs of the cerebellum in the sagittal plane. Both climbing fibres from the inferior olive and mossy fibres from prece-rebellar nuclei and spinal cord leave collaterals in the deep cerebellar nuclei. **Adapted from Spaeth L. (2019) Modular information processing in the cerebellar cortex.**

B) Projection of single mossy (*Bi*) and climbing (*Bii*) fibres in cerebellar lobules. The unfolded view of the cerebellar cortex (*Biii*) indicates terminations of both fibres. **Adapted from Sugihara et al., (2001) and Zhang et al., (2021).**

C) Outputs from the deep cerebellar nuclei to targets. **Adapted from Spaeth L. (2019) Modular information processing in the cerebellar cortex.**

5N, trigeminal nuclei; CP, copula; CrI/II, crus I/II; DCN, deep cerebellar nuclei; DCNu, dorsal column nuclei; GL, granular layer; IO, inferior olive; LRN, lateral reticular nucleus; LVN, lateral vestibular nucleus; MDJ, mesodiencephalic junction; ML, molecular layer; Par, parame-dian lobule; PN, pontine nuclei; RF, reticular formation; RN, red nucleus; Sim a/b, simplex lobule a/b; SupC, superior colliculus/tectum; VTA, ventral tegmental area.

I.2.2.2. The spino-cerebellum

The spino-cerebellum (composed of the vermis and the paravermis, *Figure I2C*) appears later in evolution and governs posture, locomotion and eye movements. It receives extensive inputs from the dorsal and the ventral spinocerebellar tracts as well as the dorsal column nuclei in the brainstem (gracile and cuneate nuclei, *Figure I3A*). Spinocerebellar pathways and dorsal column nuclei convey proprioceptive and tactile information from limbs, tail, head and neck.

These inputs are directed to the vermis and the intermediate parts of the hemispheres, the paravermis. The vermis receives somatic inputs from head and limbs as well as visual, auditory and vestibular inputs. Neurons in the vermis project by way of the medial nucleus (*Figure I2D*) to vestibular nuclei to modulate posture, to nuclei in the reticular formation to modulate medial descending pathways controlling proximal muscles of limbs, and to the ventrolateral thalamus connected to prefrontal and motor cortices (*Figure I3C*, Fujita et al., 2020). The paravermis integrates somatosensory information from the limbs. It connects to the anterior interposed nucleus (*Figure I2D*) projecting to the red nucleus in the brainstem to modulate the rubrospinal tract (*Figure I3C*). The interposed nuclei also connect to motor cortices via the ventrolateral thalamus to modulate the corticospinal tract (*Figure I3C*). Ultimately, the modulation of these descending tracts allows the paravermis to control distal muscles of the limbs and digits.

I.2.2.3. The cerebro-cerebellum

The recent appearance of the cerebellar hemispheres marks a massive cerebro-cerebellar communication organized in multiple reciprocal loops actively participating in planning and timing of movements as well as visuospatial and affective processes. Information flow from the cerebral cortex is predominantly relayed via the pontine nuclei (*Figure I3A*, (Nagao, 2004). Neurons in the lateral hemisphere project to the lateral nucleus and the posterior interposed nucleus (*Figure I2D*). In turn, the lateral nucleus connects to motor, premotor and parietal areas via several thalamic nuclei (*Figure I3C*, Amino et al., 2001; Shinoda et al., 1993). Neurons in the lateral nucleus also target the prefrontal cortex (Kelly et al., 2020) and the basal ganglia (Chen et al., 2014) via a thalamic relay and the red nucleus (*Figure I3C*, Flumerfelt et al., 1973). This tight connectivity leads to fine tuning of movements (Guo et al., 2020) and timing prediction of specific directed motor skills (Chabrol et al., 2019).

I.3. The cerebellum's duties

The cerebellum plays a key role in motor learning, coordination of movements and control of gate and balance through a dialogue with the spinal cord, the brainstem and the thalamocortical pathways. Reaching a glass of water with the hand and bring it to the mouth requires right metrics and fluidity controlled by the cerebellum. A growing body of studies demonstrate that the cerebellum is also involved in cognitive functions.

I.3.1. The sensorimotor cerebellum

The first well documented function of the cerebellum is undoubtedly the adaptation of movement. Smooth and accurate execution of a movement requires planning of the motor sequence. Because feedback loops are too slow and have small gain, fast and coordinated movements can't be executed under pure feedback control (Wolpert et al., 1998). To overcome this timing issue, the cerebellum implements prediction strategies though multiple internal models (Bastian, 2006; Wolpert et al., 1998). Two types of internal models have been proposed. First, the *forward model* predicts the future state of the action (e.g. position, velocity, acceleration, amplitude, Diedrichsen et al., 2005) based on the current state and the motor command. Second, the *inverse model* predicts the motor command required to achieve the desired state (Bastian, 2006; Ito, 2006; Shidara et al., 1993; Wolpert et al., 1998).

During a movement, the motor cortices transfer to the cerebellum a copy of the motor command sent to the spinal cord. In parallel, proprioceptive, tactile, visual and auditory systems convey contextual sensory information to the cerebellum. In this way, the cerebellum is constantly informed on the state of the body in real-time. As the movement progresses, the cerebellum learns to predict the next step of the action (*forward model*) and compares this prediction with the current sensory feedback for motor correction (*inverse model*). This correction operates through a dialogue from the cerebellum to motor cortices and motor nuclei in the brainstem to ensure coordinated timed actions.

Discrimination of self-generated motion and passive motion from external stimuli is fundamental to not consider our own actions as externally generated actions. Yet, both types of motion induce sensory feedback. How does the cerebellum make the difference? Self-generated and external motion should produce specific sensory consequences. The cerebellum uses the forward model to compare the prediction of these consequences to the actual sensory feedback. If the two variables of the equation do not match, an error signal may be used by the cerebellum to decrease or delete the cerebellar activity (Blankemore et al., 1998). This has been observed in monkeys: the cerebellar activity reported during voluntary

head rotation is abolished during passive head rotation (Cullen et al., 2011; Cullen & Brooks, 2015). Therefore, the cerebellum *cancels* the sensory feedback from the self-generated behavior to sort only relevant sensory information from the environment. This explains why trying to tickle oneself is a waste of time.

I.3.2 The cognitive cerebellum

Cognitive functions are well known to be associated to different brain areas as prefrontal cortex, hippocampus, basal ganglia, parietal cortex and amygdala. However, a wealth amount of recent studies demonstrate that the cerebellum contributes to non-motor tasks (D'Angelo & Casali, 2012). Studies in animals reported that the cerebellum shapes the hippocampal spatial representation during a path integration task (Rochefort et al., 2011). Functional neuroimaging investigations demonstrated the activation of specific cerebellar regions during visual attention tasks (Allen et al., 1997; Ghajar & Ivry, 2009). Other studies highlighted the involvement of the cerebellum in working memory (Justus et al., 2005).

When interacting with someone, social cognition refers to the cognitive processes to understand and regulate social behavior. Perception of emotions and feelings is based on observable information from others. More recently, clinical observations reported that the cerebellum is engaged in verbal fluency and metalinguistic (Guell et al., 2015) and contributes to social cognition through perception of emotions from the face (Hoche et al., 2016). These non-motor function are increasingly investigated nowadays.

Since the present work is focusing more on the sensorimotor part of the cerebellum, the cognitive aspect is not further developed.

I.4. When the cerebellum gets sick

I.4.1. Movement disorders

Cerebellar motor disorders severely impact the movement parameters though never suppressing it. Usual impairments are loss of coordination, tremor, altered motor metrics, simultaneous contraction of agonists and antagonists muscles (dystonia) and impaired saccadic eye movements (nystagmus). These symptoms are found in patients suffering from ataxia and cerebellar injuries.

Ataxia is an acquired, inherited or sporadic disorder of balance and coordination of movements involving the cerebellum and its afferent and efferent connections (Akbar &

Ashizawa, 2015). The symptoms can be acute after a lesion or appear slowly and progressively in the wake of genetic mutations as in the clinical cases of spinocerebellar ataxia and episodic ataxia. Dominant mutations in tens of genes have been reported in genetic forms of spinocerebellar ataxia leading to functional alteration (Walter et al., 2006) and neuronal loss (Meera et al., 2016) years before the onset of symptoms.

The pathological cerebellar phenotype is associated to the site of the lesion that can be a strokes or a tumors. Lesions in the flocculonodular lobe lead to abnormal saccadic eye movements, a phenomenon called nystagmus (Patel & Zee, 2015), and abolish the ability of the VOR to undergo adaptation (Lisberger et al., 1984). Similarly, lesions in the vermis impair the control of oculomotor saccades (Takagi et al., 2003) and decrease the latency of eyelid closure in eyeblink conditioning (Perrett et al., 1993). Clinical studies demonstrated that lesions in vermis impair gait and balance while lesions in the cerebellar hemispheres cause deficits in arms movements, resulting in an ataxic phenotype.

I.4.2. Born without cerebellum

The medical literature describes only eight cases of complete primary cerebellar agenesis, first reported by Combettes in 1831 (Combettes, 1831). In a 24-year old female patient, the posterior cranial fossa is filled with cerebrospinal fluid. For more than 20 years, she suffered from dizziness and was unable to walk steadily due to important lack of coordination and dysmetria (Yu et al., 2015). The ability to stand on her own appeared around 4 years old and walk started at the age of seven with persistent unsteady gait. The patient began to speech intelligible at 6 years old despite the persistent dysarthria and voice tremor. Hence, living without cerebellum makes basic daily life tasks extremely constraining.

Part II. Cerebellar neuronal architecture and physiology

II.1. The two main inputs

The cerebellum integrates sensorimotor and cognitive information via the two main glutamatergic inputs: mossy fibres (MF) and climbing fibres (CF).

II.1.1. Mossy fibres

The name *mossy* was given by Cajal owing to the resemblance between the shape of the termination and the Spanish moss *Tillandsia usneoides*. MFs originate in the spinal cord and different pre-cerebellar nuclei in the brainstem (***Figure I3A***). They relay sensorimotor information to the first layer of the cerebellar cortex, the granular layer, and leave collaterals in the deep cerebellar nuclei (***Figure I4***). One single myelinated MF diverges information as it makes multiple spread collaterals in the cerebellar cortex (***Figure I3Bi-Biii*** and ***I4B***; Quy et al., 2011; Wu et al., 1999).

II.1.1.1. Mossy fibres from the spinal cord

Spinocerebellar tracts gather MFs originating in the spinal cord (***Figure I3A***) and convey proprioceptive and exteroceptive information from hindlimbs and forelimbs. These tracts can be divided in 5 anatomical pathways based on lower and upper body parts.

MFs conveying sensory information from the lower body part are part of the dorsal and the ventral spinocerebellar tracts. The *dorsal spinocerebellar tract* originates in the nucleus dorsalis of Clarke (from the first thoracic to the second lumbar spinal segments). It connects to vermal lobules I-VIII, lobule X and hemispheres via the inferior cerebellar peduncle (Kitamura & Yamada, 1989; Yaginuma & Matsushita, 1989) and conveys ipsilateral information of touch, pressure, Golgi's tendons and joint position from hindlimbs (Walmsley & Nicol, 1990). The *ventral spinocerebellar tract* originates in the lumbosacral segments. It connects the vermal lobule VIII and hemispheres via the superior cerebellar peduncles (Grant & Xu, 1988; Kitamura & Yamada, 1989; Matsushita & Ikeda, 1980). Neurons composing this tract send contralateral information from wide receptive fields of the entire hindlimb (Kim et al., 1986).
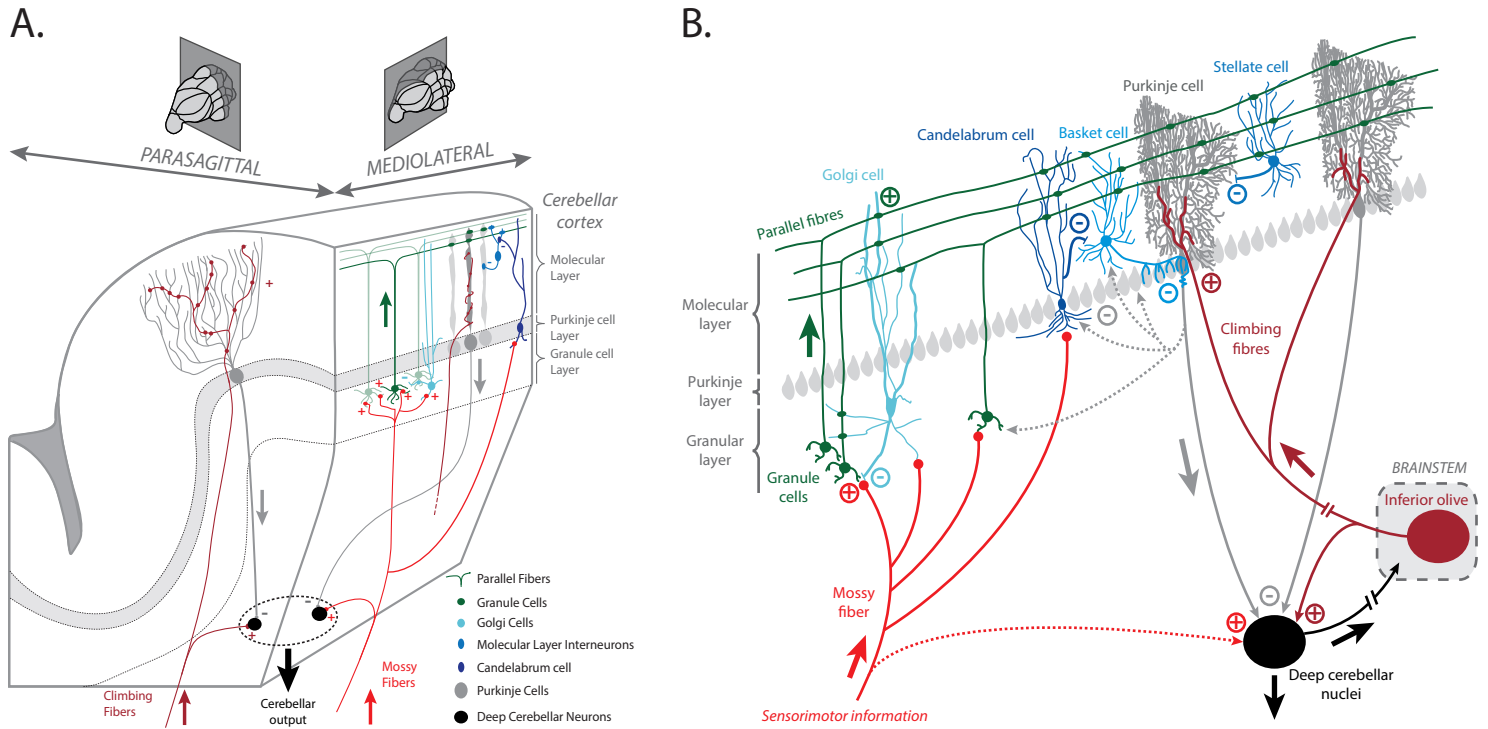
Figure I4: Neuronal architecture of the cerebellar cortex.

A) Parasagittal and mediolateral section of the cerebellum illustrating the major neuronal types. Mossy fibres and climbing fibres are the two major excitatory inputs of the cerebellar cortex and leave collaterals in the deep cerebellar nuclei.

B) Major neuronal types in the cerebellar cortex. Mossy fibres convey sensorimotor information to granule, golgi and candelabrum cells and leave colleterals in the deep cerebellar nuclei. Granule cells form excitatory contacts with Golgi, candelabrum, basket/stellate and Purkinje cells. Golgi cells provide feedback and feedforward inhibition onto granule cells. Candelabrum cells inhibit basket and stellate cells which provide feedforward inhibition onto Purkinje cells, the sole output of the cerebellar cortex inhibiting deep cerebellar nuclei. Purkinje cells also send collaterals to candelabrum, basket/stellate, granule and Purkinje cells. The deep cerebellar nuclei project out of the cerebellum and onto the inferior olive conveying integrated information through climbing fibres onto Purkinje cells. Climbing fibres leave collaterals in the deep cerebellar nuclei. Excitatory and inhibitory synapses are indicated by positive and inhibitory signs, respectively.

Arrows indicate the flow of information.

MFs carrying sensory information from the upper body part make the spinocuneocerebellar, the rostral spinocerebellar and the spinoreticulocerebellar tracts. The first two are considered as the respective forelimb homologues of the dorsal and the ventral spinocerebellar tracts. The spinocuneocerebellar pathway originates in the cervical spinal cord and involves both the cuneate and external cuneate nuclei (i.e. dorsal column nuclei, *Figure I3A*). It enters the cerebellum via the inferior peduncles. MFs from the cuneate nucleus mainly project to the lateral hemispheres (*paramedian* and *simple* lobules) while MFs from the external cuneate connect to vermal lobules I-V and VIII-IX (Quy et al., 2011). The rostral spinocerebellar pathway also originates in the cervical spinal cord. It enters the cerebellum via the inferior and the superior peduncles. The axons of this tract terminate mainly in vermal lobules IV and V and in the hemispheres to a lesser extent (Wiksten, 1985). The spinoreticulocerebellar tract starts in the central cervical nucleus and is relayed in the lateral reticular nucleus (*Figure I3A*; Bloedel, 1973). MFs from this pathway provide cuntaneous and proprioceptive signals from wide receptive fields to the whole cerebellum excepting the lobule X (Wu et al., 1999).

II.1.1.2. Mossy fibres from pre-cerebellar nuclei

Numerous pre-cerebellar nuclei send MFs to the cerebellar cortex carrying sensory and motor information from the body and the cerebral cortex (*Figure I3A*). Four pre-cerebellar nuclei give rise to the majority of MFs.

The lateral reticular nucleus (*Figure I3A*) is a crossroad of ascending and supraspinal afferents. It integrates information from the spinal cord, the cerebral cortex, the red nucleus and trigeminal nuclei. Hence, MFs from the lateral reticular nucleus provide sensory and motor information to the entire vermis, paravermis and hemispheres.

Pontine nuclei are the major source of MFs in the cerebellar cortex (*Figure I3A*). These nuclei receive inputs from all the cerebral areas (*Figure I3A*), hence relay somatosensory, visual and auditive information. Pontocerebellar MFs mainly project to the lateral hemispheres via the middle cerebellar peduncles. However, projections have been found in vermal lobules VI-IX and vestibulo-cerebellar lobule X to a lesser extent (Serapide et al., 2001).

Face proprioceptive as well as exteroceptive information are relayed in the trigeminal nuclei (*Figure I3A*). MFs originating in this nucleus connect to vermal lobules VI and VII as well as to hemispheres and lobule X (Ikeda & Matsushita, 1992) via the inferior peduncles.

MFs also originate in the vestibular nuclei (*Figure I3A*) integrating information related to balance, posture and head movements. They connect to vermal lobules I-II, paramedian lobules V-VII, lobules IX and X and hemispheres (Kotchabhakdi & Walberg, 1978; Voogd et al., 1996).

II.1.1.3. Fractured somatotopy

Spinocerebellar and brainstem terminations in the granular layer unveil a complex topography. Electrophysiological micromapping of cutaneous stimulation revealed a patchy distribution of precise receptive fields in the granular layer of Crus I, Crus II and paramedian hemisphere lobules in rats (Shambes et al., 1978). The same receptive field is encoded in multiple patches, hence giving a fractured somatotopy of the body (**Figure 5**; Apps & Hawkes, 2009; Shambes et al., 1978). Similar experiments in cats demonstrated the patchy organization of forelimb receptive fields in the paravermal lobules IV and V (Garwicz et al., 1998). Other findings in rats unveiled patches of trigeminal MFs conveying facial receptive fields signals in lateral lobules Simplex, Crus I and Crus II as well as in lobule IX (Woolston et al., 1981).

This representation is consistent with the fact that a single mossy fibre terminates in multiple areas of the granular layer (Quy et al., 2011; Wu et al., 1999). Hence, a given modality is integrated in different granule cells (GCs) spatially distributed.

II.1.2. Climbing fibres

The second glutamatergic cerebellar afferents are CFs originating in the inferior olive (IO), a nucleus in the ventral medulla (**Figure I3A**). The mammalian inferior olive is composed of 3 main nuclei: the principal olive, the dorsal and the medial accessory olives. These nuclei receive afferents from reticular formation, periaqueducal grey, mesodiencephalic junction, red nucleus, dorsal column nuclei, trigeminal nuclei, spinal cord and cerebral cortex hence integrating somatosensory, visual and motor information (Berkley & Worden, 1978). Olivary neurons are electrically coupled via gap junctions to synchronize oscillatory activity (Llinas et al., 1974; Sotelo et al., 1974). Each CF directly targets primary and secondary dendrites of several PC (**Figure I3Bii**), principal neurons of the cerebellum and sole output of the cerebellar cortex (**Figure I4**). In contrast, a PC is contacted by a single CF making a thousand of excitatory synapses with PCs and leaving collaterals in the deep cerebellar nuclei (**Figure I4**; Wlklund et al., 1984). CFs are so named because they wrap around PCs dendrites like a vine on a tree.
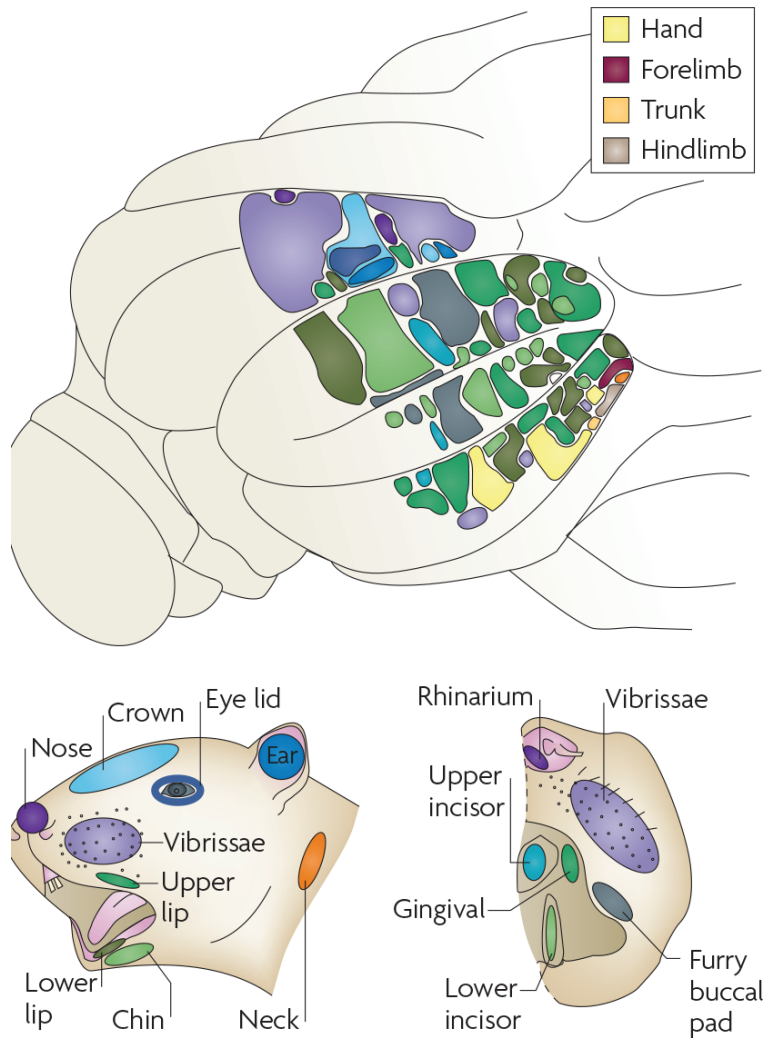
Figure I5: Fractured somatotopy of mossy fibres.

Dorso-posterior view of the left hand side of the rat cerebellum showing the spatial distribution of receptive fields recorded in the granular layer in response to mechanical stimulation of different body parts as detailed in the panels below. Note the multiple representations of the same body parts to produce a "fractured somatotopical" mosaic pattern of variable sized patches. *From Apps & Hawkes, 2009*.

The IO integrates instructive signals to promote cerebellar learning and timing processing (De Zeeuw et al., 1998). A typical behavioral model to illustrate this function is pavlovian eyeblink conditioning. An air puff (i.e. the *unconditional* stimulus conveyed by MFs) is applied on the cornea after a precise time interval following a tone (i.e. the *conditional* stimulus conveyed by CFs). The animal learns to associate both stimuli to close the eyelid at the right time after the tone without air puff (Mauk & Ruiz, 1992). CFs provide a teaching signal conveyed to the cerebellar cortex to prevent or induce extinction of the conditioned response (Medina et al., 2002) and regulate timing via synaptic plasticity in PCs (Ito, 2001; Ito & Kano, 1982; Suvrathan et al., 2016).

II.2. The cerebellar cortex

Despite the macroscopic isotropy of the cerebellum, the cerebellar cortex is compartmentalized into anatomically stereotyped but molecularly and functionally distinct microcircuits standing at the basis of its modular organization (*see section II.5*). Each of these circuits is divided in three distinct layers containing specific neurons and glial cells: the granular, the molecular and the Purkinje layer (***Figure I4***). Unipolar brush, Lugaro and globular cells are not introduced as they are not targeted by GCs and are not part of the project.

II.2.1. Input stage: the granular layer

The granular layer stands has the input layer of the cerebellar cortex. It receives MFs inputs and is mainly composed of glutamatergic GCs, and inhibitory Golgi cells (GoC) to a lesser extent (***Figure I4B***). The volume of the granular layer represents 41% of the total cerebellar volume in mice and 27% in rats (Harvey & Napper, 1991).

II.2.1.1. The granule cell

GCs represent the most numerous neurons in the nervous system and are densely packed in the granular layer ($1.77.10^4$ cells/mm^2, Harvey & Napper, 1991). The soma diameter is 5.5 µm with 3 to 5 emerging small thin dendrites ending in claws. MFs from different origins (Huang et al., 2013) connect to the dendritic claws making a big structure called glomerulus. In addition, recent finding reported that GCs receive inhibitory collaterals from PCs (***Figure I4B***; Guo et al., 2016). This connectivity is prominent in lobules regulating eye movements and processing vestibular information (i.e. lobules VI, IX and X).

The amyelinated axon of GCs is composed of two segments. The first segment emerges from the soma and ascends perpendicularly to the granular layer (***Figure I4B***). The

ascending axon separates as a "T-shaped" bifurcation in the molecular layer hence forming parallel fibres (PF), the second segments (***Figure I4B***). Beams of PFs bilaterally extend up to 2 mm length in mice (Huang et al., 2006) and 4.7 mm length in rats (Harvey & Napper, 1991; Pichitpornchai et al., 1994).

Both ascending axon and PFs display a high density of small varicosities called *ascending* and *en-passant* boutons, respectively (***Figure I4B***). Although the size of varicosities is variable, smallest have an average area of 0.58 μm^2 while biggest have an area of 1.59 μm^2 (Zhang & Linden, 2009, 2012). The intervaricosity interval increases as one moves away from the T zone to the extremity of the PF and ranges from 1 μm to 14 μm with an average of 5.2 μm in rats (Pichitpornchai et al., 1994). Recent data in mice reported similar intervaricosity intervals ranging from 2 to 17 μm with a mean of 5.5 μm (Lanore et al., 2021). The mean density of varicosities on the ascending axon is estimated at 0.106 varicosities/μm while PFs count 0.146/μm (Huang et al., 2006).

A single GC forms excitatory contacts with dendrites of multiple neurons in the molecular layer (***Figure I4B***). The majority (91%) of these contacts are monosynaptic, although double synapses induced by motor learning (Federmeier et al., 2002) have been reported on PCs spines (Pichitpornchai et al., 1994). In contrast with PFs, the ascending axon forms multiple synapses with inhibitory interneurons such as GoCs (Cesana et al., 2013; Hámori, 1981), molecular layer interneurons (MLI, Sultan & Bower, 1998) and likely with a single PC. As the PF runs long distances in the molecular layer, the high number of boutons make synapses mainly on dendritic spines of PCs (Napper & Harvey, 1988b; Palay & Chan-Palay, 1974; Pichitpornchai et al., 1994) as well as on smooth dendrites of MLIs, GoC and candelabrum cells (CC, ***Figure I4B***; Osorno et al., 2022) to a lesser extent. The ratio of PF to PC versus PF to inhibitory cells is estimated at 9/1 (Pichitpornchai et al., 1994).

The present work focuses essentially on the functional aspect of single PF boutons in mice. The functional connectivity of GCs and the dynamic properties of its boutons are respectively detailed in *section II.4* and *section III*.

II.2.1.2. The Golgi cell

Discovered by Camillo Golgi in 1873, Golgi cells are inhibitory interneurons in the cerebellar cortex whose soma is localized in the granular layer (***Figure I4B***). The huge dendritic tree is ramified in apical and basolateral dendrites. Apical dendrites extend in the sagittal plane of the molecular layer with a poor mediolateral diffusion (Sillitoe et al., 2008) while basolateral dendrites are restricted to the granular layer and extend in the mediolateral

axis. The axonal plexus is densely branched and is restricted to the granular layer making inhibitory contacts with GCs dendrites in a large volume (Palay & Chan-Palay, 1974).

Subtypes of GoCs have been identified based on morphology, neurochemical markers and receptors (Geurts et al., 2001; Simat et al., 2007). GoCs release both γ-Aminobutiryc acid (GABA) and glycine although some release either GABA or glycine to a lesser extent. Golgi cells are activated by local GCs (Valera et al., 2016) via both the ascending axon (Cesana et al., 2013) and parallel fibres on basolateral and apical dendrites, respectively. GoCs projection onto their target provides an inhibitory feedback loop on GCs (*Figure I4B*; Holtzman et al., 2011). Although the contact of the GoC and the GC is axo-dendritic, the GoC can also form an axo-axonal contact with the MF in the glomerulus. This influences the activity of the MF hence modulating the synaptic integration in the GC (Mitchell & Silver, 2000). In parallel, basolateral dendrites also receive inputs from MFs (Kanichay & Silver, 2008) consequently providing feedforward inhibition to modulate GCs excitability (*Figure I4B*; Jörntell & Ekerot, 2006). Gap junctions on basolateral dendrites electrically couple GoCs to trigger oscillatory synchronized activity providing rhythmic inhibition of GCs (Maex & Schutter, 1998; Simões de Souza & De Schutter, 2011; Vervaeke et al., 2010). This synchronicity is important to integrate sensorimotor information conveyed by MFs (Dugué et al., 2009).

II.2.2. Intermediate stage: the molecular layer

The molecular layer accounts for 41% of the total cerebellar volume (Harvey & Napper, 1991) and takes into account GCs axons, neuronal dendrites and GABAergic molecular layer interneurons (MLI, Gabbott et al., 1986).

II.2.2.1. Two morphological distinct interneurons: Basket cells and Stellate cells

MLIs are the only cells whose soma is localized in the molecular layer and morphological studies identified two distinct groups: basket and stellate cells (BC, SC, *Figure I4B*; Palay & Chan-Palay, 1974; Sotelo, 2015; Sultan & Bower, 1998). Both expand their smooth dendrites in the parasagittal plane. In addition to excitatory PFs inputs, quantitative ultrastructural studies reported that MLIs receive other inputs on the basis of their location in the molecular layer. Those in the deepest zone are connected to a large amount of PFs and some inhibitory inputs from PCs collaterals mostly on the soma (*Figure I4B*; Larramendi & Lemkey-Johnston, 1970; Lemkey-Johnston & Larramendi, 1968; Witter et al., 2016). MLIs in the inner third, the area of BCs, receive axo-somatic and axo-dendritic PFs inputs, lesser amount of MLIs contacts (Rieubland et al., 2014) and PC collaterals (*Figure I4B*). Finally, the ones in the outer third, the area of SCs, receive only PFs (*Figure I4B*) and few SCs inputs

(Lemkey-Johnston & Larramendi, 1968; Rieubland et al., 2014). However, the boundary between the BCs zone and the SCs zone is not clear as MLIs in the middle third share morphological features with both types, hence considering MLIs as a continuum (Sultan & Bower, 1998). In addition to these chemical inputs, MLIs are electrically coupled via gap junctions in the same sagittal plane (Alcami & Marty, 2013; Rieubland et al., 2014; Sotelo & Llinás, 1972) and can be activated by CFs via glutamate spillover (Szapiro & Barbour, 2007).

The amyelinated axon extends in the parasagittal plane and is the main criteria to distinguish both types. The BCs axon spreads basally leaving collaterals forming nests around multiple PCs soma (***Figure I4B***). Distal portions of nest-like collaterals form a vortex-like arrangement called *pinceau* on the axonal initial segment. This peculiar structure is devoid of chemical synapses and provides ultrafast ephaptic inhibition of PC activity (Blot & Barbour, 2014): loops of positive charges around the PC initial segment prevent the action potential genesis. In addition, some axonal branches ascend in the molecular layer to form rare synapses on PCs distal spines (Sotelo, 2015). Unlike BCs, the axon of SCs spread in the PC dendritic tree to make inhibitory chemical synapses (***Figure I4B***).

II.2.2.2. Toward a molecular and physiological identification

Nowadays, morphology and localization are the only criteria to distinguish BCs and SCs. Investigations are being carried out to find specific molecular markers as well as physiological properties. Transcriptomic and electrophysiological investigations from the group of Regehr recently identified two populations of MLIs named MLI1 and MLI2 (Kozareva et al., 2021). Interestingly, the expression of connexin 36, the main subunit forming gap junction, is only present in MLI1. The spontaneous firing rate is higher in MLI1 while MLI2 are more excitable. However, both populations take into account BCs and SCs morphologies organized as a continuum, hence demonstrating the existence of subpopulations of BCs and SCs.

II.2.3. Output stage: the Purkinje layer

In between the granular and the molecular layer stands the Purkinje cell layer containing large, perfectly aligned cellular bodies as well as small interneurons (***Figure I4***).

II.2.3.1. The Purkinje cell

One of the most beautiful and impressive neurons of the central nervous system is undoubtedly the Purkinje cell, the sole output of the cerebellar cortex (***Figure I4B***). The peer-shaped soma has a diameter of approximately 20 µm (Takács & Hámori, 1994). A massive planar dendritic tree emerges from the soma and expands in the parasagittal plane of the

molecular layer covering a mean area of 8000 µm² (Nedelescu et al., 2018). The dendritic arbor is composed of one thick proximal dendrite, sometimes two (Nedelescu et al., 2018; Nedelescu & Abdelhack, 2013), ramifying into smaller secondary and tertiary branches. Secondary and tertiary dendrites are covered by an exquisite high density of spines – 17.2 spines/µm (Napper & Harvey, 1988a). On each PC dendritic arbor, the total number of spines is estimated between 154000 and 175000 (Napper & Harvey, 1988a).

A single PC receives up to 175000 granule cell synaptic contacts on secondary and tertiary dendrites (Palay & Chan-Palay, 1974), of which 85% are silent (Ho et al., 2021; Isope & Barbour, 2002) and only 50 need to be simultaneously active to elicit an action potential (Barbour, 1993). This compartment of the dendritic arbor also receives hundreds of MLIs terminals (**Figure I4B**). Unlike secondary and tertiary dendrites, proximal dendrites receive a thousand of synapses from a single CF directly on the dendritic shaft (**Figure I4B**). As PCs spontaneously fire action potentials around 50 Hz (Gruol & Franklin, 1987; Häusser & Clark, 1997; Latham & Paul, 1971), both excitatory and inhibitory inputs shape the spatiotemporal features of the output pattern (*see details section III.2.3.3*).

The majority of projection neurons in the central nervous system are glutamatergic. Surprisingly, PCs break the rule since they release GABA on their targets inside and outside the cerebellar cortex. As mentioned previously, the myelinated axon connects to GCs and MLIs dendrites via few collaterals mainly in the parasagittal plane (**Figure I4B**). It also makes inhibitory synapses onto the soma of other PCs (Witter et al., 2016) as well as candelabrum cells (CC, **Figure I4B**; Osorno et al., 2022). Spatially, PCs collaterals are restricted to a parasagittal zone in the cerebellar cortex. Such a negative feedback gives the output the ability to locally regulate the information processing via a fine control of the firing rate.

The axon progresses toward the white matter to connect to neurons localized in the output nuclei of the cerebellum (**Figure I4B**). PCs localized in lobules IX and X target the vestibular nuclei while PCs in the anterior vermis, paravermis and lateral hemispheres mainly target neurons in the deep cerebellar nuclei (**Figure I2C**).

II.2.3.2. The Candelabrum cell

Almost thirty years ago, Lainé & Axelrad gave the name *candelabrum* to a mysterious neuronal subtype they discovered as it looks like a candelabrum (Lainé & Axelrad, 1994). CCs are uniformly distributed in the cerebellum. The majority of the dendritic arbor emerges from the cell body (10 µm in diameter) located between PCs soma (**Figure I4B**). It expands up to 150 µm in the parasagittal plan and less than 50 µm in the mediolateral axis of the molecular

layer. Some basal dendrites emerge from the lower pole of the soma and span up to 100 μm in the upper part of the granular layer. Both apical and basal dendrites are covered by thin, irregularly distributed spines. Oddly, the ramified beaded axon can originate from a proximal dendrite. It ascends vertically in the parasagittal plane and ends in the upper part of the molecular layer.

More recently, the lab of Regehr provided *ex vivo* molecular, electrophysiological and connectivity characterization of the CC within the cerebellar cortex (Osorno et al., 2022). CCs are excited by two glutamatergic inputs. GCs, via the PFs, connect to the dendritic arbor in the molecular layer while MFs connect to the basal dendrites (***Figure I4B***). The source of inhibition comes from PCs collaterals connecting to the basal dendrites of CCs. In turn, CCs make axo-dendritic inhibitory synapses mainly on MLIs (***Figure I4B***), but also on PCs and GoC to a lesser extent. The authors reported that CCs are GABAergic even though the hypothesis of a GABA/glycine co-release is not excluded. Therefore, the CC weights both cerebellar inputs and outputs to control the flow of information and modulate the output.

Further investigations are required to understand the functional contribution of CCs in the cerebellar circuitry.

II.2.3.3. The Bergmann glia

Bergman glial cells are astrocytes which soma is localized between PCs. Their projections form radial fibres in the parasagittal plane and extend in the whole molecular layer to ensheathe the soma and dendritic spines of PCs. The radial fibres make microdomains around excitatory and inhibitory synapses onto PCs (Palay & Chan-Palay, 1974).

Bergmann glia express glutamate transporters mediating glutamate uptake (Bergles et al., 1997), Ca^{2+}-permeable α-amino-3-hydroxy-5-methyl-4-isoxazolepropionic acid (AMPA) receptors around PF-PC synapses (Bellamy & Ogden, 2005), GABA-A receptors around inhibitory synapses (Riquelme et al., 2002) and tonically release GABA (Lee et al., 2010). These investigations suggests that Bergmann glial cells actively modulate synaptic transmission.

II.3. The cerebellar outputs

The cerebellar cortex do not directly target the effective structures of an apparatus but passes by multiple nuclei to connect to them. It sends PCs axons toward the two outputs of the cerebellum: the deep cerebellar nuclei and the vestibular nuclei (***Figure I2D***, ***I3C*** and ***I4***).

In turn, neurons in both structures connect to motor as well as non-motor areas in the brainstem, the spinal cord and the neocortex.

II.3.2. The deep cerebellar nuclei

The deep cerebellar nuclei (DCN) are embedded in the white matter of the cerebellum. In rodents, four nuclei can be distinguished in the mediolateral axis: *medial*, *anterior/posterior interposed* and *lateral* (***Figure I2D***). They stand as the output of the vermis, the paravermis/lateral hemisphere and the lateral hemisphere, respectively (***Figure I2C-D***). PCs projections are the major source of connections in the DCN (De Zeeuw & Berrebi, 1995). One single neuron receives about 40 PCs inputs giving rise to a high degree of convergence from the cerebellar cortex to the cerebellar output (Person & Raman, 2012). However, only a small fraction of synchronized PCs is sufficient to influence the activity of the DCN neuron (Özcan et al., 2020; Person & Raman, 2012). In addition to a strong inhibition, neurons in the DCN also receive excitatory inputs from MFs and CFs collaterals (***Figure I4B***; Najac & Raman, 2017; Ruigrok, 1997; Shinoda et al., 2000; Shinoda et al., 1992; van der Want et al., 1989).

Each DCN contains a heterogeneous population of small GABAergic and a mix of large and small glutamatergic projecting neurons (Uusisaari et al., 2007). Inhibitory neurons are subdivided into GABAergic neurons projecting to the inferior olive (Ruigrok, 1997) and local GABAergic and/or glycinergic interneurons (Husson et al., 2014; Uusisaari & Knöpfel, 2008). The characterization of these neuronal populations has been established on the basis of intrinsic electrophysiological properties as well as on targets (Najac & Raman, 2015; Özcan et al., 2020; Uusisaari & Knöpfel, 2008; Uusisaari et al., 2007). On the other hand, the lab of Sascha Du Lac recently identified 5 subtypes of glutamatergic neurons in the fastigial nucleus based on gene expression, morphology, distribution and connectivity (Fujita et al., 2020). Each of these neurons connects to specific motor and non-motor neuronal structures via the thalamus (Aumann et al., 1994; Shinoda et al., 1993), the periaqueducal gray (Vaaga et al., 2020), the mesodiencephalic junction (Wang et al., 2021), the red nucleus (Flumerfelt et al., 1973), the tectum and the spinal cord (***Figure I3C***; Bharos et al., 1981).

Inputs from PCs on nucleo-olivary neurons emphasize a tight topographical organization between the cerebellar cortex, the DCN and the IO. This olivo-cortico-nulear loop is introduces in *section II.5*.

II.3.1. The vestibular nuclei

The vestibular nuclei (or vestibular complex) are a sensory-motor crossroad divided in four distinct nuclei: *inferior*, *lateral*, *medial* and *superior* nuclei. The lateral nucleus receives the densest cerebellar inputs arising from the vermal B zone, a sagittal stripe across lobules I-V processing tactile information from limbs (Andersson & Oscarsson, 1978; Voogd et al., 1991). Subsets of neurons in the lateral nucleus give rise to multiple vestibulospinal tracts whose targets stand at different levels in the spinal cord (Barmack, 2003; Büttner-Ennever, 1992; Rose et al., 1992). The lateral vestibulospinal tract is organized topographically in the lateral nucleus. The *dorso-caudal lateral* nucleus connects to motoneurons in the lumbosacral spinal cord allowing cerebellar inputs to provide adaptation of axial and extensor muscles (Büttner-Ennever, 1992). The *rostro-ventral lateral* nucleus projects on upper cervical motoneurons (Rose et al., 1992) innervating neck muscles thus mediating cerebellar control of head position relative to the body. Therefore, cerebellar projections onto the lateral nucleus provide adjustments of posture, gait and vestibular reflexes.

Neurons in the medial, inferior and superior nuclei receive dense projections from PCs located in lobules IX and X (***Figure I2C***; Bernard, 1987; Tabuchi et al., 1989; Wylie et al., 1994). These nuclei project to nuclei connected to extraocular muscles (oculomotor, trochlear and abducens nuclei; Barmack, 2003; Büttner-Ennever, 1992) and cervical motoneurons innervating neck muscles. Hence, cerebellar projections in these nuclei provide adaptation of voluntary and non-voluntary eye movements (i.e. VOR) as well as head stabilization in space.

II.4. Functional connectivity in the cerebellar cortex

The cerebellar cortex integrates multiple information from the whole body to compute proper output. To understand this computation, it appears fundamental to focus on (1) how sensorimotor information conveyed by MFs flow in the cerebellar microcircuit and (2) how they are processed in the granular layer and the PC.

II.4.1. Flow of sensorimotor information

Sensorimotor information take into account sensory modalities (i.e. proprioception, somatosensory, vestibular) and motor information (i.e. efferent copy of the motor command). These information carried by MFs are conveyed in the granular layer (***Figure I4B***) as bursts of action potentials at wide range frequencies, up to 1 kHz (Bengtsson & Jörntell, 2009; Rancz et al., 2007). Such relevant information are evoked by a stimulus (e.g. cutaneous stimulation) but events not associated to the signal (i.e. low-frequency spontaneous activity) must be

filtered out. The small compact morphology of GCs is associated to poor dendritic filtering and high excitability (Chadderton et al., 2004; Delvendahl et al., 2015). *In vivo* electrophysiological recordings demonstrated that GCs require at least two converging MFs inputs to fire action potentials during evoked tactile stimulations (Jörntell & Ekerot, 2006). *In vitro* recordings during single MF stimulations reported that MF elicits fast action potential bursts in GCs (Rancz et al., 2007) through the activation of AMPA and N-methyl-D-aspartate (NMDA) receptors. Such a fast transmission is enhanced by glutamate spillover from neighboring active zones in the glomerulus (DiGregorio et al., 2002; Powell et al., 2015). Similarly, during locomotion, the fast firing pattern of GCs reliably reflects the pattern of activity of MFs terminals (Powell et al., 2015). This temporal precision of GCs firing has been shown to increase with age (Cathala et al., 2003). Hence, the MF-GC synapse provides reliable transfer of sensorimotor information (Rancz et al., 2007).

One single GC receives information from MFs originating in different pre-cerebellar nuclei (Huang et al., 2013). Such a convergence gives the GC the capacity to encode and transfer multiple modalities (e.g. proprioception from the external cuneate and motor command from the pontine nuclei). This finding is in line with the discovery of electrophysiological signatures of a particular input involving short-term plasticity (*see section III.2* and **Figure I13**; Chabrol et al., 2015). Hence, GCs encode accurate representations of the body through multimodal integration.

GCs expand MF inputs in the molecular layer via the ascending axon and the PFs. Consequently to their activation, GCs emit bursts of action potentials up to 1 kHz (Chadderton et al., 2004; Jörntell & Ekerot, 2006) reliably transferred to PCs (Valera et al., 2012) as well as to GoCs, MLIs and CCs. As previously described, GoCs mediate feedback and feedforward inhibition onto GCs when activated respectively by GCs and MFs. In parallel, MLIs activated by GCs provide feedforward inhibition onto PCs. Electrical stimulations of GCs elicit excitatory postsynaptic currents in the PC followed by inhibitory currents with a delay of 1-2 ms (Mittmann et al., 2005). Feedforward inhibition improves temporal precision of postsynaptic action potentials by preventing asynchronous inputs (Mittmann et al., 2005), provides bidirectional changes in PCs firing during locomotor behaviors (Jelitai et al., 2016) and expands PCs dynamics (*see section III.2.3.3*, **Figure I15**; Grangeray-Vilmint et al., 2018). Interestingly, the activation of CCs by GCs inhibits the feedforward inhibition (Osorno et al., 2022). Such a connectivity provides disinhibition of the PC which in turn controls the activity of the CC hence forming a loop of oscillatory activity.

One single PC encodes a wealth amount of sensorimotor information generated by locomotion (Powell et al., 2015) as well as whiskers position during voluntary movements (Chen et al., 2016) through a body of GC inputs. As PCs have a pacemaker intrinsic activity, relevant sensorimotor information either decelerates or accelerates the firing pattern via feedforward excitation and inhibition with precise temporal delays (Grangeray-Vilmint et al., 2018). Selection of relevant inputs is under the control of the CF which triggers plasticity mechanisms at PF-PC synapses (*see sections II.4.2.2 and II.4.3.1*).

This connectivity stands at the basis of the Marr-Albus-Ito theory considering the cerebellum as a structure shaped for pattern separation and supervised learning.

II.4.2. The cerebellum as a neuronal machine: Marr-Albus-Ito theory

II.4.2.1. Pattern separation in the granular layer

Interacting with the environment involves detection of subtle changes from a global framework containing multiple elements (***Figure I6Ai***). The perception of the framework generates specific sensorimotor information in the brain represented by spatiotemporal patterns of activity in neuronal populations (***Figure I6Aii-Aiii***). To detect subtle changes, the neuronal network must discriminate similar patterns of activity. This process can be referred to *pattern separation*.

David Marr developed a model emphasizing pattern separation in the cerebellar cortex (***Figure I6Aii***): input information carried by a small amount of MFs should be transferred to a large number of GCs which activation threshold is regulated by a feedback inhibition (Marr, 1969). The MF information is recoded in a larger neuronal population, a process called *expansion recoding*. Each GC of this large population requires a combination of MFs to be activated (***Figure I6B-C***). This promotes sparseness of activated GCs in the granular layer hence implementing *sparse coding*. Both expansion recoding and sparse coding work together to reduce the overlap between spatiotemporal patterns. This process articulates the granular layer as a pattern separator of sensorimotor information.

In parallel, James Albus developed an independent theory on pattern separation (Albus, 1971). He argued that trial-to-trial patterns of activity carried by MFs are restrained to a low-dimensional space where each dimension represents the activity of one MF (i.e. *dimensional coding*; ***Figure I6Aiii***). In this space, each point is associated to a trial of the pattern activity encoded in each neuron (i.e. in each dimension). The transfer to a higher number of neurons (i.e. GCs) involves additional dimensions that increase the linear separability of each pattern (e.g. a cloud of birds can be better visualized in a 3D space rather
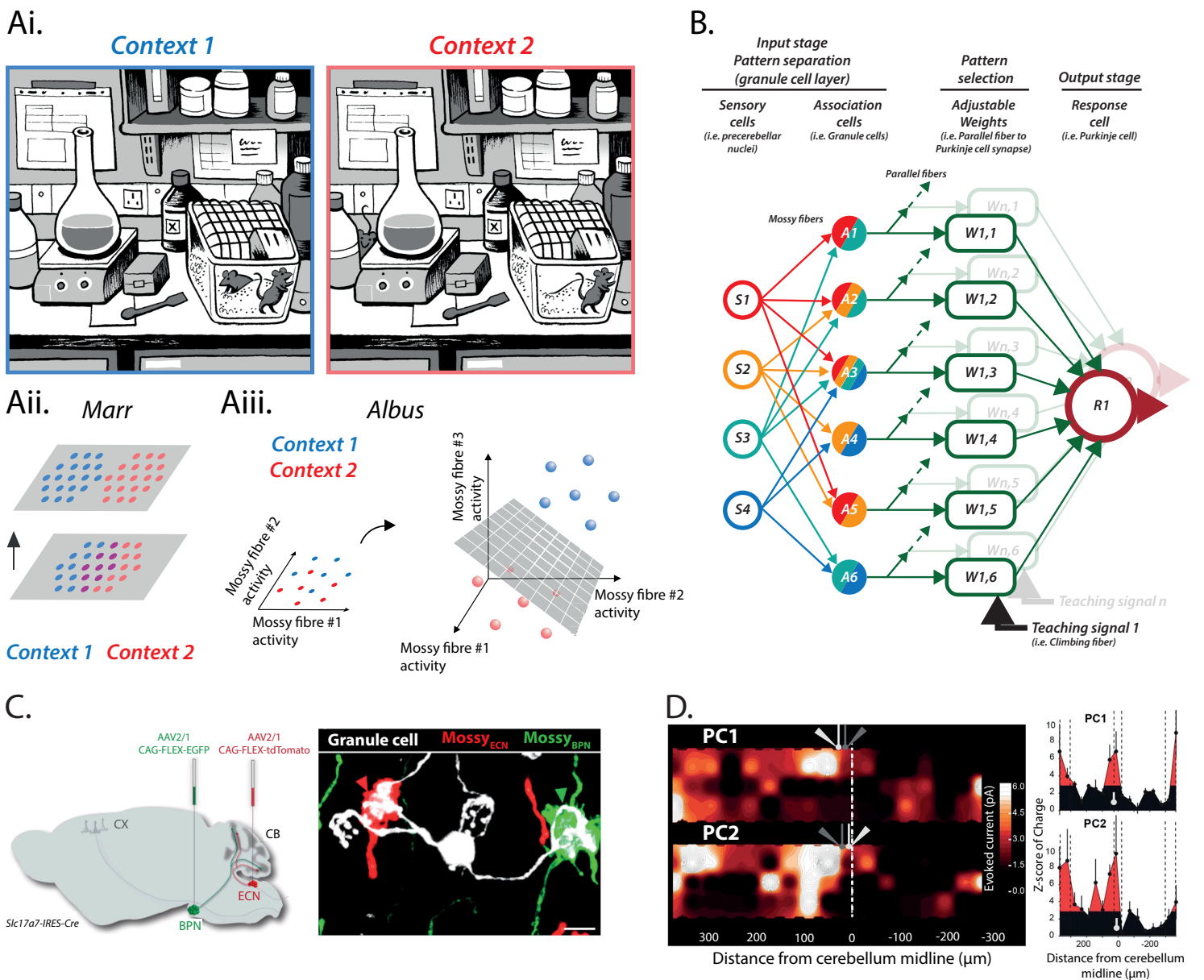
Figure I6: Marr-Albus-Ito model for pattern separation and supervised learning.

A) Illustration of Marr and Albus models for pattern separtion. *Ai*, Spot the difference. This classic children's puzzle requires the reader to hunt for small differences between two near-identical images. In this example, however, the relocation of the escaped mouse is immediately clear. This demonstrates the brain's ability to recognize small differences between similar scenes. Illustrastion by Matteo Farinella. *Aii*, Marr hypothesized that neural activity patterns by activating distinct ensembles of neurons. Neurons that are active under context 1 are shown in blue, and those active under context 2 are shown in red. Gray represents neurons that are silent in both contexts. *Aiii*, Albus argued that the cerebellar cortex separates patterns in neural activity space by expanding the dimensionality, enabling a downstream decoder neuron to linearly classify them. Blue or red represents neural activity patterns in different trials during context 1 or 2. Gray inclined plane indicates hyperplane in activity space that separates the two contexts. ***From Cayco-Gajic & Silver, 2019***.

B) Cerebellar cortex as a perceptron algorithm based on Marr, Albus and Ito models. Mossy fibres from precerebellar nuclei and spinal cord (S1-S4) scatter sensorimotor information (i.e. patterns of activity) in the granular layer to multiple granule cells (A1-A6). Granule cells associate modalities from different mossy fibres. Synaptic weights of parallel fibre to Purkinje cell synapses are tuned by the climbing fibre to select relevant patterns. The Purkinje cell fires only under specific sensorimotor context. ***Adapted from Spaeth L. (2019) Modular information processing in the cerebellar cortex.***

C) Combination of mossy fibres on a single granule cell. ECN and BPN mossy fibres (right) are specifically labeled using adeno-associated viruses expressing tdTomato and EGFP. *BPN, basopontine nuclei; ECN, external cuneate nucleus.* ***Adapted from Huang et al., 2013***.

D) Neighboring Purkinje cells share similar sparse granule cell input patterns. Two neighboring Purkinje cells (PC1 and PC2) are simultaneously recorded during glutamate uncaging. *Left*, Map of the recorded synaptic charge measured in PC1 (white cell, top) and PC2 (white cell, bottom). Right, Corresponding mediolateral granule cell connectivity pattern to PC1 and PC2 expressed as Z-score of synaptic charge. Only red spots indicate active sites (i.e. eliciting detectable currents in PCs). PC positions are indicated in white. ***Adapted from Valera et al., 2016***.

34

than in a 2D space). Dimensional coding is determined by the size of the neuronal population, which is set by the sparseness of GCs activated by a combination of MFs (*Figure I6B-C*), and the dynamic range of activity of each neuron. Hence, expansion recoding and sparse coding together map the set of patterns in a higher-dimensional space to reduce pattern overlap (*Figure I6Aiii*).

Conversely, Wagner and colleagues reported that the similar task-encoding activity between cortical layer 5 of the neocortex and granule cells is reliably represented in a low-dimensional space rather than a high-dimensional space (i.e. only few GCs, Wagner et al., 2019). As high dimensional recoding can also amplify noise, they speculated that the granular layer sacrifices dimensions to avoid cortical noise expansion.

Another problem of dimensional recoding is related to trial-to-trial diversity. Neurons with highly variable trial-to-trial pattern of activity tend to fill the whole subspace. This variability adds noise in the system hence increasing the probability of overlapping activity patterns. Averaging patterns of activity or reducing the variability are two possible strategies for neurons to increase signal-to-noise ratio. GCs adopted two main strategies: (1) a high firing threshold associated to a compact morphology for a high excitability (Delvendahl et al., 2015), and (2) integration of multiple MFs inputs on a single GC (*Figure I6B-C*; Chabrol et al., 2015; Huang et al., 2013; Ishikawa et al., 2015; Jörntell & Ekerot, 2006). Moreover, the negative feedback provided by GoCs decreases the excitability of GCs and increases the firing threshold (Hamann et al., 2002). Such an inhibition could modulate the signal-to-noise ratio by requiring multiple MFs to elicit firing in the GC (Jörntell & Ekerot, 2006).

In a dense population of GCs activated in the same temporal window, the sparseness of pattern activity is poor and forms a redundant code. The reduction in the number of activated GCs via the GoCs-mediated tonic negative feedback (*Figure I4B*) reduces the density of the population thereby increasing sparse coding and pattern separation (Hamann et al., 2002). However, how synchrony of GoCs contribute to pattern separation is still under debates. A hypothesis is that synchronized GoCs silence a population of GCs while their desynchronization specifically silence a small amount of GCs to provide sparse coding.

Recent investigation emphasize the connectivity sparseness at GC-PC and GC-MLI synapses (Spaeth et al., 2022; Valera et al., 2016). Patch-clamp recordings of GC-PC synaptic currents in cerebellar slices evoked by photostimulation of caged glutamate in patches of the granular layer revealed that neighboring PCs are always actively connected to local GCs (*Figure I6D*). However, patches of distant GCs are either actively connected or silent and two neighboring PCs receive similar GC inputs. Although MLIs connectivity maps differ from PCs,

they are similarly organized with local and distal GCs patches. This organization supports sparse coding and is correlated to behavioral performance (Spaeth et al., 2022): connectivity maps undergo rearrangement after locomotor impairments to compensate motor deficits.

Despite these results, recent experimental investigations are considering more and more dense coding with redundancy in neuronal activities during learning tasks (Gilmer & Person, 2018; Giovannucci et al., 2017; Knogler et al., 2017; Wagner et al., 2019; Wagner et al., 2017). In all these studies, Ca^{2+} imaging has been performed in GCs. Giovannucci *et al.* reported that correlation of GCs activities is necessary during eyeblink conditioning (*see section II.1.2*, Giovannucci et al., 2017). As learning progressed, the density of GCs responding to the conditional stimulus increases and trial-by-trial patterns of activity correlate to form a redundant code. Such a redundant code combined with dense coding favor low-dimensional representation of behaviors. However, technical issues may underlie this discrepancy. GCaMP6, the Ca^{2+} sensor used in these studies, do not provide the temporal resolution required to discriminate patterns of activity thereby gathering signals from single GCs into a common pattern.

The Marr-Albus model on pattern separation is still supported and has been extended, even though recent biological and computational investigations are re-evaluating the circuit mechanistic underlying this theory (Cayco-Gajic et al., 2017; Cayco-Gajic & Silver, 2019). Decorrelation of neuronal activities is a recent parameter currently explored and requires sparse coding (Cayco-Gajic et al., 2017) to provide high-dimensional pattern separation.

Pattern separation is an essential preprocessing step to split global sensorimotor information into more specific sensory cues (i.e. patterns). Therefore, it plays an important role for supervised learning.

II.4.2.2. Supervised learning by climbing fibre inputs

Storage capacity of PCs is driven by the extensive convergence of PFs. In their theories, both Marr and Albus emitted a second fundamental statement for pattern selection, the *supervised learning* by a teaching input (***Figure I6B***; Albus, 1971; Marr, 1969). The conjunctive activation of a PF with the CF should selectively change synaptic weights at unitary PF-PC connections in order to select relevant patterns of information (***Figure I6B***). Marr considered the weight being potentiated – *[…] the efficacy of that synapse is **increased**'* (Marr, 1969). Conversely, Albus speculated that the conjunctive activity of the PF and the CF decreases the activity of irrelevant synapses: *[…] if the response cell fires when it should not fire, then all synapses coming from active parallel fibers will be **weakened**; otherwise, no*

adjustments are made (Albus, 1971). The lab of Masao Ito confirmed experimentally Albus statement (Ito & Kano, 1982): the conjunctive activation of both PF and CF decreases the activity of the PF-PC connection, a process known as long-term depression (*see section II.4.3.1*). The prevailing model states that CF is activated when the executed movement is erroneous to avoid the repetition of the same motor error. However, growing evidences demonstrate that the CF is also recruited for learning of sensorimotor associations (Hull, 2020). In eyeblink conditioning (*see section II.1.2*), the CF activates after the onset of the conditional stimulus and undergoes extinction to predict the onset of the unconditional stimulus when omitted (Ohmae & Medina, 2015). Similarly, in a reward-based task cued by a sensory stimulus, the activity of the CF increases in a scalar fashion to predict the upcoming reward and is enhanced when the reward is not delivered indicating reinforcement learning (Heffley et al., 2018).

Pattern separation is a fundamental preprocessing step for supervised learning as it splits a sensorimotor information into distinct cues (i.e. patterns; ***Figure I6B***). Only relevant patterns are selected by the CF teaching signal on the PC dendritic tree. This enabled Albus to consider the cerebellum as a *perceptron-based algorithm* (***Figure I6B***; Rosenblatt, 1958): discriminated inputs converge toward the output in a feedforward manner. Each pattern of activity (i.e. activated PFs) is weighted. The linear summation of relevant weighted patterns leads to exceeding the activation threshold, hence eliciting firing in the output element. The weights are gated by an external trigger during learning to keep only relevant connections and consolidate the network.

Despite a divergent starting point, Marr and Albus predicted the cerebellar pattern separation and supervised selection of patterns during learning. The model is still supported and keep being extended (Raymond & Medina, 2018). More recent studies reported that those synapses also require long-term potentiation for motor learning (Schonewille et al., 2010).

II.4.3. Selection of neuronal inputs: the long-term plasticity

Task-encoding is limited by the capacity storage of the PC. Associative learning (e.g. eyeblink conditioning) requires a precise selection of only relevant inputs to generate an adapted output pattern. Synaptic long-term plasticity plays a key role in input selection as it controls PF synaptic weights. Hence, unraveling the underlying mechanisms of long-term plasticity is of major importance to understand synaptic selection and information processing.

II.4.3.1. Postsynaptic long-term plasticity

Long-term depression (LTD) is the first cerebellar long-term plasticity described *in vivo* (Ito & Kano, 1982). The coactivation of the CF and the PF within a precise temporal window (Jirenhed et al., 2017; Suvrathan et al., 2016; Wang et al., 2000; Wetmore et al., 2014) induces a strong postsynaptic LTD of PF-PC synapses (Coesmans et al., 2004). This LTD requires a Ca^{2+} signaling pathway activated consequently to the strong depolarization mediated by AMPA receptors and the activity of the CF. When PFs are densely activated, the depolarization elicits an important Ca^{2+} elevation spanning in the dendritic spine and in the branchelet (Wang et al., 2000). Interestingly, when PFs are sparsely activated, Ca^{2+} elevation is restricted to the dendritic spine and requires the activation of the metabotropic glutamate receptor 1 (mGluR1, Ichise et al., 2000; Wang et al., 2000). Blockade of Ca^{2+} pumps on the endoplasmic reticulum prevents LTD indicating that internal stores are also a source for Ca^{2+} elevation.

During trains or bursts of activity, the glutamate released by both the CF and the PF persists in the synaptic cleft and diffuses extrasynaptically to activate mGluR1 (Batchelor & Garthwaite, 1997). The related G_q protein activates the phospholipase C which catalyzes the cleavage of phosphatidylinositol 4,5-bisphosphate into inositol 1,4,5 trisphosphate (IP3) and diacylglycerol (DAG). IP3 triggers Ca^{2+} release from internal stores to further increase the concentration. Both high Ca^{2+} concentration and DAG activate the protein kinase Cα which phosphorylates the AMPA receptors GluR2 subunit to provide their internalization (Chung et al., 2003; Wang & Linden, 2000), thereby reducing the amplitude of postsynaptic currents.

Other studies demonstrate that postsynaptic LTD requires presynaptic NMDA receptors. High-frequency bursting activity in the PF triggers the production of nitric oxide via Ca^{2+} increase (Lev-Ram et al., 1995) through NMDA receptors (Bidoret et al., 2009; Bouvier et al., 2016; Casado et al., 2002; Piochon et al., 2010; Schonewille et al., 2021). The nitric oxide diffuses toward the postsynaptic element to trigger LTD.

At PF-PC synapses, the postsynaptic Ca^{2+}/calmodulin kinase II (CaMKII) is also involved in LTD induction. Interestingly, mice lacking this protein display LTP at PF-PC synapses with a protocol inducing LTD in physiological conditions, and vice versa (van Woerden et al., 2009). Other molecular factors are involved in postsynaptic LTD induction but they are not discussed in the present work.

A second form of postsynaptic long-term plasticity at PF-PC synapses is LTP. This latter is triggered by PF stimulations (Coesmans et al., 2004; Jörntell & Hansel, 2006; Lev-Ram et al., 2002) during bursts of high-frequency (Binda et al., 2016; Bouvier et al., 2016; Jörntell & Ekerot, 2002) or repeated pulses at 1Hz (Lev-Ram et al., 2002; Valera et al., 2016).

The depolarization induced by the activation of AMPA receptors opens $Ca_v3.1$ channels (Binda et al., 2016; Hildebrand et al., 2009; Isope et al., 2010) to elicit fast Ca^{2+} influx in the dendritic spine. The lower Ca^{2+} threshold compared to LTD may elicit CaMKII inhibition through autophosphorylation (Piochon et al., 2016) to disinhibit protein phosphatase 2B pathway (Belmeguenai, 2005; Schonewille et al., 2010). Such a signaling promotes free AMPA receptor dephosphorylation and their insertion to the postsynaptic membrane.

Investigations also reported the involvement of NMDA receptors, nitric oxide and Ca^{2+} to induce postsynaptic LTP (Bouvier et al., 2016; Lev-Ram et al., 2002; Schonewille et al., 2021). In addition, recent findings reported that MLIs favor LTP activation mechanisms (Binda et al., 2016): the activation of the GABA-A on the PC dendritic spine hyperpolarizes the membrane which de-inactivates $Ca_v3.1$ channels.

The role of postsynaptic LTP and LTD in cerebellar-dependent behaviors has been largely supported by many studies (Gao et al., 2012; Gutierrez-Castellanos et al., 2017; Schonewille et al., 2010). The specific lack of PCs PKC in mice impairs the spatial representation in hippocampal place cells (Rochefort et al., 2011) suggesting an essential role of LTD in path integration. The supervised learning carried by CFs determines whether to perform LTP or LTD. Both mechanisms involve many signaling pathways, some of which are shared. Ca^{2+} concentration has a major impact and would orient the balance on either LTP or LTD.

II.4.3.2. Presynaptic long-term plasticity

The presynaptic LTP is triggered during repetitive stimulations at 2-8 Hz (Salin et al., 1996). The induction persists even when Ca^{2+} is chelated in the PC and is completely prevented when the extracellular Ca^{2+} is removed (Salin et al., 1996). Moreover, bath application of forskolin (a direct activator of adenylyl cyclase) elicits presynaptic LTP. Hence, the Ca^{2+} build-up in the presynaptic element activates Ca^{2+}/calmodulin-sensitive adenylyl cyclase which subsequently activates cAMP-dependent kinase (i.e. protein kinase A; Linden & Ahn, 1999). However, adenylyl cyclase is also expressed in PCs and elicits postsynaptic LTP when activated by forskolin (Gutierrez-Castellanos et al., 2017).

Interestingly, the CF activity suppresses the induction of presynaptic LTP via the activation of the presynaptic cannabinoid receptor 1 (CB1, van Beugen et al., 2006). CB1 inhibit the activation of adenylyl cyclase hence preventing LTP. Other investigations reported that presynaptic LTP is enhanced by NMDA receptors/nitric oxide cascade signaling pathway (Chu et al., 2014; Qiu & Knopfel, 2007).

Alternatively, a presynaptic form of LTD has been reported *in vitro* and *in vivo* (Chu et al., 2014; Qiu & Knöpfel, 2009). This latter is induced by 4 Hz PF stimulation and is mediated by CB1 activation in a NMDA-dependent manner. Such a stimulation protocol also activates presynaptic LTP which hides presynaptic LTD, hence requiring the application of antagonists to be visualized.

At PF-MLI synapses, presynaptic LTD mechanisms differ compared to PF-PC synapses and are specific to this synapse (Soler-Llavina & Sabatini, 2006). This latter requires the activation of Ca^{2+}-permeable AMPA receptors, the postsynaptic Ca^{2+} accumulation and the activation of mGluR1. The downstream cascade triggers endocannabinoids release which activate presynaptic CB1 thereby eliciting presynaptic LTD.

II.4.3.3. Long-term plasticity underlies bidirectional modulation of Purkinje cell receptive fields

LTP and LTD are present in both presynaptic and postsynaptic components for cerebellar learning. Investigations on sensory receptive fields assessed the role of both plasticities *in vivo* (Jörntell & Ekerot, 2002, 2003). When the CF activity is paired with electrical stimulation of PF beam, the receptive field representation in individual PCs is reduced in size (i.e. many PF-PC synapses are depressed) while this representation is extended in MLIs (i.e. PF-MLI synapses are potentiated). The reciprocity occurs when the PF beam is activated and the CF stimulation omitted. These results indicate that LTP and LTD act as a bidirectional balance to provide reliable information processing (Coesmans et al., 2004; Jörntell & Hansel, 2006).

Strikingly, disruption of LTD does not necessarily impairs motor learning. Genetically preventing LTD in mice does not affect VOR, eyeblink conditioning and locomotion learning (Schonewille et al., 2011). As plasticity mechanisms are diversified, it has been suggested that long-term plasticities act synergistically so that the impairment of one of them could be compensated by the others (Chu et al., 2014; Gao et al., 2012).

Despite the vast complexity of plasticity mechanisms, investigations carried in the last thirty years confirmed the CFs control of PF-PC synaptic weights predicted by the Marr-Albus-Ito theory. Collectively, computational and biological studies refined the complex functional cerebellar connectivity maintaining earlier insights established by the theory.

Although the cerebellar architecture is crystalline, it is a mistake to believe that the cerebellar cortex is homogeneous. Anatomic, molecular and functional heterogeneities add a higher level of complexity to signal integration.

II.5. The module as an anatomo-functional cerebellar unit

Cerebellar functions have long been attributed only to the lobular organization and the three mediolateral compartments. The concept of *module* emerged fourty years ago (Oscarsson, 1979) and unveiled a new anatomo-functional organization of the cerebellum. The module is a functional stereotypic microcircuit unit processing specific information from the body. Despite the weak neuronal cerebellar diversity, the modular organization offers an exquisite higher degree of complexity on cerebellar information processing.

Although modules are not integrated in the present project, it is fundamental to understand that the molecular layer is not uniform and that PFs run across multiple modules. This section explains the broad outlines to understand the modular organization without going into the details.

II.5.1. The olivo-cortico-nuclear loop: the module and the microzone

In the 40's, Jansen & Brodal reported for the first time a somatotopic connectivity in the cerebellum (Jansen & Brodal, 1940). They noticed that a sub-nucleus in the inferior olive projects to the paravermis which in turn connects to the interposed nucleus. Later on, this somatotopy has been extended to the three parts of the cerebellum. The ramified projections of specific CFs on PCs clusters along the anteroposterior axis delimit clear cortical parasagittal stripes in the vermis, the paravermis and the lateral hemispheres (***Figure I7A***; Groenewegen & Voogd, 1977; Groenewegen et al., 1979; Oscarsson, 1979; Voogd & Ruigrok, 2004). Parasagittal stripes have been first named zones A to D in the mediolateral axis and split into smaller accurate zones later (***Figure I7A***). In turn, a given cortical zone connects to a specific subset of neurons in the DCN closing back the loop onto the involved subset of olivary neurons (***Figure I7A***; Chaumont et al., 2013; Najac & Raman, 2015). Hence, this connectivity gives rise to the olivo-cortico-nuclear loop defining the *module* (Apps & Hawkes, 2009).

The cortical part of the module is called *microzone* and takes into account all the cortical microcircuits in a stripe (Apps et al., 2018; Oscarsson, 1979). Because a subset of IO connects topographically to the cerebellar cortex, PCs from a given microzone share the receptive field conveyed by the CF (Garwicz et al., 1998; Hesslow, 1994) and synchronize via electrical coupling of olivary neurons (Llinás & Sasaki, 1989). This parasagittal topography may overlap with MF patches (*see section II.1.1.3*; ***Figure5***). Electrophysiological micromappings in rat lobule crus II reported that tactile skin stimulations elicited congruent CFs and MFs typical spikes (i.e. complex and simple spikes, respectively) in PCs, hence indicating an overlap of CFs and MFs receptive fields in the microzone (Apps & Hawkes, 2009; Brown & Bower, 2001).
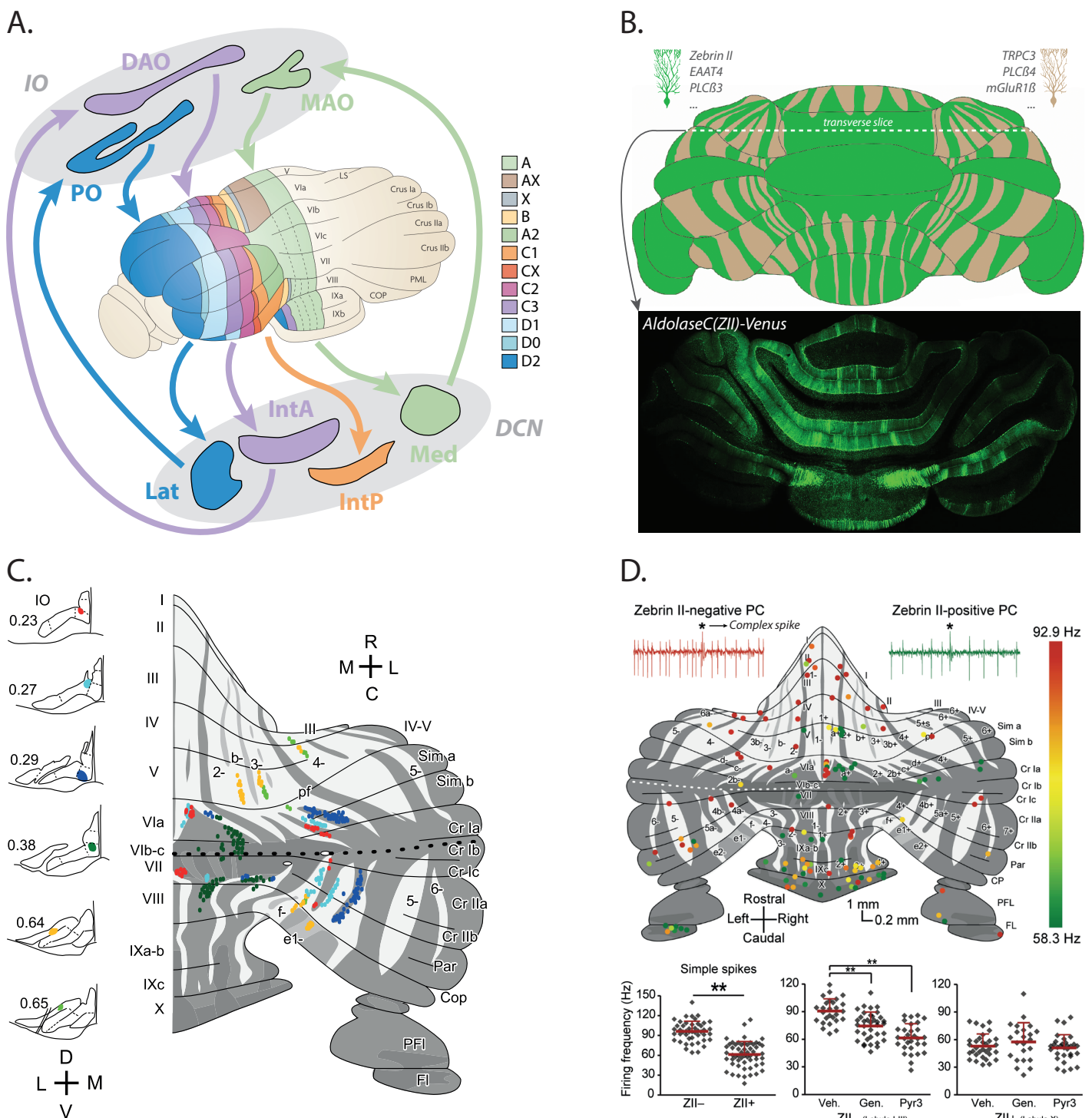
Figure I7 : Olivo-cortico-nuclear loops and Zebrin bands define the cerebellar modules.

A) Cerebellar longitudinal zones or modules. Each module is defined by a topographical closed loop of connections between subsets of neurones in the inferior olive, the cerebellar cortex and the deep cerebellar nuclei. Modules are associated to specific tasks. *Adapted from Apps & Hawkes, 2009*.

B) *Top*, Zebrin bands defined by the expression of molecular markers. *Adapted from Cerminara et al., 2015*. *Bottom*, Horizontal cerebellar slice revealing Zebrin II positive bands through the expression of AldolaseC-Venus in Purkinje cells. *From Spaeth L. (2019) Modular information processing in the cerebellar cortex*.

C) Biotynylated dextran amine injections into the mouse inferior olive (left) reveals mapping of labeled climbing fibres terminations (colored dots, right) in aldolase C bands (grey). *Adapted from Fujita & Sugihara, 2013*.

D) Differences of Purkinje cells (PC) firing activity in Zebrin positive (ZII+) and negative (ZII-) bands. The location of PCs (colored dots) is determined postmortem via immunohiostochemistry. Colors indicate the simple spike firing rate in each PC. Note the higher firing rate of PCs in ZII- bands, recorded *in vivo*. Pharmacological blockade of TRPC3 channel with genistein or pyr3 selectively decreases simple spike activity of PCs in ZII- bands. *Adapted from Apps et al., 2018*.

Abbreviations: DAO, dorsal accessory olive; DCN, deep cerebellar nuclei; EAAT4, excitatory amino-acid transporter type 4; IntA, interposed anterior nucleus; IntP, interposed posterior nucleus; IO, inferior olive; Lat, lateral nucleus; MAO, medial accessory olive; Med, medial nucleus; mGluR1ß, metabotropic glutamate receptor type 1ß; PC, Purkinje cell; PLC, phospholipase C; PO, principal olive; TRPC3, short transient receptor potential channel 3.

Inputs and outputs in the olivo-cortico-nuclear loop determine the type of information to process in the microzone. Cerminara & Apps summarized specific tasks related to some modules (Cerminara & Apps, 2011). For instance, the module B, as previously mentioned, processes limbs cutaneous information while module A is involved in balance, posture and eye movements (***Figure I7A***; Ruigrok, 2011). Selective impairments to any component of the loop lead to severe motor deficits: cerebellar modules are task-related (Hesslow, 1994).

Therefore, tracing as well as electrophysiological studies identified the topographical boundaries of modules across the cerebellar cortex. An additional level of mapping arises from the discovery of neurochemical markers of microzones.

II.5.2. Molecular compartmentalization of the cerebellar cortex

Sixty years ago, Scott noticed that the staining of the enzyme 5'-nucleotidase highlights parasagittal bands restricted to the molecular layer (Scott, 1963). Later, a wealth of other markers involved in different cellular and physiological processes have been discovered in PCs, but also in the granular layer to a lesser extent (Apps & Hawkes, 2009; Cerminara et al., 2015; Consalez et al., 2021).

The labeling of markers in PCs systematically unveil parasagittal stripes matching with CF inputs (***Figure I7B-C***; Apps & Hawkes, 2009; Sugihara & Shinoda, 2004; Voogd & Ruigrok, 2004). Neurochemical markers belonging to the Zebrin (I and II) are the most used nowadays (Gravel et al., 1987; Hawkes et al., 1985). The term Zebrin has been assigned to these markers owing to the zebra aspect of the cerebellar cortex after staining (***Figure I7B***). The lab of Hawkes assigned the term of Zebrin II to the Aldolase C (Ahn et al., 1994), an enzyme involved in glycolysis and gluconeogenesis. Immunolabeling of Zebrin II and the transgenic mouse line expressing the Aldolase C coupled to the fluorophore Venus (***Figure I7B***; Fujita et al., 2014) reveal alternating positive and negative longitudinal bands in the mediolateral axis of the cerebellar cortex (Sugihara & Shinoda, 2004).

Zebrin II compartments are correlated to functional heterogeneities. Differences in PCs intrinsic firing properties between positive and negative bands have been reported *in vivo* and *in vitro* (***Figure I7D***; Viet et al., 2021; Zhou et al., 2014). The firing rate of PCs reaches ~75 Hz in negative bands while is set at ~36 Hz in positive bands (Zhou et al., 2014). Such differences have been related to the expression of the TRPC3, a non-selective cationic channel, in negative bands (***Figure I7D***). Similar results have been attributed to a different modulation of SK channels, an activated- Ca^{2+} potassium channel (Viet et al., 2021).

Differences in long-term plasticity at GC-PC synapses in the vermis have also been described. The conjunctive stimulation of CFs and PFs elicits long-term depression at GC-PC synapses via mGluR1 (*see section II.4.3.1*) which trigger inhibitory feedback. The higher expression of the glutamate transporter EAAT4 in positive bands than negative bands prevents activation of metabotropic receptors and inhibitory feedback, hence limiting long-term depression (Wadiche 2005).

Heterogeneous molecular markers are also found in the granular layer and unveil bands, compartments and patches (***Figure I8***). For instance, expression of the type 2 vesicular glutamate transporter (VGLUT2) in dorsal/ventral spinocerebellar MFs and VGLUT1 in cuneocerebellar MFs unveil alternating bands (***Figure I8A***; Gebre et al., 2012). Other markers expressed in MF terminations such as acetylcholinesterase also show patches in the granular layer (Boegman et al., 1988). In the antero-posterior axis, multiple markers expressed in GCs delimit transvers boundaries (***Figure I8B***). For example, lineage tracing experiments unveiled GC populations expressing Ebf2 in the anterior and the central lobes, Tlx3 in the posterior lobe and Otx1 in the flocculonodular lobe (Consalez et al., 2021).

Overall, these markers highlight regional differences both in anatomical and regional organization of the cerebellar cortex (Cerminara et al., 2015) and are remarkably conserved across species (Apps & Hawkes, 2009).

GCs require a particular attention since they permit pattern separation and relay MFs information to different target neurons. High-frequencies lead to fast specific presynaptic adaptation of glutamate release. The next part is a cornerstone in the present project as it comes into focus on the functional properties of GC boutons underlying high-frequency transmission.
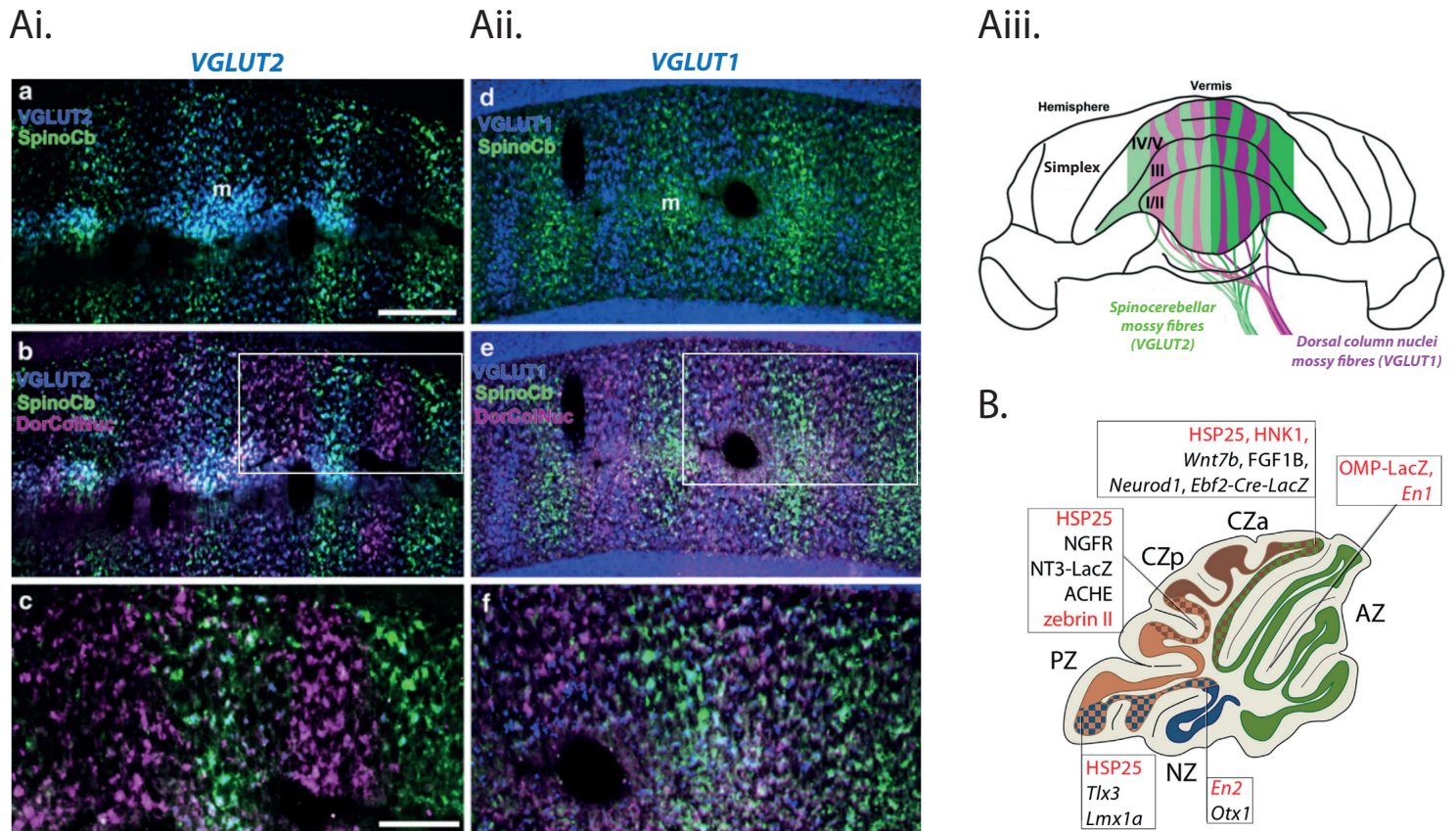
Figure I8 : Molecular compartmentation in the granular layer.

A) Expression of VGLUT1 and VGLUT2 at spinocerebellar and dorsal column nuclei mossy fibres terminating in the anterior vermal lobule III reveal alternating bands. *Ai*, VGLUT2 labeling overlaps with spinocerebellar (a) but not with dorsal column nuclei (b-c) mossy fibres. *Aii*, VGLUT1 labeling do not overlap with spinocerebellar (d) but with dorsal column nuclei (e) mossy fibres. c and f show high magnification of the boxed areas in b and e, respectively. *Aiii*, Diagram illustrating the alternative spinocerebellar and dorsal colun nuclei mossy fibres in the cerebellar cortex. *Adapted from Gebre et al., 2012*.
B) Transverse boundaries established by genes involved in cerebellar development. Granule cell and Purkinje cell specific markers are labelled in black and red, respectively. *From Consalez et al., 2021*.

Abbreviations: ACHE, acetylcholine esterase; AZ, anterior zone; CZa, anterior central zone; CZp, posterior central zone; DorColNuc, dorsal column nuclei; m, midline; NZ, nodular zone; PZ, posterior zone; SpinoCb, spinocerebellar; VGLUT, vesicular glutamatergic transporter.

Part III. High-frequency functional dynamics of granule cell boutons

Adjusting a movement takes place in a narrow time window and requires fast and reliable temporal processing. Sensorimotor information is conveyed to the cerebellar cortex by MFs at wide range of high-frequencies. GCs distribute this information to many targets over long distances via *en passant* boutons. Efficient processing of high frequencies requires adapted presynaptic mechanisms in the millisecond timescale. How GC boutons adapt to support high-frequency transmission? Does short-term presynaptic plasticity (STP) control the synaptic strength at millisecond timescale? How STP controls temporal processing of sensorimotor information? In what way STP could be a feature of pattern separation?

Because STP changes the properties of neurotransmitter release, the first section introduces the relationship between synaptic vesicular release and presynaptic Ca^{2+}. Mechanisms and involvement of STP in information processing are explored throughout the second section. Finally, the potential contribution of STP to improve pattern separation is presented in the third section.

III.1. Release of synaptic vesicles and presynaptic calcium

When an action potential reaches the synaptic terminal, the Ca^{2+} entry in the presynaptic element triggers neurotransmitter release. This dogma is common to all the chemical synapses in the central nervous system. However, GCs are specialized in high-frequency transmission and specificities in the boutons can be highlighted.

III.1.1. Pools of synaptic vesicles

The ultrastructural organization within the presynaptic bouton controls the parameters of synaptic neurotransmission. Ultrastructural analyses reported that GCs boutons contain a high density of synaptic vesicles organized as a bee swarm (***Figure I9A***; Xu-Friedman et al., 2001). Segregating synaptic vesicles into heterogeneous populations gives the bouton the capacity to finely control the quantity of neurotransmitter released. First, the *ready-releasable pool* (RRP) is the fraction of mature vesicles docked and primed to presynaptic active sites and close to voltage-gated Ca^{2+} channels (Ca_v, ***Figure I9B***). Synaptic vesicles from this pool release their content consequently to a single action potential. The size of RRP accounts for
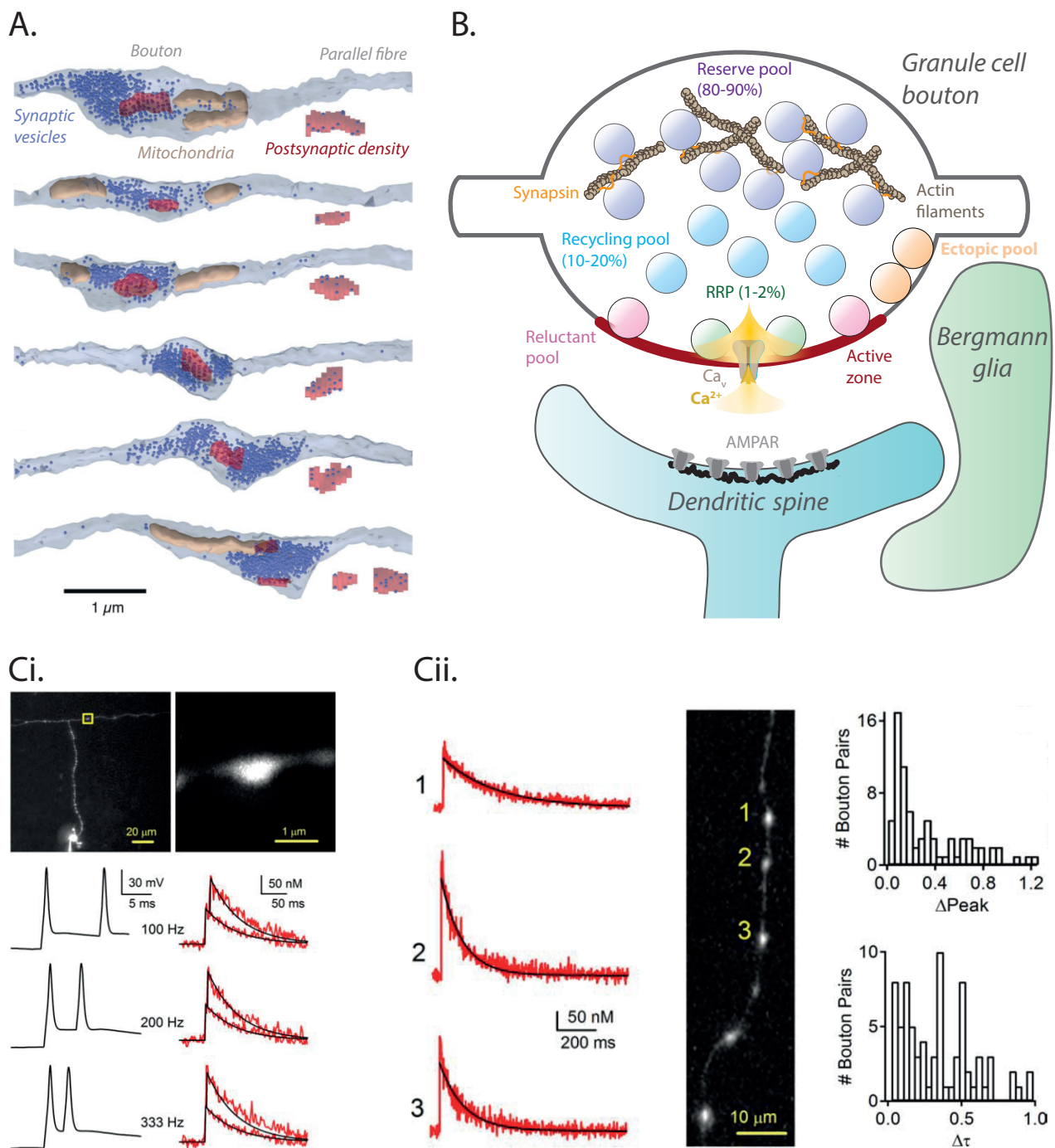
Figure I9 : Synaptic vesicles and calcium dynamics in granule cell boutons.

A) 3D reconstructions of 6 sample parallel fibre release sites. Reconstructions of each postsynaptic density with associated docked vesicles are shown under the axon. *Adapted from Xu-Friedman al., 2001*.

B) Diagram illustrating the synaptic vesicle pools in a granule cell bouton.

C) Calcium imaging in granule cell boutons. *Ci*, Action potential propagation in response to stimulus pairs of action potentials to invade presynaptic boutons is assessed by measuring calcium transients in parallel fibre bouton. *Top*, Representative experiment in which calcium levels are measured in the bouton indicated by the yellow box. *Bottom*, Pairs of action potentials are evoked at 100, 200 and 333 Hz (left). Calcium transients evoked by one and two action potentials are measured at each frequency (right; red traces). The response to a single action potential is fit with a single exponential decay (black), and the trace is shifted and superimposed to indicate the predicted calcium transient from a pair of stimuli. *Cii*, Variability in calcium signalling between neighboring boutons. The properties of calcium signals evoked by single action potentials are compared for neighboring boutons. Granule cells are loaded with fluo-5F. The volume, decay-time constant and peak calcium are different between the three boutons shown. The histograms resume the relative change in peak and decay-time constant between multiple adjacent boutons. *Adapted from Brenowitz & Regehr, 2007*.

Abbreviations: AMPAR, AMPA receptors; Ca$_v$ voltage-gated Ca^{2+} channels; RRP, ready-releasable pool.

1-2% of the total amount of vesicles and only 7-8 vesicles belonging to this pool are docked to the active zone (Xu-Friedman et al., 2001). The exocytosis of ready-releasable vesicles is permitted by the soluble N-ethylmaleimide-sensitive-factor attachment protein receptor (SNARE) complex (Yoon & Munson, 2018). This complex is formed by two elements: synaptobrevin attached to synaptic vesicles (or v-SNARE) and syntaxin/SNAP-25 included at the target membrane (or t-SNARE).

Second, the *reserve pool* consists of vesicles set back from the RRP and linked to actin microfilaments (***Figure I9B***). The releasable pool is a major source of synaptic vesicles being delivered to the active zone during intense synaptic activity: it fosters the replenishment of the RRP to counterbalance vesicles depletion caused by bursts of activity (Crowley et al., 2007; Moulder & Mennerick, 2006).

Third, the *recycling pool* gathers vesicles formed by compensatory endocytosis and is located in the periphery of active sites (***Figure I9B***). Vesicles belonging to this pool provide replenishment of both RRP and reserve pool during fast synaptic activity (Xie et al., 2017). The high firing rate of GC constrains fast dynamic pools replenishment. At GC-SC synapses, the velocity of this process has been estimated at 15-20 ms (Crowley et al., 2007) while it reaches 30-65 ms at GC-PC synapses (Valera et al., 2012). These measures vary according to the amount of ready-release vesicles.

Interestingly, some studies reported that a small amount of vesicles localized out of the active zone mediate ectopic glutamate release on Bergmann glia (***Figure I9B***; Balakrishnan et al., 2014; Dobson & Bellamy, 2015; Dobson et al., 2018). However, further investigations are needed to characterize the functional contribution of ectopic release.

Therefore, the number of mature vesicles and their recruitment as well as the recycling kinetic are fundamental to support high-frequency transmission.

III.1.2. Calcium domains in the presynaptic active zone

The presynaptic active zone is a dense specialized area devoted to fusion of ready-releasable vesicles with the membrane for neurotransmitter release in the synaptic cleft. It faces the postsynaptic density containing receptors for appropriate neurotransmission. The arrival of an action potential depolarizes the presynaptic membrane which opens Ca_v producing a Ca^{2+} influx. Specialized proteins linked to vesicles anchored to the active zone are sensitive to Ca^{2+} and trigger vesicle fusion. In GCs boutons, the Ca^{2+} channels involved in synaptic exocytosis are the P/Q type (i.e. $Ca_v2.1$) and the N-type (i.e. $Ca_v2.2$; Mintz et al., 1995). Pharmacological experiments reported that specific blockers of $Ca_v2.1$ reduce by 50% the Ca^{2+} influx and by 93% the synaptic vesicle release, whereas blocking $Ca_v2.2$ prevents

27% of the Ca^{2+} influx and 50% of the vesicular release (Mintz et al., 1995). Hence, these channels act together in the fast synchronous release process of synaptic vesicles with a major efficiency of $Ca_v2.1$. R-type channels ($Ca_v2.3$) are also expressed at the GC bouton but are rather involved in induction of presynaptic LTP at GC-PC synapses (Myoga & Regehr, 2011).

Ca_v within the active zone are more or less tightly coupled to synaptic vesicles anchored to the plasma membrane (Schneggenburger et al., 2012). The organization of Ca_v can reflect clusters where the number of channels as well as their vicinity with synaptic vesicles regulate the intensity and the diffusion of Ca^{2+} influx. This influx can be reliably measured with Ca^{2+} imaging during high-frequency stimulation of GCs (up to 333 Hz) where dye signals sum linearly in the bouton (***Figure I9Ci***; Brenowitz & Regehr, 2007). The elevated Ca^{2+} concentration surrounding the channels may extend more or less than 100 nm, defining respectively microdomains and nanodomains (Eggermann et al., 2012). In GC boutons, recent nanotopographical investigations reported that the distance between clusters of Ca_v and Ca^{2+}-sensors on ready-releasable vesicles approximates 50 nm (Rebola et al., 2019), identifying nanodomain loose coupling.

Vesicular Ca^{2+} sensors such as synaptotagmins interact with the SNARE complex and phospholipids to trigger vesicle fusion with the membrane and release the content. Synaptotagmins are membrane-associated proteins that include eight isoforms with different Ca^{2+} affinities and binding kinetics to phospholipids (Jackman & Regehr, 2017; Südhof, 2002). For example, low-affinity and fast kinetics of synaptotagmins 1, 2 and 9 allow rapid fusion of vesicles with the membrane leading to fast synchronous release (Xu et al., 2007). Conversely, high-affinity and low kinetics of synaptotagmin 7 delay vesicular fusion to promote asynchronous release and short-term facilitation (*see sections III.2.1* and *III.2.2.3*, ***FigureI12D***; Jackman et al., 2016; Turecek & Regehr, 2018). The spatial propagation of residual Ca^{2+} required to activate Ca^{2+} sensors is mainly buffered and stabilized by calretinin and by calmodulin to a lesser extent (Bastianelli, 2003; Résibois & Rogers, 1992; Schmidt et al., 2013). Specialized Ca^{2+} pumps then provide the extrusion of Ca^{2+} to reestablish the initial concentration. Therefore, Ca^{2+} sensors are central for high-frequency synaptic transmission.

III.1.3. Heterogeneous calcium dynamics

As introduced above, Ca^{2+} is a key determinant for neurotransmitter release through activation of isoforms of Ca^{2+}-sensitive proteins. Fluctuations of Ca^{2+} concentration in the presynaptic bouton may regulate the synaptic vesicle fusion and affect neurotransmission. *Ex-vivo* imaging experiments reported heterogeneous amplitude and decay-time constant of Ca^{2+} signals between single GC boutons on the same PF (***Figure I9Cii***; Brenowitz & Regehr, 2007;

Zhang & Linden, 2009, 2012). The diversity in decay-time is also marked between the inner and the outer molecular layer. Boutons in the inner molecular layer display faster kinetics than boutons in the outer molecular layer (Zhang & Linden, 2012). These results suggest heterogeneous Ca^{2+} dynamics and clearance efficiency that may have an important impact on long-term as well as short-term plasticity.

III.2. Short-term synaptic plasticity

Transmission of high-frequencies requires fast release of neurotransmitter in a millisecond timescale. This implies setting a fast mechanism providing adaptation of the amount of synaptic vesicles to release and their fast recycling at each action potential of the burst. Because Ca^{2+} is a major modulator of release probability (P_r) through interaction with Ca^{2+}-sensitive proteins, Ca^{2+} dynamics in the bouton must be accurately controlled.

STP is a presynaptic plasticity mobilized exclusively during repetitive presynaptic firing from few milliseconds to hundreds of seconds providing activity-dependent changes in synaptic vesicular release and synaptic strength. It can be modulated by synaptic neuromodulators. The goal of the present work was to study STP organization at boutons belonging to the same PF. The mechanisms of STP, its modulation, its physiological importance and its potential contribution in pattern separation are introduced in this section.

III.2.1. Presynaptic facilitation and depression

The two major profiles of STP are short-term facilitation (STF) and short-term depression (STD, *Figure I10*). STF increases synaptic vesicle release during the high-frequency burst of stimulation to sustain neurotransmission while vesicles are progressively depleted in STD to promote phasic transmission. What are the mechanisms and functions of such a plasticity?

III.2.1.1. Synaptic vesicles, calcium contribution and synaptic strength

STP is exclusively evoked during high-frequency burst of electrical stimulations. STF occurs when residual Ca^{2+} is still present at the second action potential (*Figure I10Ai*). Facilitating synapses are associated to low initial P_r: a small fraction of synaptic vesicles from the RRP is released at the first spike (*Figure I10Ai*). The Ca^{2+} build-up at the second spike increases P_r (Atluri & Regehr, 1996) leading to release of a higher amount of synaptic vesicles.
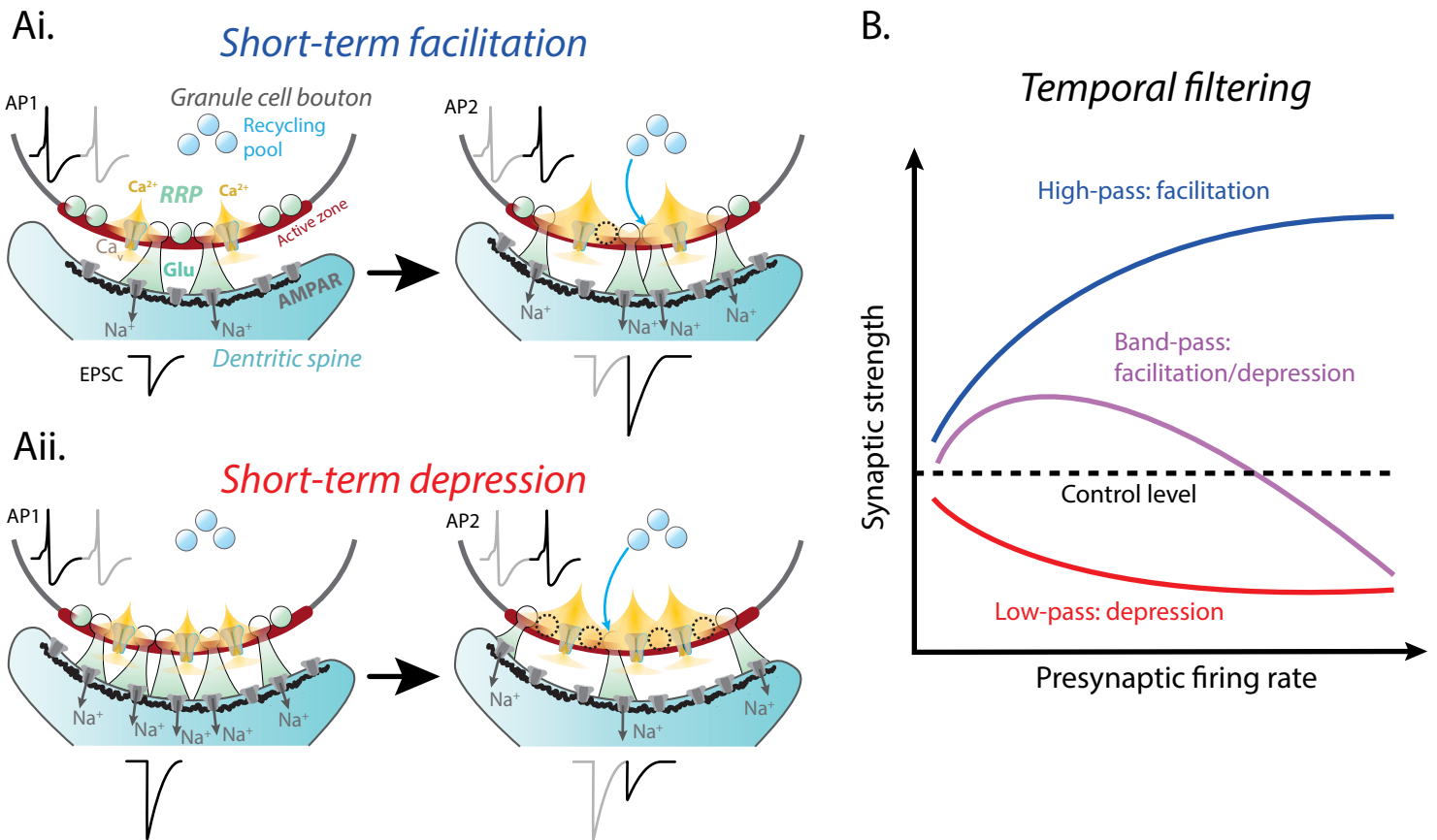
Figure I10 : Mechanisms of short-term facilitation/depression and temporal filtering.

A) Diagram illustrating the classical model of presynaptic short-term plasticity. *Ai,* Short-term facilitation. *Left*, An action potential (AP) depolarizes the presynaptic bouton which opens voltage-gated Ca^{2+} channels (Ca_v). Ca^{2+} influx forms a nanodomain in which high $[Ca^{2+}]$ triggers vesicles fusion with the plasma membrane and glutamate release in the synaptic cleft. Glutamate opens AMPA receptors (AMPAR) on the dendritic spine eliciting Na^+ influx and an excitatory postsynaptic current (EPSC). *Right*, The residual Ca^{2+} from the first AP (AP1) extends progressively. The arrival of a second AP (AP2) shortly after depolarizes the membrane and elicits a second Ca^{2+} influx that sums with residual Ca^{2+} and triggers more vesicular release. This results in a second EPSC with a larger amplitude. Sites where the vesicle has been released (dotted circles) can be reloaded with fresh vesicles from the recycling pool. *Aii,* short-term depression. *Left,* The Ca_v-mediated Ca^{2+} influx elicited by AP1 triggers release of many synaptic vesicles, resulting in a first large EPSC. *Right,* As the majority of vesicles have been depleted during AP1, the arrival of AP2 triggers the release of a poor amount of vesicles. This results in a second EPSC with a smaller amplitude.
B) Schematic of the functional role of short-term plasticity in temporal filtering at the level of single synapses. Short-term plasticity conveys frequency-filtering properties to synapses. During repetitive activity, facilitating synapses are high-pass filters because they are strongest at high frequencies, depressing synapses are low-pass filters because they are strongest at low frequencies, and synapses exhibiting both facilitation and depression are band-pass filters. ***From Anwar et al., 2017***.

Abbreviations: AMPAR, AMPA receptors; AP, action potential; Ca_v, voltage-gated Ca^{2+} channels; EPSC, excitatory postsynaptic current; Glu, glutamate; RRP, ready-releasable pool.

The amplitude of the second postsynaptic current results greater compared to the first one thereby increasing gradually the synaptic strength.

Conversely, STD takes place when P_r is high. The first spike triggers the release of a large amount of synaptic vesicles from the RRP (***Figure I10Aii***). As almost all vesicles have been depleted, the second spike triggers the release of the few remaining available synaptic vesicles despite increase of P_r. The second postsynaptic current has a smaller amplitude thereby decreasing gradually the synaptic strength.

Increasing experimentally the extracellular Ca^{2+} enhances the synaptic strength shifting from STF to STD (Zucker & Regehr, 2002). However, at facilitating GC boutons, the synaptic strength tend to be stronger at high Ca^{2+} but still no STD could be elicited (Valera et al., 2012) suggesting recruitment of particular synaptic vesicles specialized in sustained high-frequency transmission (*see section III.2.1.2*). Heterogeneous ultrastructural and molecular mechanisms may explain this heterogeneity.

GCs boutons are largely accepted as weak synapses because they have a low initial P_r and show STF during high-frequency bursts (Bao et al., 2010; Dittman et al., 2000; Dorgans et al., 2019; Grangeray-Vilmint et al., 2018; Isope & Barbour, 2002; Turecek & Regehr, 2018; Valera et al., 2012). In contrast, SC terminals are strong synapses since they display high initial P_r and STD (Grangeray-Vilmint et al., 2018). Rebola *et al.* recently reported that the coupling Ca_v/RRP associated to a different amount of Ca_v contribute to the differences in synaptic strength between GC and SC terminals (Rebola et al., 2019). As investigations reported STD at GC-MLI synapses (Bao et al., 2010; Dorgans et al., 2019), it is not excluded that such a topography differs from one GC bouton to another and may change in the same boutons between two time points.

III.2.1.2. Adaptation to high-frequency transmission: the reluctant pool

A specific sub-pool belonging to the RRP have recently been reported at GC boutons, the *reluctant pool* (***Figure I11***; Doussau et al., 2017). Unlike the majority of the RRP, vesicles of the reluctant pool are not released consequently to a single action potential. Doussau *et al.* recorded postsynaptic currents in PCs during stimulations of PFs with 300 pulses at 2 Hz to depress the synapse, a process the authors called *low-frequency depression* (***Figure I11A***). Strikingly, the application of a consecutive high-frequency burst immediately elicits strong postsynaptic currents (***Figure I11A***). Interestingly, not all GCs boutons exhibit this phenomenon indicating heterogeneous mechanisms supporting high-frequency transmission. These results confirm similar heterogeneous dynamics previously reported at the calyx of Held (Muller et al., 2010). The presence of the reluctant pool may act as a high-pass filter to
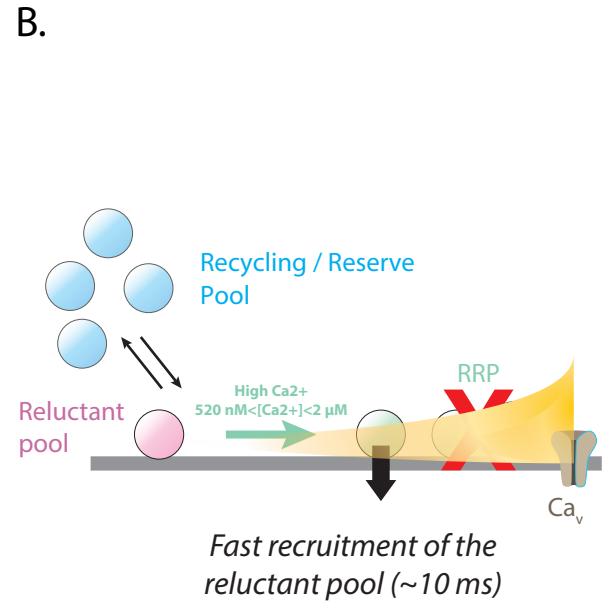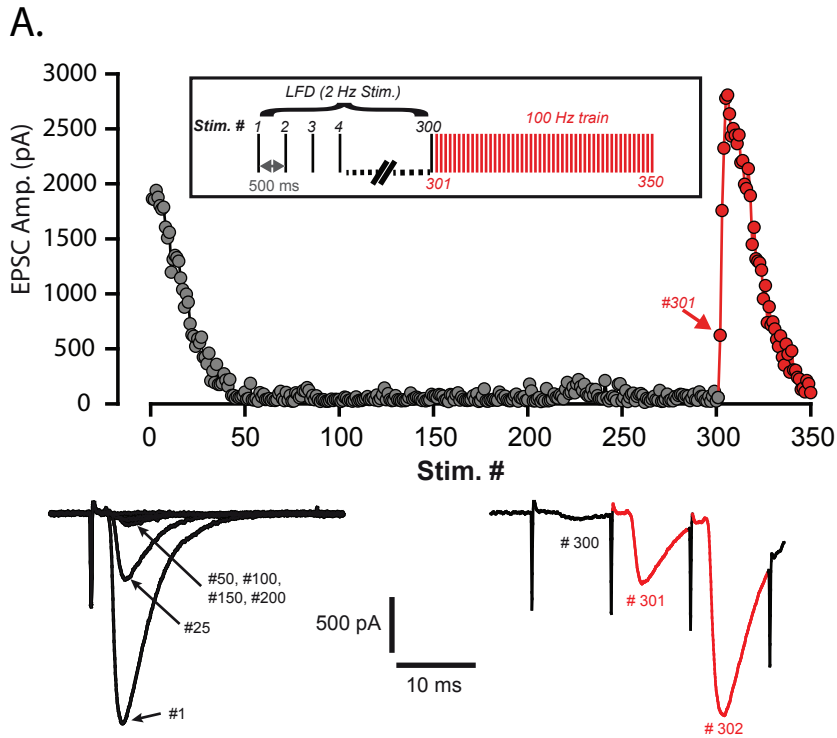
Figure I11 : The reluctant pool is adapted for high-frequency transmission.

A) Ultrafast recovery from low-frequency depression (LFD) by high-frequency trains. *Top*, Typical experiment illustrating the time course of EPSC amplitude during LFD (gray dots, stimulation at 2 Hz) and the fast recovery from LFD mediated by high-frequency trains (red dots, stimulation 100 Hz). Inset: protocol of stimulation. Stimulus #1 corresponds to the beggining of the 2 Hz stimulation. *Bottom*, Recording traces of superimposed EPSCs recorded during 2 Hz stimulation (left) and during the following 100 Hz train (right) at the indicated stimulus number from *Top*. Note the ultrafast recovery from depression at 100 Hz (stimulus #301). **Adapted from Doussau et al., 2017**.

B) Simulation of recruitment of the reluctant pool. Reluctant vesicles are far from Ca^{2+} channels ($Ca_v2.X$). Once almost all ready-releasable vesicles (RRP) have been exhausted as a result of LFD, the high [Ca^{2+}] in the active zone elicited by the high-frequency train triggers the recruitment of the reluctant pool and recover synaptic activity. Vesicles from recycling and reserve pools may transit to reluctant state to refill the reluctant pool and vice versa.

Abbreviations: Ca_v, voltage-gated calcium channels; EPSC, excitatory postsynaptic current; LFD, low-frequency depression; RRP, ready-releasable pool.

discriminate relevant information during a movement from noise during rest. However, whether the release of the reluctant vesicles is direct or goes first from the reluctant to the ready-releasable state and even the distance between the vesicles and the membrane are still unknown.

Reluctant vesicles are likely localized far enough from active sites and Ca^{2+} domains to be mobilized only during high-frequency bursts of activity (***Figure I9B*** and ***I11B***). Going from the reluctant state to the ready-releasable state takes more time than a direct release. A hypothesis is that the Ca^{2+} build-up in the Ca^{2+} domains due to the second action potential at high-frequency reach the reluctant vesicles, thereby triggering their release (***Figure I11B***). This idea can be supported by the fact that at GCs boutons Ca_v are excluded from docked vesicles perimeter (Rebola et al., 2019).

III.2.1.3. Short-term plasticity implements temporal filtering

Information filtering in neuronal populations is essential to distinguish relevant signals from noise. STP filters information flow across the synapse by adapting the synaptic strength (Anwar et al., 2017; Blackman et al., 2013; Jackman & Regehr, 2017). Facilitating synapses have a low initial P_r and unreliably transmit a single action potential. However, facilitation gradually increases P_r in the time course of a burst of activity. This enhances postsynaptic currents which trigger suprathreshold firing. In this way, only high frequencies are reliably transmitted while low frequencies (i.e. noise or onset of the pattern of activity) are filtered out, thereby making these synapses high-pass filters (***Figure I10B***; Dittman et al., 2000). GC-PC synapses are known as high-pass filters since they reliably transfer MFs high-frequency sensorimotor information (Valera et al., 2012). In contrast, at depressing synapses, the P_r decreases as the burst of activity progresses. Postsynaptic suprathreshold responses are elicited at the onset of the burst only, thereby making depressing synapses low-pass filters (***Figure I10B***; Abbott et al., 1997). Such a filter increases the sensitivity of postsynaptic neurons to subtle frequency changes in firing patterns. Some GC-MLI synapses are low-pass filters (Bao et al., 2010; Dorgans et al., 2019) likely to activate feedforward inhibition on PCs when particular changes in pattern activity occur. Synaptic strength can be shaped by the coexistence of both facilitation and depression to form a band-pass filter (***Figure I10B***; Dittman et al., 2000) so that only a particular range in the pattern of activity is encoded. GC-MLI synapses can be band-pass filter (Dorgans et al., 2019) and may select the precise temporal window in the pattern of activity to activate feedforward inhibition onto PCs.

III.2.2. Modulation of short-term plasticity

Studying STP is challenging as it acts with other synaptic plasticities in a global framework to provide efficient neurotransmission. STP dynamics are modulated by presynaptic receptors and an exquisite wealth amount of presynaptic proteins involved in multiple signaling pathways. How is STP modulated? Pharmacological experiments help to isolate STP as much as possible in experimental investigations.

III.2.2.1. Presynaptic receptors

Receptors expressed on the presynaptic bouton as well as on the postsynaptic element influence the dynamics of STP. GC boutons express CB1 activated by endocannabinoids. At GC-PC synapses, short bursts of action potentials activate postsynaptic mGluR1 through glutamate spill-out from the synaptic cleft (Batchelor & Garthwaite, 1997). Activation of mGluR1 elevates locally the Ca^{2+} concentration which triggers endocannabinoids release (Brown et al., 2003). The retrograde activation of CB1 inhibits the presynaptic Ca^{2+} influx (Brown et al., 2003; Brown et al., 2004) that strongly attenuates glutamate release and increases PPR at GC-PC and GC-SC synapses (*Figure I12A*), suggesting modification of P_r (Zhang & Linden, 2009). Interestingly, the regulation of the dendritic Ca^{2+} spread via calcium-activated potassium channels sets the threshold for such a retrograde modulation of the synaptic strength (Rancz & Häusser, 2006). This retrograde inhibition is enhanced by the coactivation of PFs and CF (Brenowitz & Regehr, 2005).

In addition, GC boutons also express adenosine A1 (*Figure I12A*) and GABA-B receptors. Pharmacological activation of A1 receptors inhibits $Ca_v2.2$ to a greater extent than $Ca_v2.1$ while GABA-B receptors mainly inhibit $Ca_v2.1$ and $Ca_v2.2$ to a lesser extent (Dittman & Regehr, 1996). In either case, inhibition mediated by these receptors reduces glutamate release (*Figure I12A*; Zhang & Linden, 2009) and simultaneously increases facilitation during bursts of activity (Kreitzer & Regehr, 2000). Hence, decreasing the synaptic strength through the inhibition mediated by A1 and GABA-B enhance the signal-to-noise ratio during high-frequency activity.

The sensitivity of GC boutons to neuromodulators differs from one bouton to another. Zhang & Linden reported a correlation between the sensitivity to adenosine/endocannabinoids and boutons volume (Zhang & Linden, 2009). Small boutons are more sensitive to adenosine while big boutons are more sensitive to endocannabinoids. Similarly, pharmacological blockade of NMDA receptors differently affects fluorescent signals during Ca^{2+} imaging of GC
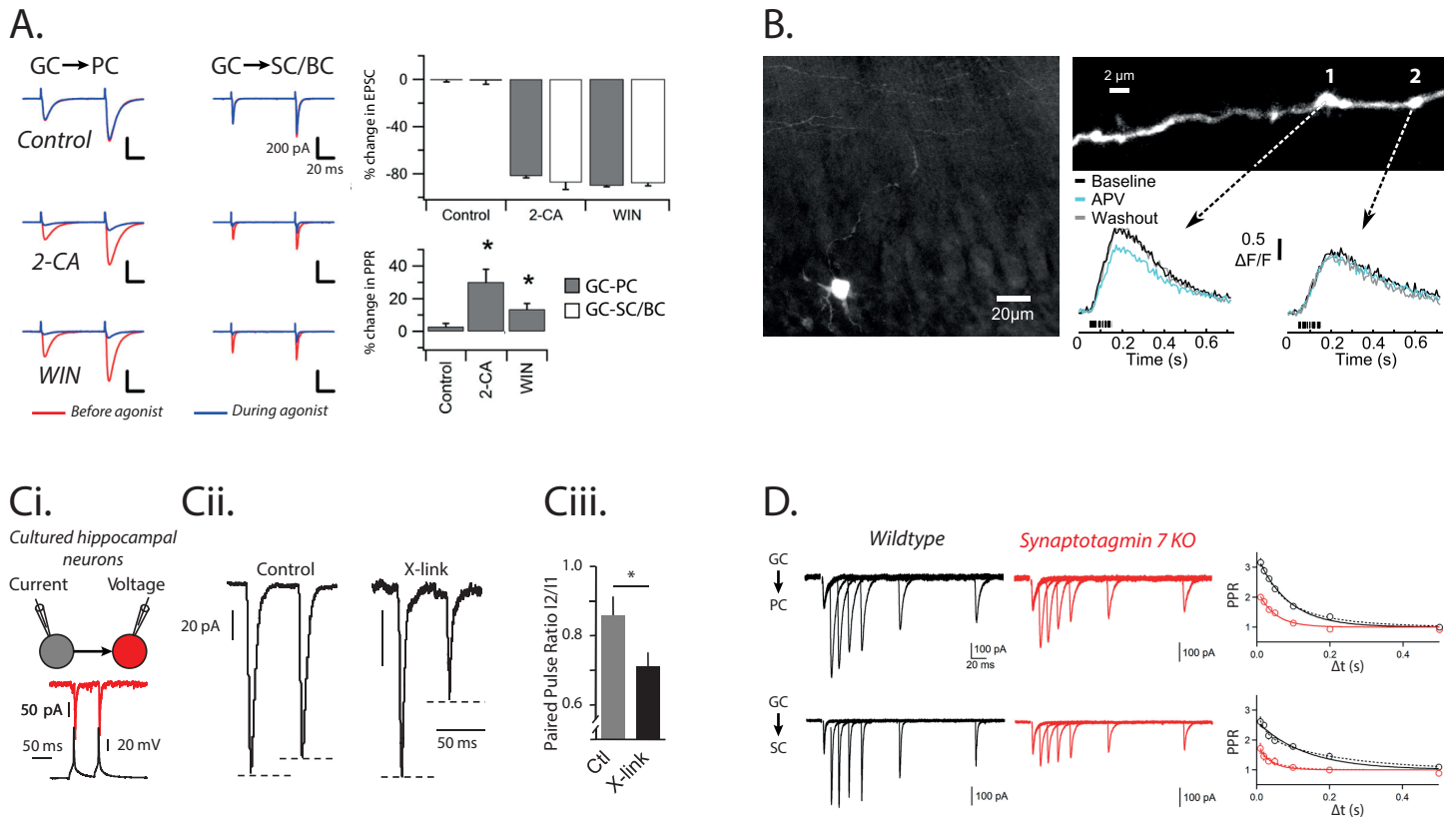
Figure I12 : Modulation of glutamate release, calcium signalling and short-term plasticity.

A) Granule cell (GC) to Purkinje cell (PC) and GC to Stellate/Basket cell (SC/BC) synapses are sensitive to presynaptic neuromodulators. Pharmacological activation of adenosine receptor 1 (agonist 2-CA) and endocannabinoid receptor 1 (agonist WIN) attenuates the current amplitudes evoked by paired-pulse stimulation of GCs with an 80 ms interval and increases paired-pulse ratio (PPR). *Adapted from Zhang et al., 2009*.

B) Two-photon Ca^{2+} imaging of GCaMP5G electroporated GCs (left) at single boutons on the same parallel fibre. Fluorescence signals evoked by parallel fibre electrical stimulation at 200 Hz are decreased in bouton 1 during bath application of D-APV (antagonist of NMDA receptors but are unchanged in bouton 2. *Adapted from Bouvier et al., 2016*.

C) AMPA receptors immobilization increases short-term depression at CA1 synapses of cultured hippocampal neurones. *Ci*, whole-cell recodings of a connected pair of cultured CA1 hippocampal neurons. The presynaptic neuron (grey) is recorded in current-clamp at 0 pA and the postsynaptic neuron in voltage-clamp at -60 mV. The presynaptic action potentials and the postsynaptic AMPA receptor-mediated currents are evoked by an electrical paired-pulse in the presynaptic neuron. *Cii-Ciii*, paired pulse currents in control condition or after blocking surface AMPA receptors mobility via X-link. Note the reduction of the second peak during X-link highlighting enhancement of short-term depression. *Adapted from Heine et al., 2008*.

D) Short-term facilitation at GC-PC (top) and GC-SC (bottom) synapses in wildtype (left) and synaptotagmin 7 KO (middle) mice. Paired-pulse currents are recorded at different inter-pulse intervals. Note the attenuation of the facilitation and the PPR as a function of interstimulus interval (Δt, right) in synaptotagmin 7 KO mice. *Adapted from Turecek & Regehr, 2018*.

Abbreviations: BC, basket cell; GC, granule cell; PC, Purkinje cell; SC, stellate cell.

boutons on the same PF, thereby indicating that NMDA receptors are not expressed on all GC boutons (***Figure I12B***; Bouvier et al., 2016). These results indicate heterogeneous modulations of glutamate release between GCs boutons.

III.2.2.2. Postsynaptic receptors: AMPA receptors mobility

STP is generally accepted as an exclusive presynaptic mechanism. However, investigations in CA1 hippocampal neurons reported that the postsynaptic element can modulate the synaptic strength via AMPA receptors mobility during fast transmission. Desensitized receptors in the postsynaptic density travel estimated distances of 150 nm/10 ms (Choquet, 2010) to be exchanged with neighboring functional ones (Heine et al., 2008). This diffusional velocity allows AMPA receptors to cross the postsynaptic density in less than 20 ms (Choquet, 2010). Blocking the diffusion of both desensitized and fresh receptors by cross-linking methods potentiates STD during paired stimulation of a connected pair of neurons at 20 Hz (***Figure I12C***; Heine et al., 2008). Similarly, trapping AMPA receptors at synapses via phosphorylation of AMPA-subunit stargazin by CaMKII strongly increases STD (Opazo et al., 2010). Conversely, accelerating the diffusion by suppression of the extracellular matrix decreases STD (Frischknecht et al., 2009). These results emphasize the major role of AMPA receptors mobility in regulation of STP that likely also occurs at GC synapses. Therefore, this process should be taken into account in electrophysiological recordings of STP.

III.2.2.3. Presynaptic proteins

The GC bouton contains a constellation of proteins involved in STP regulation. Some are briefly listed hereafter.

Among the wealth diversity of presynaptic proteins, synaptotagmins are a large family of membrane-associated Ca^{2+} sensors involved in synaptic vesicle fusion with the membrane for neurotransmitter release (Südhof, 2002). Synaptotagmin 7 plays an important role in STF (Jackman et al., 2016) and disrupting it at GC-PC and GC-SC synapses decreases STF during paired recordings at high-frequency stimulation without affecting the initial P_r (***Figure I12D***; Turecek & Regehr, 2018).

Other proteins in the active zone have been reported as important regulators of STP. Munc13 isoforms are essential proteins for synaptic vesicle priming to the membrane. In GC boutons, Munc13-1 regulates the nanotopographical arrangement of the synaptic vesicle/Ca_v couple and may support differences in synaptic strength (*see III.2.1.1.*, Rebola et al., 2019). In addition, deletion of the Munc13-3 isoform (the most expressed in GCs) reduces P_r and

enhances STF at GC-PC (Augustin et al., 2001) and GC-BC synapses (Bao et al., 2010; Ishiyama et al., 2014).

Last but not least, synapsin II plays a major role in STP diversity. Synapsin II is a presynaptic protein that links the reserve pool of vesicles to the actin cytoskeleton. Phosphorylation of this protein by CaMKII or cAMP-dependent protein kinase A (PKA) unleashes the reserve vesicles to translocate them toward the RRP (Song & Augustine, 2015). Interestingly, synapsin II is heterogeneously expressed at GCs boutons and its knock down impairs STP variability (**Figure I14B**; Dorgans et al., 2019).

III.2.3. Diversity of short-term plasticity

GCs integrate a combination of heterogeneous MFs information conveyed in a wide range of high-frequencies. This sets a particular pattern of firing at a given frequency in the GC and implies to refine STP mechanisms for reliable encoding of a specific information. How do GCs adapt to a high dynamic range of high-frequencies to encode a wide range of sensorimotor information? To reliably encode different frequencies, STP must not be only limited to a given profile of facilitation or depression but extend to more complex dynamics. Chabrol *et al.* labelled MFs from specific precerebellar nuclei and recorded MF-GC synaptic currents in lobule X during 100 Hz electrical stimulation to demonstrate that each MF input on a single GC is characterized by a precise profile of STP (**Figure I13A**; Chabrol et al., 2015). This profile is related to the MF origin, thereby creating a temporal signature of a particular modality (**Figure I13B**). The combination of MFs with heterogeneous STP dynamics on the same GC strongly affects the delay of occurrence of the first action potential (**Figure I13B**). At the next stage, can GC boutons adapt STP dynamics? How does STP diversity affect the PC firing downstream?

Exploring the organization of STP diversity and underlying mechanisms in the cerebellar cortex is fundamental to understand how the cerebellum temporally encodes sensorimotor information.

III.2.3.1. Target-dependency

High-frequency bursts of action potentials trigger STP mechanisms that can either sustain or depress glutamate release. The idea that a given mechanism can be specific to the identity of the postsynaptic target has been largely assessed in the hippocampus and the neocortex but poorly in the cerebellum (Blackman et al., 2013). PCs can regulate presynaptic STP via endocannabinoids during high-frequency bursts while GoCs are unable to such a regulation despite the presynaptic expression of CB1 (Beierlein et al., 2007). This result unveil
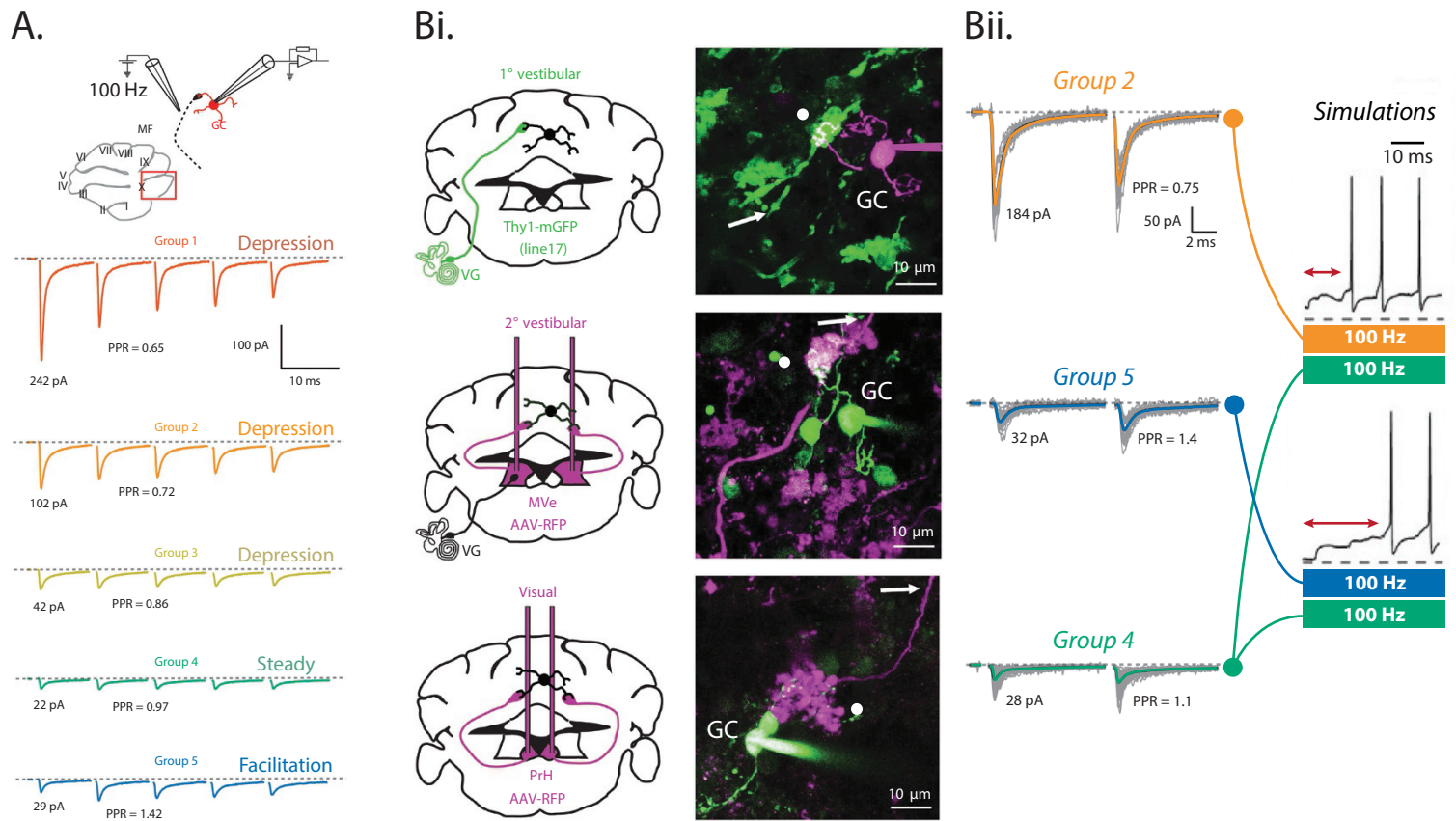
Figure I13 : Pathway-specific short-term plasticity at mossy fibre to granule cell synapses shape the postsynaptic firing delay.

A) Indentification of mossy fibre to granule cell (MF-GC) input types. *Top*, Diagram of a parasagittal slice of cerebellar vermis, showing the vestibular region (lobule X) where single MF-GC connections are recorded using extracellular stimulation and postsynaptic whole-cell voltage-clamp recording of unitary EPSCs. *Bottom*, Average evoked EPSCs across all cells unveil 5 groups of MC-GC connections based on their short-term plasticity properties.

B) Pathway-specific MF-GC synaptic properties. *Bi*, *left*, Schematic diagram showing the labelled primary (top), secondary (middle) and visual (bottom) MFs from the vestibular ganglion (VG), the medial vestibular nucleus (MVe) and the nucleus prepositus hypoglossi (PrH), respectively. *Right*, Corresponding two-photon scanning microscopy images of identified connection (•) between a labelled MF and a GC filled with a fluorescent dye during whole-cell recording. Arrow indicates the position of the stimulation pipette, close to the MF axone. *Bii*, Corresponding unitary EPSCs (left) and simulation of the GC firing delay (right). Synaptic properties depend on the origin of the MF and the combination of inputs firing at 100 Hz on a single GC affects the delay of occurrence of the first postsynaptic spike.

Abbreviations: EPSC, excitatory postsynaptic current; GC, granule cell; MF, mossy fibre; MVe, medial vestibular nucleus; PPR, paired-pulse ratio; PrH, nucleus prepositus hypoglossi; VG, vestibular ganglion.

Adapted from Chabrol et al., 2015.

that the target-dependence of STP can be mediated by heterogeneous expression of neuromodulators from one target to another.

Target-dependency may be related to the presynaptic bouton. By applying high-frequency electrical stimulations on beams of PFs, Bao *et al.* reported exclusive STD at GC-BC synapses while GC-SC synapses exclusively display STF (Bao et al., 2010). Since the PC compartment targeted by BCs and SCs are different, this target-dependent organization suggests specific functionality. As BCs make perisomatic inhibition on PCs, the low-pass filter provided by STD would induce a strong inhibition at the onset of the burst thereby blocking the transfer of information. In contrast, SCs connect to PCs dendrites and the high-pass filter provided by STF would lately inhibit PCs. Hence, such a target-dependency on MLIs would lead to sequential inhibition of the PC.

III.2.3.2. Granule cell to molecular layer interneuron synapse

MLIs receive GCs excitatory inputs and provide disynaptic feedforward inhibition onto PCs. Feedforward inhibition influences spatiotemporal activation of PCs (Mittmann et al., 2005) and contributes in shaping the output pattern of activity.

Diversity in STP can be related to location-dependent dendritic integration (Abrahamsson et al., 2012). In SCs, STF decreases in a distance-dependent manner from the soma to the dendrites. This gradient of STP is related to passive properties of thin SCs dendrites generating a gradient of driving-force that may affect the spatiotemporal activation of the feedforward inhibition.

More recently, Dorgans *et al.* demonstrated that a single MLI receives heterogeneous functional GCs inputs (***Figure I14***; Dorgans et al., 2019). Minimal electrical high-frequency bursts of PFs evoked unitary postsynaptic currents in MLIs (***Figure I14A***). Four distinct STP profiles have been unveiled on both SCs and BCs (***Figure I14A***): one depressed, two facilitated and one was steady. In the steady profile, the invariable amplitude of postsynaptic currents suggests *monoquantal release*: at these synapses, vesicles may be released only at a single active site thereby constraining release of one vesicle per action potential. Such a diversity breaks the target-dependent STP reported by Bao *et al* (2010, *see section III.2.3.1*). Moreover, this diversity is related to the heterogeneous expression of synapsin II. Deleting this protein abolishes the depression profile, increases the amount of facilitating and steady synapses and delays the first spike latency (***Figure I14B***). Hence, diversifying STP expands MLIs temporal coding of sensorimotor information: the feedforward inhibition can be recruited at precise time points of the GC pattern of activity. However, how STP is organized along the same PF is still unknown and is the hot topic of the present project.
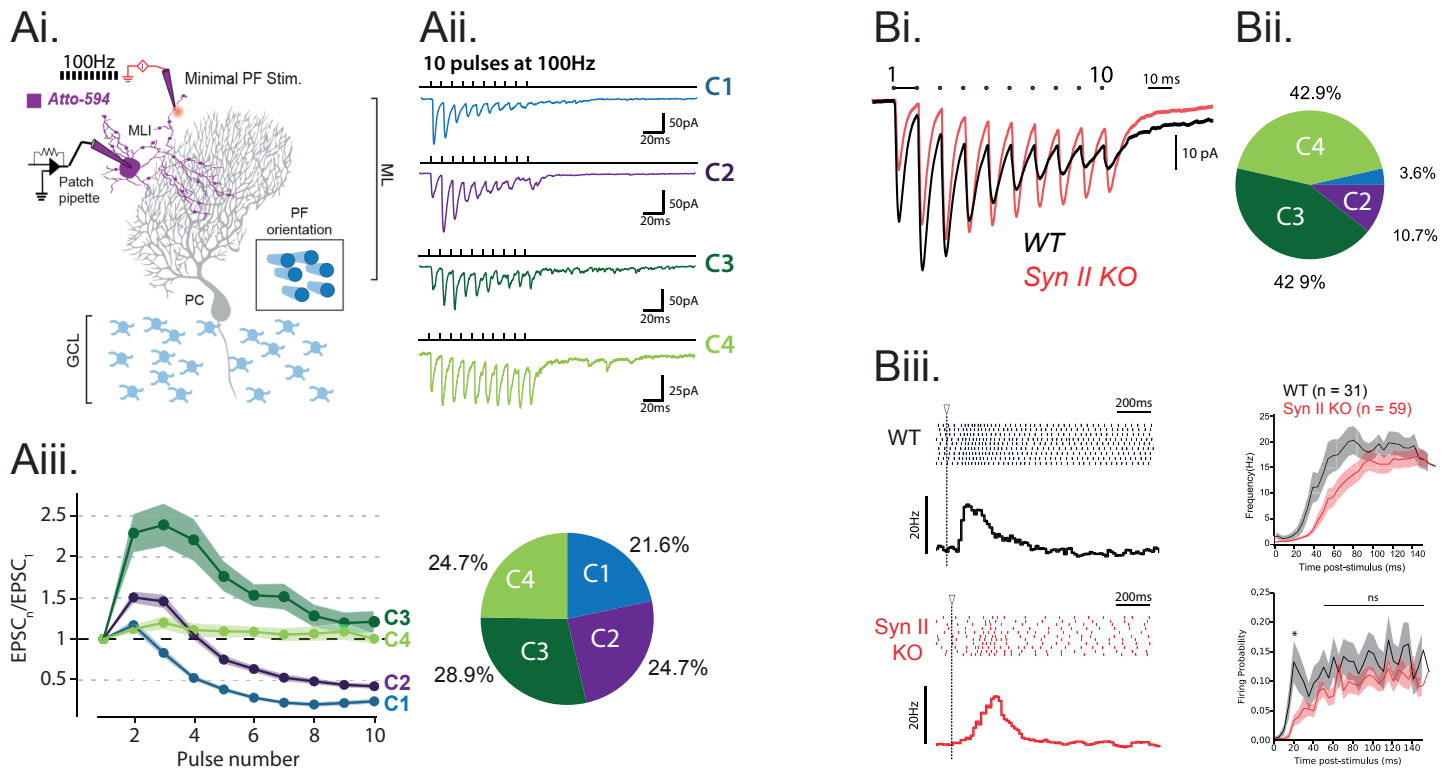
Figure I14 : Diversity of short-term plasticity at unitary granule cell to molecular layer interneuron synapses.

A) Granule cell (GC) to molecular layer interneurons (MLI) show four distinct profiles of short-term plasticity. *Ai*, Diagram illustrating the method used for minimal stimulation protocole. Patch and stimulation pipettes are filled with Atto-594 to visualize the dendritic tree of the recorded MLI and to position the stimulating pipettes in close vicinity of MLI dendrite, respectively. Recordings are performed in parasagittal cerebellar slices to optimize the identification of MLI morphology. *Aii*, Representative traces of the four classes of GC inputs (C1-C4) determined during 10 minimal stimulations of unitary inputs at 100 Hz. *Aiii*, Averaged short-term plasticity profiles in each group determined by the ratio $EPSC_n/EPSC_1$. The pie chart indicates the relative proportion of each category of input from 96 unitary GC-MLI synapses.
B) Synapse-specific expression of synapsin II (syn II) diversifies the profile of excitatory drives on MLIs and expands the coding range of MLIs. *Bi*, Averaged synaptic currents evoked by 10 electrical pulses at 100 Hz in WT mice (black trace) and in Syn II KO mice (red trace). The mean EPSC charge of the first responses is strongly reduced in Syn II KO mice. *Bii*, Pie chart indicating the proportion of input groups shown in A in Syn II KO mice. Note the near complete disappearance of C1 and C2 connections. *Biii, left*, Typical raster plots and peristimulus histogram obtained in WT and Syn II KO mice at unitary GC-MLI synapses following photostimulation of caged glutamate on single GC. The onsets of photostimulation are represented with white arrowheads and dashed lines. *Right*, Means values of the firing frequency (top) and the firing probability (bottom) of MLIs following photostimulation of unitary GC-MLI synapses in WT and Syn II KO mice (black and red lines, respectively).

Abbreviations: EPSC, excitatory postsynaptic current; GC, granule cell; GCL, granular layer; MLI, molecular layer interneuron; PF, parallel fibre; Syn II, synapsin II.

Adapted from Dorgans et al., 2019.

III.2.3.3. Physiological implication on Purkinje cells activity

PCs have pacemaker activity around 50 Hz and provide the sole output of the cerebellar cortex. Timing and shaping this activity is fundamental for sensorimotor integration during movement (Brown & Raman, 2018; Chen et al., 2016) and locomotion (Jelitai et al., 2016). The excitatory/inhibitory balance provided by GCs and MLIs plays a key role in shaping PC firing rate (Jelitai et al., 2016). Grangeray-Vilmint *et al.* recently demonstrated that STP controls the excitatory/inhibitory balance (***Figure I15***; Grangeray-Vilmint et al., 2018). Recordings of PCs firing activity and synaptic currents during high-frequency electrical bursts applied in the granular layer (***Figure I15A***) unveiled a diversity of STF at excitatory synapses (i.e. GC-PC), and STF and STD at inhibitory synapses (i.e. MLI-PC, ***Figure I15B***). At the onset of the burst, the higher synaptic strength of inhibition decelerates the PC firing rate. When the number of pulses in the burst is increased, the synaptic strength of inhibition decreases while the synaptic strength of excitation is enhanced (***Figure I15B***) leading to a shift in PC firing from deceleration to acceleration (***Figure I15C***). Interestingly, this striking effect of STP on excitatory/inhibitory balance is not present in all PCs. Some are characterized by either deceleration or acceleration indicating that initial synaptic weights (i.e. long-term plasticity) determine the firing of these PCs.

Computational modeling reveal that varying STP at excitatory and inhibitory synapses accurately shapes the output pattern of PCs (Grangeray-Vilmint et al., 2018; Tang et al., 2021; Tauffer & Kumar, 2021). Tang *et al.* modeled PCs firing as a function of GCs firing (i.e. Input/Output function) with or without feedforward inhibition and/or STP (Tang et al., 2021). Briefly, at the single cell level, STP dynamically modulates the input/output function in a non-linear manner and shapes the delay of spike occurrence in PC. These effects are even more important when feedforward inhibition is incorporated in the model. At the network level, the dynamic excitatory/inhibitory balance phase-locks PCs temporal spike patterns based on the input frequency, thereby synchronizing PCs populations. Such a synchronicity is required to act on the activity of downstream targets (Person & Raman, 2012). Moreover, the combination of excitatory STP and feedforward inhibition in the model is required to elicit a pause after PCs firing (Tang et al., 2021), a well-known mechanism driving eyelid response during eyeblink conditioning (De Zeeuw et al., 2011; Jirenhed et al., 2017).

Taken together, these results suggest that STP in the GC-MLI-PC pathway expands PC dynamics to temporally encode GCs sensorimotor patterns. Further experimental investigations are required to validate such an important function of STP. The present work provides some data that could be taken into account in future computational models.
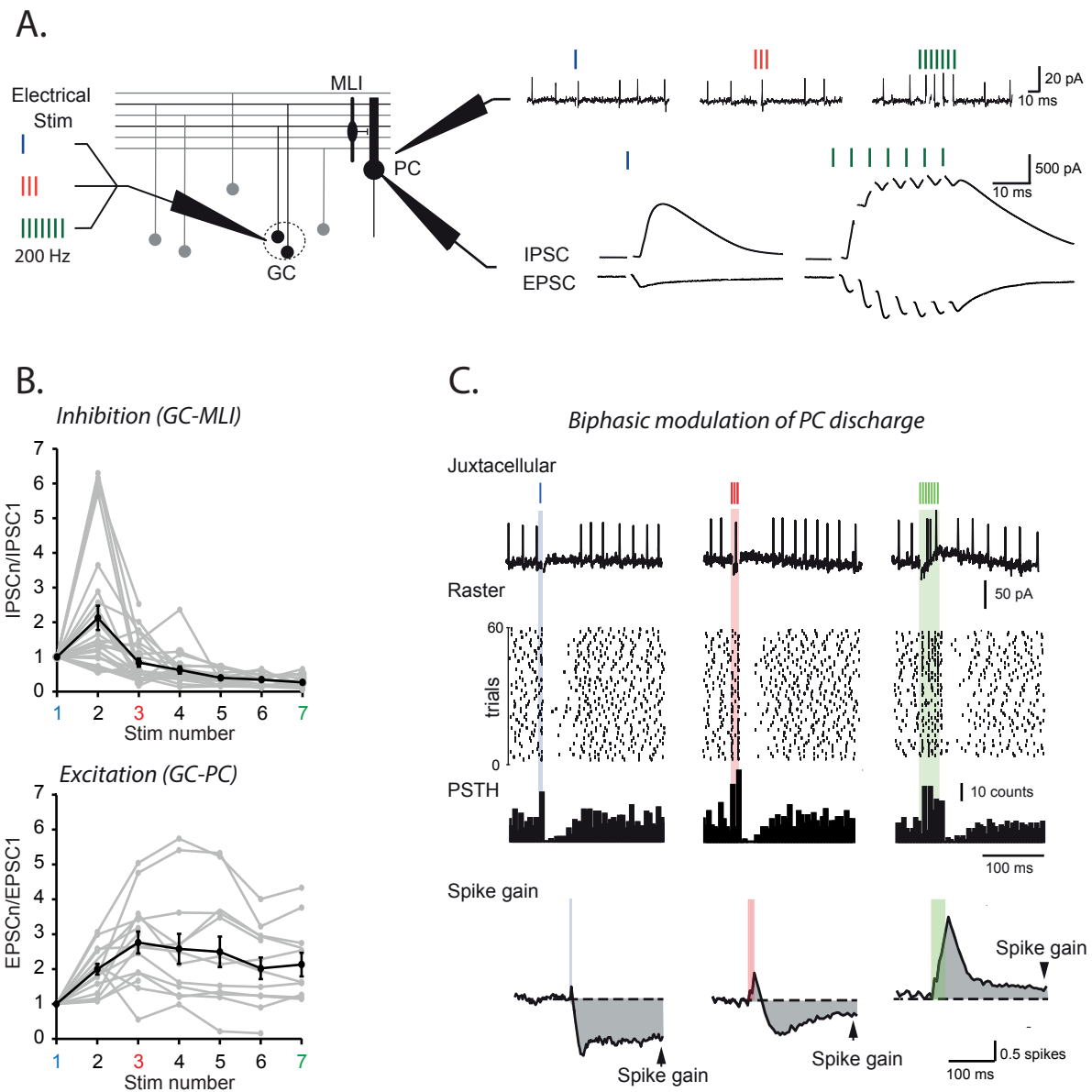
Figure I15 : Diversity of short-term plasticity influences the excitatory/inhibitory balance in Purkinje cells.

A) Left, Diagram of the feedforward inhibitory circuit in the cerebellar cortex. Granule cells (GC) were stimulated with 1, 3 and 7 electrical pulses at 200 Hz. Purkinje cells (PC) were first recorded in juxtacellular mode to monitor discharge (top right), then whole-cell patch-clamped to measure synaptic weights and excitatory/inhibitory balance (bottom right). Excitation is recorded at $V_m = -60$ mV, inhibition at $V_m = 0$ mV.

B) Short-term dynamics of inhibition (top) and excitation (bottom) at each stimulus number in a train (1-7 stimuli) of GC stimuli at 200 Hz. Short-term dynamics are determined by the ratio $EPSC_n/EPSC_1$. Gray traces represent all individual cells. Black traces represent overal mean.

C) *Left*, Example of a biphasic modulation of PC discharge by GC stimulation and determination of the spike gain. From the raster plots, a mean peristimulus histogram (PSTH) is determined and the baseline is subtracted. The spike gain is estimated by integrating this subtracted mean PSTH. *Right*, Two opposite examples of modulation of PC discharge by GC stimulations.

Abbreviations: EPSC, excitatory postsynaptic current; GC, granule cell; IPSC, inhibitory postsynaptic current; MLI, molecular layer interneuron; PC, Purkinje cell; PSTH, peristimulus histogram.

Adapted from Grangeray-Vilmint et al., 2018.

III.3. Short-term plasticity and pattern separation

What is the contribution of STP in behaviors is certainly the question all researchers working on STP ask themselves. Behavior can be defined as the way an individual acts in response to a stimulus. This requires perception of environmental cues, anticipation of a reward, learning and complex motor planning. In all cases, behaviors are composed of ordered sequences of items (e.g. a sequence of muscles contraction) where each item is activated within a precise temporal window. As explained earlier, the cerebellum is at the heart of this process. The *timed sequence* must be reliably computed by cerebellar neurons. Therefore, the question can be clarified as follow: *how STP provides representation of precise well-timed behaviors?*

The granular layer acts as a pattern separator promoting expansion recoding, sparse coding and decorrelation of MFs sensorimotor information. This is permitted through the spatial distribution of MFs inputs in the granular layer, their firing pattern and the huge amount of GCs whose firing is set by a threshold. However, these features do not provide accurate temporal dynamics for the representation of a timed sequence. One could think about MF firing at different times. But what if two MFs conveying different modalities with similar patterns fire at the same time? STP adapts the postsynaptic currents amplitudes to transfer a particular fragment of the pattern in a non-linear fashion. If the two MFs have heterogeneous STP dynamics, the GCs firing delay as well as their firing pattern are different. The two connected GCs are activated at different times with different burst durations hence promoting temporal decorrelation. This challenges *in vivo* results on dense coding emphasized in calcium imaging investigations (Giovannucci et al., 2017; Knogler et al., 2017; Wagner et al., 2017, 2019) where the limited temporal resolution may not support temporal discrimination of patterns thereby giving the illusion of a simultaneous activation of the GCs population (Spaeth & Isope, 2022). Therefore, temporal decorrelation may promote sparseness even in a dense population of activated GCs.

The temporal sequence of items in behaviors could be represented in GCs within precise temporal windows. In eyeblink conditioning (*see section II.1.2*), the learning of the interval between conditional and unconditional stimuli is reliably encoded in PCs through the pause in activity (De Zeeuw et al., 2011; Jirenhed et al., 2017). Barri *et al.* modeled the PC firing within a cerebellar-perceptron algorithm including the variability of STP at MF-GC synapses (Barri et al., 2022; Chabrol et al., 2015). For a given time interval, the PC pause is gradually learned as trials progress. However, without STP diversity, the PC fails to learn the pause indicating that this mechanism at MF-GC synapses is required for behavioral learning. Interestingly, the amplitude of the pause and the time precision of the PC firing decrease when

the interval is longer as demonstrated *in vivo* (Halverson et al., 2015). These results indicate that temporal decorrelation in the granular layer sets the timescale of PCs firing to encode behavioral temporal dynamics. In this way, each GC may encode a particular context at a precise time as hippocampal place cells.

The diversity of STP is not restricted to the granular layer as it has been recently demonstrated in the excitatory/inhibitory balance of PCs (*see section III.2.3.2* and *III.2.3.3*, **Figure I15**; Dorgans et al., 2019; Grangeray-Vilmint et al., 2018). Adding such a diversity expands the temporal coding in MLIs and PCs suggesting further refinement of the PC firing to provide an extremely accurate representation of behaviors. But what if boutons belonging to the same GC express heterogeneous STP? This question is assessed in the present work and no further details are given in this section to better appreciate the results.

Studying temporal expansion recoding requires reliable methods with high temporal resolution to monitor STP at single synapses and provide evidence for computational models. The last part deals with fast optical imaging methods and molecular tools designed to monitor fast glutamatergic neurotransmission.

Part IV. Optical tools for visualization of fast glutamatergic neurotransmission

Monitoring neuronal information transfer through chemical synapses requires high spatiotemporal precision. Electrophysiological methods such as patch-clamp provide reliable recordings of neurotransmission even at the level of single synapses. However, patch-clamp is time consuming, highly challenging *in vivo* and the presynaptic release is measured through postsynaptic AMPA receptors having dynamic properties. Therefore, assessing the accuracy of presynaptic dynamics as well as the quantity of neurotransmitter released in the synaptic cleft can be challenging.

In the last decades, the development of optic tools and imaging methods enabled considerable progress in this field and can be combined to electrophysiology. Fluorescent biosensors allow both *in vivo* and *in vitro* real-time direct measurements of dynamics from tens of single boutons and/or single cells. Spatial and temporal resolutions are function of the biosensor physico-chemical properties and engineering. Therefore, the selection of a particular biosensor should take into consideration the technical experimental conditions.

The first step of the present work has been to develop a method for reliable monitoring of fast glutamate release from several boutons belonging to the same GC. The rise of genetically encoded glutamate sensors allowed great refinements on real-time visualization of glutamatergic neurotransmission. Since GCs are glutamatergic, this part focuses on the intensity-based glutamate-sensing fluorescent reporter (iGluSnFR) used to develop the method of the present work.

Although multiple other fluorescent sensors have been generated to bind neurotransmitters such as GABA, acetylcholine, nicotine or serotonine (Leopold et al., 2019; Marvin et al., 2019; Sabatini & Tian, 2020), they are not further introduced.

IV.1. Early generations of fluorescent glutamate sensors

Glutamate is the major excitatory neurotransmitter in the central nervous system and plays crucial roles in neuronal function. Synaptic glutamate release is associated to transient high glutamate concentrations that can spill out the synaptic cleft. Since early generations of glutamate sensors, considerable efforts are being made to improve brightness, affinity, targeting to synaptic sites and kinetics for reliable measurements of fast synaptic glutamate release (Hao & Plested, 2022). Early generations of fluorescent glutamate sensors relate to sensors exogenously applied on one hand and genetically encoded on the other.

IV.1.1. Exogenous sensors

Exogenous sensors are usually composed of a glutamate-binding subunit coupled to a fluorescent molecule. Glutamate Optical Sensor (EOS) is a hybrid molecule consisting of an AMPA receptor GluA2 subunit and a small synthetic fluorescent dye, the Oregon green (Namiki et al., 2007). When glutamate binds to the binding domain, the conformational change of the sensor increases fluorescence in a dose-dependent manner. Since EOS is exogenously applied, immobilizing it on the cell surface requires a biotin-streptavidin tag coupled to the sensor reacting with biotinylated cells. Despite the modest fluorescence increase and the low spatiotemporal precision when binding glutamate, EOS demonstrated spatial heterogeneity of evoked glutamate release in cultured hippocampal neurons (Namiki et al., 2007).

Site-directed mutagenesis in the glutamate binding domain improved EOS performance hence generating K716A-EOS and L401C-EOS with higher signal-to-noise ratio (Okubo et al., 2010). These variants are linked to Alexa 488 having lower sensitivity to photobleaching than Oregon green from the original EOS. K716A-EOS has a high-affinity for glutamate similar to the original EOS but produces a greater maximal amplitude in fluorescence intensity. These features are adapted for *in vitro* extrasynaptic glutamate dynamics assessment during synaptic activity. However, as small amounts of glutamate induce great amplitudes, high glutamate concentrations can saturate the sensor thereby masking a fraction of the signal. L401C-EOS is a low-affinity glutamate indicator with a greater maximal signal amplitude. Such a variant has been used *in vivo* within the rat somatosensory cortex during hindpaw tactile stimulations (Okubo et al., 2010). Sensory inputs triggered a local glutamate increase reaching micromolar concentrations in the extrasynaptic space as a consequence of synaptic activity.

Original EOS and associated variants greatly contributed to imaging glutamatergic neurotransmission. However, these sensors have two major drawbacks. First, the slow decay is not adapted for STP monitoring. Second, the exogenous feature of these sensors do not allow their expression in a specific cell type. Therefore, genetically encoded sensors have been created to overcome this issue.

IV.1.2. Genetically encoded sensors

The major advantage of genetically encoded glutamate sensors is the expression in a specific cellular subtype and the addressing to a targeted cellular or subcellular compartment. Genetic sensors usually combine the Glt1 subunit from the bacterial glutamate/aspartate ABC

transporter to fluorescent proteins. A platelet-derived growth factor receptor (PDGFR) transmembrane sequence is integrated to the genetic construct for sensor display. The gene encoding the sensor can be delivered in target cells *in vivo* via moderate invasive methods as viral injections, genetic recombination or electroporation.

The fluorescent indicator protein for glutamate (FLIP) is based on Föster resonance energy transfer (FRET) from an enhanced cyan fluorescent protein (eCFP) to Venus, an enhanced yellow fluorescent protein (Okumoto et al., 2005). Both proteins are linked to the glutamate/aspartate binding protein Glt1. At the basal state, the distance between the two proteins is short enough to induce FRET thereby resulting in a high Venus/eCFP ratio of emission intensity. When glutamate binds to Glt1, changing in conformational state pulls the proteins away from each other hence decreasing the emission ratio in a dose-dependent manner. This effect has been observed during electrical stimulations of cultured hippocampal neurons expressing FLIP. Site-directed mutagenesis generated variants with lower affinities for glutamate.

Similarly, other FRET-based sensors have been created: glutamate-sensing fluorescent reporter (GluSnFR; Tsien, 2005) and its variant SuperGluSnFR (Hires et al., 2008). SuperGluSnFR exhibits a 6.2-fold increase in signal amplitude compared to GluSnFR and assessed glutamate concentration and spillover in cultured hippocampal neurons. However, kinetics are not fast enough to resolve fast glutamatergic synaptic transmission.

Altogether, FRET-based genetically encoded glutamate sensors take advantage of ratiometric properties to approximate the glutamate concentration. However, they have slight brightness and too low dynamics for rapid glutamate transients despite the improvement of their physico-chemical properties. Moreover, fluorescent proteins have large excitation and emission spectral bandwidths that tend to overlap hence limiting multiplex imaging. Therefore, FLIP and SuperGluSnFR can be employed for basal glutamate concentration assessments but not for STP monitoring.

IV.2. Intensity-based glutamate-sensing fluorescent reporter: a recent single-wavelength genetically encoded sensor

The major ambition of the last ten years has been to improve real-time measurements of glutamate transients during high-frequency activity. The FRET system replacement by a single excitation wavelength dynamic system was required for such an optimization and gave rise to the intensity-based glutamate-sensing fluorescent reporter (iGluSnFR, Marvin et al.,

2013). Although measurement of glutamate concentration is more efficient with FRET ratiometry, iGluSnFR greatly optimized glutamate monitoring with appreciable subcellular resolution and millisecond temporal precision.

IV.2.1. Engineering and performance

iGluSnFR combines the well-known Glt1 binding protein to the circularly permutated green fluorescent protein (cpGFP, ***Figure I16A***). Single wavelength excitation of cpGFP is a great advantage as it simplifies imaging. The structure of cpGFP is interesting as the amino and carboxy terminals are dissociated from the whole structure and can be reconnected to emit fluorescence. After thousands of screenings, the optimal insertion of the cpGFP is made on residue 253 of Glt1 (***Figure I16A***). A first linker L1LV connects the residue 253 to the cpGFP amino terminal while the second linker L2NP connects the cpGFP carboxy terminal to the residue 264. The distortion in the ligand-free state (i.e. without glutamate) avoids cpGFP closure. Interestingly, this conformation emits a basal fluorescence when excited at 488 nm (i.e. the excitation wavelength for GFP) hence allowing visualization of cells expressing iGluSnFR (***Figure I16Bi***). Glutamate binding changes the conformation of Glt1 which relinks cpGFP terminals (***Figure I16A***). This closed state is bright as it increases the fluorescence intensity of the cpGFP. Therefore, iGluSnFR produces a variation in fluorescence intensity in glutamate-binding state usually normalized by the ligand-free state basal fluorescence (i.e. *ΔF/F*).

The maximal dynamic range of iGluSnFR intensity reaches 4.5 *ΔF/F in vitro* and the affinity ranges from 4 to 107 µM according to the assay and the biological support (***Table I1***; Marvin et al., 2013). In acute hippocampal slices, iGluSnFR has been delivered via viral injection of an adeno-associated virus (AAV). Two-photon glutamate uncaging close to dendritic spines produces a large, fast and variable iGluSnFR signal from single spines. *In vivo* iGluSnFR imaging in the cortical layer V reported glutamate transients with moderate kinetics from virally transfected pyramidal cells during running. Since its development, iGluSnFR has been employed to assess synaptic and extrasynaptic glutamate dynamics in multiple neuronal structures, in Huntington disease and even in zebrafish (for ref, see Hao & Plested, 2022).

Experimentally, the decay-time varies from ~50ms to ~100 ms (***Table I1***; Barnes et al., 2020; Hao et al., 2021; Marvin et al., 2013) even though an astonishing very fast decay-time of 15.6 ms has been reported (***Table I1***; Helassa et al., 2018). Although resolving high-frequency glutamate transients above 10-20 Hz is still challenging, iGluSnFR is a powerful tool allowing quantal analysis of glutamate release at hippocampal Schaffer collateral synapses (Dürst et al., 2020; Jensen et al., 2019; Jensen et al., 2017; Soares et al., 2019).
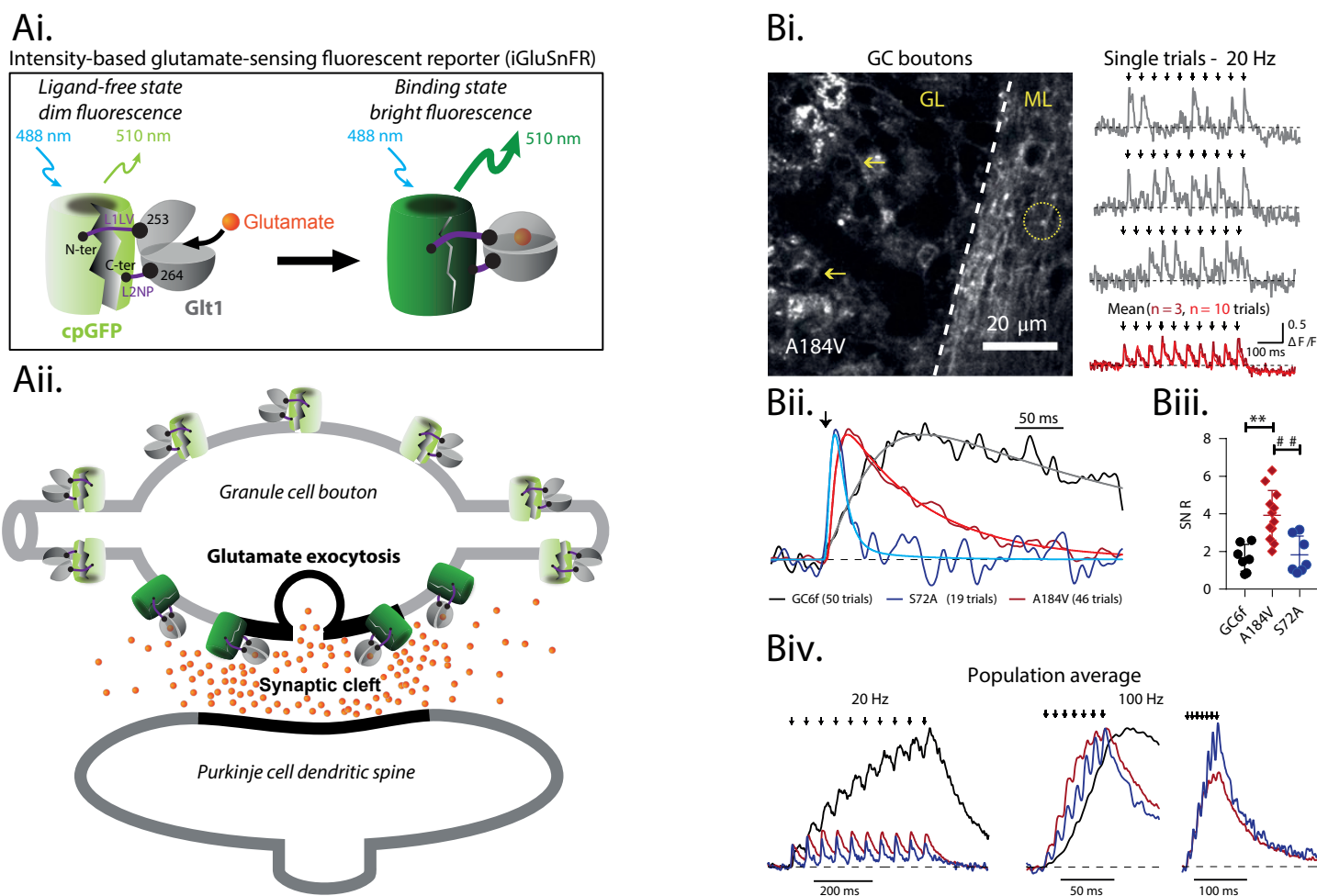
Figure I16 : Sensor engineering and imaging of glutamate release at single granule cell boutons.

A) Engineering of intensity-based glutamate-sensing fluorescent reporter (iGluSnFR). *Ai*, the Glt1 glutamate binding protein is combined to a circular permuted green fluorescent protein (cpGFP) via L1LV and L2NP linkers from residues 253 and 264 to N-ter and C-ter, respectively. Changing in conformational state in glutamate-binding state changes the conformation of iGluSnFR and increases the fluorescence intensity. ***Inspired by Marvin et al., 2013***. *Aii*, diagram illustrating the expression of iGluSnFR on the surface of the bouton membrane. iGluSnFR detects glutamate released in the synaptic cleft.

B) The variants SF-iGluSnFR-S72A and A184V permit resolution of multiple glutamate-release events in single cerebellar granule cell boutons. *Bi*, Two-photon fluorescence image of granule cells (arrows) and axonal boutons (dotted circle) expressing SF-iGluSnFR.A184V in an acute cerebellar slice. Single trials (grey) and mean traces (dark blue, average of 3 trials; light blue, average of 10 trials) of SF-iGluSnFR.A184V responses to 20 Hz extracellular stimulation. *Bii*, Normalized averaged fluorescence traces from single boutons expressing GCaMP6f (GC6f; black; 2mM $[Ca^{2+}]_e$), SF-iGluSnFR.A184V (A184V; red; 1.5 mM $[Ca^{2+}]_e$), and SF-iGluSnFR.S72A (S72A; blue; 1.5 mM $[Ca^{2+}]_e$) in response to a single action potential. *Biii*, Summary plot of signal-to-noise ratio (SNR) from GC6f, A184V and S72A. *Biv*, Population-averaged response at 1.5 mM $[Ca^{2+}]_e$ to 20 Hz stimulation, normalized to the peak of the first response, and to 100 Hz, normalized to the maximum amplitude or to the peak of the first response. Black arrows indicate 60 µs extracellular voltage pulse times. ***Adapted from Marvin et al., 2018***.

Abbreviations: GL, granular layer; iGluSnFR, intensity-based glutamate-sensing fluorescent reporter; ML, molecular layer; SNR, signal-to-noise ratio.

Name	Principle	Affinity (µM)	Rise time (ms)	Decay time (ms)	Dynamic Range $(\Delta F/F)_{max}$	References
iGluSnFR	Single-wavelength genetically-encoded sensor	107, 33[#], 84 * (in vitro)	15 (neuron, evoked)	92 (neuron, evoked)	4.5 (in vitro) 4, 1[#], 2.5^ (HEK293)	Marvin et al. (2013)
		4, 3[#], 24^, 49[‡] (HEK293)	30 (astrocyte, evoked)	85 (astrocyte, evoked)	1 (neuron, titration) 0.14 (neuron, evoked)	*Marvin et al. (2018)
		5, 2.1* (neuron, titration)	1.1 (in vitro)[#]	8.5 (in vitro) 16 (neuron, evoked)[#]	0.07 (astrocyte, evoked)	# Helassa et al. (2018) ‡Wu et al. (2018) ^Hao et al. (2021)
iGluSnFR-S72T (iGlu_u)	iGluSnFR variant	600 (in vitro) 53 (HEK293)	1.1 (in vitro)	1.5 (in vitro) 2.6 (neuron, evoked)	1.7 (HEK293)	Helassa et al. (2018)
SF-iGluSnFR-S72A	iGluSnFR variant	200 (in vitro) 34 (neuron,	3 (neuron, evoked)	10.6 (neuron, evoked)	2.5 (in vitro) 2.5 (neuron, titration)	Marvin et al. (2018)
SF-iGluSnFR-A184V	iGluSnFR variant	41 (in vitro) 2.1 (neuron,	5 (neuron, evoked)	29.1 (neuron, evoked)	9 (in vitro) 9 (neuron, titration)	Marvin et al. (2018)
SF-mTurquoise2-iGluSnFR	iGluSnFR variant	395 (in vitro)	N/A	N/A	3 (in vitro)	Marvin et al. (2018)
iGluSnFR-γ8	iGluSnFR variant	32 (HEK293)	N/A	70 (HEK293)	1.6 (HEK293) 0.45 (neuron, spontaneous)	Hao et al. (2021)
iGluSnFR3	iGluSnFR variant	196 (in vitro) 8.2 (neuron)	18.9 (neuron, evoked)	N/A	54 (in vitro)	Aggarwal et al. (2022)

Table I1: Summary of glutamate biosensor properties.

For the type of assay used, *in vitro* means measurements on the soluble form of glutamate sensor, without the membrane targeting domain. *HEK293* means titrations on the sensor as expressed on the surface of HEK293 cell. For experiments where the sensors were expressed on the surface of neurons, the type of stimulus used is noted, with *titration* meaning exogeneously applied glutamate. ***Adapted from Hao & Plested, 2022***.

4

IV.2.2. Variants

Glutamate concentration in the synaptic cleft is variable and usually reaches high magnitudes (1.1 mM; Clements et al., 1992). Glutamate dissociation kinetic (i.e. K_{off}) is slower on the Glt1 binding domain than AMPA receptors. This decreases the dissociation constant K_d which results in a high affinity for glutamate. Therefore, high glutamate concentrations dramatically saturate iGluSnFR and lengthen the signal decay resulting in too low temporal resolution for STP measurements.

In the last five years, substantial efforts are being made to create iGluSnFR variants with higher performance and specific addressing to the synaptic cleft to avoid extrasynaptic contamination (*Table I1*).

IV.2.2.1. Kinetics and brightness improvement

High kinetics are paramount to monitor STP plasticity at single boutons. Decreasing affinity via mutagenesis increases off-kinetics but tend to decrease the signal amplitude. Helassa *et al.* introduced the mutations E25D and S72T in Glt1 to produce iGlu$_f$ and iGlu$_u$ variants (also called fast and ultrafast variants) showing high dissociation constant (137 µM and 600 µM respectively, *Table I1*; Helassa et al., 2018). Both variants have promising fast kinetics (5.2 ms and 2.6 ms, respectively) at single boutons of Schaffer collateral in organotypic slices during electrical stimulations at 100 Hz. However, although iGlu$_u$ shows a higher resolution of glutamate transients, its signal amplitude is reduced.

In parallel, Marvin *et al.* introduced two great modifications to the original iGluSnFR (Marvin et al., 2018). First, exchange of cpGFP with circularly-permuted superfolder GFP (SF) provided more stable SF-iGluSnFR during imaging (Pédelacq et al., 2006). Second, mutations in Glt1 produced variants SF-iGluSnFR-A184V and SF-iGluSnFR-S72A with respectively modest and low glutamate affinity (40 µM and 200 µM) as well as fast and very fast off-kinetics (29.1 ms and 10.6 ms, *Figure I16Bi-Bii*, *Table I1*). Such an optimization improved the signal-to-noise ratio (i.e. brightness) of A184V variant compared to the original iGluSnFR with no change for the S72A variant (*Figure I16Biii*). However, S72A shows promising temporal resolution of STP dynamics at single GCs boutons during electrical stimulations of parallel fibres at 20 and 100 Hz (*Figure I16Biv*; Marvin et al., 2018). Furthermore, although the variant iGlu$_u$ has faster decay kinetics, S72A shows higher signal amplitudes (*Table I1*).

In the present work, the choice fell on SF-iGluSnFR-S72A as it gives the best parameters to monitor STP at single GC boutons in cerebellar slices. The lab of David

DiGregorio opted for SF-iGluSnFR-A184V for *in vivo* assessment of glutamate dynamics at MF-GC synapses owing to the high signal-to-noise ratio and kinetics performance.

Additionally, colour variants of iGluSnFR allow multicolor imaging (Marvin et al., 2018). Briefly, cpGFP is exchanged by other chromophores as Azurite (blue), mTurquoise2 (cyan, *Table I1*), Venus (yellow) and even circularly-permuted red fluorescent protein (red; Hao & Plested, 2022).

Last but not least, a new generation of iGluSnFR optimizing a large panel of performance recently came out (*see section IV.2.2.3*, *Table I1*; Aggarwal et al., 2022).

IV.2.2.2. Restriction to the synaptic cleft

Dense expression of iGluSnFR allows visualization of the entire cell and do not requires injection of a morphological dye. However, the absence of anchor proteins ensuring exclusive enrichment at synapses increases the probability of extrasynaptic signaling inference with synaptic glutamate. Kim *et al.* developed the variant iGluSnFRpre specifically expressed in the axonal segment of cultured hippocampal neurons (Kim et al., 2020). To provide presynaptic addressing, the PDGFR transmembrane domain from the original iGluSnFR has been replaced by Neurexin 1, a transmembrane presynaptic cell-adhesion protein. Performance of iGluSnFRpre are identical to the original form and provided insight into multivesicular release from a single action potential as well as recovery of the RRP.

These findings motivated Hao *et al.* to generate the variants SnFR-γ2 and SnFR-γ8 targeted to the postsynaptic density (*Table I1*; Hao et al., 2021). The truncated form of the original iGluSnFR has been coupled to Stargazin, a protein involved in AMPA receptors docking at the postsynaptic density. In this way, signals from both variants are confined to the synapse. Since hippocampal neurons display low firing rates, performance have been assessed in cultured hippocampal neurons expressing either variants during electrical bursts at 5 Hz. Despite slight decreased performance according to the variant compared to the original form, SnFR-γ2 and SnFR-γ8 better discriminate STP dynamics between two spatially close regions.

Altogether, these targeted variants offer the possibility to significantly reduce the contamination from extrasynaptic glutamate and are promising starts for future optimizations. However, cerebellar GCs fire at exquisitely higher frequencies than hippocampal neurons. Therefore, the current targeted variants are not adapted for cerebellar STP monitoring at high-frequency rates.

IV.2.2.3. Third generation

Nowadays, there is no genetically encoded glutamate sensor summarizing all the performance required to assess neurotransmission in any structure. However, very recently, the new variant iGluSnFR3.v857 combines the optimization of brightness, kinetics and synaptic targeting *in vitro* as well as *in vivo* (***Table I1***; Aggarwal et al., 2022). The engineering started with the SF-Venus-iGluSnFR-A184V (Marvin et al., 2018) as a template for screening since it has the highest rate-limiting glutamate concentration and a large two-photon cross-section (i.e. the probability of two-photon absorption by the fluorophore). After mutagenesis and a series of screenings, Aggarwal *et al.* generated the variant iGluSnFR3.v857 (the 857th variant screened in neurons). The greatly optimized saturation kinetics offer reliable measures of high glutamate concentrations owing to improved linearity of signals. Brightness and signal-to-noise ratio are dramatically enhanced in cultured cortical and hippocampal neurons during electric field stimulations. The coexpression of iGluSnFR3.v857 and the tetanus toxin light chain peptide (i.e. a blocker of synaptic vesicle fusion) in neurons almost completely abolishes the fluorescent transient evoked by a single action potential indicating highly reliable assessment of synaptic glutamate. Furthermore, the exchange of the PDGFR transmembrane domain with stargazin restrains iGluSnFR3.v857 to nanoscopic localization in the postsynaptic density thereby improving the specific detection of synaptic glutamate. *In vivo*, iGluSnFR3.v857 signals from single boutons are sharp and resolve fast glutamate transients during directed visual tasks and sensory inputs. However, although kinetics have been optimized, resolving glutamate transients above ~30 Hz during STP might be challenging.

This first variant from the third generation offers promising directions for future iGluSnFR generations. The panel of performance of iGluSnFR3.v857 should be considered in the future to monitor more reliably glutamate dynamics in cerebellar microcircuits *in vitro* and *in vivo*.

IV.2.3. Employing for short-term plasticity studies and quantal analysis at single boutons

Since its release, researchers aim to exploit iGluSnFR performance to visualized STP dynamics and quantal release of glutamate. Jansen *et al.* applied multi-Gaussian fit on the histogram of iGluSnFR-A184V signals to demonstrate that single boutons from hippocampal pyramidal neurons release up to four vesicles (Jensen et al., 2019). The absence of an evoked signal in a trial reflected release failures, an important measure to determine P_r. Interestingly, P_r was heterogeneous from one bouton to another on the same axon thereby reflecting the diversity of STP reported in this study. Similarly, Dürst *et al.* used the original iGluSnFR in

hippocampal neurons to demonstrate that vesicular release probability is highly variable between single boutons and predicts synaptic strength (Dürst et al., 2022). At low external Ca^{2+}, the vesicular release probability is strongly correlated to the synaptic strength while N predominates at high external Ca^{2+}. This indicates that the number of RRP vesicles limits the synaptic strength when P_r is high and may modulate STP.

In addition, when the external Ca^{2+} is increased, the variant iGluSnFR-S27A efficiently resolves the switch from STF to STD at 10-20 Hz (Kim et al., 2020; Marvin et al., 2018). At 50 Hz and 100 Hz, glutamate transients are discriminated although the build-up of the signal likely reflects residual glutamate, saturation and spillover (Marvin et al., 2018). Conversely, transients from STD assessed with the variant iGlu$_u$ reveal complete clearance of glutamate after each electrical pulse during bursts at 100 Hz (Helassa et al., 2018).

Fluctuations in photophysical properties and non-linear response of iGluSnFR variants bias the measurement of glutamate transients. Hence, high performance and mathematical modelling are required for resolution of individual quanta. Variations related to heterogeneous functional and ultrastructural mechanisms between individual synapses have to be isolated from background noise and extrasynaptic glutamate. Spatial targeting enhances the precision of quantal analysis as it filters out glutamate spillover to focus on glutamate at the point of release (Aggarwal et al., 2022; Hao et al., 2021).

Genetically-encoded glutamate sensors are a state-of-the-art powerful tools designed to monitor glutamatergic neurotransmission and are usually associated to two-photon microscopy. The selection of a particular variant definitely depends on biological models, dynamic mechanisms and technical experimental conditions and can be combined to calcium and voltage imaging. The development and optimization of new variants is now well established and will provide significant refinement on glutamatergic synaptic transmission studies to become a mainstream technique. Here, SF-iGluSnFR-S72A is used to monitor STP diversity at boutons belonging to the same GC and determine quantal parameters underlying this diversity.

V. Materials & Methods

The first part of my PhD thesis was dedicated to the development of a method allowing SF-iGluSnFR.S72A expression in GCs to monitor glutamate release at single PF boutons. The *section V.6* in the present chapter describes the development of this method.

V.1. Ethics

All experiments were conducted in accordance with the guidelines of the Ministère de l'Education Supérieure et de la Recherche and the local ethical committee, the Comité Régional en Matière d'Expérimentation Animale de Strasbourg under the agreement no A67-2018-38 (delivered on the animal facility Chronobiotron, UMS3415, Université de Strasbourg).

V.2. Mice

Three strains of male and female mice were used for the experiments: 128 CD1 wild-type, 9 L7-cre (#004146, B6.129-Tg(pcp2-cre)2Mpin/J, The Jackson Laboratory; Barski et al., 2000) and 16 tdTomato (#007909, B6.Cg-Gt(ROSA)26Sor$^{tm9(CAG-tdTomato)Hze}$/J, The Jackson Laboratory; Madisen et al., 2010). L7-cre and tdTomato mice backcrossed on a CD1 background were bred together and 118 L7-tdTomato juvenile were used. In these mice, cre-recombinase is expressed under the PC-specific L7 promoter (L7-Cre). Mice were bred in the animal facility present in the building (Chronobiotron, CNRS UMS 3415, Strasbourg) and housed with all littermates and parents from birth to weaning age (21 days old).

Prior to stereotaxic injections, littermates of the same sex were housed 3-5 per cage. Mice were provided with food and water *ad libitum* in a 12/12h light/dark cycle with constant hygrometry (45-50%) and temperature (21-22°C). After surgery, mice were put back together in their cage and health conditions were daily monitored.

V.3. Viral vector

The adeno-associated virus (AAV) plasmid coding for SF-iGluSnFR.S72A under the hSynapsin promoter (AddGene #106176, Marvin et al., 2018) was given to the Molecular Biology & Virus service (IGBMC, Illkirch, Strasbourg) to be introduced in an AAV-DJ capside resulting from the fusion of 8 AAV serotypes and promoting superior *in vitro* transduction efficacies (Holehonnur et al., 2014). The titer reached $5,6.10^{13}$ GC/ml and was not diluted for stereotaxic injection.

V.4. Stereotaxic injection

CD1 or L7-tdTomato mice were anesthetized by inhalation of isoflurane 4% (Vetflurane, Vibrac, France) set with the vaporizer on the station Minihub-V2 (TEM SEGA, France) mixed with O_2, with a flux of 0.8 L/min and aspiration of 0.4 L/min. Mice were then placed on the stereotaxic frame (model 68526, RWD Life Science) in flat skull position and maintained anesthetized with 2–2.5% isoflurane. Body temperature was constantly monitored via a rectal probe connected to a heat pad (TC-1000, Bioseb Lab) and set at 37°C. Eyes were moisturized with Ocry-gel (TVM, France).

Absence of reflexes was checked prior to any injection or incision. The scalp was shaved and cleaned with Betadin 10% and ethanol 70%. Bupivacaïne (2 mg/kg) was mixed with Lurocaïne (2 mg/kg) and injected subcutaneously prior to scalp incision to prevent pain. Craniotomy was performed using a manual driller (OmniDrill35 Micro Drill, World Precision Instruments) with a ball mill tip of 0.5 mm diameter (Ball Mill, Carbide, #1/4, 0.5 mm Diameter, World Precision Instruments). The coordinates for unilateral viral injection in vermal lobules IV-VI were determined from The Mouse Brain Atlas (Franklin and Paxinos, 2007) and adapted on CD1 mice as follow (from Bregma): 6.5 mm caudal, 0.2 mm mediolateral, 1.05 mm ventral from the top of the tissue. Viral particles were loaded in a graduated glass pipette (Drummond Calibrated Pipets, USA) with a piston for manual injection at an infusion rate of ~100 nl/min and a total volume of ~200 nl. The placement of the pipette in the dorsoventral axis was performed using a motorized micromanipulator (IVM Mini Single, Scientifica, UK). The pipette was left 5 min in place for an effective diffusion of the virus. After gently removing the pipette, the wound was closed with surgical staples (7.5x1.75, Michel Suture Clips). An interscapular subcutaneous injection of Metacam (2 mg/kg) was performed to prevent inflammation and OralMetacam (2 mg/kg) was added in the water bottle for the two days post-surgery. Injected mice were kept for at least 2 weeks to allow transgene expression in GCs.

V.5. Slice preparation for two-photon imaging and electrophysiology

Cerebellar slices were prepared from postnatal day 21–80 male and female CD1 or L7-tdTomato mice. Mice were anesthetized as described in *section V.4* and killed by decapitation. The cerebellum was quickly dissected out and immersed in ice-cold (1-4°C) artificial cerebrospinal fluid (ACSF) bubbled with carbogen (95% O_2 and 5% CO_2) containing (in mM): NaCl (120), KCl (3), $NaHCO_3$ (26), NaH_2PO^4 (1.25), $CaCl_2$ (2.5), $MgCl_2$ (2), glucose (10) and minocycline (5.10^{-5}) (Sigma-Aldrich, USA). The cerebellum was then transferred in the tank of a vibrating microtome (Microm HM 650V, Microm, Germany) to prepare 300 mm-thick transverse acute slices in ice-cold (1-4°C) N-methyl-D-aspartate (NMDG) based solution containing (in mM): NMDG (93), KCl (2.5), $NaHCO_3$ (30), NaH_2PO^4 (1.2), $CaCl_2$ (0.5), $MgCl_2$ (10), glucose (25), HEPES (20), sodium ascorbate (5), sodium pyruvate (3), N-acetyl-cystein (1) and kynurenic acid (1). The pH and the osmolarity of this solution were adjusted at 7.3–7.4 and 300 mOsm, respectively. Slices were maintained in ACSF first at 32°C and bubbled with carbogen for 45 minutes, then kept at room temperature (22°C) prior to experiments.

For both two-photon imaging and electrophysiology, cerebellar slices were transferred in a recording chamber with continuous perfusion of bubbled ACSF at 32-34°C. To block long-term plasticity and neuromodulators, blockers (Abcam or Tocris, UK) of GABA-A receptors (100 µM picrotoxin), GABA-B receptors (10 µM CGP52432; 3-[[(3,4-Dichlorophenyl)- methyl] amino] propyl (diethoxymethyl) phosphinic acid), NMDA receptors (100 µM D-AP5; D-(-)–2-Amino-5-phosphonopentanoic acid), CB1 receptors (1 µM AM251; 1-(2,4-Dichlorophenyl)–5-(4-iodophenyl)–4-methyl-N-(piperidin-1-yl)–1H-pyrazole-3-carboxamide), mGluR1 receptors (2 µM JNJ16259685; 3,4-Dihydro-2H-pyrano[2,3-b]quinolin-7-yl)-(cis-4-methoxycyclohexyl)-methanone) and A1 receptors (2 µM DPCPX; Dipropylcyclopentylxanthine) were added to ACSF.

V.6. Two-photon imaging

V.6.1. Two-photon resolution: fluorescence microbeads

Lateral and axial point-spread functions (PSF) were measured using yellow-green (ex505/em515) fluorescent microbeads (0.1µm Ø, FluoSpheres™ carboxylate, Invitrogen) diluted in ethanol 100% at 1/10000 and mounted on a slide. Microbeads were identified using a SliceScope Pro 2000 two-photon scanning head (Scientifica, UK) mounted on an Olympus BX-2 illuminator equipped with a water-immersion objective XLUMPLFLN20XW (20x/1.0-NA, Olympus, Tokyo, Japan), two galvanometer mirrors (Galvo Scan, Scientifica, UK) and

photomultipliers (S-MDU-PMT-20, Scientifica, UK). Two-photon excitation was performed with a pulsed Ti:Sapphire laser (Mai Tai, Spectra Physics, France) tuned to 920 nm for imaging microbeads. The laser intensity was set at 10 mW using a pockels cell (350-80-02, Conoptics, Danbury, USA).

Microbeads were imaged in both lateral (XY) and axial (Z) axis performing z-stacks with 0.2 µm spacing between planes. Each plane was imaged at 0.75 Hz using a dwell time of 4µs. To avoid distortion artefacts at the edge of the field of view, only microbeads inside an area from 5 µm from the edge of the field of view were analysed (**Figure M1A**). Lateral and axial resolutions were calculated on ImageJ/Fiji freeware. For lateral resolution, z-stacks were averaged and pixel intensity of single microbeads was determined via a straight line bisecting the centre (**Figure M1B**). The intensity was fitted with a Gaussian function to calculate the full width at half maximum (FWHM) reflecting the resolution (i.e. PSF):

$$FWHM = \sigma \times 2.355$$

For axial resolution, the FWHM was calculated over the Gaussian fit from the smir signal on Z projection of the microbead (**Figure M1C**). Over 40 microbeads, the lateral resolution was 0.62 ± 0.02 µm which is largely satisfying for GCs boutons imaging (**Figure M1D**). However, the high axial resolution of 5.08 ± 0.86 µm may lead to imaging 2–4 boutons at a time. Therefore, boutons were imaged on PFs as isolated as possible.

V.6.2. Granule cell boutons imaging

Two weeks after stereotaxic viral injection (**Figure M2Ai**), GCs and PFs expressing SF-iGluSnFR.S72A were identified using the two-photon setup described in *section V.6.1*. Two-photon excitation wavelength was tuned to 920 nm for imaging SF-iGluSnFR.S72A and the laser intensity was adjusted at 8–20 mW. A massive number of GCs and PFs express SF-iGluSnFR.S72A close to the injection site (**Figure M2Aii**). boutons were imaged far from the injection site for two reasons. First, since the promoter hSynapsin is not GC-specific, multiple neurons (i.e. MLIs, GoCs and CC) express the fluorescent sensor and overlap with PFs fluorescence. Second, the PFs divergence with distance increases the probability to identify isolated PFs.
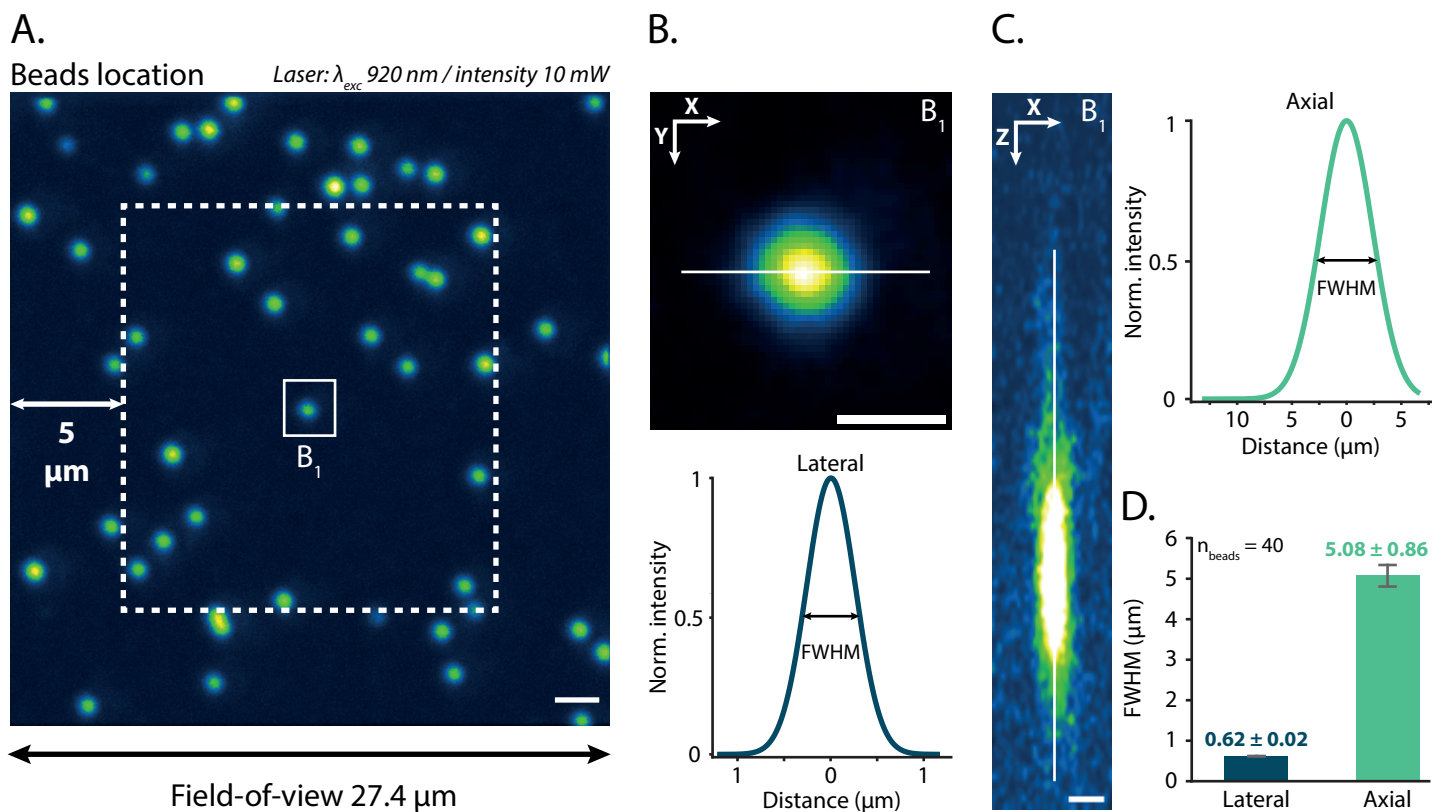
Figure M1 : Two-photon resolution.

A) Average of two-photon z-stack imaging of fluorescence microbeads. Only microbeads localized beyond 5 µm from the edge of the fied-of-view (dotted line square) are analyzed for resolution. The central microbead B_1 is shown as an example to determine lateral and axial resolution. Scale bar: 2 µm.

B) Lateral resolution of the microbead B_1 (XY plane). The white line on the image (top) bisects the microbead to determine the gaussian of the pixel intensity (bottom). The full width at half maximum (FWHM) gives the point-spread-function of the microbead. Scale bar: 1 µm.

C) Axial resolution of the microbead B_1 (XZ plane). Scale bar: 1 µm.

D) Comparison of $FWHM_{lateral}$ and $FWHM_{axial}$.
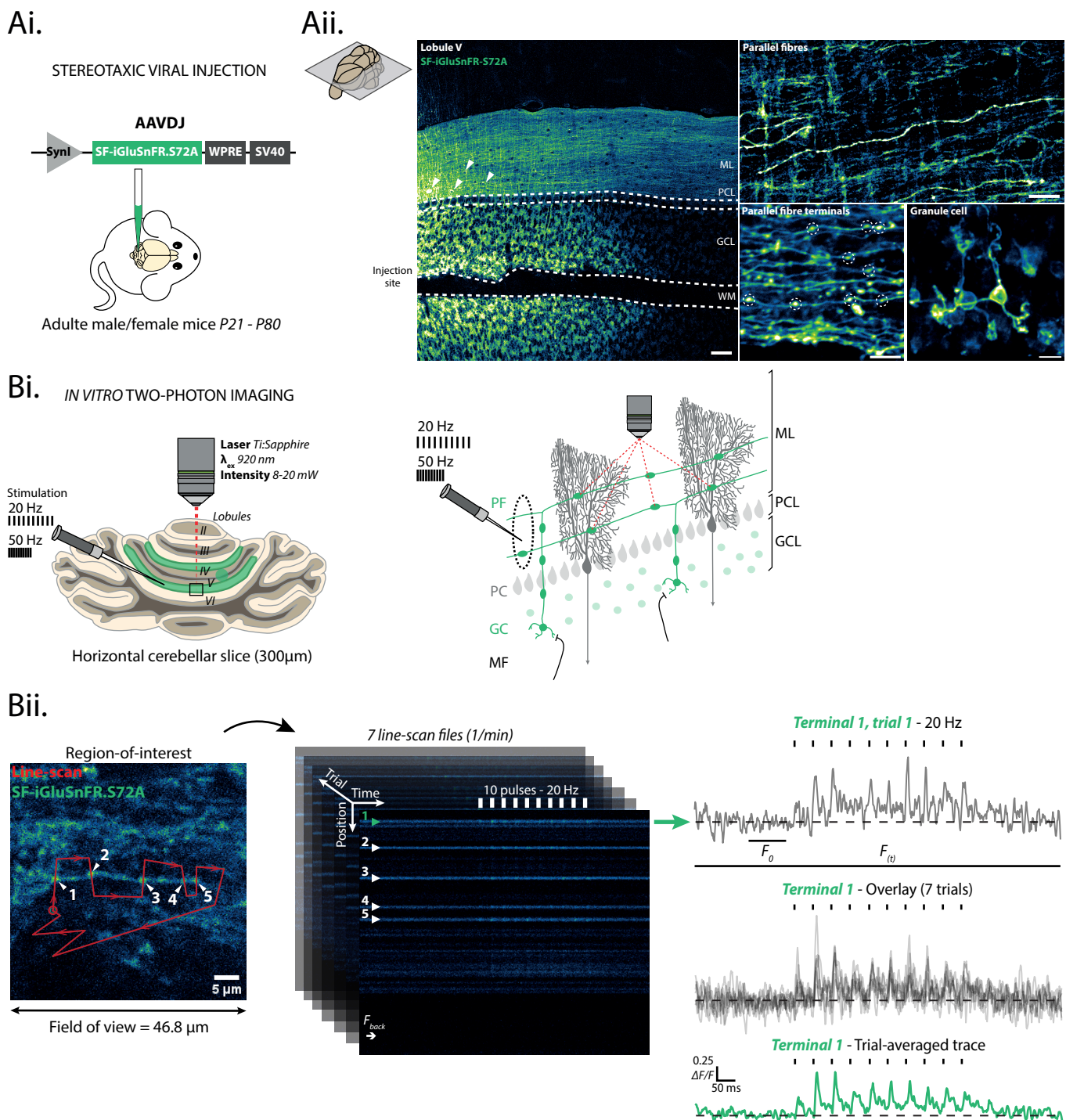
Figure M2 : Protocole for SF-iGluSnFR.S72A expression and two-photon imaging of granule cell terminals.

Ai) Stereotaxic injection of AAVDJ.hSynapsin.SF-iGluSnFR.S72A in the cerebellar cortex.

Aii) Granule cells and parallel fibres expressing SF-iGluSnFR.S72A in the vermal lobule V. On the low magnification image, white arrowheads indicate MLIs expressing SF-iGluSnFR.S72A. On the image illustrating PFs, dotted circles indicate terminals. Scale bar for the low magnification image: 50µm. Scale bar for the others: 10 µm. *GCL, granule cells layer; ML, molecular layer; PCL, Purkinje cells layer; WM, white matter.*

Bi) Two-photon *in vitro* imaging of single granule cell terminals on horizontal cerebellar slices 2 weeks after stereotaxic injection. The diagram on the right illustrates the cerebellar circuitry and the protocole applied on granule cells terminals.

Bii) Line-scan applied on terminals and fluorescence traces. On the region-of-interest image (left), the line-scan (red line) orthogonally bisects 5 terminals (white arrowheads and numbers) on the same parallel fibre. The red circle indicates the start position of the line-scan. Red arrows indicate the direction of the laser. The line-scan is repeated every minute and generates a two dimensional image (central) where time is represented on the x-axis and the position on the line as y-axis. The position of each terminal (white arrowheads associated to numbers) on the line-scan image is reported from the position of terminals on the red line on the region-of-interest image. Background noise (F_{back}) is determined on a region deprived of fluorescence signal. Baseline fluorescence (F_0) and fluorescence trace ($F_{(t)}$) required for $\Delta F/F_0$ calculation are indicated at respective positions on the extracted raw trace (right, top) for terminal 1. All fluorescence traces (right, middle) are then averaged (right, bottom).

81

Variations of fluorescence signals from SF-iGluSnFR.S72A evoked by synaptic glutamate were identified during extracellular PFs stimulations (10 pulses at 20Hz or 50Hz, 50 µs per pulse, **Figure M2B**) delivered with a stimulator (Iso-stim 01D, NPI Electronic Instruments for the Life Sciences). A patch pipette of ~5 MΩ containing ACSF supplemented with 10 mM HEPES and 50 µM Atto 488 (Sigma-Aldrich, Germany) to respectively adjust pH and visualize the pipette was linked to a monopolar electrode. The stimulation pipette was typically placed in the molecular layer close to PFs expressing the fluorescent sensor (**Figure M2Bi**). Boutons on PFs were identified with a frame scan at 6–12 Hz. The stimulation intensity was progressively decreased until fluorescence transients were restrained to the targeted PF and some PFs around. Line-scan fluorescence imaging of all single boutons on the targeted PF segment was performed using a dwell time of 2 µs for ~1.5 sec on SciScan freeware (LabView 2012, Scientifica, UK). At least 7 trials (1trial/min) were performed at a scanning rate of ~500–900Hz. The line-scan was orthogonally oriented to the PF and bisected the boutons (**Figure M2Bii**). The position of the bouton on the line was identified on the Region of Interest image and reported on each line-scan file using Python custom-written scripts to extract the trial trace. Background fluorescence (F_{back}) was measured 1 µm away from parallel fibre signal. Fluorescence signals were averaged over 0.4–2 µm width of the line-scan fraction bisecting the bouton. Fluorescence traces were corrected by subtracting F_{back} from each trial. After removing F_{back}, the fluorescence variation was calculated as follow:

$$\frac{\Delta F}{F} = \frac{(F_{(t)} - F_{back}) - (F_0 - F_{back})}{(F_0 - F_{back})}$$

where $F_{(t)}$ is the fluorescence trace and F_0 the mean of baseline fluorescence calculated on a time window over 100 ms prior to stimulation.
Trial-to-trial stability was assessed using a z-score calculated as follow:

$$-3\sigma > \frac{F_{0_{(i)}} - F_{0_{(average)}}}{\sigma_{F_{0_{(average)}}}} < 3\sigma$$

where $F_{0_{(i)}}$ is the F_0 value from the trial, $F_{0_{(average)}}$ and $\sigma_{F_{0_{(average)}}}$ are respectively the value and the standard deviation of F_0 from the trial-averaged trace. Trials exceeding ±3σ were discarded.

For each bouton, trial-averaged fluorescence traces underwent 9-points smoothing using Savitzky-Golay filter prior to analyses of amplitudes and decay-time constant (**Figure M3**). Photobleaching prior to stimulation was fitted with a mono-exponential function, extrapolated to the end of the trial-averaged trace and subtracted to the trace. Boutons were analyzed when stimulation elicited averaged transients exceeding 3σ of the baseline noise. The decay-time constant (τ_{decay}) was calculated on the descending phase of each transient fitted with a mono-exponential function (**Figure M3**).

V.6.3. Saturation of SF-iGluSnFR.S72A

Frequencies of electrical pulses above 20Hz trigger SF-iGluSnFR.S72A fluorescence signal build-up (**Figure M4A**). Saturating signals may lead to a decrease of transients' amplitudes as the burst of stimulation progresses. To test SF-iGluSnFR.S72A saturation at 50Hz from single boutons, a unique trial of stimulation with 3 pulses at 50Hz followed by 25 pulses at 200Hz (500 ms later) was applied on PFs with either 2.5 mM or 4 mM extracellular $[Ca^{2+}]$ (**Figure M4B**). The burst at 200Hz was used to release a saturating quantity of glutamate from the bouton and determine the maximal $\Delta F/F_0$ ($\Delta F/F_0$ max, **Figure M4Bi**). The $[Ca^{2+}]$ had no effect on $\Delta F/F_0$ *max* (2.5mM: μ = 3.76 ± 0.83; 4mM: μ = 4.12 ± 1.05; **Figure MBii**). $\Delta F/F_0$ induced by triplet stimulation were divided by the corresponding $\Delta F/F_0$ *max* and fitted by a sigmoid curve. Normalized amplitudes A_1 to A_3 were in the linear phase of the sigmoid curve at both extracellular Ca^{2+} concentration. Transients above 80% of $\Delta F/F_0$ *max* are in the saturation phase (**Figure M4Bii**). Trial-averaged fluorescence traces acquired during electrical bursts at 50Hz where amplitudes were above the threshold were rejected. At 4 mM $[Ca^{2+}]$, all transients from A_4 in 50 Hz-stimulation trial-averaged traces were saturating and were neither used for clustering nor STP analyses.

V.6.4. Synaptic probability of success

The first two transients from each single trial of a bouton underwent 9-point smoothing using Savitski-Golay filter. Since single trials are highly noised, bootstrapping was used on transients to assess failure probability (**Figure M5**). A time window of 12 ms after the stimulation containing 6 points underwent 5000 cycles of bootstrap to extract a histogram of mean amplitudes distribution. Same method was used during baseline: at each of the 5000 cycles, 6 random points from a time window of 300 ms were averaged to extract a histogram.
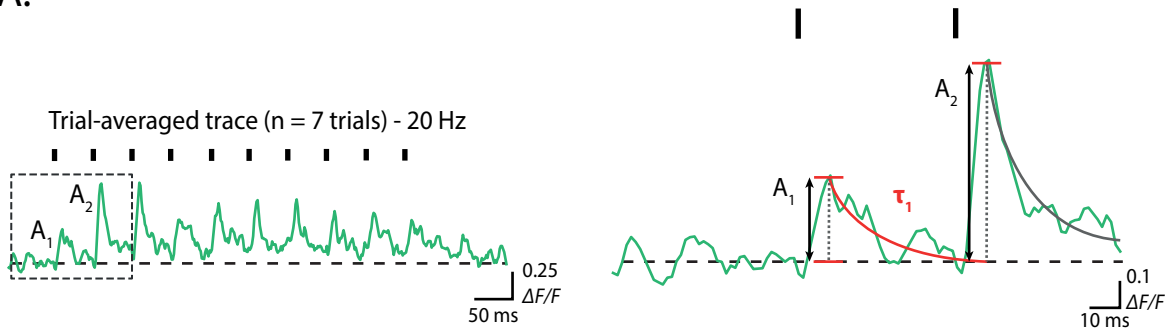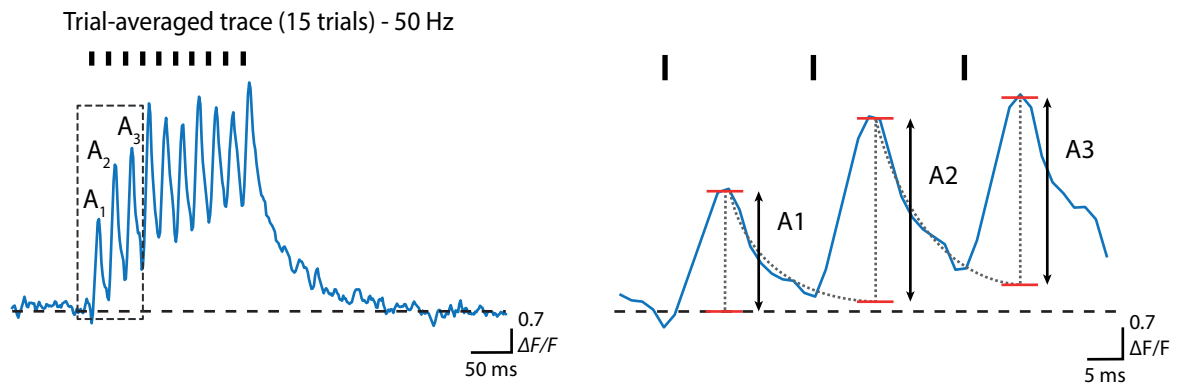
Figure M3 : Determination of amplitude and decay-time from trial-averaged fluorescence transients.

A) Trial-averaged fluorescence trace from a terminal evoked during 10 elctrical pulses of parallel fibres at 20 Hz. The amplitude of the first transient (A_1) is calculated from the baseline to the peak while amplitudes of the next transients (A_2 to A_{10}) are calculated from the extrapolation of the exponential fit (i.e. decay-time, τ_1) on the previous transient to the peak.
B) Same as A) for 10 pulses at 50 Hz.
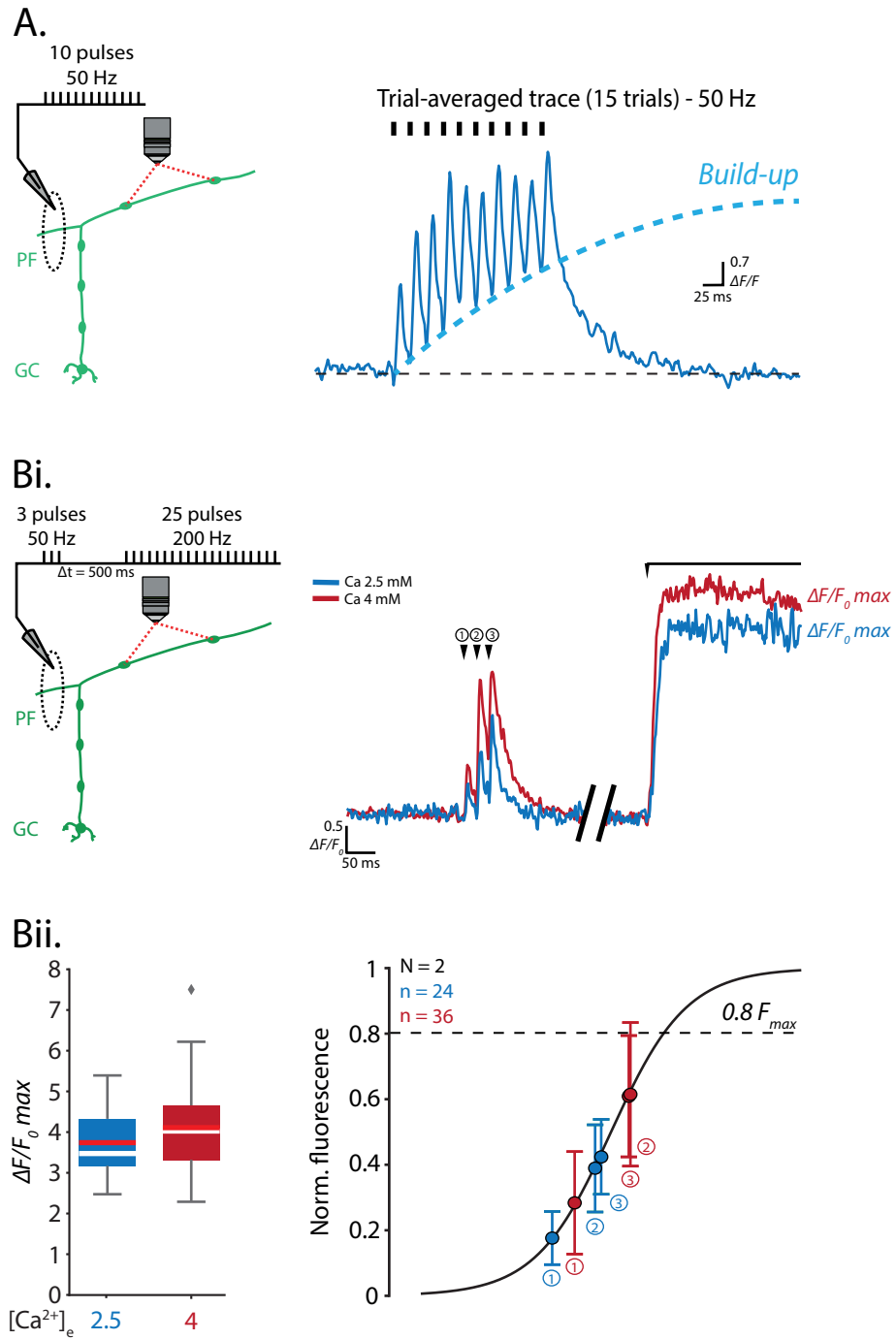
Figure M4 : Saturation of SF-iGluSnFR.S72A.

A) Trial-averaged fluorescence trace from a terminal evoked during 10 elctrical pulses of parallel fibres at 50 Hz. The build-up is represented by the blue dotted line.

Bi) Single fluorescence trials from single terminals evoked by electrical stimulations of parallel fibres with 3 pulses at 50 Hz and 25 pulses at 200 Hz, 500 ms later, under either 2.5 mM (blu) or 4 mM (red) extracellular Ca^{2+} concentration. Fluorescence transients are indicated on traces by numbers 1 to 3. Saturation is represented by the $\Delta F/F_0$ max (plateau) during stimulations at 200 Hz.

Bii) Threshold determination for staturation. $\Delta F/F_0$ max under both Ca^{2+} conditions (p = 1.0, two-sided Mann-Whitney U test with Bonferroni correction) are compared in the boxplot. Amplitudes of transients 1 to 3 are normalized by the corresponding $\Delta F/F_0$ max and reported on the sigmoid curve. Transients are saturating if their amplitudes are beyond the arbitrary threshold set at 0.8 $\Delta F/F_0$ max.

A z-score was used to compare both histograms: a transient was deemed a *success* if the z-score was greater than 3σ of the noise histogram. The percentage of failures of a bouton was determined and was used to calculate the synaptic probability of success $P_{success}$, which corresponds to the probability to release at least one vesicle:

$$P_{success} = 1 - (\frac{\%_{fail}}{100})$$

V.6.5. Number of released vesicles

The quantal release (i.e. the number of vesicles released in the synaptic cleft) was determined using the histogram of distribution of A_1 from trial-averaged traces without failures at 1.5 mM extracellular $[Ca^{2+}]$. To calculate quantal release at high $[Ca^{2+}]$ or with forskolin (50 µM, Sigma-Aldrich, Germany), amplitudes of transients were determined without failures and divided by the corresponding A_1 at 1.5 mM $[Ca^{2+}]$. The cumulative sum of quantal release was used to determine the number of vesicles released over the train of ten electrical pulses.

V.6.6. Assessment of the putative granule cell to Purkinje cell synapse

Vicinity between single boutons expressing SF-iGluSnFR.S72A and td-Tomato from PCs dendrites was assessed in L7-tdTomato mice. A z-stack at 0.38 Hz, 2 µs dwell time and 0.5 µm spacing between planes was performed after line-scan imaging. Z-stacks were analyzed using ImageJ/Fiji freeware. Both fluorescence signals were identified on X, Y and Z axes using the plugin Orthogonal View (***Figure M6***), then projected on the XZ or YZ axes similarly to microbeads. The very close vicinity or the overlap of both intensities was considered as a putative contact between the GC bouton and PC dendrite.

V.7. Patch-clamp recordings

PCs in vermal lobules III-VI were identified under infrared transmitted light through a XLUMPLFLN20XW objective (20x/1.0-NA, Olympus, Tokyo, Japan) and a CCD camera (Retiga, Qimaging, Canada) on the slicescope described in *section V.6.1*. Whole-cell patch-clamp recordings in voltage-clamp mode were obtained using a Multiclamp 700B (Molecular Devices, USA) and acquired with the freeware WinWCP 5.3.3 (John Dempster, University of Strathclyde, UK). Cells were held at a resting membrane potential of -60 mV not corrected for junction potential. Synaptic currents were low-pass filtered at 2.4 kHz and sampled at 10 kHz. Borosilicate thin wall capillaries (model G150T-4, Warner Instruments) were pulled using a
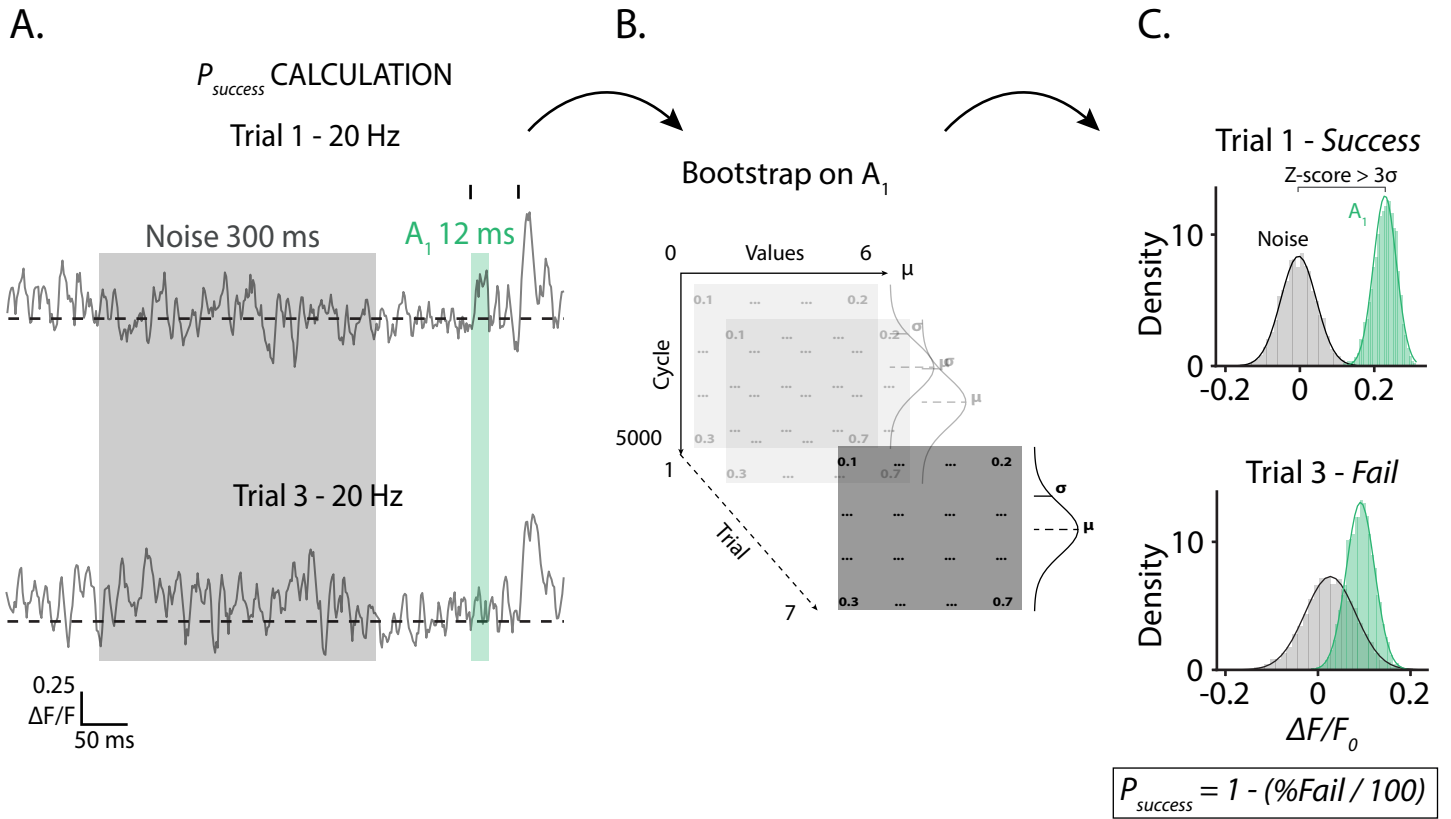
Figure M5 : Bootstrap algorithm for detection of glutamate release failures.

A) Baseline and first two transients of trial fluorescence traces from a single terminal during electrical stimulation of parallel fibres at 20 Hz. In both examples illustrated (trial 1 and 3), 6 values of the first transient (A_1) are extracted from a window of 12 ms around the peak. For noise, 6 random values are extracted from a 300 ms window in the baseline.

B) Bootstrap algorithm applied on the 6 points of A_1 from trials 1 and 3. The 6 values undewent 5000 bootstrap cycles to extract the distribution of $\Delta F/F_0$. For noise, 6 different random values were extracted at each cycle and averaged to determine the distribution histogram as for A_1.

C) Distribution histograms of $\Delta F/F_0$ for A_1 and noise from trials 1 and 3. Unlike trial 3, trial 1 shows significant A_1 amplitude (z-score > 3σ) compared to noise and is labeled as a success. The proportion of successes and failures is used to calculate $P_{success}$.
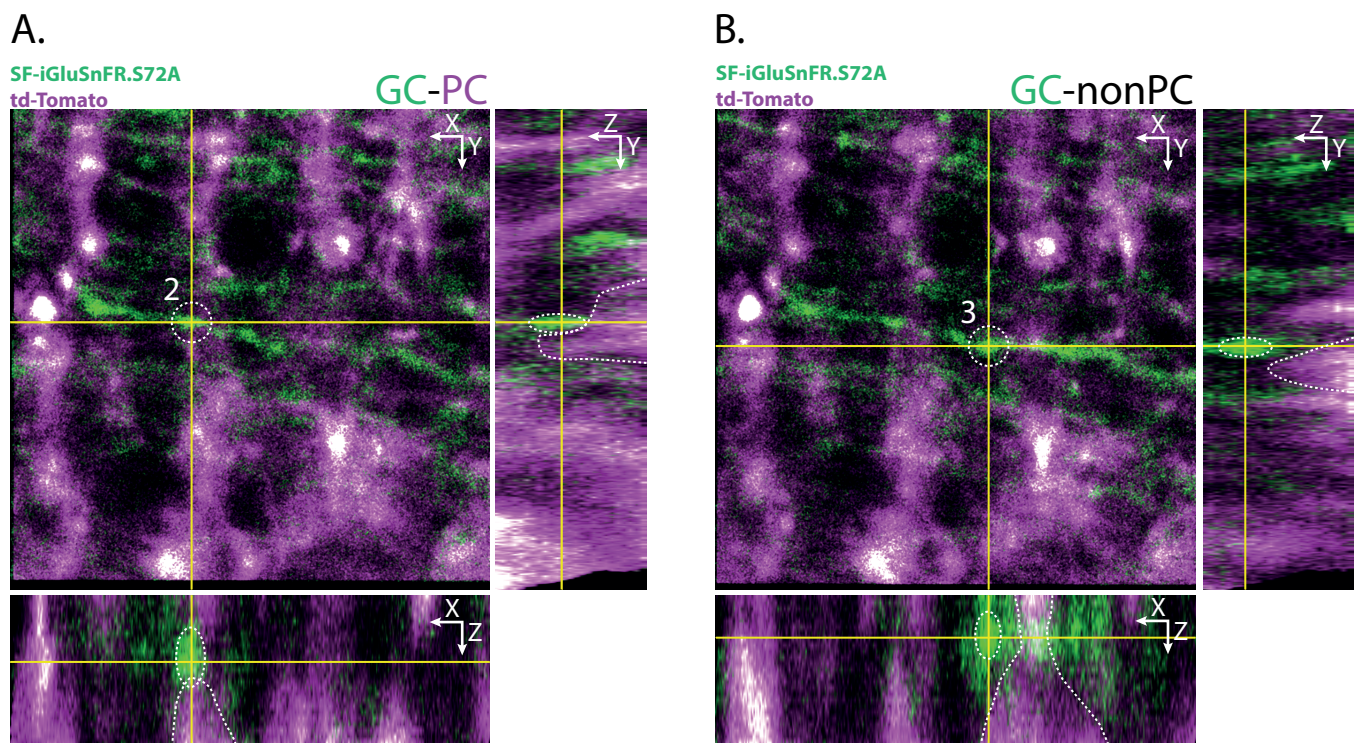
Figure M6 : Qualitative determination of putative granule cell to Purkinje cell synapses.

A) Orthogonal views of a terminal connected to a Purkinje cell from the z-stack. The terminal (green) and the Purkinje cell (magenta) are delimited by the white dashed lines.

B) Same as A) for a terminal not connected to a Purkinje cell.

gravitational puller (model PC12, Narishige, Japan) to reach 3-4 MΩ resistance. Series resistance was monitored and compensated (40% – 80%). The intra-cellular medium contained (in mM): $CsCH_3SO_3$ (140), NaCl (6), HEPES (10), Na_2GTP (0.4) and MgATP (4). The medium was supplemented with 50 μM Atto 594 (Sigma-Aldrich, Germany) to visualize the patched cell. Osmolarity was set at 300 mOsm and pH was adjusted to 7.3–7.4 with HCl or KOH. Electrical stimulations (3 pulses at 20Hz or 50Hz) were realized in the molecular layer as described in *section V.6*. Recordings where leak current exceeded 1 nA were discarded.

V.8. Immunohistochemistry

L7-tdTomato mice were deeply anesthetized by intraperitoneal injection of Zoletil (2 mg/kg) and xylazine (2 mg/kg) and perfused with PBS containing 4% paraformaldehyde. The cerebellum was gently extracted and kept in the same solution overnight. Horizontal and sagittal slices (80 μm thickness) were performed using a vibrating microtome (VT 1000S, Leica, Germany) and washed in PBS (3x10 min) at room temperature (22°C). Membranes were permeabilized with 0.1% Triton X100 and non-specific antigens were blocked with a mix of 1% Bovin Serum Albumin and 10% Normal Goat Serum overnight. PCs were stained using a solution containing 0.1% Normal Goat Serum and mouse anti-Calbindin D-28K monoclonal IgG1 (Sigma-Aldrich, Germany) diluted at 1/300 for 3 hours. To target primary antibodies, slices were washed and incubated with a solution containing goat-anti mouse polyclonal IgG coupled to Alexa Fluor 488 (Life Technologies, USA) and 0.1% of Normal Goat Serum for 3 hours. Slices were subjected to a final washing, mounted using an adapted medium (Dako, USA) and visualized by confocal microscopy (Leica SP5 II, Germany).

V.9. Data analyses

V.9.1. Analytical tools

Image analyses were performed on ImageJ/Fiji freeware. Other analyses were performed implementing custom-written scripts in Python (Spyder4.2.5, Anaconda 3 Navigator) available at:

https://github.com/TeamNeuralNetworks/Two-photon-imaging
https://github.com/TeamNeuralNetworks/PCA-and-Clustering

Various open-source packages were used:

- *Numpy*: data handling and bas vector functions.
- *Matplotlib* and *Seaborn*: plots generators.
- *Pandas*: dataframe structures and related operations.
- *Neo*: electrophysiological data handling.
- *Scipy*: statistical analyses.
- *Scikit-learn*: machine learning methods (dimensionality reduction, clustering, linear regression).
- *PySimpleGUI*: graphical user interface generator.

V.9.2. Principal Component Analysis and Hierarchical Clustering

Principal component analysis (PCA) is a linear transformation examining the main source of variance of a high dimensional dataset and projecting it to a lower dimensional Euclidean subspace. The algorithm creates a covariance matrix between k variables from the original dataset and transforms the data into vectors called *eigenvalues* embedded in the subspace. The orthogonal axes of this new subspace are the *Principal Components* where the first two explain the highest variance of the original dataset. PCA was computed using the Python-based *Scikit-learn* package using 13 variables from profiles recorded at 2.5 mM extracellular [Ca^{2+}]: amplitudes of the first two transients and related $P_{success}$, and amplitudes 2–10 normalized by the first one (i.e. the STP profile). These variables were centered and normalized. Observations at 1.5/4mM [Ca^{2+}] as well as after forskolin did not take part to eigenvalues calculation but were transformed as additional values and overlaid to the subspace of 2.5 mM [Ca^{2+}] data.

To highlight clusters of boutons sharing common features, PCA was computed as a preprocessing step for Hierachical Clustering of Principal Components (HCPC). HCPC calculates a linkage matrix between each individual in the subspace using the Ward's method (F. Husson et al., 2010):

$$\sum_{k=1}^{K}\sum_{q=1}^{Q}\sum_{i=1}^{I_q}(x_{iqk} - \bar{x}_k)^2 = \sum_{k=1}^{K}\sum_{q=1}^{Q}I_q(\bar{x}_{qk} - \bar{x}_k)^2 + \sum_{k=1}^{K}\sum_{q=1}^{Q}\sum_{i=1}^{I_q}(x_{iqk} - \bar{x}_{qk})^2$$

$$\qquad Total\ variance \qquad\qquad Between\ variance \qquad\qquad Within\ variance$$

where x_{iqk} is the value of the variable k for the individual i belonging to the cluster q, $\bar{x}_{qk}$ is the mean of the variable k for cluster q, $\bar{x}_k$ is the overall mean of the variable k and I_q is the number of individuals in the cluster q. At each step of the algorithm, the Ward's method aims to aggregate clusters by maximizing the homogeneity inside each cluster (i.e. minimizing the within variance) and the variance between clusters. The growing aggregation unveil a hierarchy represented by a dendrogram where the height of each node reflects the gain of within variance.

The number of clusters is chosen based on the nodes variance in the dendrogam and whether the clusters make sense in the dataset (i.e. if at least two clusters are significantly different for at least one measure).

V.9.3.Statistics

Data are presented as mean +/- SD or SEM and N (number of mice) and n (number of boutons) are provided in the figure. Normality and homogeneity were assessed using Shapiro-Wilk test and Levene test, respectively. For comparisons between two independent datasets, either two-sided Student t-test (parametric) or Mann-Whitney U-test (non-parametric) was used. For comparisons between two paired datasets, non-parametric Wilcoxon signed-rank test was used. For comparisons of three or more datasets, non-parametric Kruskal-Wallis and post hoc Dunn's multiple-comparisons tests were used. For linear regression, Pearson correlation coefficient r and p-value were used. For comparisons of proportions, one-way Chi^2 test was used.

VI. Results

The second part of my PhD project aims to monitor the diversity of short-term plasticity at single GCs boutons using the method developed in the first part (*see details in section V.6*). The first section briefly explores a parallel axis related to silent synapses in the cerebellar cortex. The second section focuses on the diversity of fast glutamate release properties across all boutons of PFs and between boutons belonging to the same PF. The third section investigates the relationship between the STP and the identity of the postsynaptic target between GC-PC and GC-nonPC synapses. The fourth section looks at the contribution of presynaptic calcium dynamics on multivesicular release and STP diversity. Finally, the fifth section demonstrates the heterogeneous involvement of the presynaptic adenylyl cyclase pathway on glutamate release between boutons.

The majority of results raises from analyses computed on data acquired during PF electrical stimulations at 20 Hz (i.e. the biggest dataset). Multiple antagonists were used to avoid modulation of glutamate release and long-term plasticity (*see section V.2.4.3*).

VI.1. Glutamate is released from all granule cell boutons

Electrophysiological experiments reported that ~85% of GC-PC synapses do not evoke postsynaptic currents during GC electrical stimulations (Isope & Barbour, 2002). This observation raised a substantial question: is the presynaptic bouton unable to release glutamate or is the postsynaptic density deprived of AMPA receptors or both?

Two-photon imaging of SF-iGluSnFR.S72A turns useful to resolve part of this question through direct measurement of glutamate released by the presynaptic bouton (*see section V.6*). Fluorescence signals evoked by glutamate release from single GC boutons in vermal lobules III–VI were collected during evoked electrical bursts of PFs at high-frequency (20Hz or 50Hz; **Figure R1A**). Distances between consecutive boutons were variable with an average of 7 ± 3.9 µm ($n = 230$, $n_{PF} = 52$, $N = 22$; **Figure R1B**) which is consistent with previous findings. Boutons were considered *active* if at least one fluorescent peak was evoked (3σ above noise level, *see section V.6.2*) during the train of stimulations. Strikingly, all boutons were *active* on 79.5% of PFs while at least 1 bouton was *inactive* on 20.5% of PFs (1 inactive: 15.4%, 3 inactive: 2.6%, 6 inactive: 2.6%, $n = 197$, $n_{PF} = 38$, $N = 20$; **Figure R1C**). *Inactive* boutons may correspond to silent release sites or to photodamage of the PF or misidentification of a synaptic bouton (e.g. mitochondria inside the PF). These results indicate that all GC boutons release glutamate thereby suggesting that silent synapses observed by Isope & Barbour (2002) may be related to a lack of postsynaptic AMPA receptors.
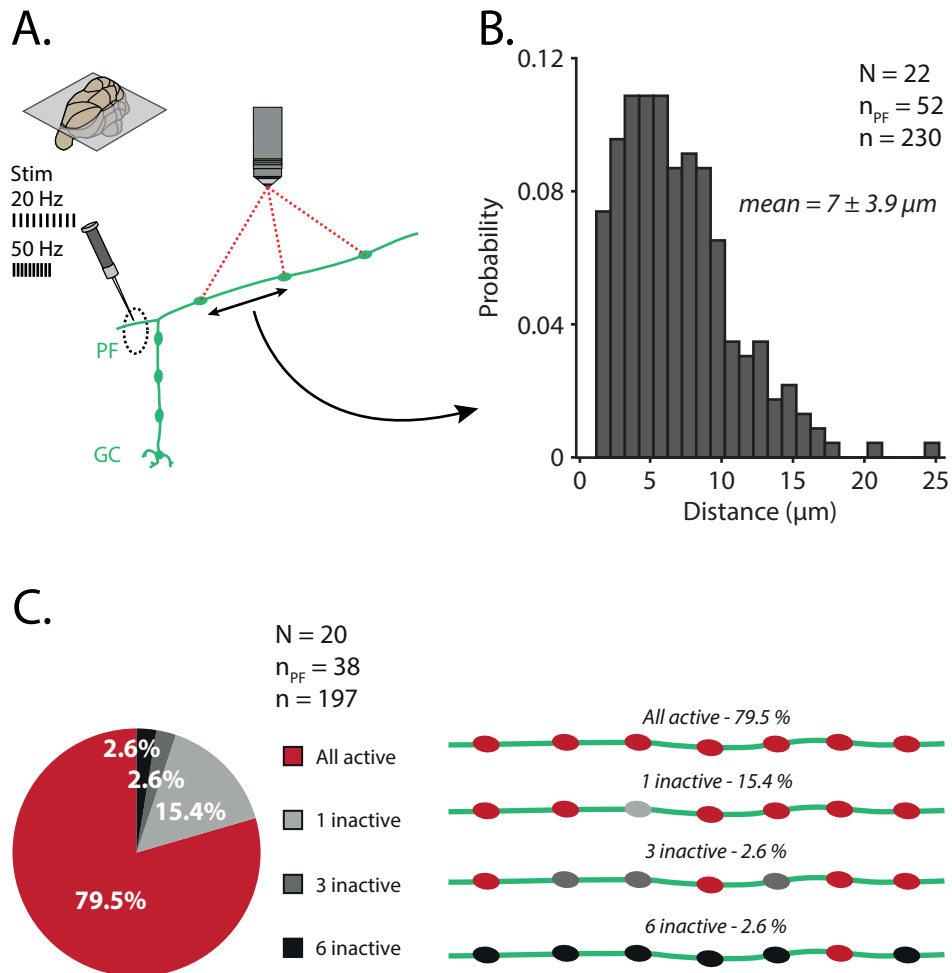
Figure R1 : Functional state of single granule cell terminals.

A) Two-photon imaging of single terminals during electrical pulses at 20 Hz or 50 Hz applied on parallel fibres. *GC, granule cell; PF, parallel fibre.*

B) Distribution histogram of the distance between consecutive terminals.

C) Proportion of parallel fibres whose terminals release glutamate (active state) and parallel fibres where no fluorescence transients are detected (inactive state) during evoked electrical. At least 4 terminals on the same parallel fibre were required.

VI.2. Dynamics of glutamate release are highly heterogeneous between granule cells boutons

Previous works from the team reported heterogeneous STP dynamics at GC-MLIs or GC-MLI-PC synapses (Dorgans et al., 2019; Grangeray-Vilmint et al., 2018) using postsynaptic current recordings. These findings raised a fundamental question: are glutamate release properties heterogeneous between single GC boutons and do they differ along the PF?

VI.2.1. Properties of glutamate release are widely heterogeneous during high-frequency bursts

Glutamate release properties were determined based on measurements from fluorescence traces recorded during repeated PF train stimulation at 20Hz (n = 145, N = 18) or 50Hz (n = 45, N = 8; **Figure R2A**). The first peak (A_1) showed rapid kinetics with an average decay-time constant of 6.7 ± 5.8 ms (n = 176; **Figure R2B**). At both frequencies, amplitudes of the second peak (A_2) were significantly higher than A_1 but did not differ each other (A_1: 0.41 $\pm$ 0.23, n = 190; A_2-20Hz: 0.74 $\pm$ 0.37, n = 145; A_2-50Hz: 0.68 $\pm$ 0.31, n = 45; **Figure R2C**). The wide variability of amplitudes was related to the high diversity of the probability of success ($P_{success}$; **Figure R2C**). $P_{success}$ increased significantly from A_1 to A_2 for both stimulation frequencies (A_1: 0.61 $\pm$ 0.23, A_2-20Hz: 0.84 $\pm$ 0.18, A_2-50Hz: 0.87 $\pm$ 0.14). Surprisingly, paired-pulse ratio (PPR) values did not differ between 20Hz and 50Hz (PPR-20Hz: 1.84 $\pm$ 0.54, PPR-50Hz: 2.08 $\pm$ 0.74) and were highly variable. As expected, PPR was anti-correlated to A_1 for both frequencies (**Figure R2D**). To assess the variability of STP profiles, averaged fluorescence traces were normalized by the amplitude of the peak elicited by the first stimulation. At both 20Hz and 50Hz, STP profiles varied a lot, from slightly depressing to strongly facilitating profiles (**Figure R2E**). As expected, averaging all profiles showed similar facilitation than previous electrophysiological measurements (Dorgans et al., 2019; Doussau et al., 2017). These results demonstrate that glutamate release is heterogeneous between GC boutons during high-frequency stimulations.
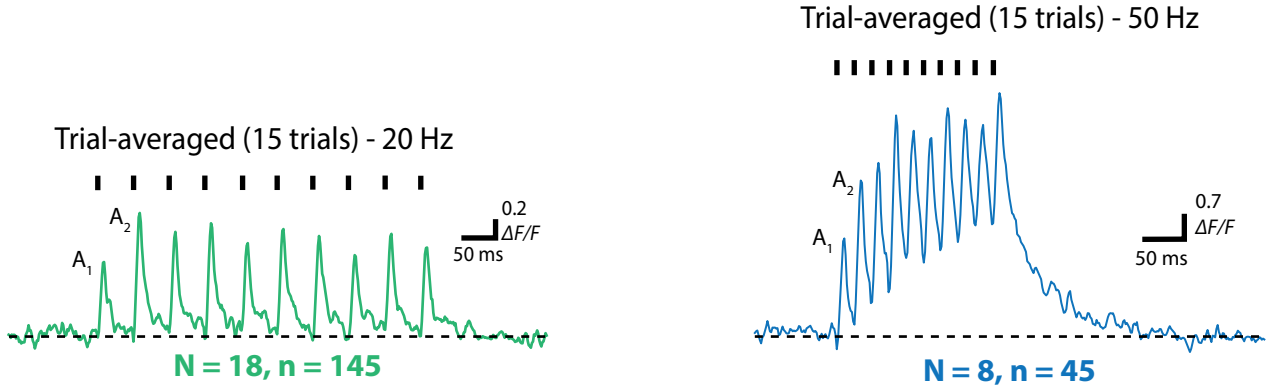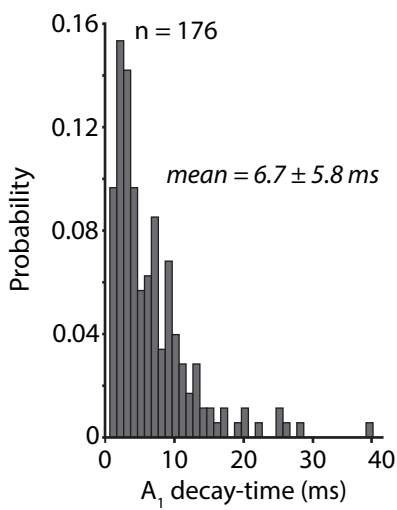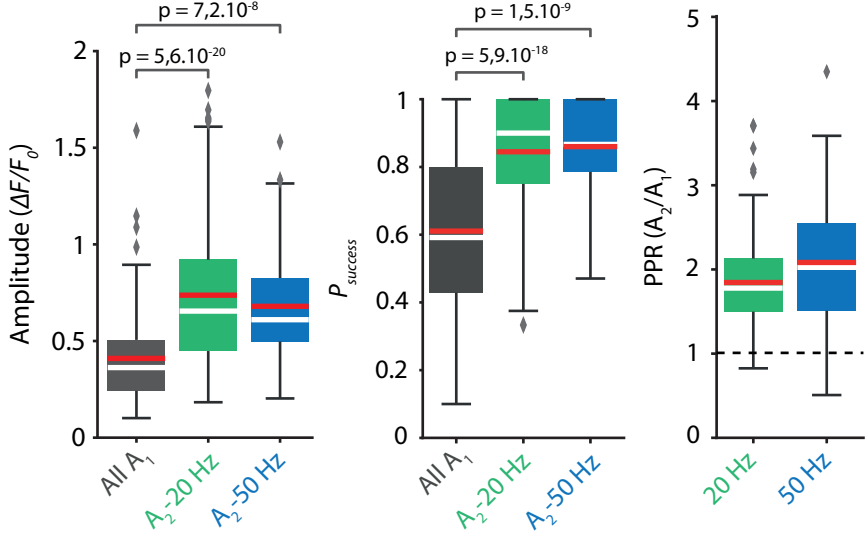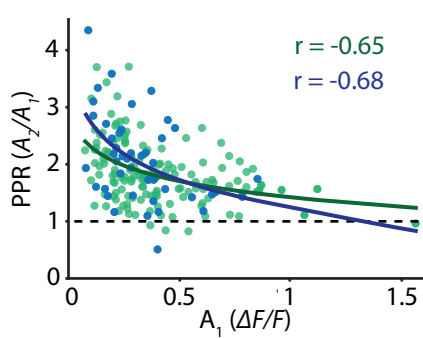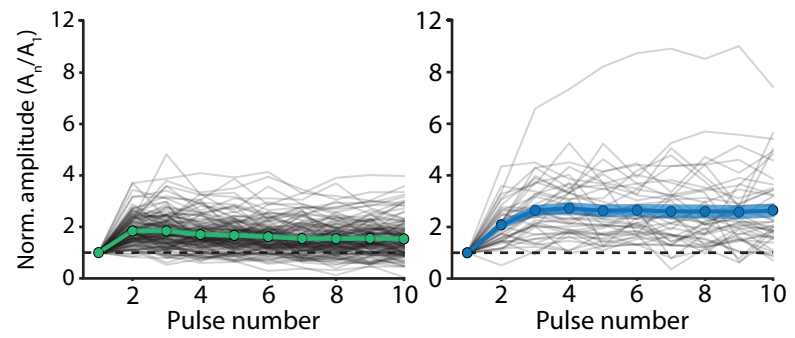
Figure R2 : Diversity of glutamate release from granule cell terminals.

A) Trial-averaged fluorescence traces during evoked electrical bursts at 20Hz and 50Hz. Transients 1 and 2 are referred to as A_1 and A_2, respectively.

B) Distribution of the decay-time constant of A_1 from all trial-averaged traces. Mean ± SD.

C) Amplitudes and $P_{success}$ of A_1 and A_2 (p = $1,3.10^{-20}$, Kruskal-Wallis test with posthoc Dunn's multiple comparison) and PPR at 20Hz and 50Hz (p = $6,4.10^{-2}$, two-sided Mann Whitney U test with Bonferroni correction). Means and medians are in red and white, respectively.

D) Variation of PPR against A_1 (*r* : Pearson correlation coefficient).

E) Normalized amplitudes (A_n/A_1) of all trial-averaged traces (grey lines) at 20Hz and 50Hz. Note the high variability of profiles (i.e. short-term plasticity). Means (colored circles) ± SD (shaded area).

VI.2.2. The diversity of glutamate release does not depend on the quantity of SF-iGluSnFR.S72A expressed at single boutons

Previous computational investigations reported that iGluSnFR may act as a buffer of glutamate and produce signals whose amplitude and decay are related to its concentration (Armbruster et al., 2020). Experimentally, the concentration of SF-iGluSnFR.S72A at single GC boutons is related to the basal fluorescence F_0, widely distributed over the dataset (**Figure R3A**). To assess whether the diversity of glutamate release was related to the quantity of sensor at single boutons, parameters measured from trial-averaged traces at 20 Hz were plotted against F_0. No correlation was found between F_0 and A_1, A_2, $A_2 P_{success}$ and PPR (**Figure R3A-D**). These results indicate that, in these experiments, the quantity of SF-iGluSnFR.S72A expressed at single GC boutons or the quality of the recordings do not account for the variability of glutamate release.

VI.2.3. Four classes of granule cell boutons based on their glutamate release properties

The diversity of glutamate release raised the hypothesis that GC boutons may be classified on the basis of their release properties and STP profile. This required first to determine which parameters drove most the diversity of glutamate release at GC boutons. PCA was performed on amplitudes and $P_{success}$ of the first two peaks and normalized amplitudes (A_2/A_1 to A_{10}/A_1, i.e. STP profile) from trial-averaged traces collected during electrical bursts at 20Hz. The first two principal components captured most of the variance contained in the dataset (PC1: 58.3%, PC2: 20.2%) suggesting that the dataset can be reduced to reduce to the first two dimensions (**Figure R4A**). Respective contribution of each of the thirteen variables to the variance of PC1 and PC2 are represented in the correlation circle (**Figure R4B**). The STP profile as well as the amplitude and $P_{success}$ of the second peak appeared to contribute the most to the variability of glutamate release. Amplitude and $P_{success}$ of the first peak equally contributes to variability on both components hence participating to the variability of glutamate release.
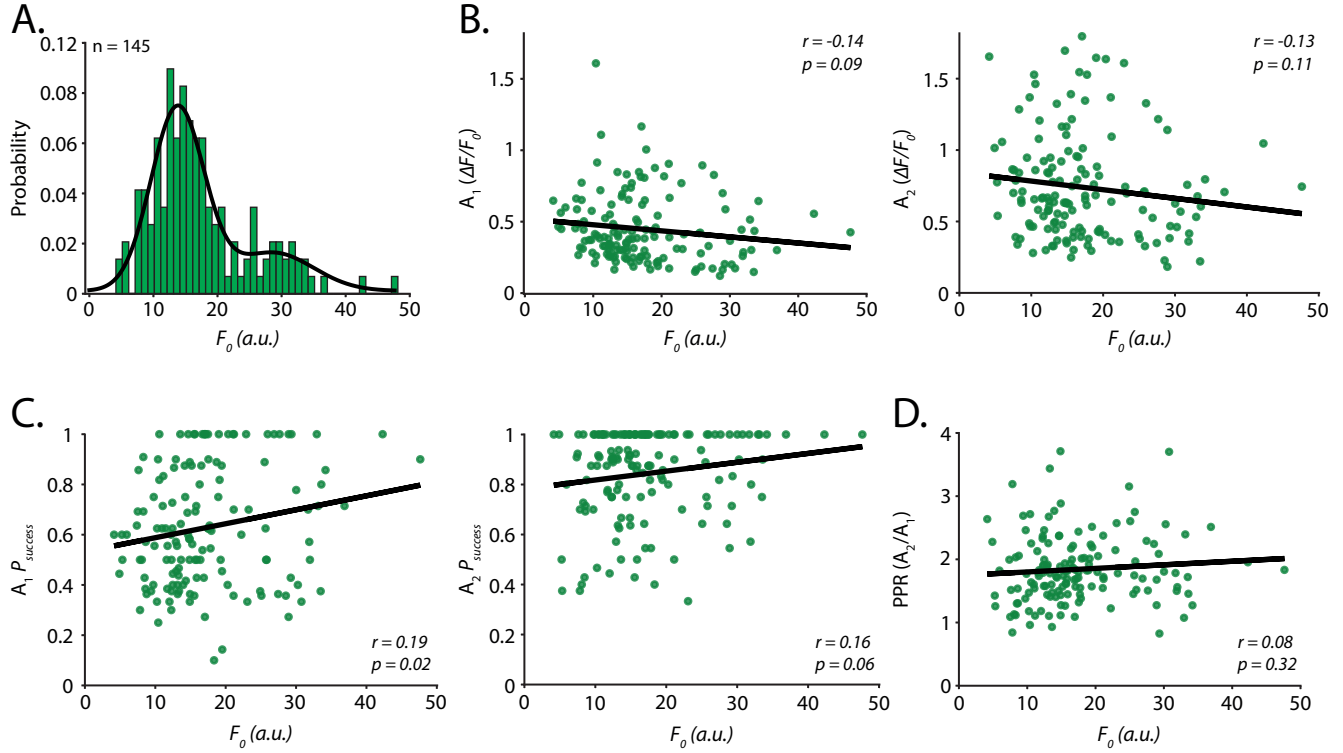
Figure R3 : Uncorrelation between the diversity of glutamate release and the amount of SF-iGluSnFR.S72A.

A) Distribution of F_0 from trial-averaged traces. *A.u., arbitrary unit.*

B) Amplitude of the first two transients (A_1 and A_2) against F_0. Both A_1 and A_2 are uncorrelated to F_0 (A_1: r=-0.14, p=0.09; A_2: r=-0.13, p=0.11).

C) Probability of success ($P_{success}$) of the first two transients against F_0. $A_1 P_{success}$ is slightly correlated to F_0 while $A_2 P_{success}$ is uncorrelated to F_0 ($A_1 P_{success}$: r=-0.19, p=0.02; $A_2 P_{success}$: r=-0.16, p=0.06).

D) PPR against F_0. No correlation to F_0 is observed (PPR: r=-0.08, p=0.32; $A_2 P_{success}$: r=-0.16, p=0.06).

B-D) Statistical test: Pearson correlation coefficient and p-value.
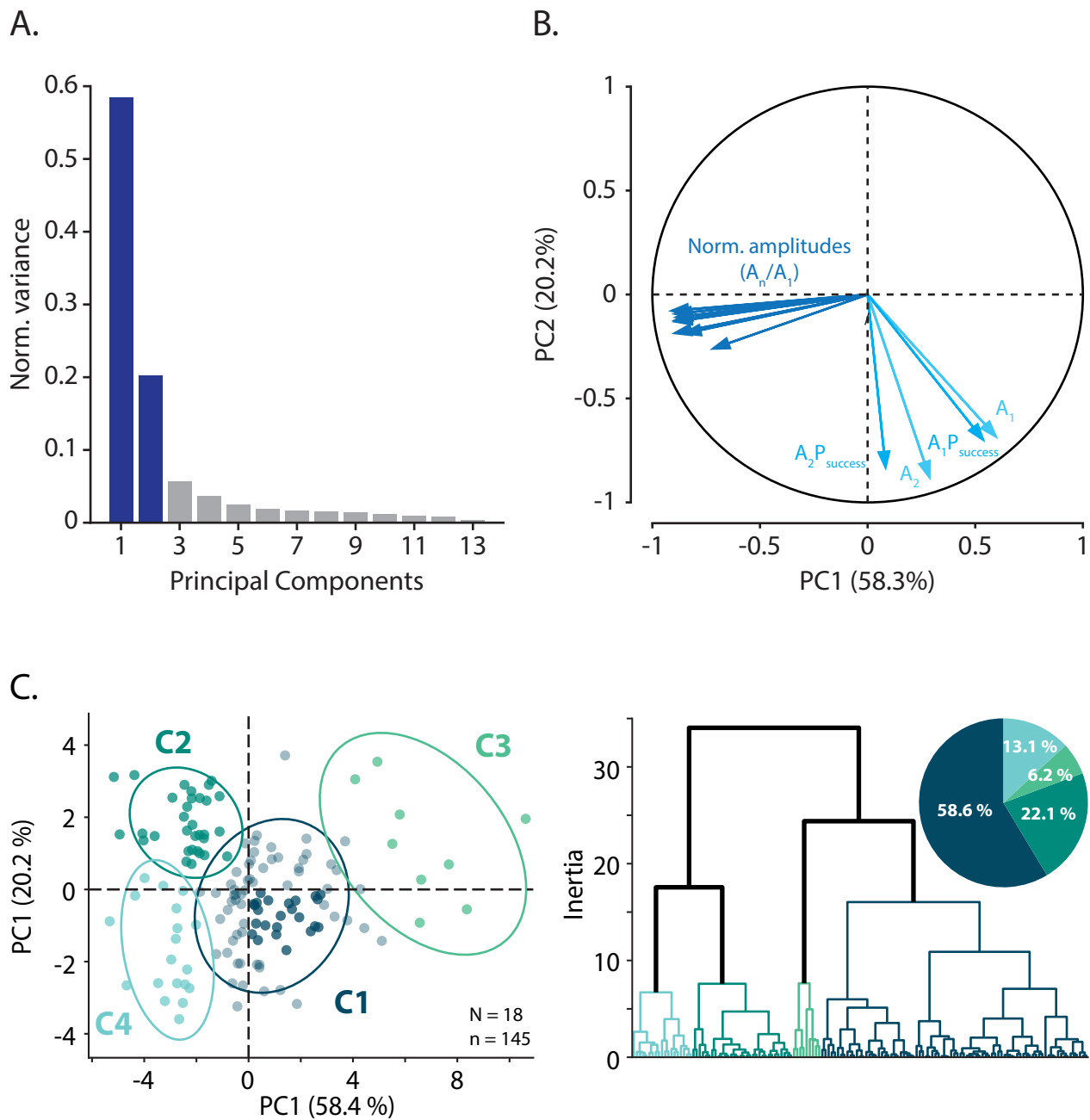
Figure R4 : Identification of four classes of granule cell terminals by Principal Component Analysis and Hierarchical Clustering.

A) Explained variance for each principal component generated from trial-averaged traces during 10 pulses at 20 Hz. The highest variance of the dataset is explained by the first two principal components (78.5%, PC1 and PC2, blue bars).

B) Correlation circle of the respective contribution of the 13 parameters on PC1 and PC2. Parameters are : amplitudes of the first two transients (A_1 and A_2), probability to release at least 1 vesicle for A_1 and A_2 ($A_1P_{success}$ and $A_2P_{success}$) and amplitudes from transient 2 to transient 10 normalized by A_1 (A_2/A_1 to A_{10}/A_1, i.e. short-term plasticity profile). The radius of the circle represents the correlation coefficient between th parameter and the principal component. Normalized amplitudes are highly and poorly correlated to negative values of PC1 and PC2, respectively. A_1 and $A_1P_{success}$ are modestly and highly correlated to positive values of PC1 and negative values of PC2, respectively. A_2 and $A_2P_{success}$ are poorly and highly correlated to positive values of PC1 and negative values of PC2, respectively. Positive PC1 values indicate terminals with high normalized amplitudes. Positive PC2 values indicate terminals with high amplitudes and $P_{success}$ on A_1 and A_2.

C) Bidimentional euclidean subspace containing all terminals imaged and classes revealed by Hierarchical Clustering. Fours classes of terminals (C1-C4) are unveiled. Proprotions of terminals in each class are represented on the dendrogram and the pie plot. C1 gathers the majority of terminals.

Four classes of GC boutons (C1 to C4) were objectively extracted by computing Hierarchical Clustering on PC1 and PC2 so that the inter-class variance was maximized (N = 18, n = 145; **Figure R4C**). The limited overlap between confidence ellipses indicates that classes of boutons are well discriminated by the algorithm. Classes display variable proportions of boutons whose majority belongs to C1 (C1: 58.6%, C2: 22.1%, C3: 6.2%, C4: 13.1%). An averaged profile trace was extracted from each class to determine the representative STP profile (**Figure R5A**). C1 and C2 were facilitating at the second pulse and showed respectively stability and decrease of glutamate release during the burst. C3 was strongly facilitating until the third pulse prior to stabilization. C4 displayed a steady-state profile characterized by poor variation of peaks amplitudes during the burst. The heterogeneity of STP profiles was confirmed by significantly different PPR between all classes (C1: 1.98 ± 0.49, C2: 1.63 ± 0.27, C3: 2.65 ± 0.47, C4: 1.21 ± 0.22; **Figure R5B**).

The classical view of PPR claims that this parameter is inversely proportional to the amplitude of the first peak as well as the corresponding $P_{success}$. Heterogeneous amplitudes and $P_{success}$ from the first two peaks were compared between classes (**Figure R5Ci and Cii**). Values are summarized in the table of **Figure R5D**. For all parameters, C1 was significantly smaller than C2 confirming differences in PPR values. Only the amplitude of the first peak was significantly smaller in C1 than C4. C2 stood out from all classes through significantly higher amplitudes related to higher $P_{success}$. Strikingly, no significant differences were found neither in amplitudes nor in $P_{success}$ between C1 and C3 and between C3 and C4 despite different PPR. This observation is in apparent contradiction with the classical view of PPR, suggesting that other parameters such as the number of release sites (*N*) may influence the diversity of STP profiles between these classes (*see section VI.4*).

VI.2.4. Short-term plasticity is heterogeneous along the same parallel fibre

Previous findings suggested either heterogeneous populations of GCs expressing a given STP profile or a diversity of STP profiles along the same PF (Dorgans et al., 2019). To assess the organization of the diversity presented in *section VI.2.3*, STP profiles were measured from boutons belonging to the same PF during bursts of electrical pulses at 20 Hz. On the example illustrated in **Figure R6A**, boutons 1 and 4 display large peaks amplitudes typical of class C2 which facilitate at the second pulse and then tend to depress (**Figure R6B**). Although peak amplitudes from the bouton 2 are small, normalized amplitudes unveiled a sustained facilitation typical of class C1. Finally, bouton 3 shows stable peak amplitudes typical of class C4 with a slight depression from the third peak. Therefore, boutons from a single GC can express different STP profiles.
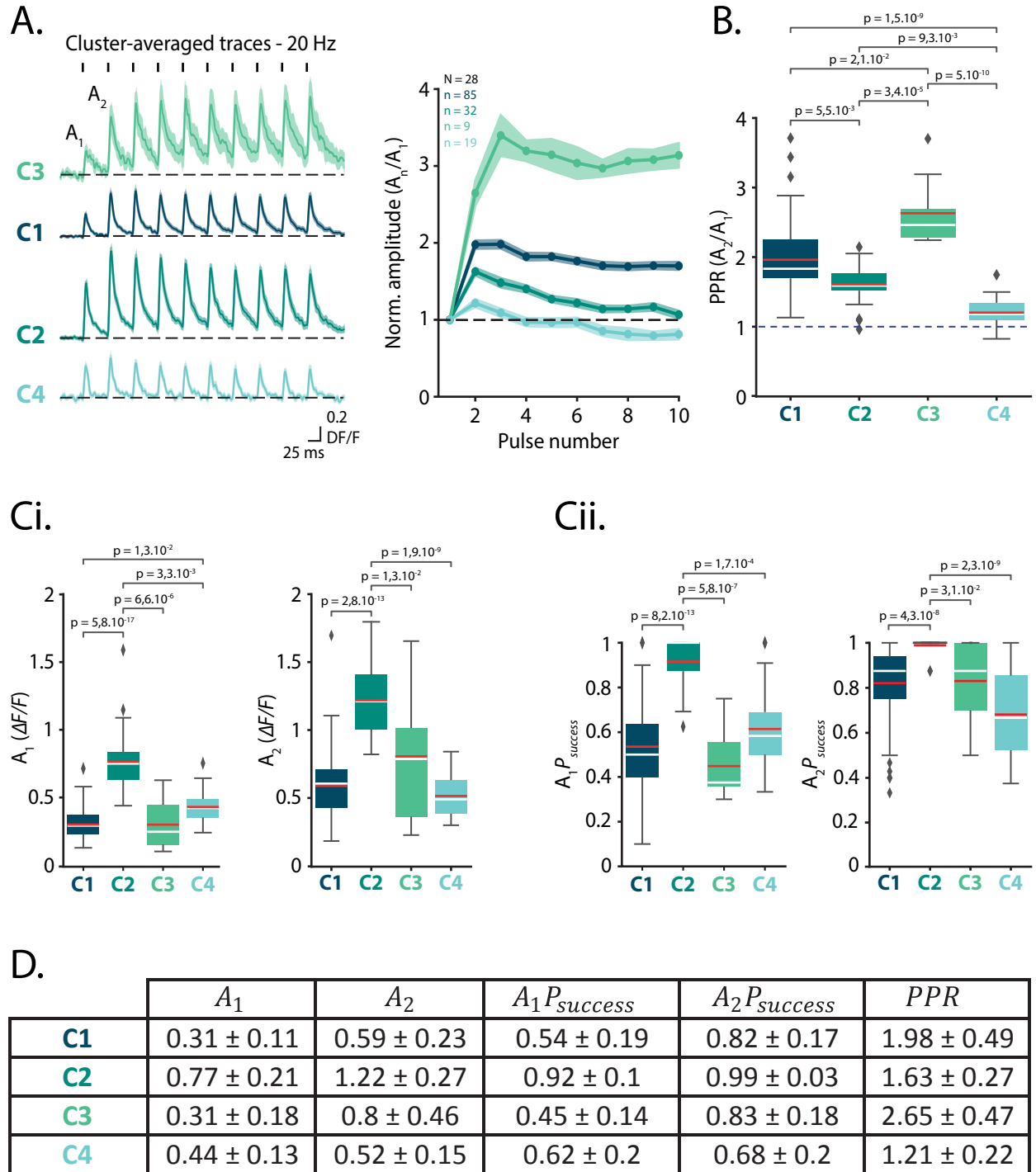
Figure R5 : Functional properties of the four classes of granule cell terminals.

A) Class-averaged traces for classes C1-C4 and corresponding normalized amplitudes evoked by 10 pulses at 20Hz. Means (colored line) ± SEM (shaded area).

B) PPR comparison between classes. $p = 4.5 \cdot 10^{-13}$, Kruskal-Wallis test with posthoc Dunn's multiple comparisons.

Ci) A_1 and $A_1 P_{success}$ measures for each class of terminals (A_1: $p = 8.8 \cdot 10^{-17}$, $A_1 P_{success}$: $p = 2.8 \cdot 10^{-13}$, Kruskal-Wallis test with posthoc Dunn's multiple comparisons).

Cii) Same as Ci) for the second transient (A_2: $p = 6.1 \cdot 10^{-14}$, $A_1 P_{success}$: $p = 2.2 \cdot 10^{-10}$, Kruskal-Wallis test with posthoc Dunn's multiple comparisons).

D) Mean ± SD values for all parameters measured in classes of boutons.

B-C) Red bars refer to means and white bars to medians.
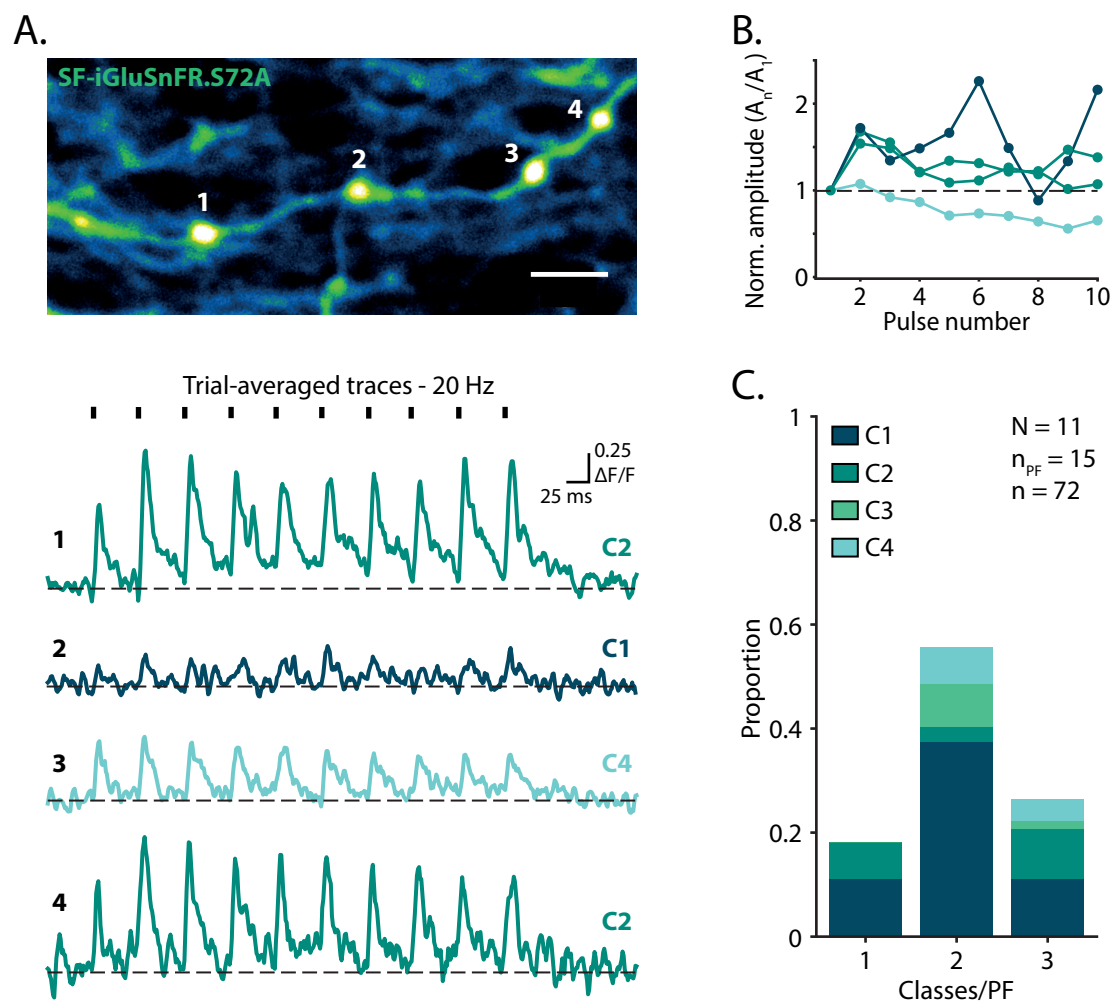
Figure R6 : Diversity of short-term plasticity along a single parallel fibre.

A) Parallel fibre with 4 terminals and corresponding trial-averaged fluorescence traces during ten evoked electrical pulses at 20Hz. Scale bar: 5 μm. Terminals 1 and 4 belong to class C2 while terminals 2 and 3 belong to classes C1 and C4, respectively.

B) Normalized amplitudes for terminals shown in A.

C) Proportion of parallel fibres displaying either 1 class of terminals or a combination of 2 or 3 classes of terminals. No parallel fibres have a combination of 4 classes of terminals. Only parallel fibres with at least 4 terminals are represented in this barplot.

The diversity of STP profiles in individual PF was observed in 15 PFs and 72 boutons. Although the proportion of PFs expressing 1, 2 or 3 different STP profiles was largely variable, the majority of PFs display a combination of 2 STP profiles while no PFs showed a combination of 4 profiles (1 profile: 18.1%, 2 profiles: 55.6%, 3 profiles: 26.4%, 4 profiles: 0%; *Figure R6C*). The class C1 was predominantly found on all PFs (1 profile: 11.1%, 2 profiles: 37.5%, 3 profiles: 11.1%) as demonstrated earlier (*Figure R5Ci and Cii*).

Taken together, these results demonstrate that GC boutons express heterogeneous STP profiles ranging from stead-state to multiple facilitations of glutamate release. An appealing hypothesis would be that such a diversity along PFs correspond to the identity of the postsynaptic cell.

VI.3. Target-independent short-term plasticity at granule cell to Purkinje cell and granule cell to non-Purkinje cell synapses on the same parallel fibre

Target-dependent STP profiles have been described at GC-BC and GC-SC synapses (Bao et al., 2010). These results were contradicted by Dorgans *et al* (2019) emphasizing that both BCs and SCs receive heterogeneous GC inputs. Moreover, investigations from Grangeray-Vilmint *et al* (2018) reported a diversity of STP between excitatory and inhibitory synapses on PCs. In this section, the question is raised as follow: is STP at GC boutons along the PF target-dependent between PCs and the other cell types?

To address this question, STP was measured at single GC boutons using two-photon imaging of SF-iGluSnFR.S72A in L7-tdTomato mice. This mouse line allowed to discriminate PCs from the other cell types.

The reliability of tdTomato expression in PCs was assessed using an immunohistochemistry anti-calbindin. PCs from thin cerebellar slices (80 μm) made from L7-tdTomato mice were stained with an anti-calbindin antibody. 100% of PCs expressed both tdTomato and calbindin on sagittal slices (n = 112, N = 1; *Figure R7A*) and on horizontal slices (n = 92, N=1; *Figure R7B*).

To assess the relation between STP at single boutons along the PF and the identity of the postsynaptic target, viral injection of AAVDJ.SF-iGluSnFR.S72A were performed in L7-tdTomato mice (*Figure R8A*). Glutamate release from PF boutons was evoked by electrical stimulations of PFs at 20 Hz and the vicinity between the bouton and the PC was determined
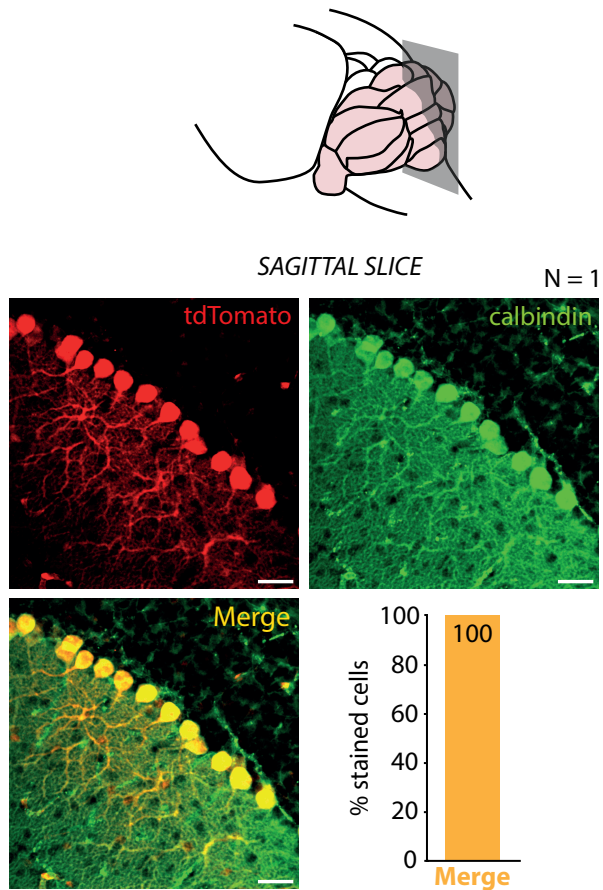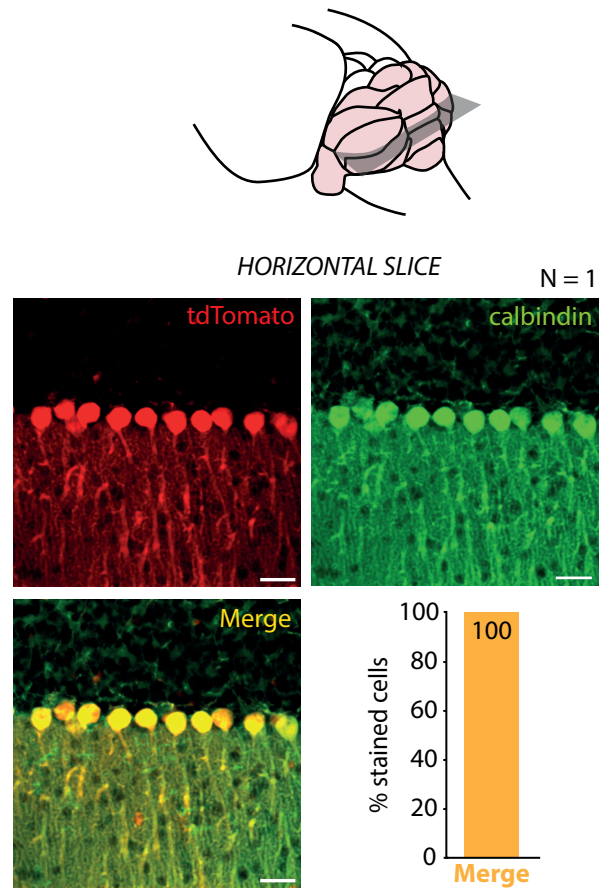
Figure R7 : Calbindin immunostaining of Purkinje cell in L7-tdTomato mice.

A) PCs-calbindin immunostaining on a cerebellar sagittal slice of L7-tdTomato mice. Percentage of stained PCs are indicated in the bar plot (p = 0.74, one-way Chi^2 test).

B) PCs-calbindin immunostaining on a cerebellar horizontal slice. Percentage of stained PCs are indicated in the bar plot (p = 0.91, one-way Chi^2 test).

Scale bars: 30 μm

by a z-stack. On the example illustrated in ***Figure R8B***, bouton 2 was extremely close to the PC dendrite and was classified as a putative GC-PC synapse. Boutons 4 and 5 have similar arrangements (not shown). Conversely, bouton 3 does not overlapped with PC dendrite and was classified as a GC-nonPC synapse (similar result for bouton 1). Interestingly, boutons 1, 3 and 4 display similar facilitation of glutamate release over the burst of stimulations and belong to class C1 despite different postsynaptic targets (***Figure R8C-D***). Similarly, boutons 2 and 4 display limited variation of glutamate release typical of the class C4. Hence, on this PF, C1 was present at both GC-PC and GC-nonPC synapses while C4 was found only at GC-PC synapses.

To identify the distribution of STP over all boutons and classes, parameters of STP profiles were highlighted in the subspace of the PCA based on the type of postsynaptic target (*see section VI.2.3*). Although C3 is barely represented, GC-PC synapses were found in all classes but C3 (***Figure R8E***) with variable proportions (GC-PC/ C1: 59.5%, C2: 17%, C3: 0%, C4: 23.4%, n = 47; GC-nonPC/ C1: 70%, C2: 10%, C3: 5%, C4: 15%, n = 20; N = 9; ***Figure R8F***). Overall, STP profiles from GC-PC and GC-nonPC synapses are similarly distributed between classes (***Figure R8G***) and the compound STP profile recapitulates electrophysiological measurements (Doussau et al., 2017).

Taken together, these results indicate that the organization of STP diversity along the PF is not based on the identity of the postsynaptic cell between GC-PC and GC-nonPC synapses. This suggests that STP diversity is driven essentially by presynaptic mechanisms.

VI.4. High dynamic range of glutamate release at granule cell boutons

The capacity of GCs to reliably transfer sensorimotor information over high-frequency bursts of activity requires fast mobilization and turnover of synaptic vesicles. Previous works from Valera *et al* (2012) and Doussau *et al* (2017) reported that GC boutons can recruit specific pools of vesicles during high-frequency transmission. The topography of synaptic vesicles associated to Ca^{2+} nanodomains (Rebola et al., 2019) and the presynaptic dynamics of Ca^{2+} entry during high-frequency activity could engage mobilization of such specific pools, thereby influencing glutamate release and STP.

One hypothesis raised here is that STP diversity is related to the regulation of Ca^{2+} and Ca^{2+}-dependent dynamics in GCs boutons. Glutamate release from single boutons expressing SF-iGluSnFR.S72A was assessed consecutively at low (1.5 mM) and high (4 mM) extracellular Ca^{2+} concentration during electrical bursts at 20 or 50Hz.
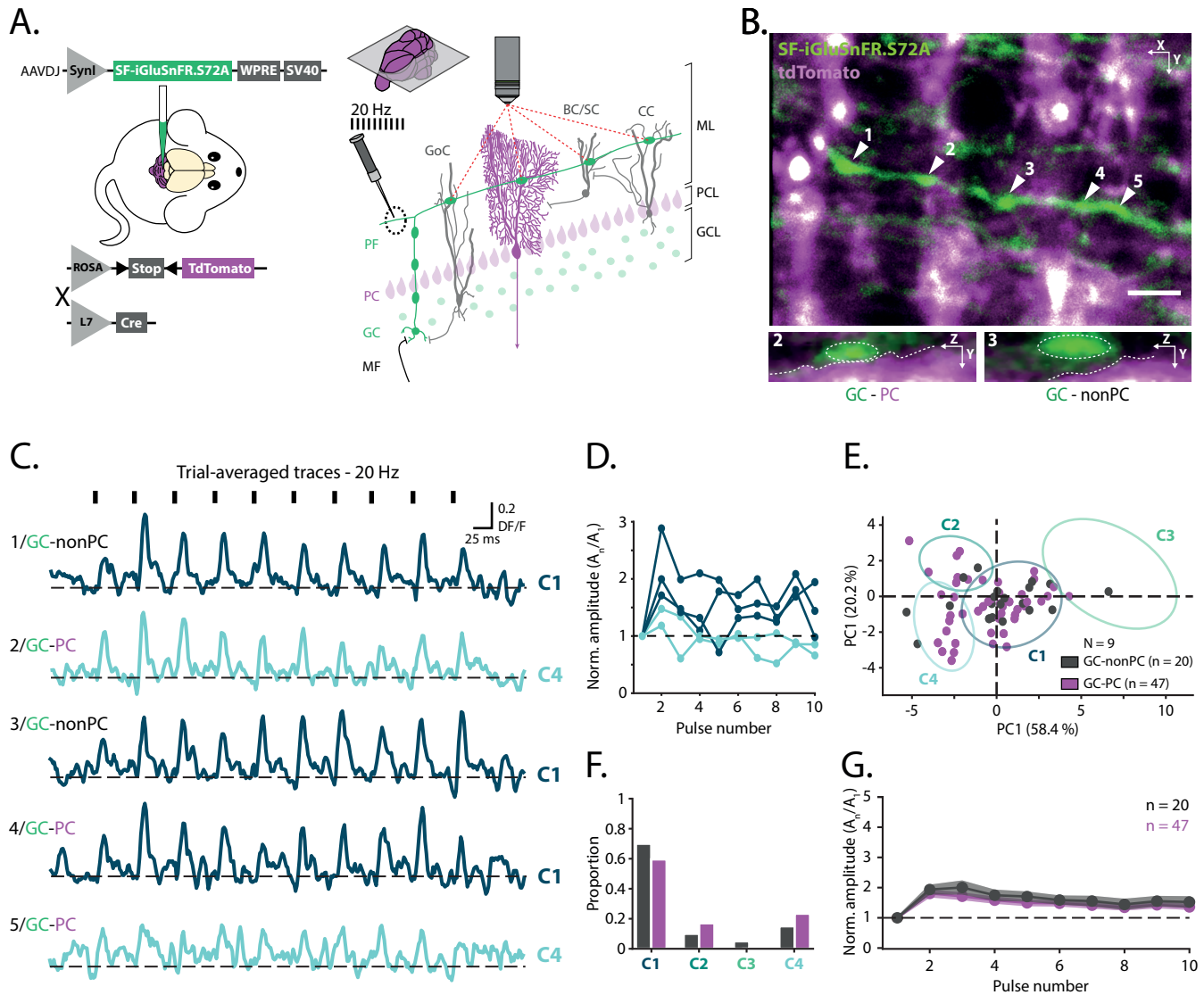
Figure R8 : Target-independent short-term plasticity at granule cell terminals along the parallel fibre.

A) Stereotaxic injection of AAVDJ.SF-iGluSnFR.S72A in GCs of L7-tdTomato mice. The mouse line Rosa26-tdTomato ubiquitously expressing the floxed stop codon upstream of the gene is crossed with a mouse line specifically expressing the Cre-recombinase in the PCs via the L7 promoter. Terminals on the same PF are line-scanned on horizontal cerebellar slices. *BC, basket cell; CC, candelabrum cell; GC, granule cell; GCL, granule cells layer ; GoC, Golgi cell; MF, Mossy fibre; ML, molecular layer; PC, Purkinje cell; PCL, Purkinje cells layer; PF, parallel fibre; SC, stellate cell.*

B) Two-photon imaging of 5 terminals on the same PF and PCs. YZ projections of terminals 2 and 3 are represented below. Both terminals and PC dendrite are delimited by a white dashed line. Terminal 2 forms a synapse with a PC (GC-PC) while terminal 3 is connected to another postsynaptic target (GC-nonPC). Scale bar: 5 µm. *nPC, non-Purkinje cell.*

C) Trial-averaged fluorescence traces from terminals 1-5 shown in *B* during ten pulses at 20Hz. Terminals 1, 3 and 4 belong to the class C1 while terminals 2 and 5 belong to the class C4.

D) Normalized amplitudes of trial-averaged traces shown in *C.*

E) Spatial distribution of trial-averaged traces from terminals connected to PCs and terminals connected to non-PC targets across classes defined by Principal Component Analysis and Hierarchical Clustering.

F) Proportion of GC-PC and GC-nonPC synapses in each class of terminals.

G) Averaged normalized amplitudes for GC-PC and GC-nonPC synapses.

VI.4.1. High calcium concentration increases multivesicular release at single boutons

Trial-averaged fluorescence peaks evoked by glutamate release were collected under 1.5 mM Ca^{2+} and 4 mM Ca^{2+} conditions applied on the same bouton during 10 pulses at 20Hz (n = 21, N = 5) or 50Hz (n = 10, N = 4). Glutamate was dramatically increased when elevating $[Ca^{2+}]$ at both frequencies and kept sustained over the burst (1.5 mM: 0.33 ± 0.16 $\Delta F/F_0$, 4 mM: 1.44 ± 0.59 $\Delta F/F_0$; N = 7, n = 31; **Figure R9A, B**). $P_{success}$ increased as well (1.5 mM: 0.47 ± 0.17, 4 mM: 0.97 ± 0.06; N = 7, n = 31; **Figure R9B**). Therefore, at high $[Ca^{2+}]$, a large quantity of glutamate is released at each pulse.

To determine the number of vesicles released at unitary synapses, the amplitude of the fluorescence signal evoked by the release of a single vesicle was first estimated. The amplitude of the first peak was calculated without release failures at both $[Ca^{2+}]$. The distribution of the first amplitude was restrained to a single mode around 0.36 ± 0.14 $\Delta F/F_0$ at 1.5 mM $[Ca^{2+}]$ while at 4 mM $[Ca^{2+}]$ several modes were observed, indicating multiple release of vesicles (**Figure R9C**). For each bouton, the distribution of the ratio of the first amplitude at 4 mM Ca^{2+} over the first amplitude at 1.5 mM Ca^{2+} was used as a proxy to calculate the quantal release of glutamate (i.e. the number of vesicles released) and was extended to all peaks in the train at 20 Hz. At 4 mM $[Ca^{2+}]$, 3.3 ± 2 more quanta were released compared to 1.5 mM $[Ca^{2+}]$ (n = 26, N = 6; **Figure R9D**). The cumulative quantal release over the burst revealed a large amount of quanta released under high $[Ca^{2+}]$ (Pulse#10 1.5mM: 9.6 ± 0.8 quanta, Pulse#10 4mM: 41.6 ± 5.8; N = 5, n = 16; **Figure R9E**). Therefore, GC boutons release not more than 2 vesicles after each pulse under low $[Ca^{2+}]$ but experience multivesicular release under high $[Ca^{2+}]$.

VI.4.2. Measures of glutamate release with SF-iGluSnFR.S72A differ from postsynaptic responses

The canonical relation between Ca^{2+} and glutamate release asserts that PPR decreases when amplitudes are increased by high $[Ca^{2+}]$ and has been confirmed by electrophysiological experiments. However, in the example illustrated in **Figure R9Ai-Aii**, the second peak is still greater than the first peak at 4 mM Ca^{2+}. The first two peaks from trial-averaged fluorescence traces were compared to patch-clamp recordings of postsynaptic AMPA currents in PCs evoked by paired-pulse stimulation of GCs at 20Hz or 50Hz under both Ca^{2+} concentrations (**Figure R10A-B**). As expected, high Ca^{2+} significantly increased the amplitude of the first current (1.5mM: 81.5 ± 63 pA, 4mM: 288.6 ± 208.1 pA; N = 3, n = 13; **Figure R10C**) and decreased PPR values for both frequencies (20Hz: 1.91 ± 0.24 vs 1.48 ± 0.15, N = 3, n = 6; 50Hz: 2 ± 0.21 vs 1.49 ± 0.15, N = 3, n = 7; **Figure R10D**). Strikingly, PPR
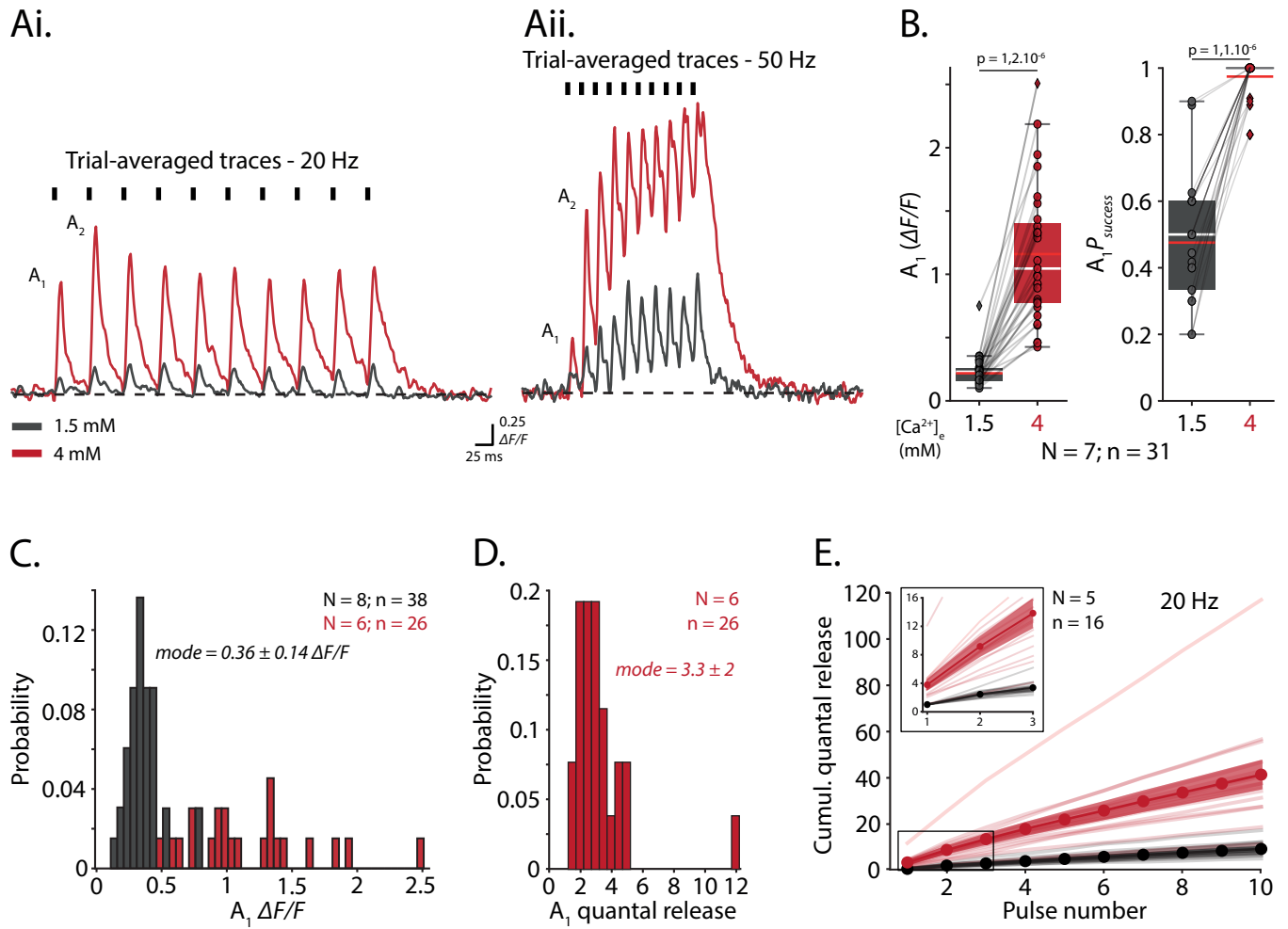
Figure R9 : High dynamic range of glutamate vesicular release modulated by Ca²⁺ dynamics.

Ai) Trial-averaged traces at 1.5 mM (grey) and 4 mM (red) extracellular Ca²⁺ from the same GC terminal during ten evoked electrical pulses at 20 Hz. The first two transients are indicated by A_1 and A_2.

Aii) Same as Ai) for pulses at 50 Hz.

B) Comparison of A_1 and probability of release success for A_1 ($A_1P_{success}$) between both Ca²⁺ concentrations. Means and medians are respectively represented by light-red and white bars (A_1: p = 1,2.10⁻⁸; A_1P_{syn}: p = 1,1.10⁻⁶, Wilcoxon signed-rank test with Bonferroni correction).

C) Distribution histogram of A_1 without failures for both Ca²⁺ concentrations.

D) Distribution histogram of quantal release for A_1 at 4 mM Ca²⁺ and cumulative quantal release during the train of pulses at 20Hz. Quantal release is calculated by dividing the amplitude of the first transient at 4 mM Ca²⁺ by the corresponding amplitude at 1.5 mM Ca²⁺ without failures.

E) Cumulative values for high Ca²⁺ are determined by diving the amplitude of each transient at 4 mM Ca²⁺ from the trial-averaged trace by A_1 at 1.5 mM Ca²⁺ without failures. For low Ca²⁺, cumulative values are calculated over all amplitudes from the trial-average trace normalized by A_1 without failures. Insert: magnification of the cumulative quantal release on the first three pulses.
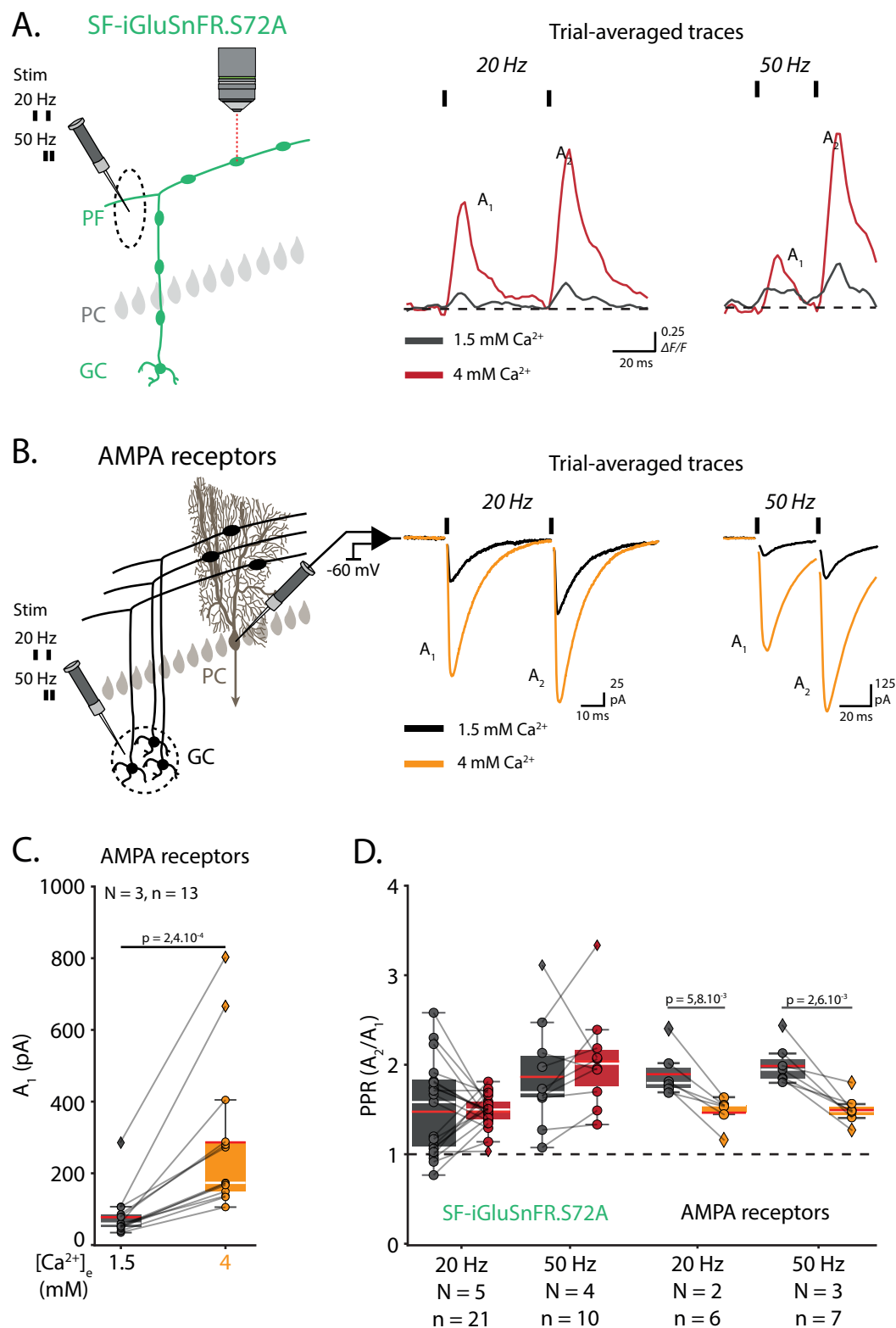
Figure R10 : Comparison between SF-iGluSnFR.S72A imaging of glutamate release and patch-clamp recordings of granule cell to Purkinje cell synaptic currents.

A) Trial-averaged fluorescence transients from single terminals evoked by paired-pulse stimulation of parallel fibres at 20 Hz or 50 Hz under 1.5 mM or 4 mM extracellular Ca^{2+} concentration.

B) Trial-averaged synaptic currents evoked by paired-pulse stimulation of granule cells at 20 Hz or 50 Hz under 1.5 mM or 4 mM extracellular Ca^{2+} concentration. Synaptic currents from AMPA receptors are measured using whole-cell patch-clamp (-60 mV) of Purkinje cells.

C) Amplitude of the first synaptic current under 1.5 mM and 4 mM Ca^{2+} concentrations.

D) PPR comparison between fluorescence transients and synaptic currents under 1.5 mM and 4 mM Ca^{2+} concentrations.

C-D) Means and medians are indicated in red and white, respectively. Statistical test: Wilcoxon signed-rank test.

from fluorescence peaks did not change significantly from 1.5 mM to 4 mM Ca^{2+} at both frequencies (20Hz: 1.49 ± 0.51 vs 1.48 ± 0.19, N = 5, n = 21; 50Hz: 1.87 ± 0.59 vs 2.05 ± 0.55, N = 4, n = 10; **Figure R10D**). Moreover, by considering single boutons, PPR increased from low to high Ca^{2+} at some boutons. These results contradict the classical equation between Ca^{2+} and PPR and suggest that GC boutons recruit specific pools of vesicles as well as active sites from the second pulse at high $[Ca^{2+}]$.

VI.4.3. Multivesicular release reduces short-term plasticity diversity

To assess the effect of Ca^{2+} dynamics on STP, peaks from trial-averaged traces were normalized by the amplitude of the first peak to extract STP profiles. At both stimulation frequencies, GC boutons showed stable sustained facilitation of glutamate release from the second peak at 1.5 mM $[Ca^{2+}]$ (N = 5, n = 21; **Figure R11A**). On the contrary, while glutamate release facilitated at the second pulse at 4 mM $[Ca^{2+}]$ (as shown in **Figure R10D**), it gradually returned to the first peak level (n = 10, N = 4; **Figure R11A**). Although STP depression at high $[Ca^{2+}]$ is well established, GC boutons sustain glutamate release thereby comforting previous conclusions on multivesicular release and recruitment of new releasing sites. On the PCA subspace used in *section VI.2.3*, boutons under low Ca^{2+} condition were found inside and around classes C1 and C4 (**Figure R11B**). Although class C3 was deprived of boutons at low $[Ca^{2+}]$ in this section, some were found in a following set of experiments (*see section VI.5.2*). Interestingly, high $[Ca^{2+}]$ moved all boutons toward class C2 as shown by vectors directions (from 1.5mM to 4mM) represented on the polar plot (**Figure R11B**). These findings demonstrate that elevation of $[Ca^{2+}]$ reduces the diversity of STP and suggests that glutamate release properties of boutons from class C2 at 2.5 mM $[Ca^{2+}]$ (*see section VI.2.3*) are similar to properties at 4 mM $[Ca^{2+}]$.

Taken together, these results indicate that Ca^{2+} dynamics in GC boutons is determinant for recruitment of multiple active sites and modulate multivesicular release and STP diversity. Moreover, unlike electrophysiological recordings, SF-iGluSnFR.S72A imaging demonstrated that GC boutons sustain glutamate release at high $[Ca^{2+}]$. Such a difference suggests that (1) part of glutamate is not detected by AMPA receptors, and/or (2) desensitization of AMPA receptors during electrophysiological recordings.
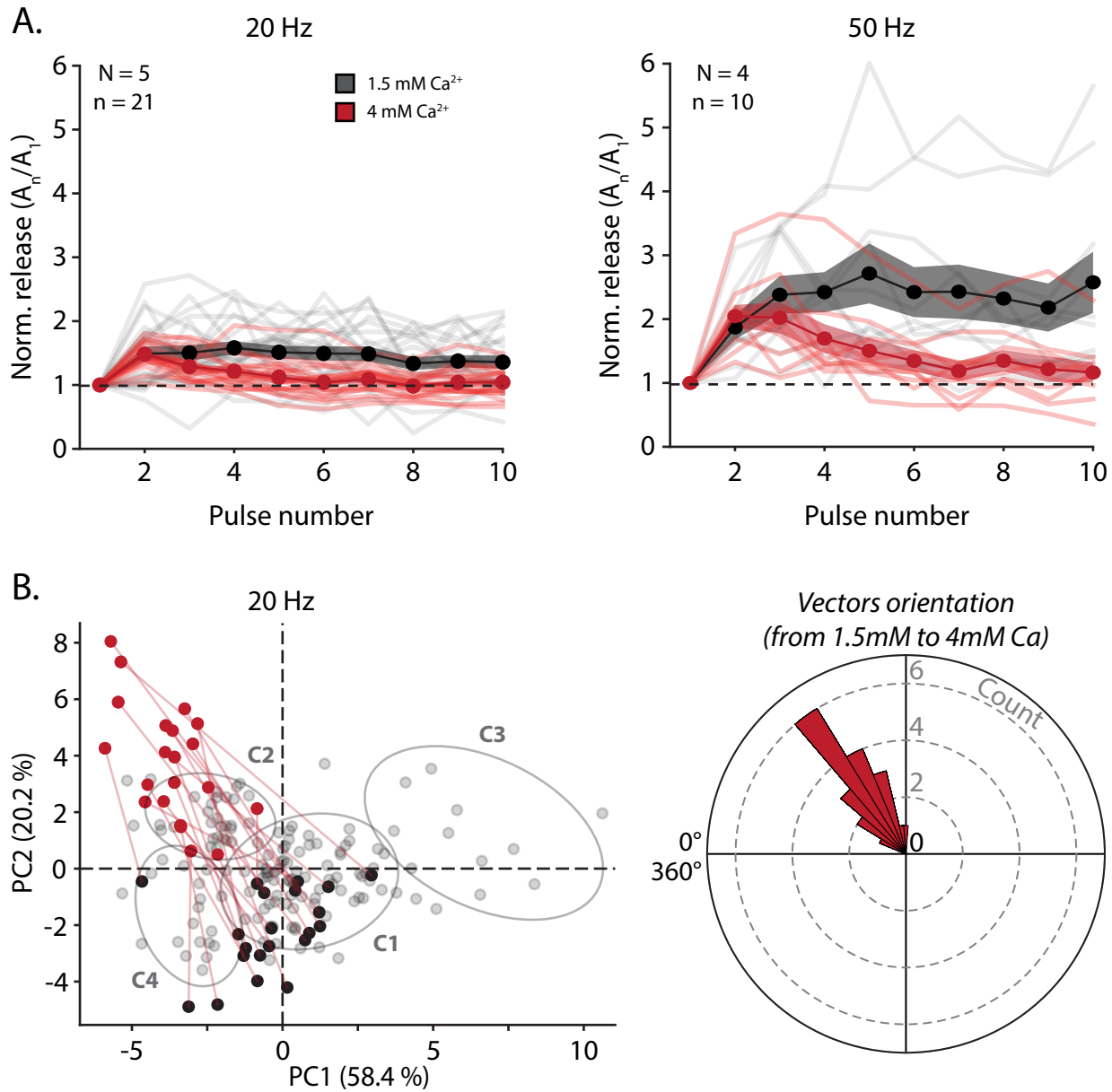
Figure R11 : Impact of elevating extracellular Ca²⁺ concentration on short-term plasticity diversity.

A) Normalized glutamate release evoked by ten pulses at 20 Hz or 50 Hz under 1.5 mM and 4 mM extracellular Ca²⁺ concentrations. Amplitudes from trial-averaged fluorescence traces are normalized by the first amplitude to extract the short-term plasticity profile.

B) Spatial location on the PCA subspace and vectors directions of terminals stimulated at 20 Hz under 1.5 mM and 4 mM Ca²⁺ concentrations. Vectors from low to high Ca²⁺ are indicated by light-red lines. On the polar plot, the origin of each vector represents the dots at 1.5 mM Ca²⁺. The distribution of the angles of the vectors is given by the histogram.

VI.5. Activation of presynaptic adenylyl cyclase at granule cell boutons

Calcium imaging and electrophysiology experiments reported that heterogeneous expression of receptors and proteins between GC boutons modulates calcium signalling and glutamate release (*see section III.2.2*). Adenylyl cyclase expressed at the membrane of the presynaptic bouton increases glutamate release by increasing levels of AMPc (Salin et al., 1996). However, the impact of adenylyl cyclase activation at single GC boutons has never been assessed. The question is addressed as follow: does adenylyl cyclase affect glutamate release in the same fashion between GC boutons and how is STP diversity modulated?

Glutamate release from boutons expressing SF-iGluSnFR.S72A was evoked during 10 pulses at 20 Hz under fixed extracellular $[Ca^{2+}]$ (1.5mM or 2.5mM). Single boutons were imaged before and during pharmacological activation of adenylyl cyclase by forskolin (FSK, 50 µM) added in the bath.

VI.5.1. Forskolin effects on glutamate release are heterogeneous between GC boutons

In the example illustrated in ***Figure R12Ai***, glutamate release was observed at five boutons belonging to the same PF. Activation of adenylyl cyclase by FSK increased glutamate release during the train (***Figure R12Aii***). However, differences between boutons were detected. Fold change (ratio Amplitude$_{FSK}$/Amplitude$_{control}$) showed that bouton 1 released 1.31 and 1.16 more glutamate after the first two pulses, while bouton 3 released 3.06 and 2.02 more glutamate, respectively (***Figure R12Aii***). On average, glutamate release facilitated on the second peak and became stable over the burst in control condition while it facilitated until the third peak prior to stabilization in FSK condition (***Figure R12Aiii***). Similar results were obtained when $[Ca^{2+}]$ was fixed at 1.5 mM (***Figure A1Ai-Aiii***). Therefore, activation of adenylyl cyclase differently affects glutamate release between boutons on the same PF.

Effects of adenylyl cyclase activation were assessed across all boutons. FSK induced heterogeneous changes of glutamate release from the first two pulses (n=13 and N=2 for 1.5 mM Ca^{2+} dataset; n=28 and N=5 for 2.5 mM Ca^{2+} dataset; ***Figure R12B, Figure Ann1B***). Glutamate release was increased in most of boutons while it was unchanged or decreased in others (***Figure R12B, Figure Ann1B***). The amplitude of the first peak was significantly larger during activation of adenylyl cyclase (Control: 0.45 ± 0.23 *ΔF/F$_0$*, FSK: 0.58 ± 0.29 *ΔF/F$_0$*, N=5, n = 28; ***Figure R12C***) and was consistent with PPR decrease (Control: 1.94 ± 0.54, FSK: 1.64 ± 0.48). No significant differences were detected neither in amplitude nor in PPR at 1.5 mM $[Ca^{2+}]$ owing to small samples size and high variability (A$_1$: 0.21 ± 0.07 *ΔF/F$_0$* vs 0.3 ± 0.17 *ΔF/F$_0$*, PPR: 1.87 ± 0.69 vs 1.87 ± 1; ***Figure Ann1C***).
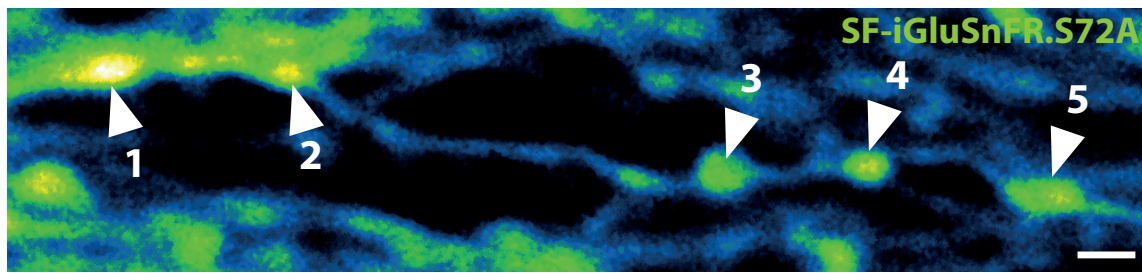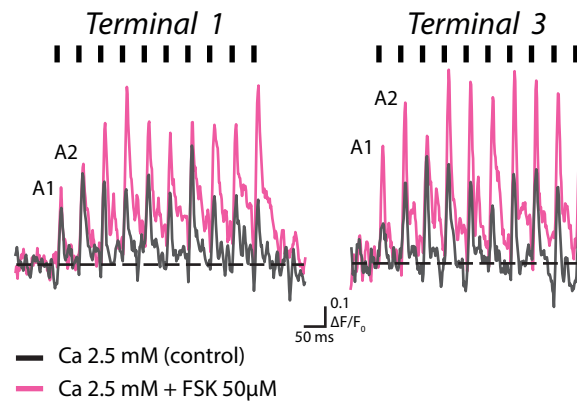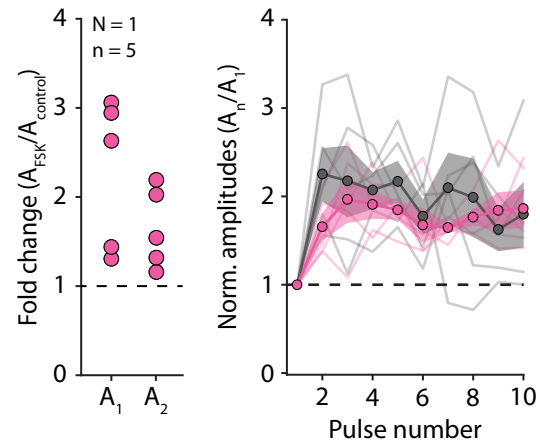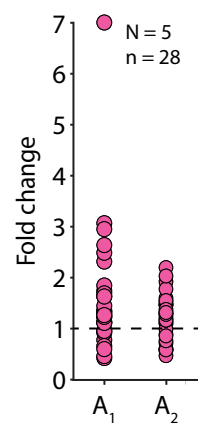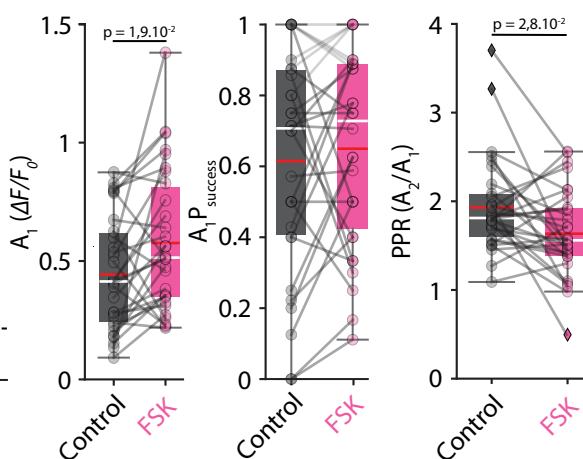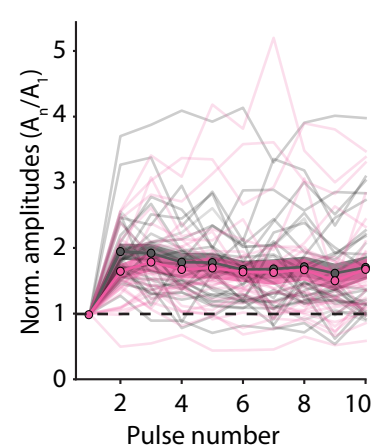
Figure R12 : Heterogeneous contribution of adenylyl cyclase on glutamate release between granule cell terminals under 2.5 mM extracellular Ca²⁺ concentration.

Ai) Two-photon imaging of 5 terminals along the same parallel fibre expressing SF-iGluSnFR.S72A. Scale bar: 2 µm.

Aii) Trial-averaged fluorescence traces from terminals 1 and 3 evoked by ten pulses at 20 Hz in control and FSK conditions and fold change of the first two amplitudes (A_1 and A_2). The fold change for A_1 and A_2 is calculated by the ratio A_1FSK/A_1Control and A_2FSK/A_2Control.

Aiii) Normalized amplitudes of trial-averaged fluorescence traces from terminals 1 to 5 evoked by ten pulses at 20 Hz under control and FSK conditions. Means (colored lines and dots) ± SEM.

B) Same as fold change in Aii) for all terminals imaged.

C) Comparison of A_1, $A_1 P_{success}$ and PPR beween control and FSK conditions. Means and medians are indicated by red and white bars (A_1: p = 1,9.10⁻², paired Student t-test with Bonferroni correction; PPR: p = 2,8.10⁻², $A_1 P_{success}$: p = 9,4.10⁻¹, Wilcoxon signed-rank test with Bonferroni correction).

D) Same as Aiii) for all terminals imaged.

Despite the small sample size in this dataset, the distribution of the quantal release for the first peak (deprived of release failures) demonstrated that 1.62 ± 0.21 more quanta were released in FSK condition (**Figure Ann2A**). However, no conclusion could be made on the comparison of cumulative quantal release plots (same calculation method as high Ca^{2+}, *see section VI.4.1*) between control and FSK conditions (**Figure Ann2B**). In both 1.5 mM and 2.5 mM $[Ca^{2+}]$ datasets, FSK did not significantly changed $P_{success}$ owing to the wide variability of values (1.5mM: 0.49 ± 0.16 vs 0.5 ± 0.23, 2.5mM: 0.62 ± 0.3 vs 0.65 ± 0.27; **Figure R12C**, **Figure Ann1C**). Normalized amplitudes showed a huge variability of STP profiles in both control and FSK conditions for both $[Ca^{2+}]$ datasets (**Figure R12D**, **Figure Ann1D**), although averaged profiles only differed by the PPR value in 2.5 mM $[Ca^{2+}]$ dataset. These results indicate heterogeneous involvement of adenylyl cyclase on glutamate release and STP diversity between GC boutons.

VI.5.2. Activation of adenylyl cyclase do not affect the diversity of short-term plasticity

To assess whether FSK effects on STP diversity differ from 4 mM $[Ca^{2+}]$ (*see section VI.4.3*), a qualitative comparison of PCA subspaces and polar plots was made. As for high Ca^{2+}, boutons imaged in control and FSK conditions under 1.5 mM Ca^{2+} were transformed to fit in the PCA subspace to determine their spatial location across classes. In both control and FSK conditions, boutons were found in classes C1, C3 and C4 with only one bouton in C2 with FSK (**Figure R13A**). Interestingly, FSK moved some boutons from one class to another (C3 to C1, C1 to C3, C1 to C2, C1 to C4) while movement was restricted to a given class for others. This indicates that adenylyl cyclase can change the STP profile in specific boutons in a heterogeneous fashion. Moreover, vectors on the polar plot were pointing toward multiple directions (**Figure R13A**) thereby indicating that FSK did not reduced STP diversity as reported for 4 mM Ca^{2+} condition (**Figure R13B**). Same conclusions could be done on the spatial location and the direction of vectors from the 2.5 mM Ca^{2+} dataset with and without FSK (**Figure Ann3**).

Taken together, these results show that adenylyl cyclase modulates glutamate release in a heterogeneous manner between GC boutons to change the STP profile without affecting STP diversity. Such a contribution of adenylyl cyclase suggests modulation of the availability of synaptic vesicles.
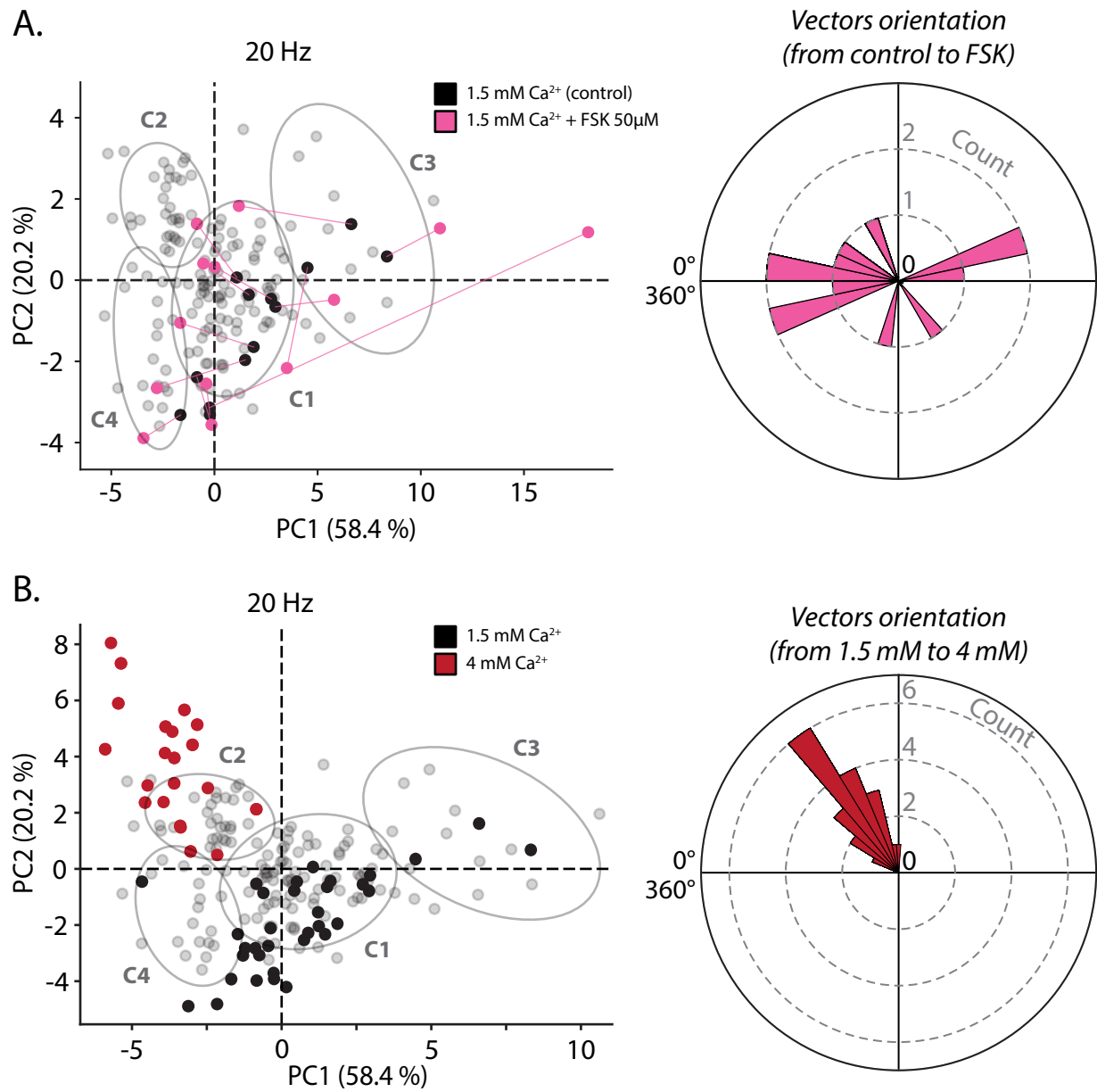
Figure R13 : Contribution of adenylyl cyclase on short-term plasticity diversity differs from contribution of high Ca²⁺.

A) Spatial location on the PCA subspace and vectors orientation of terminals stimulated at 20 Hz under control and FSK conditions. Vectors from control to FSK are indicated by light-pink lines. On the polar plot, the origin of each vector represents the dots in control condition. The distribution of the angles of the vectors is given by the histogram.

B) Same as A) for 1.5 mM and 4 mM Ca2+ concentrations. On the PCA subspace, terminals imaged in control condition (1.5 mM Ca²⁺) in A) are added to better visualize the diversity under low Ca²⁺ condition.

VII. Discussion

The goal of my PhD project was to investigate the functional properties of glutamate release at GC boutons along the PF during high-frequency activity. I developed a state-of-the-art two-photon method combined to SF-iGluSnFR.S72A expression in GCs in cerebellar slices. First, I demonstrated that all GC boutons release glutamate. Then I showed that STP is heterogeneous and target-independent along the PF. Changing [Ca^{2+}] affected STP diversity and unveiled that GC boutons contain a large amount of synaptic vesicles allowing sustained glutamate release. This tonic release was not fully reported by patch-clamp recordings of GC-PC synaptic currents and indicated that part of the glutamate may not be detected by AMPA receptors. Finally, activation of presynaptic adenylyl cyclase heterogeneously modulated glutamate release between GC boutons without affecting STP diversity.

This project provides for the first time simultaneous measurements of glutamate release from multiple GC boutons along the PF and suggests that GC boutons can temporally encode sensorimotor information.

VII.1. Analysis on two-photon imaging of granule cell boutons expressing SF-iGluSnFR.S72A

The first part of my thesis was to develop a two-photon imaging method combined to iGluSnFR to monitor glutamate release from single GC. The innovation provided by this method was to measure glutamate release along the PF. The use of the variant SF-iGluSnFR.S72A is discussed in the present section.

VII.1.1. Technical issues

Glutamate release and STP from single GC boutons were evoked during repetitive stimulation of PFs at high frequency (20 Hz or 50 Hz). To visualize fast releasing events, fast-decaying SF-iGluSnFR.S72A was used to obtain precise measurements. In cerebellar slices, the decay-time (~7 ms) was similar to previous measures (10.6 ms; Marvin et al., 2018) and minimized the fluorescence build-up. However, build-up was prominent at 50 Hz and progressively led to saturation of the sensor in most boutons. This finding strongly limited the possibility to increase stimulation frequency hence impeding to reach the fastest firing rates of GCs (i.e. up to 250 Hz; Chadderton et al., 2004).

The glutamate released in the synaptic cleft can spill out to elicit heterosynaptic communication and its concentration decays during extrasynaptic diffusion and reuptake (Barbour et al., 1994; Barbour & Häusser, 1997). SF-iGluSnFR.S72A was also selected for the low affinity for glutamate to limit spillover detection. As spillover is delayed and slows transients (Barbour et al., 1994; DiGregorio et al., 2002), the rapid kinetic (< 10 ms) in the majority of boutons indicated reliable measures of synaptic glutamate. A minority of boutons showed low kinetics (>10 ms) which might relate on glutamate spillover. If so, the decay of fluorescence transients should display a first fast kinetic elicited by the synaptic glutamate followed by a slow kinetic from spillover. A biexponential measure of the decay phase would indicate whether glutamate spillover contaminates the measures in these boutons. However, GC-PC synapses form tripartite synapses with glial cell which express glutamate transporters suggesting that spillover detection from neighboring synapses is even more limited. High values of decay-time might also relate to the ability of SF-iGluSnFR.S72A to act as a buffer of glutamate hence competing with EAAT transporters expressed on GC boutons (Armbruster et al., 2020).

In the viral construction, the promoter hSynapsin was used in the genetic sequence to express SF-iGluSnFR.S72A in neurons. The high density of PFs allowed to image boutons from multiple PFs on the same cerebellar slice and collect fluorescence signals from a large amount of boutons. However, the lack of specificity led to expression of the sensor in multiple neuronal types, especially around the injection site. The high density of labelling led to overlap of PFs and challenged imaging of isolated boutons. This constrained to find isolated PFs far from the injection site and apply stimulations in the molecular layer which increase the probability to trigger glutamate spillover (Barbour & Häusser, 1997). Promoting specificity and sparseness labelling could improve spatial precision of boutons imaging on the ascending axon and the PF during stimulation of the GC soma (*see section VII.7*).

VII.1.2. Estimation of $P_{success}$.

Single trial fluorescence traces are noisy as SF-iGluSnFR.S72A signal-to-noise ratio is small (Marvin et al., 2018). Bootstrap was used as an objective method to estimate failures of glutamate release and calculate $P_{success}$ which increased from 0.47 at 1.5 mM to 0.97 at 4mM [Ca^{2+}]. Similarly, Dürst *et* al (2022) reported $P_{success}$ elevation from 0.26 at 1 mM to 0.87 at 4mM [Ca^{2+}] with iGluSnFR (original version) imaging from single boutons at cultured hippocampal Schaffer collaterals during single electrical stimulation (Dürst et al., 2022). Moreover, our $P_{success}$ value at low [Ca^{2+}] matched with GC-PC electrophysiological pair recordings in slices showing $P_{success}$ of 0.44 at 1.5 mM [Ca^{2+}] (Valera et al., 2012). Therefore, bootstrap reliably estimated $P_{success}$ in the present study.

$P_{success}$ is usually estimated from a transient evoked by a single or two pulses over a high number of trials limiting illumination duration (Dürst et al., 2022). In this project, two reasons led us to limit the number of trials. First, the low signal-to-noise ratio of SF-iGluSnFR.S72A required high laser intensity leading to photobleaching and photodamage. Second, since PFs were stimulated with a train of 10 electrical pulses, boutons were illuminated for 1 second per trial. Hence, $P_{success}$ might be overestimated or underestimated by the small number of repetitions. To better estimate $P_{success}$, SF-iGluSnFR.S72A could be substituted by SF-iGluSnFR.A184V since it provides a 2-fold larger signal-to-noise ratio (Marvin et al., 2018).

VII.1.3. Identification of targets of granule cell boutons

The target of GC boutons was identified during real-time imaging using L7-tdTomato mice. After z-stack, the vicinity between the red signal from the PC spine and the green signal from SF-iGluSnFR.S72A was deemed as a putative GC-PC synapse. The proportion obtained was 70% of GC-PC and 30% of GC-nonPC which is slightly different from previously reported values (80% GC-PC, 9% GC-nonPC and 11% mitochondrion; Pichitpornchai et al., 1994). Boutons containing mitochondrion could not be considered as GC-nonPC since they do not release glutamate. Although the proportion of GC-PC synapses remains higher, these data indicate that part of these synapses was probably misidentified by the method developed in this project. This raises an appealing question: Is the STP plasticity at GC boutons really target-independent? On the same PF, the distance between consecutive boutons was ~5 μm, which is consistent with previous studies (Pichitpornchai et al., 1994). The fact that 4/5 (80%) consecutive boutons make a synapse with a PC clearly indicates that the diversity of STP profiles observed between these boutons is not related to the type of postsynaptic target. Therefore, misidentification of the postsynaptic target do not call into question the target-independent nature of STP at boutons along the same PF. Moreover, posthoc immunostaining of target cells could not be used for two reasons. First, thick cerebellar slices challenge antibodies penetration for immunostaining. Second, the high density of PFs expressing SF-iGluSnFR.S72A does not allow to find the imaged PF posthoc. Hence, the L7-tdTomato mouse line was the most adapted tool to identify the target.

VII.2. Granule cell to Purkinje cell silent synapses

SF-iGluSnFR.S72A imaging of GC boutons was first used to investigate putative GC-PC silent synapses. Synapses are considered silent when no detectable responses are measured at the soma of the PC during presynaptic neuronal activity. They can be either *mute* (no glutamate release from the presynaptic bouton) or *deaf* (no postsynaptic AMPA receptors). The results obtained here revealed that almost all GC boutons release glutamate indicating that 85% of GC-PC silent synapses (Isope & Barbour, 2002) lack AMPA receptors. The capacity of GC boutons to release glutamate at silent synapses unveil three possible interpretations:

1. The GC bouton is ready to awake the synapse to transfer relevant information.
2. The GC bouton undergoes low-frequency depression to avoid glutamate release evoked by non-relevant information.
3. The GC bouton interacts with surrounding Bergmann glial cells to avoid awakening of the synaptic.

The first hypothesis would occur during behavioural task eliciting intense activity of GCs to trigger AMPA receptors insertion at the postsynaptic density (*see section II.4.3.1*). High-frequency stimulation may induce a strong build-up of glutamate in the synaptic cleft spilling out to activate extrasynaptic receptors. Investigations reported that electrical bursts of 15 pulses at 100 Hz repeated every 3 seconds for a period of 5 minutes applied on PFs in cerebellar slices elicit LTP at GC-PC synapses mediated by the conjunctive activation of extrasynaptic mGluR1 and GABA-A receptors on PC (Binda et al., 2016). This activates low-threshold Ca_v3 channels that might inhibit CaMKII through Ca^{2+} influx hence promoting AMPA receptors insertion via phosphatase 2B (Belmeguenai, 2005; Piochon et al., 2016; Schonewille et al., 2010) to awake the synapse. Such a mechanism may explain *in vivo* expansion of PCs cutaneous receptive fields on forelimb skin after LTP induction (same protocol as Binda *et* al., 2016) applied via microstimulations of PFs (Jörntell & Ekerot, 2002).

Awakening of silent synapses may also occur at low-frequency. Experiments using photostimulation of caged glutamate in cerebellar slices reported synaptic maps of connected and silent patches of GCs on neighbouring PCs (Spaeth et al., 2022; Valera et al., 2016). Photostimulation of silent patches with an LTP protocol consisting of 300 light pulses at 1 Hz led to awakening of GC-PC synapses and changed the synaptic maps (Valera et al., 2016). Low-frequency LTP is mGluR1 and GABA-A independent and requires NO production (Lev-Ram et al., 2002) and phosphatase 2B (Schonewille et al., 2010) which may mediate AMPA receptors insertion at the postsynaptic density to awake the synapse.

Synaptic awakening may account for locomotor adaptation. Mapping experiments similar to Valera *et al* (2016) have been reported across different locomotor contexts (Spaeth et al., 2022). When the animal learns to compensate a locomotor deficit (e.g. cuff on the sciatic nerve), synaptic maps undergo re-organization and lead to an increase in the total GC-PC synaptic weights without changing the averaged amount of connected GC sites (Spaeth et al., 2022). This suggests that high and low frequency mechanisms of LTP may awake silent GC-PC synapses to accurately shape synaptic maps and adjust behaviors.

The second hypothesis would assume that the GC bouton contains a mechanism that decreases glutamate release. As discussed above, low frequencies (1 Hz) can trigger LTP at GC-PC synapses. In GCs transmitting high frequencies related to relevant sensorimotor information, low frequencies may be considered as non-relevant information. How to avoid non-relevant information to trigger erroneous awakening of a silent synapse? One way would be to silence the bouton. Doussau *et al* (2017) reported that GC-PC synaptic currents evoked by 300 electrical stimulations of PFs at 2 Hz are gradually depressed until full blockage of synaptic transmission (*see section III.2.1.2*, Doussau et al., 2017). Such a low-frequency depression would avoid any release of glutamate elicited by the non-relevant information.

The third hypothesis would claim that the Bergmann glia elicits structural changes impeding awakening of the synapse. Bergmann glia engulfs synaptic structures such as boutons, spines and dendrites to promote synaptic pruning through phagocytic processes (Morizawa et al., 2022). Synaptic pruning is fundamental to refine neuronal networks for efficient learning. Investigations at PC spines demonstrated that Bergmann glia engulfment reduces the volume of the spine and pharmacological blockade of this process inhibits learning of nystagmus reflex, a cerebellar-dependent compensatory eye movement for stabilizing the image on the retina during horizontal movement of vertical stripes (Morizawa et al., 2022). The GC bouton can activate Bergmann glia through Ca^{2+}-permeable AMPA receptors. Glutamate release elicited by non-relevant information might dictate Bergmann glia to engulf and nibble the dendritic spine to avoid LTP induction and erroneous awake of the synapse. This process may participate in regulating the amount of silent synapses to promote efficient learning. If a particular sensorimotor information needs to be transmitted, the massive release from the GC bouton elicited by the high-frequency would block the engulfment process to allow synapse awakening via the processes described in the first hypothesis.

VII.3. Hypotheses on differences between SF-iGluSnFR.S72A and patch-clamp

In patch-clamp methods, synaptic currents are usually measured at the soma of the cell. These measures are affected by saturation, desensitization and moving of AMPA receptors as well as dendritic filtering. The advantage of SF-iGluSnFR.S72A is to provide measurements of glutamate release directly on the presynaptic bouton. Unlike electrophysiological recordings of GC-PC currents, GC boutons imaging reported no differences in PPR from low to high $[Ca^{2+}]$ during stimulations at either 20 Hz or 50 Hz. A similar discrepancy have been recently observed at Shaffer collateral boutons to CA1 using imaging of original iGluSnFR and paired recordings of CA3-CA1 synapses at low $[Ca^{2+}]$ (Dürst et al., 2022). Two interpretations are possible to explain the results obtained here:

1. Part of glutamate is not detected by synaptic AMPA receptors and acts on extrasynaptic receptors or participates in ectopic release on glial cells.
2. GC boutons release a high concentration of glutamate in the synaptic cleft which desensitize postsynaptic AMPA receptors.

The first hypothesis suggests that GC boutons release glutamate from ectopic active sites located out of the synaptic cleft, a process known as ectopic release (Balakrishnan et al., 2014; Dobson et al., 2018; Dobson & Bellamy, 2015; Matsui et al., 2005). Glutamate released from ectopic sites directly faces AMPA receptors on Bergmann glial cells (Matsui et al., 2005) and is not detected by synaptic AMPA receptors. Paired-pulse stimulation of PFs at 50 Hz elicits strong facilitating currents in Bergmann glia recorded by patch-clamp (Matsui et al., 2005). Since SF-iGluSnFR.S72A is expressed all over the membrane of the GC bouton, ectopic glutamate detected by the sensor would add to detection of synaptic glutamate thereby influencing PPR from low to high $[Ca^{2+}]$. In addition, increase or decrease of PPR from low to high $[Ca^{2+}]$ in some boutons might underlie heterogeneous properties of ectopic glutamate release between GC boutons.

The second hypothesis is based on our results at high $[Ca^{2+}]$ showing that GC boutons undergo multivesicular release by recruiting heterogeneous pools of synaptic vesicles. GC boutons contain reluctant synaptic vesicles (*see section III.2.1.2*; (Doussau et al., 2017). Assuming that these vesicles are remote from Ca^{2+} nanodomains, high $[Ca^{2+}]$ in the active zone of the bouton and coupling to a high-affinity/low-binding kinetics synaptotagmin (*see section III.1.2*; (Jackman et al., 2016; Jackman & Regehr, 2017) might trigger their release.

Glutamate from reluctant vesicles is detected by SF-iGluSnFR.S72A after the second pulse keeping PPR high. At the postsynaptic sites, although desensitized AMPA receptors are rapidly replaced by fresh ones to support neurotransmission (Heine et al., 2008), glutamate released during the first pulse would desensitize the majority of AMPA receptors. During the second pulse, additional glutamate from reluctant vesicles competes with AMPA receptors turnover by amplifying the number of desensitized receptors thereby reducing PPR. Paired-pulse electrical stimulation of a connected pair of hippocampal neurons in culture evokes short-term depression which is enhanced when turnover is prevented (Heine et al., 2008). This indicates desensitization of AMPA receptors linked at the postsynaptic density. Interestingly, preventing turnover and desensitization of AMPA receptors switch PPR to slight facilitation (Heine et al., 2008), indicating that part of glutamate released in the synaptic cleft is masked by AMPA receptors features. These results may confirm the hypothesis discussed here and underestimation of PPR by electrophysiological measurements.

VII.4. Calcium and adenylyl cyclase modulate synaptic diversity at unitary granule cell boutons

VII.4.1. Ca^{2+} signalling modulates P_r and recruitment of active sites

At GC boutons, we observed a wide range of STP profiles at 1.5 mM and 2.5 mM $[Ca^{2+}]$ from steady-state to facilitation. Steady-state profiles display stable amplitudes of fluorescence transients suggesting that vesicles are released one by one from a single active site (univesicular release, Biró et al., 2005; Silver et al., 2003), although GC boutons may contain 7-8 active sites (Valera et al., 2012; Xu-Friedman et al., 2001). Univesicular release would assume that the number of vesicles released in the synaptic cleft after a stimulation do not increase with P_r during Ca^{2+} accumulation elicited by high-frequency bursts. P_r increase would not be sufficient to promote the switch from putative univesicular profiles at 1.5 mM $[Ca^{2+}]$ to a sustained facilitation observed at 4 mM Ca^{2+}. High $[Ca^{2+}]$ might unlock synaptic active sites to trigger massive release of ready-releasable and reluctant vesicles (*see section VII.3*) rapidly recycled leading to standardization of STP. In GC boutons showing facilitation in STP profiles at 1.5 mM and 2.5 mM $[Ca^{2+}]$, glutamate release from multiple active sites might be controlled by P_r at low $[Ca^{2+}]$. However, high $[Ca^{2+}]$ would increase P_r at sites already active and recruits new sites to release reluctant vesicles thereby standardizing STP. At the calyx of Held, elevation of $[Ca^{2+}]$ enhances current amplitudes and STD evoked during electrical stimulations at 100 Hz indicating increase in P_r (Thanawala & Regehr, 2013). Such an enhancement also

accompanies an increase in RRP size (Thanawala & Regehr, 2013). Reduction of Ca^{2+} influx via GABA-B/Ca_v signalling (*see section III.2.2.1*) decreases P_r and RRP size leading to a switch from short-term depression to short-term facilitation (Thanawala & Regehr, 2013). Although the synaptic machinery of GC boutons is different than calyx of Held, these results may explain our hypothesis on Ca^{2+} dependence modulation of recruitment of active sites releasing reluctant P_r to shape synaptic strength. Moreover, modelling studies at boutons from Schaffer collaterals reported that synaptic strength is dictated by P_r at low [Ca^{2+}] while it is correlated to the number of active sites at high [Ca^{2+}] (Dürst et al., 2022), hence reinforcing present assumptions.

VII.4.2. Regulation of adenylyl cyclase influences the availability of synaptic vesicles

Activation of adenylyl cyclase at GC boutons elicited heterogeneous modulation of glutamate release along the PF. In the majority of boutons, adenylyl cyclase potentiated glutamate release in accordance with previous studies (Falcón-Moya et al., 2018; Fourcaudot et al., 2009; Salin et al., 1996). Adenylyl cyclase activates cAMP/PKA signalling pathway which phosphorylate multiple targets including synapsins (Hosaka et al., 1999). This promotes bidirectional shift between univesicular and multivesicular release via a P_r-independent modulation of RRP size (Vaden et al., 2019) and may control the active site occupancy by synaptic vesicles. In our dataset, it is not excluded that adenylyl cyclase potentiates glutamate release in some boutons via an increase in RRP size to shift from univesicular to multivesicular release mode and change the STP profile.

PKA mediating regulation of multivesicular release is absent in triple synapsin knock-out (i.e. deletion of synapsins I, II and III; Vaden et al., 2019). Synapsin II is heterogeneously expressed at GC-MLI synapses and contributes to STP diversity by generating steady (i.e. putative univesicular), facilitating and depressing (i.e. multivesicular) profiles during 100 Hz repetitive stimulations (Dorgans et al., 2019). Its deletion increases the proportion of steady and facilitating profiles, while decreases the proportion of depressing profiles (Dorgans et al., 2019). In our data, the unchanged glutamate release at some GC boutons during activation of adenylyl cyclase might be related to the lack of synapsin II and raises two possible interpretations. First, lack of synapsin II in steady boutons may prevent the modulation of RRP size from univesicular to multivesicular release. Second, facilitating boutons lacking synapsin II are already in a potentiated state experimenting multivesicular release (Vaden et al., 2019), thereby occluding effects of adenylyl cyclase activation (Salin et al., 1996). Therefore, the lack of synapsin II may prevent adenylyl cyclase-dependent changes in the STP profile.

In a subset of GC boutons, activation of adenylyl cyclase reduced glutamate release. Kainate receptors are known to depress glutamate release. At GC-PC synapses, Falcon-Moya

et al (2019) reported that pharmacological blockade of cAMP or PKA suppresses the decrease in current amplitude evoked by activation of kainate receptors during stimulation of PFs (Falcón-Moya et al., 2019). Since kainate receptors were not blocked in our study, it is not excluded that this subset of boutons mobilise a specific adenylyl cyclase-induced signalling pathway to activate kainate receptors. Such a depression might switch the release mode from multivesicular to univesicular and change the STP profile.

Given the complexity of our dataset, it would be useful to split these three subsets of GC boutons to investigate more in details on whether the activation of adenylyl cyclase promotes the bidirectional modulation of univesicular/multivesicular release.

VII.4.3. Presynaptic and postsynaptic contributions of adenylyl cyclase on synaptic transmission

Among GC boutons, measurements of glutamate release are partially consistent with previous electrophysiological measurements at GC-PC synapses (Gutierrez-Castellanos et al., 2017; Salin et al., 1996). Salin *et al* (1996) reported that adenylyl cyclase activation elicited 50% increase in current amplitudes and 20% reduction of PPR thereby claiming presynaptic effects of adenylyl cyclase (Salin et al., 1996). However, in our experiments, the amplitude of the first fluorescence transient showed a 30% increase and a 15% decrease in PPR. Conversely, Gutierrez-Castellanos *et al* (2017) reported 130% increase in current amplitudes and no change in PPR, albeit an increase in the frequency of miniature, thereby claiming postsynaptic effects of adenylyl cyclase (Gutierrez-Castellanos et al., 2017). This postsynaptic effect is related to modulation of AMPA receptor conductance via Epac signalling pathway activated by cAMP (Gutierrez-Castellanos et al., 2017). In this thesis project, glutamate release measures are free of the postsynaptic element and highlight for the first time the exclusive contribution of presynaptic adenylyl cyclase in heterogeneous synaptic transmission.

VII.5. Short-term plasticity diversity at granule cell boutons expands pattern separation in the molecular layer

At the input stage of the cerebellar cortex, each GC contributes to expansion recoding and sparse coding by integrating the modalities conveyed by a small number of MFs (Cayco-Gajic & Silver, 2019). The convergence of MFs from different origins with heterogeneous STP profiles onto single GC provides modality-specific temporal signatures enhancing pattern decorrelation of sensorimotor information (Chabrol et al., 2015a). Diversity in STP profiles is also observed in the molecular layer where it controls feedforward inhibition at the GC-MLI

synapse by shaping the MLIs firing delay (Dorgans et al., 2019) and at the GC-PC and MLI-PC synapses where it underlies the excitatory/inhibitory control of PCs during train of stimuli (Grangeray-Vilmint et al., 2018). The fact that STP vary from bouton to bouton along the PF in an apparent target-independent manner and the very short inter-bouton distance (~5 µm) suggests intra-modular STP diversity in the cerebellar cortex (modules are typically 100-300 µm wide). What would be the purpose of having a lot of variability within a module? It would imply that neighboring PCs of a same module, which learn from a same set of CFs, integrate information from the same groups of GCs (Spaeth et al., 2022; Valera et al., 2016) and project to the same regions of the DCN, can receive information from a single GC with variable temporal dynamics. This variability in STP profiles may further expand temporal coding by shaping individual PC firing and enable more complex temporal profiles within a module in response to the activation of a given set of GCs. Therefore, STP diversity along the PF would further expand high-dimensional representation of behaviors (Lanore et al., 2021). Such a "*temporal" expansion recoding* would act as an additional feature for pattern separation and should be considered in computational models of well-timed behaviors (Barri et al., 2022).

VII.6. Conclusions and future directions

This work assessed for the first time glutamate release from multiple GC boutons along the PF and provided new understandings on functional heterogeneities between single boutons. Besides the results reported here, some questions and experiments worth asking in the future.

Concerning the method developed in this project, specificity and sparseness of iGluSnFR expression in GCs should be improved at first. The lab of Jean Livet recently developed plasmids based on an integration-coupled On genetic switch (iOn) expressed through transposition into the host genome and introduced by electroporation (***Figure D2A***; Kumamoto et al., 2020). The ***Figure D2*** illustrates preliminary data from our lab for iOn plasmids expressing eGFP and ChR2-tdTomato as an example. To target GCs, both iOn plasmids are electroporated in the external granular layer formed by GCs progenitors at the surface of the cerebellum in juvenile mice (P6-P7, ***Figure D2B***). Electroporation limits the number of progenitors integrating the plasmids and the integrative feature of the plasmid allows its expression in daughter cells during mitotic division and migration. This allows to identify sparse GCs through cytoplasmic eGFP and membrane expression of ChR2 (***Figure D2C***). An iOn plasmid expressing SF-iGluSnFR.S72A is currently being created. By using this method with the iOn plasmid carrying SF-iGluSnFR.S72A combined to an iOn plasmid expressing
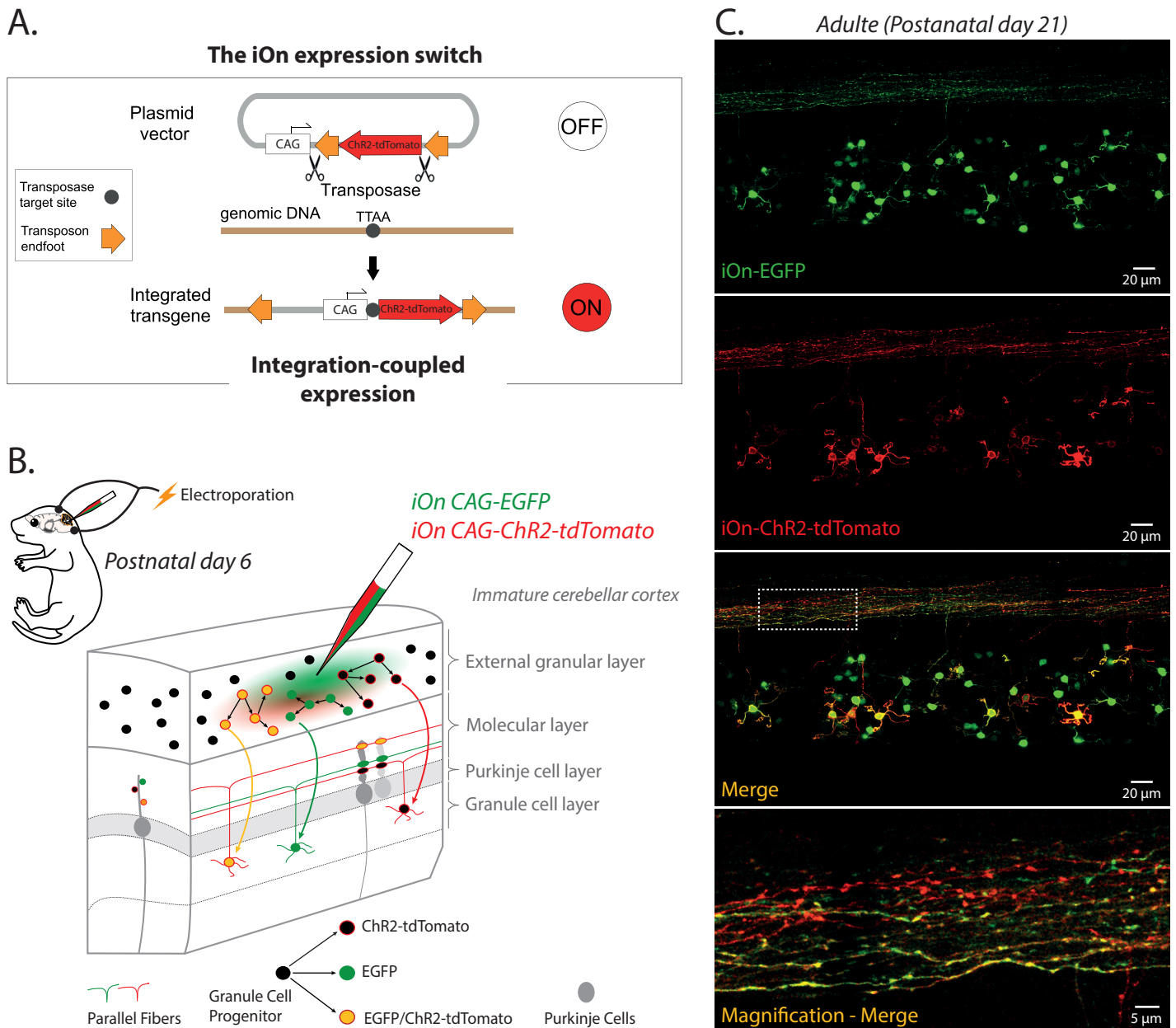
Figure D1: Electroporation of iOn plasmids in granule cell progenitors promotes specificity and sparsness of expression in mature granule cells.

A) Principle of genome-integrating iOn vectors. ChR2-tdTomato expression is conditioned by transposase action that reunites the promoter (CAG) and ChR2-tdTomato. The same principle is applied for EGFP as a gene of interest. ***Adapted from Kumamoto et al., 2020***.

B) Electroporation of iOn plasmids in the external granular layer of pups at postnatalday 6. Granule cell progenitors integrate and express one of the plasmids or both or neither. Progenitors undergo symmetrical mitotic division (black arrows) prior to migration in the granular layer.

C) Identification of granule cells in adult electroporated mice. Individual channels and merge are shown for both plasmids expression. The bottom image illustrates a magnification of parallel fibres in the dotted square from merge (second to last image). Note the the high specificity and sparsness of expression. ***Images credit: Adriana Basnakova & Frédéric Doussau, INCI***.

Abbreviations: EGFP, enhanced green fluorescent protein; ChR2, channelrhodopsin 2.

cytoplasmic RFP, GCs will be identified through RFP and imaging of SF-iGluSnFR.S72A performed at boutons during high frequency stimulations of the soma. Therefore, in addition to high specificity and sparseness, spillover, photobleaching and photodamage would be considerably limited.

An appealing question in cerebellar processing is how a specific modality is encoded on the MF-GC-PC pathway. MFs from a precise precerebellar nucleus could be revealed with viral injections of a trans-synaptic virus (e.g. AAV1) expressing the Cre-recombinase. By floxing the SF-iGluSnFR.S72A gene in the iOn plasmid integrated in GCs, only GCs which received the Cre-recombinase from connected MFs could express the glutamate sensor. The MF to GC transmission may be imaged on dendrites and firing activity recorded at the same time using electrophysiological loose-cell attached configuration on the soma. In addition, glutamate release from GC boutons may be assessed on the ascending axon and the PF meanwhile juxtacellular recordings of PC firing. This would provide important understandings on the transfer function of MFs sensorimotor information and related temporal processing in PCs.

Lastly, the diversity of STP explored at GC boutons raises important questions on molecular supports of such a diversity. Synapsin II is heterogeneously expressed at GC-MLI synapses and its disruption reduces STP diversity. However, how synapsin II is expressed along the PF is still unknown. After SF-iGluSnFR.S72A imaging from single boutons, the GC may be patched with a solution containing fluorescent small single domain binding proteins termed nanobodies (de Beer & Giepmans, 2020) targeting synapsin II. Biocytin would be added to the solution to identify the GC post-hoc. As an additional molecular support, the topography of Cav/Munc13/synaptic vesicles might also contribute to shape STP diversity between GC boutons. Electron microscopy and gold particles could be used to label Cav2.1 and Munc13 as reported in previous studies (Rebola et al., 2019).

Bibliography

Abbott, L. F., Varela, J. A., Sen, K., & Nelson, S. B. (1997). Synaptic Depression and Cortical Gain Control. *Science*, *275*(5297), 221–224. https://doi.org/10.1126/science.275.5297.221

Abrahamsson, T., Cathala, L., Matsui, K., Shigemoto, R., & DiGregorio, D. A. (2012). Thin Dendrites of Cerebellar Interneurons Confer Sublinear Synaptic Integration and a Gradient of Short-Term Plasticity. *Neuron*, *73*(6), 1159–1172. https://doi.org/10.1016/j.neuron.2012.01.027

Aggarwal, A., Liu, R., Chen, Y., Ralowicz, A. J., Bergerson, S. J., Tomaska, F., Hanson, T. L., Hasseman, J. P., Reep, D., Tsegaye, G., Yao, P., Ji, X., Kloos, M., Walpita, D., Patel, R., Mohr, M. A., Tilberg, P. W., Mohar, B., Team, T. G. P., … Podgorski, K. (2022). Glutamate indicators with improved activation kinetics and localization for imaging synaptic transmission. *BioRxiv*, 2022.02.13.480251. https://www.biorxiv.org/content/10.1101/2022.02.13.480251v2%0Ahttps://www.biorxiv.org/content/10.1101/2022.02.13.480251v2.abstract

Ahn, A. H., Dziennis, S., Hawkes, R., & Herrup, K. (1994). The cloning of zebrin II reveals its identity with aldolase C. *Development*, *120*(8), 2081–2090. https://doi.org/10.1242/dev.120.8.2081

Akbar, U., & Ashizawa, T. (2015). Ataxia. *Neurol Clin.*, *33*(1), 225–248. https://doi.org/10.1016/j.ncl.2014.09.004

Albus, J. S. (1971a). A theory of cerebellar function. *Mathematical Biosciences*. https://doi.org/10.1016/0025-5564(71)90051-4

Albus, J. S. (1971b). A theory of cerebellar function. *Mathematical Biosciences*, *10*(1–2), 25–61. https://doi.org/10.1016/0025-5564(71)90051-4

Alcami, P., & Marty, A. (2013). Estimating functional connectivity in an electrically coupled interneuron network. *Proceedings of the National Academy of Sciences*, *110*(49). https://doi.org/10.1073/pnas.1310983110

Allen, G., Buxton, R. B., Wong, E. C., & Courchesne, E. (1997). Attentional activation of the cerebellum independent of motor involvement. *Science*, *275*(5308), 1940–1943. https://doi.org/10.1126/science.275.5308.1940

Amino, Y., Kyuhou, S. ichi, Matsuzaki, R., & Gemba, H. (2001). Cerebello-thalamo-cortical projections to the posterior parietal cortex in the macaque monkey. *Neuroscience Letters*, *309*(1), 29–32. https://doi.org/10.1016/S0304-3940(01)02018-3

Andersson, G., & Oscarsson, O. (1978). Projections to lateral vestibular nucleus from cerebellar climbing fiber zones. *Experimental Brain Research*, *32*(4), 549–563. https://doi.org/10.1007/BF00239552

Anwar, H., Li, X., Bucher, D., & Nadim, F. (2017). Functional roles of short-term synaptic plasticity with an emphasis on inhibition. *Current Opinion in Neurobiology*, *43*, 71–78. https://doi.org/10.1016/j.conb.2017.01.002

Apps, R., & Hawkes, R. (2009). Cerebellar cortical organization: a one-map hypothesis. *Nature Reviews Neuroscience*, *10*(9), 670–681. https://doi.org/10.1038/nrn2698

Apps, R., Hawkes, R., Aoki, S., Bengtsson, F., Brown, A. M., Chen, G., Ebner, T. J., Isope, P., Jörntell, H., Lackey, E. P., Lawrenson, C., Lumb, B., Schonewille, M., Sillitoe, R. V., Spaeth, L., Sugihara, I., Valera, A., Voogd, J., Wylie, D. R., & Ruigrok, T. J. H. (2018). Cerebellar Modules and Their Role as Operational Cerebellar Processing Units. *Cerebellum*, *17*(5), 654–682. https://doi.org/10.1007/s12311-018-0952-3

Armbruster, M., Dulla, C. G., & Diamond, J. S. (2020). Effects of fluorescent glutamate indicators on neurotransmitter diffusion and uptake. *ELife*, *9*, 1–27. https://doi.org/10.7554/eLife.54441

Armstrong, D. M., Harvey, R. J., & Schild, R. F. (1974). Topographical localization in the olivo-cerebellar projection: An electrophysiological study in the cat. *Journal of Comparative Neurology*, *154*(3), 287–302. https://doi.org/10.1002/cne.901540305

Atluri, P. P., & Regehr, W. G. (1996). Determinants of the time course of facilitation at the granule cell to Purkinje cell synapse. *Journal of Neuroscience*. https://doi.org/10.1523/jneurosci.16-18-05661.1996

Augustin, I., Korte, S., Rickmann, M., Kretzschmar, H. A., Südhof, T. C., Herms, J. W., & Brose, N. (2001). The cerebellum-specific Munc13 isoform Munc13-3 regulates cerebellar synaptic transmission and motor learning in mice. *The Journal of Neuroscience : The Official Journal of the Society for Neuroscience*, *21*(1), 10–17. https://doi.org/21/1/10 [pii]

Aumann, T. D., Rawson, J. A., Finkelstein, D. I., & Horne, M. K. (1994). Projections from the lateral and interposed cerebellar nuclei to the thalamus of the rat: A light and electron microscopic study using single and double anterograde labelling. *The Journal of Comparative Neurology*, *349*(2), 165–181. https://doi.org/10.1002/cne.903490202

Balakrishnan, S., Dobson, K. L., Jackson, C., & Bellamy, T. C. (2014). Ectopic release of glutamate contributes to spillover at parallel fibre synapses in the cerebellum. *The Journal of Physiology*, *592*(7), 1493–1503. https://doi.org/10.1113/jphysiol.2013.267039

Bao, J., Reim, K., & Sakaba, T. (2010). Target-dependent feedforward inhibition mediated by short-term synaptic plasticity in the cerebellum. *The Journal of Neuroscience : The Official Journal of the Society for Neuroscience*, *30*(24), 8171–8179. https://doi.org/10.1523/JNEUROSCI.0276-10.2010

Barbour, B. (1993). Synaptic currents evoked in purkinje cells by stimulating individual granule cells. *Neuron*, *11*(4), 759–769. https://doi.org/10.1016/0896-6273(93)90085-6

Barbour, B., & Häusser, M. (1997). Intersynaptic diffusion of neurotransmitter. *Trends in Neurosciences*, *20*(9), 377–384. https://doi.org/10.1016/S0166-2236(96)20050-5

Barbour, B., Keller, B. U., Llano, I., & Marty, A. (1994). Prolonged presence of glutamate during excitatory synaptic transmission to cerebellar Purkinje cells. *Neuron*, *12*(6), 1331–1343. https://doi.org/10.1016/0896-6273(94)90448-0

Barmack, N. H. (2003). Central vestibular system: Vestibular nuclei and posterior cerebellum. *Brain Research Bulletin*, *60*(5–6), 511–541. https://doi.org/10.1016/S0361-9230(03)00055-8

Barnes, J. R., Mukherjee, B., Rogers, B. C., Nafar, F., Gosse, M., & Parsons, M. P. (2020). The Relationship Between Glutamate Dynamics and Activity-Dependent Synaptic Plasticity. *The Journal of Neuroscience*, *40*(14), 2793–2807. https://doi.org/10.1523/JNEUROSCI.1655-19.2020

Barri, A., Wiechert, M. T., Jazayeri, M., & DiGregorio, D. A. (2022). Synaptic basis of a sub-second representation of time. *BioRxiv*, 2022.02.16.480693. https://www.biorxiv.org/content/10.1101/2022.02.16.480693v1%0Ahttps://www.biorxiv.org/content/10.1101/2022.02.16.480693v1.abstract

Barski, J. J., Dethleffsen, K., & Meyer, M. (2000). Cre recombinase expression in cerebellar Purkinje cells. *Genesis*, *28*(3–4), 93–98. https://doi.org/10.1002/1526-968X(200011/12)28:3/4<93::AID-GENE10>3.0.CO;2-W

Bastian, A. J. (2006). Learning to predict the future: the cerebellum adapts feedforward movement control. In *Current Opinion in Neurobiology*. https://doi.org/10.1016/j.conb.2006.08.016

Bastianelli, E. (2003). Distribution of calcium-binding proteins in the cerebellum. *The Cerebellum*, *2*(4), 242–262. https://doi.org/10.1080/14734220310022289

Batchelor, A. M., & Garthwaite, J. (1997). Frequency detection and temporally dispersed synaptic signal association through a metabotropic glutamate receptor pathway. *Nature*, *385*(6611), 74–77. https://doi.org/10.1038/385074a0

Beierlein, M., Fioravante, D., & Regehr, W. G. (2007). Differential Expression of Posttetanic Potentiation and Retrograde Signaling Mediate Target-Dependent Short-Term Synaptic Plasticity. *Neuron*. https://doi.org/10.1016/j.neuron.2007.06.002

Bellamy, T. C., & Ogden, D. (2005). Short-term plasticity of Bergmann glial cell extrasynaptic currents during parallel fiber stimulation in rat cerebellum. *Glia*, *52*(4), 325–335. https://doi.org/10.1002/glia.20248

Belmeguenai, A. (2005). A Role for Protein Phosphatases 1, 2A, and 2B in Cerebellar Long-Term Potentiation. *Journal of Neuroscience*, *25*(46), 10768–10772. https://doi.org/10.1523/JNEUROSCI.2876-05.2005

Bengtsson, F., & Jörntell, H. (2009). Sensory transmission in cerebellar granule cells relies on similarly coded mossy fiber inputs. *Proceedings of the National Academy of Sciences*, *106*(7), 2389–2394. https://doi.org/10.1073/pnas.0808428106

Bergles, D. E., Dzubay, J. A., & Jahr, C. E. (1997). Glutamate transporter currents in Bergmann glial cells follow the time course of extrasynaptic glutamate. *Proceedings of the National Academy of Sciences*, *94*(26), 14821–14825. https://doi.org/10.1073/pnas.94.26.14821

Berkley, K. J., & Worden, I. G. (1978). Projections to the inferior olive of the cat I. Comparisons of input from the dorsal column nuclei, the lateral cervical nucleus, the spino-olivary pathways, the cerebral cortex and the cerebellum. *The Journal of Comparative Neurology*, *180*(2), 237–251. https://doi.org/10.1002/cne.901800204

Bernard, J.-F. (1987). Topographical organization of olivocerebellar and corticonuclear connections in the rat?An WGA-HRP study: I. Lobules IX, X, and the flocculus. *The Journal of Comparative Neurology*, *263*(2), 241–258. https://doi.org/10.1002/cne.902630207

Bharos, T. B., Kuypers, H. G. J. M., Lemon, R. N., & Muir, R. B. (1981). Divergent collaterals from deep cerebellar neurons to thalamus and tectum, and to medulla oblongata and spinal cord: Retrograde fluorescent and electrophysiological studies. *Experimental Brain Research*, *42–42*(3–4), 399–410. https://doi.org/10.1007/BF00237505

Bidoret, C., Ayon, A., Barbour, B., & Casado, M. (2009). Presynaptic NR2A-containing NMDA receptors implement a high-pass filter synaptic plasticity rule. *Proceedings of the National Academy of Sciences*, *106*(33), 14126–14131. https://doi.org/10.1073/pnas.0904284106

Binda, F., Dorgans, K., Reibel, S., Sakimura, K., Kano, M., Poulain, B., & Isope, P. (2016). Inhibition promotes long-term potentiation at cerebellar excitatory synapses. *Scientific Reports*, *6*(1), 33561. https://doi.org/10.1038/srep33561

Biró, A. A., Holderith, N. B., & Nusser, Z. (2005). Quantal size is independent of the release probability at hippocampal excitatory synapses. *The Journal of Neuroscience : The Official Journal of the Society for Neuroscience*, *25*(1), 223–232. https://doi.org/10.1523/JNEUROSCI.3688-04.2005

Blackman, A. V, Abrahamsson, T., Costa, R. P., Lalanne, T., & Sjöström, P. J. (2013). Target Cell-Specific Short-Term Plasticity in Local Circuits. *Frontiers in Synaptic Neuroscience*, *5*. https://doi.org/10.3389/fnsyn.2013.00011

Blankemore S. J, Wolpert D. M, & Frith C. D. (1998). Central cancellation of self-produced tickle sensation. *Nature Neuroscience*, *1*(7), 635–640.

Bloedel, J. R. (1973). Cerebellar afferent systems: A review. *Progress in Neurobiology*, *2*(PART 1), 3–68. https://doi.org/10.1016/0301-0082(73)90006-3

Blot, A., & Barbour, B. (2014). Ultra-rapid axon-axon ephaptic inhibition of cerebellar Purkinje cells by the pinceau. *Nature Neuroscience*, *17*(2), 289–295. https://doi.org/10.1038/nn.3624

Boegman, R. J., Parent, A., & Hawkes, R. (1988). Zonation in the rat cerebellar cortex: patches of high acetylcholinesterase activity in the granular layer are congruent with Purkinje cell compartments. *Brain Research*, *448*(2), 237–251. https://doi.org/10.1016/0006-8993(88)91261-9

Bouvier, G., Higgins, D., Spolidoro, M., Carrel, D., Mathieu, B., Léna, C., Dieudonné, S., Barbour, B., Brunel, N., & Casado, M. (2016). Burst-Dependent Bidirectional Plasticity in the Cerebellum Is Driven by Presynaptic NMDA Receptors. *Cell Reports*, *15*(1), 104–116. https://doi.org/10.1016/j.celrep.2016.03.004

Brenowitz, S. D., & Regehr, W. G. (2005). Associative Short-Term Synaptic Plasticity Mediated by Endocannabinoids. *Neuron*, *45*(3), 419–431. https://doi.org/10.1016/j.neuron.2004.12.045

Brenowitz, S. D., & Regehr, W. G. (2007). Reliability and Heterogeneity of Calcium Signaling at Single Presynaptic Boutons of Cerebellar Granule Cells. *Journal of Neuroscience*, *27*(30), 7888–7898. https://doi.org/10.1523/JNEUROSCI.1064-07.2007

Brown, I. E., & Bower, J. M. (2001). Congruence of mossy fiber and climbing fiber tactile projections in the lateral hemispheres of the rat cerebellum. *The Journal of Comparative Neurology*, *429*(1), 59–70. https://doi.org/10.1002/1096-9861(20000101)429:1<59::AID-CNE5>3.0.CO;2-3

Brown, S. P., Brenowitz, S. D., & Regehr, W. G. (2003). Brief presynaptic bursts evoke synapse-specific retrograde inhibition mediated by endogenous cannabinoids. *Nature Neuroscience*, *6*(10), 1048–1057. https://doi.org/10.1038/nn1126

Brown, S. P., Safo, P. K., & Regehr, W. G. (2004). Endocannabinoids inhibit transmission at granule cell to Purkinje cell synapses by modulating three types of presynaptic calcium channels. *Journal of Neuroscience*, *24*(24), 5623–5631. https://doi.org/10.1523/JNEUROSCI.0918-04.2004

Brown, S. T., & Raman, I. M. (2018). Sensorimotor Integration and Amplification of Reflexive Whisking by Well-Timed Spiking in the Cerebellar Corticonuclear Circuit. *Neuron*. https://doi.org/10.1016/j.neuron.2018.06.028

Büttner-Ennever, J. A. (1992). Patterns of Connectivity in the Vestibular Nuclei. *Annals of the New York Academy of Sciences*, *656*(1 Sensing and C), 363–378. https://doi.org/10.1111/j.1749-6632.1992.tb25222.x

Casado, M., Isope, P., & Ascher, P. (2002). Involvement of Presynaptic N-Methyl-D-Aspartate Receptors in Cerebellar Long-Term Depression. *Neuron*, *33*(1), 123–130. https://doi.org/10.1016/S0896-6273(01)00568-2

Cathala, L., Brickley, S., Cull-Candy, S., & Farrant, M. (2003). Maturation of EPSCs and intrinsic membrane properties enhances precision at a cerebellar synapse. *Journal of Neuroscience*, *23*(14), 6074–6085. https://doi.org/10.1523/jneurosci.23-14-06074.2003

Cayco-Gajic, N. A., Clopath, C., & Silver, R. A. (2017). Sparse synaptic connectivity is required for decorrelation and pattern separation in feedforward networks. *Nature Communications*, *8*(1), 1116. https://doi.org/10.1038/s41467-017-01109-y

Cayco-Gajic, N. A., & Silver, R. A. (2019). Re-evaluating Circuit Mechanisms Underlying Pattern Separation. *Neuron*, *101*(4), 584–602. https://doi.org/10.1016/j.neuron.2019.01.044

Cerminara, N. L., & Apps, R. (2011). Behavioural Significance of Cerebellar Modules. *The Cerebellum*, *10*(3), 484–494. https://doi.org/10.1007/s12311-010-0209-2

Cerminara, N. L., Lang, E. J., Sillitoe, R. V., & Apps, R. (2015). Redefining the cerebellar cortex as an assembly of non-uniform Purkinje cell microcircuits. *Nature Reviews Neuroscience*, *16*(2), 79–93. https://doi.org/10.1038/nrn3886

Cesana, E., Pietrajtis, K., Bidoret, C., Isope, P., D'Angelo, E., Dieudonné, S., & Forti, L. (2013). Granule cell ascending axon excitatory synapses onto Golgi cells implement a potent feedback circuit in the cerebellar granular layer. *Journal of Neuroscience*, *33*(30), 12430–12446. https://doi.org/10.1523/JNEUROSCI.4897-11.2013

Chabrol, F. P., Arenz, A., Wiechert, M. T., Margrie, T. W., & DiGregorio, D. A. (2015a). Synaptic diversity enables temporal coding of coincident multisensory inputs in single neurons. *Nature Neuroscience*, *18*(5), 718–727. https://doi.org/10.1038/nn.3974

Chabrol, F. P., Arenz, A., Wiechert, M. T., Margrie, T. W., & DiGregorio, D. A. (2015b). Synaptic diversity enables temporal coding of coincident multisensory inputs in single neurons. *Nature Neuroscience*, *18*(5), 718–727. https://doi.org/10.1038/nn.3974

Chabrol, F. P., Blot, A., & Mrsic-Flogel, T. D. (2019). Cerebellar Contribution to Preparatory Activity in Motor Neocortex. *Neuron*, *103*(3), 506-519.e4. https://doi.org/10.1016/j.neuron.2019.05.022

Chadderton, P., Margrie, T. W., & Häusser, M. (2004). Integration of quanta in cerebellar granule cells during sensory processing. *Nature*, *428*(6985), 856–860. https://doi.org/10.1038/nature02442

Chaumont, J., Guyon, N., Valera, A. M., Dugué, G. P., Popa, D., Marcaggi, P., Gautheron, V., Reibel-Foisset, S., Dieudonné, S., Stephan, A., Barrot, M., Cassel, J.-C., Dupont, J.-L., Doussau, F., Poulain, B., Selimi, F., Léna, C., & Isope, P. (2013). Clusters of cerebellar Purkinje cells control their afferent climbing fiber discharge. *Proceedings of the National Academy of Sciences*, *110*(40), 16223–16228. https://doi.org/10.1073/pnas.1302310110

Chen, C. H., Fremont, R., Arteaga-Bracho, E. E., & Khodakhah, K. (2014). Short latency cerebellar modulation of the basal ganglia. *Nature Neuroscience*, *17*(12), 1767–1775. https://doi.org/10.1038/nn.3868

Chen, S., Augustine, G. J., & Chadderton, P. (2016). The cerebellum linearly encodes whisker position during voluntary movement. *ELife*, *5*. https://doi.org/10.7554/eLife.10509

Choquet, D. (2010). Fast AMPAR trafficking for a high-frequency synaptic transmission. *European Journal of Neuroscience*. https://doi.org/10.1111/j.1460-9568.2010.07350.x

Chu, C.-P., Zhao, G.-Y., Jin, R., Zhao, S.-N., Sun, L., & Qiu, D.-L. (2014). Properties of 4 Hz stimulation-induced parallel fiber-Purkinje cell presynaptic long-term plasticity in mouse cerebellar cortex in vivo. *European Journal of Neuroscience*, *39*(10), 1624–1631. https://doi.org/10.1111/ejn.12559

Chung, H. J., Steinberg, J. P., Huganir, R. L., & Linden, D. J. (2003). Requirement of AMPA receptor GluR2 phosphorylation for cerebellar long-term depression. *Science*, *300*(5626), 1751–1755. https://doi.org/10.1126/science.1082915

Clements, J. D., Lester, R. A. J., Tong, G., Jahr, C. E., & Westbrook, G. L. (1992). The Time Course of Glutamate in the Synaptic Cleft. *Science*, *258*(5087), 1498–1501. https://doi.org/10.1126/science.1359647

Coesmans, M., Weber, J. T., De Zeeuw, C. I., & Hansel, C. (2004). Bidirectional Parallel Fiber Plasticity in the Cerebellum under Climbing Fiber Control. *Neuron*, *44*(4), 691–700. https://doi.org/10.1016/j.neuron.2004.10.031

Consalez, G. G., Goldowitz, D., Casoni, F., & Hawkes, R. (2021). Origins, Development, and Compartmentation of the Granule Cells of the Cerebellum. *Frontiers in Neural Circuits*, *14*(January), 1–23. https://doi.org/10.3389/fncir.2020.611841

Crowley, J. J., Carter, A. G., & Regehr, W. G. (2007). Fast Vesicle Replenishment and Rapid Recovery from Desensitization at a Single Synaptic Release Site. *Journal of Neuroscience*, *27*(20), 5448–5460. https://doi.org/10.1523/JNEUROSCI.1186-07.2007

Cullen, K. E., & Brooks, J. X. (2015). Neural Correlates of Sensory Prediction Errors in Monkeys: Evidence for Internal Models of Voluntary Self-Motion in the Cerebellum. *Cerebellum*, *14*(1), 31–34. https://doi.org/10.1007/s12311-014-0608-x

Cullen, K. E., Brooks, J. X., Jamali, M., Carriot, J., & Massot, C. (2011). Internal models of self-motion: Computations that suppress vestibular reafference in early vestibular processing. *Experimental Brain Research*, *210*(3–4), 377–388. https://doi.org/10.1007/s00221-011-2555-9

D'Angelo, E., & Casali, S. (2012). Seeking a unified framework for cerebellar function and dysfunction: From circuit operations to cognition. *Frontiers in Neural Circuits*, *6*(DEC), 1–23. https://doi.org/10.3389/fncir.2012.00116

de Beer, M. A., & Giepmans, B. N. G. (2020). Nanobody-Based Probes for Subcellular Protein Identification and Visualization. *Frontiers in Cellular Neuroscience*, *14*(November), 1–16. https://doi.org/10.3389/fncel.2020.573278

De Zeeuw, C. I., Hoebeek, F. E., Bosman, L. W. J., Schonewille, M., Witter, L., & Koekkoek, S. K. (2011). Spatiotemporal firing patterns in the cerebellum. *Nature Reviews Neuroscience*, *12*(6), 327–344. https://doi.org/10.1038/nrn3011

De Zeeuw, C. I., Hoogenraad, C. C., Koekkoek, S. K. E., Ruigrok, T. J. H., Galjart, N., & Simpson, J. I. (1998). Microcircuitry and function of the inferior olive. *Trends in Neurosciences*, *21*(9), 391–400. https://doi.org/10.1016/S0166-2236(98)01310-1

Delvendahl, I., Straub, I., & Hallermann, S. (2015). Dendritic patch-clamp recordings from cerebellar granule cells demonstrate electrotonic compactness. *Frontiers in Cellular Neuroscience*, *9*, 93. https://doi.org/10.3389/fncel.2015.00093

DiGregorio, D. A., Nusser, Z., & Silver, R. A. (2002). Spillover of Glutamate onto Synaptic AMPA Receptors Enhances Fast Transmission at a Cerebellar Synapse. *Neuron*, *35*(3), 521–533. https://doi.org/10.1016/S0896-6273(02)00787-0

Dittman, J., & Regehr, W. (1996). Contributions of calcium-dependent and calcium-independent mechanisms to presynaptic inhibition at a cerebellar synapse. *The Journal of Neuroscience*, *16*(5), 1623–1633. https://doi.org/10.1523/JNEUROSCI.16-05-01623.1996

Dittman, J. S., Kreitzer, A. C., & Regehr, W. G. (2000). Interplay between facilitation, depression, and residual calcium at three presynaptic terminals. *The Journal of Neuroscience : The Official Journal of the Society for Neuroscience*, *20*(4), 1374–1385.

Dobson, K. L., & Bellamy, T. C. (2015). Localization of Presynaptic Plasticity Mechanisms Enables Functional Independence of Synaptic and Ectopic Transmission in the Cerebellum. *Neural Plasticity*, *2015*, 1–11. https://doi.org/10.1155/2015/602356

Dobson, K. L., Smith, Z. H., & Bellamy, T. C. (2018). Distribution of vesicle pools in cerebellar parallel fibre terminals after depression of ectopic transmission. *PLOS ONE*, *13*(7), e0200937. https://doi.org/10.1371/journal.pone.0200937

Dorgans, K., Demais, V., Bailly, Y., Poulain, B., Isope, P., & Doussau, F. (2019). Short-term plasticity at cerebellar granule cell to molecular layer interneuron synapses expands information processing. *ELife*. https://doi.org/10.7554/eLife.41586

Doussau, F., Schmidt, H., Dorgans, K., Valera, A. M., Poulain, B., & Isope, P. (2017). Frequency-dependent mobilization of heterogeneous pools of synaptic vesicles shapes presynaptic plasticity. *ELife*, *6*(e28935), e28935. https://doi.org/10.7554/eLife.28935

Dugué, G. P., Brunel, N., Hakim, V., Schwartz, E., Chat, M., Lévesque, M., Courtemanche, R., Léna, C., & Dieudonné, S. (2009). Electrical Coupling Mediates Tunable Low-Frequency Oscillations and Resonance in the Cerebellar Golgi Cell Network. *Neuron*, *61*(1), 126–139. https://doi.org/10.1016/j.neuron.2008.11.028

Dürst, C. D., Wiegert, J. S., Schulze, C., Helassa, N., Török, K., & Oertner, T. G. (2022). Vesicular release probability sets the strength of individual Schaffer collateral synapses. *Nature Communications*, *13*(1), 6126. https://doi.org/10.1038/s41467-022-33565-6

Eccles, J. C., Ito, M., & Szentagotai, J. (1967). *The cerebellum as neuronal machine*. Springer-verlag.

Eggermann, E., Bucurenciu, I., Goswami, S. P., & Jonas, P. (2012). Nanodomain coupling between Ca2+ channels and sensors of exocytosis at fast mammalian synapses. *Nature Reviews Neuroscience*, *13*(1), 7–21. https://doi.org/10.1038/nrn3125

Falcón-Moya, Losada-Ruiz, & Rodríguez-Moreno. (2019). Kainate Receptor-Mediated Depression of Glutamate Release Involves Protein Kinase A in the Cerebellum. *International Journal of Molecular Sciences*, *20*(17), 4124. https://doi.org/10.3390/ijms20174124

Falcón-Moya, R., Losada-Ruiz, P., Sihra, T. S., & Rodríguez-Moreno, A. (2018). Cerebellar Kainate Receptor-Mediated Facilitation of Glutamate Release Requires Ca2+-Calmodulin and PKA. *Frontiers in Molecular Neuroscience*, *11*(June), 1–10. https://doi.org/10.3389/fnmol.2018.00195

Federmeier, K. D., Kleim, J. A., & Greenough, W. T. (2002). Learning-induced multiple synapse formation in rat cerebellar cortex. *Neuroscience Letters*, *332*(3), 180–184. https://doi.org/10.1016/S0304-3940(02)00759-0

Flumerfelt, B. A., Otabe, S., & Courville, J. (1973). Distinct projections to the red nucleus from the dentate and interposed nuclei in the monkey. *Brain Research*, *50*(2), 408–414. https://doi.org/10.1016/0006-8993(73)90742-7

Fourcaudot, E., Gambino, F., Casassus, G., Poulain, B., Humeau, Y., & Lüthi, A. (2009). L-type voltage-dependent Ca2+ channels mediate expression of presynaptic LTP in amygdala. *Nature Neuroscience*, *12*(9), 1093–1095. https://doi.org/10.1038/nn.2378

Frischknecht, R., Heine, M., Perrais, D., Seidenbecher, C. I., Choquet, D., & Gundelfinger, E. D. (2009). Brain extracellular matrix affects AMPA receptor lateral mobility and short-term synaptic plasticity. *Nature Neuroscience*. https://doi.org/10.1038/nn.2338

Fujita, H., Aoki, H., Ajioka, I., Yamazaki, M., Abe, M., Oh-Nishi, A., Sakimura, K., & Sugihara, I. (2014). Detailed Expression Pattern of Aldolase C (Aldoc) in the Cerebellum, Retina and Other Areas of the CNS Studied in Aldoc-Venus Knock-In Mice. *PLoS ONE*, *9*(1), e86679. https://doi.org/10.1371/journal.pone.0086679

Fujita, H., Kodama, T., & Lac, S. du. (2020). Modular output circuits of the fastigial nucleus mediate diverse motor and nonmotor functions of the cerebellar vermis. *BioRxiv*. https://doi.org/10.1101/2020.04.23.047100

Gabbott, P. L. A., Somogyi, J., Stewart, M. G., & Hamori, J. (1986). GABA-immunoreactive neurons in the rat cerebellum: A light and electron microscope study. *The Journal of Comparative Neurology*, *251*(4), 474–490. https://doi.org/10.1002/cne.902510404

Gao, Z., van Beugen, B. J., & De Zeeuw, C. I. (2012). Distributed synergistic plasticity and cerebellar learning. *Nature Reviews Neuroscience*, *13*(9), 619–635. https://doi.org/10.1038/nrn3312

Garwicz, M., Jörntell, H., & Ekerot, C.-F. (1998). Cutaneous receptive fields and topography of mossy fibres and climbing fibres projecting to cat cerebellar C3 zone. *The Journal of Physiology*, *512*(1), 277–293. https://doi.org/10.1111/j.1469-7793.1998.277bf.x

Gebre, S. A., Reeber, S. L., & Sillitoe, R. V. (2012). Parasagittal compartmentation of cerebellar mossy fibers as revealed by the patterned expression of vesicular glutamate transporters VGLUT1 and VGLUT2. *Brain Structure and Function*, *217*(2), 165–180. https://doi.org/10.1007/s00429-011-0339-4

Geurts, F. J., Timmermans, J. P., Shigemoto, R., & De Schutter, E. (2001). Morphological and neurochemical differentiation of large granular layer interneurons in the adult rat cerebellum. *Neuroscience*, *104*(2), 499–512. https://doi.org/10.1016/S0306-4522(01)00058-6

Ghajar, J., & Ivry, R. B. (2009). The predictive brain state: Asynchrony in disorders of attention? *Neuroscientist*, *15*(3), 232–242. https://doi.org/10.1177/1073858408326429

Gilmer, J. I., & Person, A. L. (2018). Theoretically Sparse, Empirically Dense: New Views on Cerebellar Granule Cells. In *Trends in Neurosciences*. https://doi.org/10.1016/j.tins.2018.09.013

Giovannucci, A., Badura, A., Deverett, B., Najafi, F., Pereira, T. D., Gao, Z., Ozden, I., Kloth, A. D., Pnevmatikakis, E., Paninski, L., De Zeeuw, C. I., Medina, J. F., & Wang, S. S. H. (2017). Cerebellar granule cells acquire a widespread predictive feedback signal during motor learning. *Nature Neuroscience*, *20*(5), 727–734. https://doi.org/10.1038/nn.4531

Glickstein, M., Strata, P., & Voogd, J. (2009). Cerebellum: history. *Neuroscience*, *162*(3), 549–559. https://doi.org/10.1016/j.neuroscience.2009.02.054

Grangeray-Vilmint, A., Valera, A. M., Kumar, A., & Isope, P. (2018). Short term plasticity combines with excitation-inhibition balance to expand cerebellar Purkinje cell dynamic range. *The Journal of Neuroscience : The Official Journal of the Society for Neuroscience*, *38*(1–15), 1–15. https://doi.org/10.1523/JNEUROSCI.3270-17.2018

Grant, G., & Xu, Q. (1988). Routes of entry into the cerebellum of spinocerebellar axons from the lower part of the spinal cord - An experimental anatomical study in the cat. *Experimental Brain Research*, *72*(3), 543–561. https://doi.org/10.1007/BF00250600

Gravel, C., Leclerc, N., Rafrafi, J., Sasseville, R., Thivierge, L., & Hawkes, R. (1987). Monoclonal antibodies reveal the global organization of the cerebellar cortex. *Journal of Neuroscience Methods*, *21*(2–4), 145–157. https://doi.org/10.1016/0165-0270(87)90112-9

Groenewegen, H. J., & Voogd, J. (1977). The parasagittal zonation within the olivocerebellar projection. I. Climbing fiber distribution in the vermis of cat cerebellum. *The Journal of Comparative Neurology*, *174*(3), 417–488. https://doi.org/10.1002/cne.901740304

Groenewegen, H. J., Voogd, J., & Freedman, S. L. (1979). The parasagittal zonation within the olivocerebellar projection. II. Climbing fiber distribution in the intermediate and hemispheric parts of cat cerebellum. *The Journal of Comparative Neurology*, *183*(3), 551–601. https://doi.org/10.1002/cne.901830307

Gruol, D. L., & Franklin, C. L. (1987). Morphological and physiological differentiation of Purkinje neurons in cultures of rat cerebellum. *The Journal of Neuroscience : The Official Journal of the Society for Neuroscience.* https://doi.org/10.1523/jneurosci.07-05-01271.1987

Guell, X., Hoche, F., & Schmahmann, J. D. (2015). Metalinguistic Deficits in Patients with Cerebellar Dysfunction: Empirical Support for the Dysmetria of Thought Theory. *Cerebellum*, *14*(1), 50–58. https://doi.org/10.1007/s12311-014-0630-z

Guo, C., Witter, L., Rudolph, S., Elliott, H. L., Ennis, K. A., & Regehr, W. G. (2016). Purkinje Cells Directly Inhibit Granule Cells in Specialized Regions of the Cerebellar Cortex. *Neuron*, *91*(6). https://doi.org/10.1016/j.neuron.2016.08.011

Guo, J., Sauerbrei, B., Cohen, J. ., Mischiati, M., Graves, A., Psianello, F., Branson, K., & Hantman, A. . (2020). Dynamics of the cortico-cerebellar loop fine-tune dexterous movement. *BioRxiv*, *637447*.

Gutierrez-Castellanos, N., Da Silva-Matos, C. M., Zhou, K., Canto, C. B., Renner, M. C., Koene, L. M. C., Ozyildirim, O., Sprengel, R., Kessels, H. W., & De Zeeuw, C. I. (2017). Motor Learning Requires Purkinje Cell Synaptic Potentiation through Activation of AMPA-Receptor Subunit GluA3. *Neuron*, *93*(2), 409–424. https://doi.org/10.1016/j.neuron.2016.11.046

Halverson, H. E., Khilkevich, A., & Mauk, M. D. (2015). Relating Cerebellar Purkinje Cell Activity to the Timing and Amplitude of Conditioned Eyelid Responses. *Journal of Neuroscience*, *35*(20), 7813–7832. https://doi.org/10.1523/JNEUROSCI.3663-14.2015

Hamann, M., Rossi, D. J., & Attwell, D. (2002). Tonic and Spillover Inhibition of Granule Cells Control Information Flow through Cerebellar Cortex. *Neuron*, *33*(4), 625–633. https://doi.org/10.1016/S0896-6273(02)00593-7

Hámori, J. (1981). Synaptic input to the axon hillock and initial segment of inhibitory interneurons in the cerebellar cortex of the rat - An electron microscopic study. *Cell and Tissue Research*, *217*(3), 553–562. https://doi.org/10.1007/BF00219363

Hao, Y., & Plested, A. J. R. (2022). Seeing glutamate at central synapses. *Journal of Neuroscience Methods*, *375*(August 2021), 109531. https://doi.org/10.1016/j.jneumeth.2022.109531

Hao, Y., Toulmé, E., König, B., Katchan, L., & Plested, A. J. (2021). Targeted Sensors for Glutamatergic Neurotransmission. *Biophysical Journal*, *120*(3), 282a. https://doi.org/10.1016/j.bpj.2020.11.1796

Harvey, R., & Napper, R. (1991). Quantitatives studies on the mammalian cerebellum. *Progress in Neurobiology*, *36*(6), 437–463. https://doi.org/10.1016/0301-0082(91)90012-P

Häusser, M., & Clark, B. A. (1997). Tonic synaptic inhibition modulates neuronal output pattern and spatiotemporal synaptic integration. *Neuron*, *19*(3), 665–678.

Hawkes, R., Colonnier, M., & Leclerc, N. (1985). Monoclonal antibodies reveal sagittal banding in the rodent cerebellar cortex. *Brain Research*, *333*(2), 359–365. https://doi.org/10.1016/0006-8993(85)91593-8

Heffley, W., Song, E. Y., Xu, Z., Taylor, B. N., Hughes, M. A., McKinney, A., Joshua, M., & Hull, C. (2018). Coordinated cerebellar climbing fiber activity signals learned sensorimotor predictions. *Nature Neuroscience*, *21*(10), 1431–1441. https://doi.org/10.1038/s41593-018-0228-8

Heine, M., Groc, L., Frischknecht, R., Béïque, J. C., Lounis, B., Rumbaugh, G., Huganir, R. L., Cognet, L., & Choquet, D. (2008). Surface mobility of postsynaptic AMPARs tunes synaptic transmission. *Science*. https://doi.org/10.1126/science.1152089

Helassa, N., Dürst, C. D., Coates, C., Kerruth, S., Arif, U., Schulze, C., Simon Wiegert, J., Geeves, M., Oertner, T. G., & Török, K. (2018). Ultrafast glutamate sensors resolve high-frequency release at Schaffer collateral synapses. *Proceedings of the National Academy of Sciences of the United States of America*. https://doi.org/10.1073/pnas.1720648115

Hesslow, G. (1994). Correspondence between climbing fibre input and motor output in eyeblink-related areas in cat cerebellar cortex. *The Journal of Physiology, 476*(2), 229–244. https://doi.org/10.1113/jphysiol.1994.sp020126

Hildebrand, M. E., Isope, P., Miyazaki, T., Nakaya, T., Garcia, E., Feltz, A., Schneider, T., Hescheler, J., Kano, M., Sakimura, K., & others. (2009). Functional coupling between mGluR1 and Cav3. 1 T-type calcium channels contributes to parallel fiber-induced fast calcium signaling within Purkinje cell dendritic spines. *The Journal of Neuroscience*, *29*(31), 9668–9682. https://doi.org/10.1523/JNEUROSCI.0362-09.2009

Hires, S. A., Zhu, Y., & Tsien, R. Y. (2008). Optical measurement of synaptic glutamate spillover and reuptake by linker optimized glutamate-sensitive fluorescent reporters. *Proceedings of the National Academy of Sciences*, *105*(11), 4411–4416. https://doi.org/10.1073/pnas.0712008105

Ho, S., Lajaunie, R., Lerat, M., Le, M., Crépel, V., Loulier, K., Livet, J., Kessler, J.-P., & Marcaggi, P. (2021). A stable proportion of Purkinje cell inputs from parallel fibers are silent during cerebellar maturation. *Proceedings of the National Academy of Sciences*, *118*(45). https://doi.org/10.1073/pnas.2024890118

Hoche, F., Guell, X., Sherman, J. C., Vangel, M. G., & Schmahmann, J. D. (2016). Cerebellar contribution to social cognition. *Annals of Neurology*, *76*(6), S1–S151. https://doi.org/10.1002/ana.24247

Holehonnur, R., Luong, J. A., Chaturvedi, D., Ho, A., Lella, S. K., Hosek, M. P., & Ploski, J. E. (2014). Adeno-associated viral serotypes produce differing titers and differentially transduce neurons within the rat basal and lateral amygdala. *BMC Neuroscience*, *15*(1), 28. https://doi.org/10.1186/1471-2202-15-28

Holtzman, T., Sivam, V., Zhao, T., Frey, O., van der Wal, P. D., de Rooij, N. F., Dalley, J. W., & Edgley, S. A. (2011). Multiple extra-synaptic spillover mechanisms regulate prolonged activity in cerebellar Golgi cell-granule cell loops. *The Journal of Physiology*, *589*(15), 3837–3854. https://doi.org/10.1113/jphysiol.2011.207167

Hosaka, M., Hammer, R. E., & Südhof, T. C. (1999). A Phospho-Switch Controls the Dynamic Association of Synapsins with Synaptic Vesicles. *Neuron*, *24*(2), 377–387. https://doi.org/10.1016/S0896-6273(00)80851-X

Houston, C. M., Diamanti, E., Diamantaki, M., Kutsarova, E., Cook, A., Sultan, F., & Brickley, S. G. (2017). Exploring the significance of morphological diversity for cerebellar granule cell excitability. *Scientific Reports*, *7*. https://doi.org/10.1038/srep46147

Huang, C.-C., Sugino, K., Shima, Y., Guo, C., Bai, S., Mensh, B. D., Nelson, S. B., & Hantman, A. W. (2013). Convergence of pontine and proprioceptive streams onto multimodal cerebellar granule cells. *ELife*, *2*. https://doi.org/10.7554/eLife.00400.001

Huang, C. C., Sugino, K., Shima, Y., Guo, C., Bai, S., Mensh, B. D., Nelson, S. B., & Hantman, A. W. (2013). Convergence of pontine and proprioceptive streams onto multimodal cerebellar granule cells. *ELife*, *2*(e00400), e00400. https://doi.org/10.7554/eLife.00400

Huang, C., Wang, L., & Huang, R. H. (2006). Cerebellar granule cell: ascending axon and parallel fiber. *European Journal of Neuroscience*, *23*(7), 1731–1737. https://doi.org/10.1111/j.1460-9568.2006.04690.x

Hull, C. (2020). Prediction signals in the cerebellum: beyond supervised motor learning. *ELife*, *9*. https://doi.org/10.7554/eLife.54073

Husson, F., Josse, J., & Pages, J. (2010). Principal component methods-hierarchical clustering-partitional clustering: why would we need to choose for visualizing data. *Applied Mathematics Department.*, 1–17.

Husson, Z., Rousseau, C. V., Broll, I., Zeilhofer, H. U., & Dieudonne, S. (2014). Differential GABAergic and Glycinergic Inputs of Inhibitory Interneurons and Purkinje Cells to Principal Cells of the Cerebellar Nuclei. *Journal of Neuroscience*, *34*(28), 9418–9431. https://doi.org/10.1523/JNEUROSCI.0401-14.2014

Ichise, T., Kano, M., Hashimoto, K., Yanagihara, D., Nakao, K., Shigemoto, R., Katsuki, M., & Aiba, A. (2000). mGluR1 in cerebellar Purkinje cells essential for long-term depression, synapse elimination, and motor coordination. *Science*. https://doi.org/10.1126/science.288.5472.1832

Ikeda, M., & Matsushita, M. (1992). Trigeminocerebellar projections to the posterior lobe in the cat, as studied by anterograde transport of wheat germ agglutinin-horseradish peroxidase. *Journal of Comparative Neurology*, *316*(2), 221–237. https://doi.org/10.1002/cne.903160207

Ishikawa, T., Shimuta, M., & Hä Usser, M. (2015). *Multimodal sensory integration in single cerebellar granule cells in vivo*. https://doi.org/10.7554/eLife.12916.001

Ishiyama, S., Schmidt, H., Cooper, B. H., Brose, N., & Eilers, J. (2014). Munc13-3 Superprimes Synaptic Vesicles at Granule Cell-to-Basket Cell Synapses in the Mouse Cerebellum. *Journal of Neuroscience*, *34*(44), 14687–14696. https://doi.org/10.1523/JNEUROSCI.2060-14.2014

Isope, P., & Barbour, B. (2002). Properties of unitary granule cell→Purkinje cell synapses in adult rat cerebellar slices. *Journal of Neuroscience*.

Isope, P., Hildebrand, M. E., & Snutch, T. P. (2010). Contributions of T-Type Voltage-Gated Calcium Channels to Postsynaptic Calcium Signaling within Purkinje Neurons. *The Cerebellum*, *11*(3), 651–665. https://doi.org/10.1007/s12311-010-0195-4

Ito, M. (2001). Cerebellar Long-Term Depression: Characterization, Signal Transduction, and Functional Roles. *Physiological Reviews*, *81*(3), 1143–1195. https://doi.org/10.1152/physrev.2001.81.3.1143

Ito, M. (2006). Cerebellar circuitry as a neuronal machine. *Progress in Neurobiology*, *78*(3–5), 272–303. https://doi.org/10.1016/j.pneurobio.2006.02.006

Ito, M., & Kano, M. (1982). Long-lasting depression of parallel fiber-Purkinje cell transmission induced by conjunctive stimulation of parallel fibers and climbing fibers in the cerebellar cortex. *Neuroscience Letters*, *33*(3), 253–258. https://doi.org/10.1016/0304-3940(82)90380-9

Ito, M., Yoshida, M., & Obata, K. (1964). Monosynaptic inhibition of the intracerebellar nuclei induced from the cerebellar cortex. *Experientia*, *20*(10), 575–576. https://doi.org/10.1007/BF02150304

Jackman, S. L., & Regehr, W. G. (2017). The Mechanisms and Functions of Synaptic Facilitation. In *Neuron* (Vol. 94, Issue 3, pp. 447–464). https://doi.org/10.1016/j.neuron.2017.02.047

Jackman, S. L., Turecek, J., Belinsky, J. E., & Regehr, W. G. (2016). The calcium sensor synaptotagmin 7 is required for synaptic facilitation. *Nature*, *529*(7584), 88–91. https://doi.org/10.1038/nature16507

Jacobs, B., Johnson, N. L., Wahl, D., Schall, M., Maseko, B. C., Lewandowski, A., Raghanti, M. A., Wicinski, B., Butti, C., Hopkins, W. D., Bertelsen, M. F., Walsh, T., Roberts, J. R., Reep, R. L., Hof, P. R., Sherwood, C. C., & Manger, P. R. (2014). Comparative neuronal morphology of the cerebellar cortex in afrotherians, carnivores, cetartiodactyls, and primates. *Frontiers in Neuroanatomy*, *8*(APR). https://doi.org/10.3389/fnana.2014.00024

Jansen, J., & Brodal, A. (1940). Experimental studies on the intrinsic fibers of the cerebellum. II. The cortico-nuclear projection. *The Journal of Comparative Neurology*, *73*(2), 267–321. https://doi.org/10.1002/cne.900730204

Javier F. Medina, William L. Nores, & Michael D. Mauk. (2002). Inhibition of climbing fibres is a signal for the extinctin of conditioned eyelid responses. *Nature*, *416*(6878), 330–333.

Jelitai, M., Puggioni, P., Ishikawa, T., Rinaldi, A., & Duguid, I. (2016). Dendritic excitation-inhibition balance shapes cerebellar output during motor behaviour. *Nature Communications*, *7*, 13722. https://doi.org/10.1038/ncomms13722

Jensen, T. P., Zheng, K., Cole, N., Marvin, J. S., Looger, L. L., & Rusakov, D. A. (2019). Multiplex imaging relates quantal glutamate release to presynaptic Ca2+ homeostasis at multiple synapses in situ. *Nature Communications*, *10*(1), 1414. https://doi.org/10.1038/s41467-019-09216-8

Jensen, T. P., Zheng, K., Tyurikova, O., Reynolds, J. P., & Rusakov, D. A. (2017). Monitoring single-synapse glutamate release and presynaptic calcium concentration in organised brain tissue. *Cell Calcium*, *64*, 102–108. https://doi.org/10.1016/j.ceca.2017.03.007

Jirenhed, D.-A., Rasmussen, A., Johansson, F., & Hesslow, G. (2017). Learned response sequences in cerebellar Purkinje cells. *Proceedings of the National Academy of Sciences*, *114*(23), 6127–6132. https://doi.org/10.1073/pnas.1621132114

Jörntell, H., & Ekerot, C.-F. (2002). Reciprocal Bidirectional Plasticity of Parallel Fiber Receptive Fields in Cerebellar Purkinje Cells and Their Afferent Interneurons. *Neuron*, *34*(5), 797–806. https://doi.org/10.1016/S0896-6273(02)00713-4

Jörntell, H., & Ekerot, C.-F. (2003). Receptive Field Plasticity Profoundly Alters the Cutaneous Parallel Fiber Synaptic Input to Cerebellar Interneurons In Vivo. *The Journal of Neuroscience*, *23*(29), 9620–9631. https://doi.org/10.1523/JNEUROSCI.23-29-09620.2003

Jörntell, H., & Ekerot, C.-F. (2006a). Properties of somatosensory synaptic integration in cerebellar granule cells in vivo. *The Journal of Neuroscience : The Official Journal of the Society for Neuroscience*, *26*(45), 11786–11797. https://doi.org/10.1523/JNEUROSCI.2939-06.2006

Jörntell, H., & Ekerot, C. F. (2006b). Properties of somatosensory synaptic integration in cerebellar granule cells in vivo. *Journal of Neuroscience*. https://doi.org/10.1523/JNEUROSCI.2939-06.2006

Jörntell, H., & Hansel, C. (2006). Synaptic Memories Upside Down: Bidirectional Plasticity at Cerebellar Parallel Fiber-Purkinje Cell Synapses. *Neuron*, *52*(2), 227–238. https://doi.org/10.1016/j.neuron.2006.09.032

Justus, T., Ravizza, S. M., Fiez, J. A., & Ivry, R. B. (2005). Reduced phonological similarity effects in patients with damage to the cerebellum. *Brain and Language*, *95*(2), 304–318. https://doi.org/10.1016/j.bandl.2005.02.001

Kanichay, R. T., & Silver, R. A. (2008). Synaptic and Cellular Properties of the Feedforward Inhibitory Circuit within the Input Layer of the Cerebellar Cortex. *Journal of Neuroscience*, *28*(36), 8955–8967. https://doi.org/10.1523/JNEUROSCI.5469-07.2008

Kelly, E., Meng, F., Fujita, H., Morgado, F., Kazemi, Y., Rice, L. C., Ren, C., Escamilla, C. O., Gibson, J. M., Sajadi, S., Pendry, R. J., Tan, T., Ellegood, J., Albert Basson, M., Blakely, R. D., Dindot, S. V., Golzio, C., Hahn, M. K., Katsanis, N., … Tsai, P. T. (2020). Regulation of autism-relevant behaviors by cerebellar–prefrontal cortical circuits. *Nature Neuroscience*, *23*(9), 1102–1110. https://doi.org/10.1038/s41593-020-0665-z

Kim, J. H., Ebner, T. J., & Bloedel, J. R. (1986). Comparison of response properties of dorsal and ventral spinocerebellar tract neurons to a physiological stimulus. *Brain Research*, *369*(1–2), 125–135. https://doi.org/10.1016/0006-8993(86)90520-2

Kim, Y., Lee, U., Choi, C., & Chang, S. (2020). Release Mode Dynamically Regulates the RRP Refilling Mechanism at Individual Hippocampal Synapses. *The Journal of Neuroscience*, *40*(44), 8426–8437. https://doi.org/10.1523/JNEUROSCI.3029-19.2020

Kitamura, T., & Yamada, J. (1989). Spinocerebellar Tract Neurons with Axons Passing through the Inferior or Superior Cerebellar Peduncles. *Brain, Behavior and Evolution*, *34*(3), 133–142. https://doi.org/10.1159/000116499

Knogler, L. D., Markov, D. A., Dragomir, E. I., Štih, V., & Portugues, R. (2017). Sensorimotor Representations in Cerebellar Granule Cells in Larval Zebrafish Are Dense, Spatially Organized, and Non-temporally Patterned. *Current Biology*, *27*(9), 1288–1302. https://doi.org/10.1016/j.cub.2017.03.029

Kotchabhakdi, N., & Walberg, F. (1978). Cerebellar afferent projections from the vestibular nuclei in the cat: An experimental study with the method of retrograde axonal transport of horseradish peroxidase. *Experimental Brain Research*, *31*(4), 591–604. https://doi.org/10.1007/BF00239814

Kozareva, V., Martin, C., Osorno, T., Rudolph, S., Guo, C., Vanderburg, C., Nadaf, N., Regev, A., Regehr, W. G., & Macosko, E. (2021). A transcriptomic atlas of mouse cerebellar cortex comprehensively defines cell types. *Nature*, *598*(7879), 214–219. https://doi.org/10.1038/s41586-021-03220-z

Kreitzer, A. C., & Regehr, W. G. (2000). Modulation of Transmission during Trains at a Cerebellar Synapse. *The Journal of Neuroscience*, *20*(4), 1348–1357. https://doi.org/10.1523/JNEUROSCI.20-04-01348.2000

Kumamoto, T., Maurinot, F., Barry-Martinet, R., Vaslin, C., Vandormael-Pournin, S., Le, M., Lerat, M., Niculescu, D., Cohen-Tannoudji, M., Rebsam, A., Loulier, K., Nedelec, S., Tozer, S., & Livet, J. (2020). Direct Readout of Neural Stem Cell Transgenesis with an Integration-Coupled Gene Expression Switch. *Neuron*, *107*(4), 617-630.e6. https://doi.org/10.1016/j.neuron.2020.05.038

Kushiro, K., Zakir, M., Sato, H., Ono, S., Ogawa, Y., Meng, H., Zhang, X., & Uchino, Y. (2000). *Saccular and utricular inputs to single vestibular neurons in cats*. *131*, 406–415.

Lainé, J., & Axelrad, H. (1994). The candelabrum cell: A new interneuron in the cerebellar cortex. *Journal of Comparative Neurology*, *339*(2), 159–173. https://doi.org/10.1002/cne.903390202

Lanore, F., Cayco-Gajic, N. A., Gurnani, H., Coyle, D., & Silver, R. A. (2021). Cerebellar granule cell axons support high-dimensional representations. *Nature Neuroscience*, *24*(8), 1142–1150. https://doi.org/10.1038/s41593-021-00873-x

Larramendi, L. M. H., & Lemkey-Johnston, N. (1970). The distribution of recurrent purkinje collateral synapses in the mouse cerebellar cortex: An electron microscopic study. *The Journal of Comparative Neurology*, *138*(4), 451–482. https://doi.org/10.1002/cne.901380405

Latham, A., & Paul, D. H. (1971). Spontaneous activity of cerebellar Purkinje cells and their responses to impulses in climbing fibres. *The Journal of Physiology*. https://doi.org/10.1113/jphysiol.1971.sp009373

Lee, S., Yoon, B.-E., Berglund, K., Oh, S.-J., Park, H., Shin, H.-S., Augustine, G. J., & Lee, C. J. (2010). Channel-Mediated Tonic GABA Release from Glia. *Science*, *330*(6005), 790–796. https://doi.org/10.1126/science.1184334

Lemkey-Johnston, N., & Larramendi, L. M. H. (1968). Types and distribution of synapses upon basket and stellate cells of the mouse cerebellum: An electron microscopic study. *The Journal of Comparative Neurology*, *134*(1), 73–111. https://doi.org/10.1002/cne.901340106

Leopold, A. V., Shcherbakova, D. M., & Verkhusha, V. V. (2019). Fluorescent Biosensors for Neurotransmission and Neuromodulation: Engineering and Applications. *Frontiers in Cellular Neuroscience*, *13*(October). https://doi.org/10.3389/fncel.2019.00474

Lev-Ram, V., Makings, L. R., Keitz, P. F., Kao, J. P. Y., & Tsien, R. Y. (1995). Long-term depression in cerebellar Purkinje neurons results from coincidence of nitric oxide and depolarization-induced Ca2+ transients. *Neuron*, *15*(2), 407–415. https://doi.org/10.1016/0896-6273(95)90044-6

Lev-Ram, V., Wong, S. T., Storm, D. R., & Tsien, R. Y. (2002). A new form of cerebellar long-term potentiation is postsynaptic and depends on nitric oxide but not cAMP. *Proceedings of the National Academy of Sciences*, *99*(12), 8389–8393. https://doi.org/10.1073/pnas.122206399

Linden, D. J., & Ahn, S. (1999). Activation of Presynaptic cAMP-Dependent Protein Kinase Is Required for Induction of Cerebellar Long-Term Potentiation. *The Journal of Neuroscience*, *19*(23), 10221–10227. https://doi.org/10.1523/JNEUROSCI.19-23-10221.1999

Lisberger, S. G., Miles, F. A., & Zee, D. S. (1984). Signals used to compute errors in monkey vestibuloocular reflex: Possible role of flocculus. *Journal of Neurophysiology*, *52*(6), 1140–1153. https://doi.org/10.1152/jn.1984.52.6.1140

Llinas, R., Baker, R., & Sotelo, C. (1974). Electrotonic coupling between neurons in cat inferior olive. *Journal of Neurophysiology*, *37*(3), 560–571. https://doi.org/10.1152/jn.1974.37.3.560

Llinás, R., & Sasaki, K. (1989). The Functional Organization of the Olivo-Cerebellar System as Examined by Multiple Purkinje Cell Recordings. *European Journal of Neuroscience*, *1*(6), 587–602. https://doi.org/10.1111/j.1460-9568.1989.tb00365.x

Madisen, L., Zwingman, T. A., Sunkin, S. M., Oh, S. W., Zariwala, H. A., Gu, H., Ng, L. L., Palmiter, R. D., Hawrylycz, M. J., Jones, A. R., Lein, E. S., & Zeng, H. (2010). A robust and high-throughput Cre reporting and characterization system for the whole mouse brain. *Nature Neuroscience*, *13*(1), 133–140. https://doi.org/10.1038/nn.2467

Maex, R., & Schutter, E. De. (1998). Synchronization of Golgi and Granule Cell Firing in a Detailed Network Model of the Cerebellar Granule Cell Layer. *Journal of Neurophysiology*, *80*(5), 2521–2537. https://doi.org/10.1152/jn.1998.80.5.2521

Manni, E., & Petrosini, L. (1997). Luciani's work on the cerebellum a century later. *Trends in Neurosciences*, *20*(3), 112–116. https://doi.org/10.1016/S0166-2236(96)10077-1

Marr, D. (1969a). A theory of cerebellar cortex. *The Journal of Physiology*. https://doi.org/10.1113/jphysiol.1969.sp008820

Marr, D. (1969b). A theory of cerebellar cortex. *The Journal of Physiology*, *202*(2), 437–470. http://www.ncbi.nlm.nih.gov/pubmed/5784296

Marvin, J. S., Borghuis, B. G., Tian, L., Cichon, J., Harnett, M. T., Akerboom, J., Gordus, A., Renninger, S. L., Chen, T. W., Bargmann, C. I., Orger, M. B., Schreiter, E. R., Demb, J. B., Gan, W. B., Hires, S. A., & Looger, L. L. (2013). An optimized fluorescent probe for visualizing glutamate neurotransmission. *Nature Methods*. https://doi.org/10.1038/nmeth.2333

Marvin, J. S., Scholl, B., Wilson, D. E., Podgorski, K., Kazemipour, A., Müller, J. A., Schoch, S., Quiroz, F. J. U., Rebola, N., Bao, H., Little, J. P., Tkachuk, A. N., Cai, E., Hantman, A. W., Wang, S. S. H., DePiero, V. J., Borghuis, B. G., Chapman, E. R., Dietrich, D., … Looger, L. L. (2018). Stability, affinity, and chromatic variants of the glutamate sensor iGluSnFR. *Nature Methods*, *15*(11), 936–939. https://doi.org/10.1038/s41592-018-0171-3

Marvin, J. S., Shimoda, Y., Magloire, V., Leite, M., Kawashima, T., Jensen, T. P., Kolb, I., Knott, E. L., Novak, O., Podgorski, K., Leidenheimer, N. J., Rusakov, D. A., Ahrens, M. B., Kullmann, D. M., & Looger, L. L. (2019). A genetically encoded fluorescent sensor for in vivo imaging of GABA. *Nature Methods*, *16*(8), 763–770. https://doi.org/10.1038/s41592-019-0471-2

Matsui, K., Jahr, Craig E, & Rubio, M. E. (2005). High-Concentration Rapid Transients of Glutamate Mediate Neural-Glial Communication via Ectopic Release. *Journal of Neuroscience*, *25*(33), 7538–7547. https://doi.org/10.1523/JNEUROSCI.1927-05.2005

Matsushita, M., & Ikeda, M. (1980). Spinocerebellar projections to the vermis of the posterior lobe and the paramedian lobule in the cat, as studied by retrograde transport of horseradish peroxidase. *Journal of Comparative Neurology*, *192*(1), 143–162. https://doi.org/10.1002/cne.901920110

Mauk, M. D., & Ruiz, B. P. (1992). Learning-Dependent Timing of Pavlovian Eyelid Responses: Differential Conditioning Using Multiple Interstimulus Intervals. *Behavioral Neuroscience*, *106*(4), 666–681. https://doi.org/10.1037/0735-7044.106.4.666

Meera, P., Pulst, S. M., & Otis, T. S. (2016). Cellular and circuit mechanisms underlying spinocerebellar ataxias. *The Journal of Physiology*, *594*(16), 4653–4660. https://doi.org/10.1113/JP271897

Mintz, I. M., Sabatini, B. L., & Regehr, W. G. (1995). Calcium control of transmitter release at a cerebellar synapse. *Neuron*, *15*(3), 675–688. https://doi.org/10.1016/0896-6273(95)90155-8

Mitchell, S. J., & Silver, R. A. (2000). GABA spillover from single inhibitory axons suppresses low-frequency excitatory transmission at the cerebellar glomerulus. *Journal of Neuroscience*, *20*(23), 8651–8658. https://doi.org/10.1523/jneurosci.20-23-08651.2000

Mittmann, W., Koch, U., & Häusser, M. (2005). Feed-forward inhibition shapes the spike output of cerebellar Purkinje cells. *The Journal of Physiology*, *563*(2), 369–378. https://doi.org/10.1113/jphysiol.2004.075028

Morizawa, Y. M., Matsumoto, M., Nakashima, Y., Endo, N., Aida, T., Ishikane, H., Beppu, K., Moritoh, S., Inada, H., Osumi, N., Shigetomi, E., Koizumi, S., Yang, G., Hirai, H., Tanaka, K., Tanaka, K. F., Ohno, N., Fukazawa, Y., & Matsui, K. (2022). Synaptic pruning through glial synapse engulfment upon motor learning. *Nature Neuroscience*, *25*(11), 1458–1469. https://doi.org/10.1038/s41593-022-01184-5

Moulder, K. L., & Mennerick, S. (2006). Synaptic Vesicles: Turning Reluctance Into Action. *The Neuroscientist*, *12*(1), 11–15. https://doi.org/10.1177/1073858405282431

Muller, M., Goutman, J. D., Kochubey, O., & Schneggenburger, R. (2010). Interaction between Facilitation and Depression at a Large CNS Synapse Reveals Mechanisms of Short-Term Plasticity. *Journal of Neuroscience*, *30*(6), 2007–2016. https://doi.org/10.1523/JNEUROSCI.4378-09.2010

Myoga, M. H., & Regehr, W. G. (2011). Calcium Microdomains Near R-Type Calcium Channels Control the Induction of Presynaptic Long-Term Potentiation at Parallel Fiber to Purkinje Cell Synapses. *Journal of Neuroscience*, *31*(14), 5235–5243. https://doi.org/10.1523/JNEUROSCI.5252-10.2011

Nagao, S. (2004). Pontine nuclei-mediated cerebello-cerebral interactions and its functional role. *Cerebellum*, *3*(1), 11–15. https://doi.org/10.1080/14734220310012181

Najac, M., & Raman, I. M. (2015). Integration of Purkinje cell inhibition by cerebellar Nucleo-Olivary neurons. *Journal of Neuroscience*. https://doi.org/10.1523/JNEUROSCI.3583-14.2015

Najac, M., & Raman, I. M. (2017). Synaptic excitation by climbing fibre collaterals in the cerebellar nuclei of juvenile and adult mice. *Journal of Physiology*. https://doi.org/10.1113/JP274598

Namiki, S., Sakamoto, H., Iinuma, S., Iino, M., & Hirose, K. (2007). Optical glutamate sensor for spatiotemporal analysis of synaptic transmission. *European Journal of Neuroscience*, *25*(8), 2249–2259. https://doi.org/10.1111/j.1460-9568.2007.05511.x

Napper, R. M. A., & Harvey, R. J. (1988a). Quantitative study of the Purkinje cell dendritic spines in the rat cerebellum. *Journal of Comparative Neurology*, *274*(2), 158–167. https://doi.org/10.1002/cne.902740203

Napper, R. M. A., & Harvey, R. J. (1988b). Number of parallel fiber synapses on an individual Purkinje cell in the cerebellum of the rat. *The Journal of Comparative Neurology*, *274*(2), 168–177. https://doi.org/10.1002/cne.902740204

Nedelescu, H., & Abdelhack, M. (2013). Comparative Morphology of Dendritic Arbors in Populations of Purkinje Cells in Mouse Sulcus and Apex. *Neural Plasticity*, *2013*, 1–12. https://doi.org/10.1155/2013/948587

Nedelescu, H., Abdelhack, M., & Pritchard, A. T. (2018). Regional differences in Purkinje cell morphology in the cerebellar vermis of male mice. *Journal of Neuroscience Research*, *96*(9), 1476–1489. https://doi.org/10.1002/jnr.24206

Ohmae, S., & Medina, J. F. (2015). Climbing fibers encode a temporal-difference prediction error during cerebellar learning in mice. *Nature Neuroscience*, *18*(12), 1798–1803. https://doi.org/10.1038/nn.4167

Okubo, Y., Sekiya, H., Namiki, S., Sakamoto, H., Iinuma, S., Yamasaki, M., Watanabe, M., Hirose, K., & Iino, M. (2010). Imaging extrasynaptic glutamate dynamics in the brain. *Proceedings of the National Academy of Sciences*, *107*(14), 6526–6531. https://doi.org/10.1073/pnas.0913154107

Okumoto, S., Looger, L. L., Micheva, K. D., Reimer, R. J., Smith, S. J., & Frommer, W. B. (2005). Detection of glutamate release from neurons by genetically encoded surface-displayed FRET nanosensors. *Proceedings of the National Academy of Sciences*, *102*(24), 8740–8745. https://doi.org/10.1073/pnas.0503274102

Ono, S., Kushiro, K., Zakir, M., Meng, H., Sato, H., & Uchino, Y. (2000). Properties of utricular and saccular nerve-activated vestibulocerebellar neurons in cats cats. *Experimental Brain Research*, *134*(1), 1–8. https://doi.org/10.1007/s002210000424

Opazo, P., Labrecque, S., Tigaret, C. M., Frouin, A., Wiseman, P. W., De Koninck, P., & Choquet, D. (2010). CaMKII triggers the diffusional trapping of surface AMPARs through phosphorylation of stargazin. *Neuron*. https://doi.org/10.1016/j.neuron.2010.06.007

Oscarsson, O. (1979). Functional units of the cerebellum - sagittal zones and microzones. *Trends in Neurosciences*, *2*(June), 143–145. https://doi.org/10.1016/0166-2236(79)90057-2

Osorno, T., Rudolph, S., Nguyen, T., Kozareva, V., Nadaf, N. M., Norton, A., Macosko, E. Z., Lee, W. C. A., & Regehr, W. G. (2022). Candelabrum cells are ubiquitous cerebellar cortex interneurons with specialized circuit properties. *Nature Neuroscience*, *25*(6), 702–713. https://doi.org/10.1038/s41593-022-01057-x

Özcan, O. O., Wang, X., Binda, F., Dorgans, K., De Zeeuw, C. I., Gao, Z., Aertsen, A., Kumar, A., & Isope, P. (2020). Differential Coding Strategies in Glutamatergic and GABAergic Neurons in the Medial Cerebellar Nucleus. *The Journal of Neuroscience*, *40*(1), 159–170. https://doi.org/10.1523/JNEUROSCI.0806-19.2019

Palay, S. L., & Chan-Palay, V. (1974). Cerebellar Cortex. In *Neurosurgery* (Vol. 2, Issue 1). Springer Berlin Heidelberg. https://doi.org/10.1007/978-3-642-65581-4

Patel, V. R., & Zee, D. S. (2015). The cerebellum in eye movement control: Nystagmus, coordinate frames and disconjugacy. *Eye (Basingstoke)*, *29*(2), 191–195. https://doi.org/10.1038/eye.2014.271

Pédelacq, J.-D., Cabantous, S., Tran, T., Terwilliger, T. C., & Waldo, G. S. (2006). Engineering and characterization of a superfolder green fluorescent protein. *Nature Biotechnology*, *24*(1), 79–88. https://doi.org/10.1038/nbt1172

Perrett, S. P., Ruiz, B. P., & Mauk, M. D. (1993). Cerebellar cortex lesions disrupt learning-dependent timing of conditioned eyelid responses. *Journal of Neuroscience*, *13*(4), 1708–1718. https://doi.org/10.1523/jneurosci.13-04-01708.1993

Person, A. L., & Raman, I. M. (2012). Purkinje neuron synchrony elicits time-locked spiking in the cerebellar nuclei. *Nature*. https://doi.org/10.1038/nature10732

Pichitpornchai, C., Rawson, J. A., & Rees, S. (1994). Morphology of parallel fibres in the cerebellar cortex of the rat: An experimental light and electron microscopic study with biocytin. *The Journal of Comparative Neurology*, *342*(2), 206–220. https://doi.org/10.1002/cne.903420205

Piochon, C., Levenes, C., Ohtsuki, G., & Hansel, C. (2010). Purkinje Cell NMDA Receptors Assume a Key Role in Synaptic Gain Control in the Mature Cerebellum. *Journal of Neuroscience*, *30*(45), 15330–15335. https://doi.org/10.1523/JNEUROSCI.4344-10.2010

Piochon, C., Titley, H. K., Simmons, D. H., Grasselli, G., Elgersma, Y., & Hansel, C. (2016). Calcium threshold shift enables frequency-independent control of plasticity by an instructive signal. *Proceedings of the National Academy of Sciences*, 201613897. https://doi.org/10.1073/pnas.1613897113

Powell, K., Mathy, A., Duguid, I., & Häusser, M. (2015). Synaptic representation of locomotion in single cerebellar granule cells. *ELife*, *4*. https://doi.org/10.7554/eLife.07290

Qiu, D. -l., & Knopfel, T. (2007). An NMDA Receptor/Nitric Oxide Cascade in Presynaptic Parallel Fiber-Purkinje Neuron Long-Term Potentiation. *Journal of Neuroscience*, *27*(13), 3408–3415. https://doi.org/10.1523/JNEUROSCI.4831-06.2007

Qiu, D. L., & Knöpfel, T. (2009). Presynaptically expressed long-term depression at cerebellar parallel fiber synapses. *Pflugers Archiv European Journal of Physiology*, *457*(4), 865–875. https://doi.org/10.1007/s00424-008-0555-9

Quy, P. N., Fujita, H., Sakamoto, Y., Na, J., & Sugihara, I. (2011). Projection patterns of single mossy fiber axons originating from the dorsal column nuclei mapped on the aldolase C compartments in the rat cerebellar cortex. *Journal of Comparative Neurology*, *519*(5), 874–899. https://doi.org/10.1002/cne.22555

Rancz, E. A., & Häusser, M. (2006). Dendritic calcium spikes are tunable triggers of cannabinoid release and short-term synaptic plasticity in cerebellar Purkinje neurons. *The Journal of Neuroscience : The Official Journal of the Society for Neuroscience*, *26*(20), 5428–5437. https://doi.org/10.1523/JNEUROSCI.5284-05.2006

Rancz, E. A., Ishikawa, T., Duguid, I., Chadderton, P., Mahon, S., & Häusser, M. (2007). High-fidelity transmission of sensory information by single cerebellar mossy fibre boutons. *Nature*, *450*(7173), 1245–1248. https://doi.org/10.1038/nature05995

Raymond, J. L., & Medina, J. F. (2018). Computational Principles of Supervised Learning in the Cerebellum. *Annual Review of Neuroscience*, *41*(1), 233–253. https://doi.org/10.1146/annurev-neuro-080317-061948

Rebola, N., Reva, M., Kirizs, T., Szoboszlay, M., Lőrincz, A., Moneron, G., Nusser, Z., & DiGregorio, D. A. (2019). Distinct Nanoscale Calcium Channel and Synaptic Vesicle Topographies Contribute to the Diversity of Synaptic Function. *Neuron*, *104*(4), 693–710.e9. https://doi.org/10.1016/j.neuron.2019.08.014

Résibois, A., & Rogers, J. H. (1992). Calretinin in rat brain: An immunohistochemical study. *Neuroscience*, *46*(1), 101–134. https://doi.org/10.1016/0306-4522(92)90012-Q

Rieubland, S., Roth, A., & Häusser, M. (2014). Structured Connectivity in Cerebellar Inhibitory Networks. *Neuron*, *81*(4), 913–929. https://doi.org/10.1016/j.neuron.2013.12.029

Riquelme, R., Miralles, C. P., & De Blas, A. L. (2002). Bergmann Glia GABA A Receptors Concentrate on the Glial Processes That Wrap Inhibitory Synapses. *The Journal of Neuroscience*, *22*(24), 10720–10730. https://doi.org/10.1523/JNEUROSCI.22-24-10720.2002

Rochefort, C., Arabo, A., André, M., Poucet, B., Save, E., & Rondi-Reig, L. (2011). Cerebellum shapes hippocampal spatial code. *Science*, *334*(6054), 385–389. https://doi.org/10.1126/science.1207403

Rose, P. K., Wainwright, K., & Neuber-Hess, M. (1992). Connections from the lateral vestibular nucleus to the upper cervical spinal cord of the cat: A study with the anterograde tracer PHA-L. *The Journal of Comparative Neurology*, *321*(2), 312–324. https://doi.org/10.1002/cne.903210210

Rosenblatt, F. (1958). The perceptron: A probabilistic model for information storage and organization in the brain. *Psychological Review*, *65*(6), 386–408. https://doi.org/10.1037/h0042519

Ruigrok, T. J. H. (1997). Cerebellar nuclei: the olivary connection. In *Progress in Brain Research* (Vol. 114, pp. 167–192). https://doi.org/10.1016/S0079-6123(08)63364-6

Ruigrok, T. J. H. (2011). Ins and outs of cerebellar modules. *Cerebellum (London, England)*, *10*(3), 464–474. https://doi.org/10.1007/s12311-010-0164-y

Sabatini, B. L., & Tian, L. (2020). Imaging Neurotransmitter and Neuromodulator Dynamics In Vivo with Genetically Encoded Indicators. *Neuron*, *108*(1), 17–32. https://doi.org/10.1016/j.neuron.2020.09.036

Salin, P. A., Malenka, R. C., & Nicoll, R. A. (1996). Cyclic AMP mediates a presynaptic form of LTP at cerebellar parallel fiber synapses. *Neuron*. https://doi.org/10.1016/S0896-6273(00)80099-9

Schmidt, H., Brachtendorf, S., Arendt, O., Hallermann, S., Ishiyama, S., Bornschein, G., Gall, D., Schiffmann, S. N., Heckmann, M., & Eilers, J. (2013). Nanodomain Coupling at an Excitatory Cortical Synapse. *Current Biology*, *23*(3), 244–249. https://doi.org/10.1016/j.cub.2012.12.007

Schneggenburger, R., Han, Y., & Kochubey, O. (2012). Ca2+ channels and transmitter release at the active zone. *Cell Calcium*, *52*(3–4), 199–207. https://doi.org/10.1016/j.ceca.2012.04.011

Schonewille, M., Belmeguenai, A., Koekkoek, S. K., Houtman, S. H., Boele, H. J., van Beugen, B. J., Gao, Z., Badura, A., Ohtsuki, G., Amerika, W. E., Hosy, E., Hoebeek, F. E., Elgersma, Y., Hansel, C., & De Zeeuw, C. I. (2010). Purkinje Cell-Specific Knockout of the Protein Phosphatase PP2B Impairs Potentiation and Cerebellar Motor Learning. *Neuron*, *67*(4), 618–628. https://doi.org/10.1016/j.neuron.2010.07.009

Schonewille, M., Gao, Z., Boele, H.-J., Vinueza Veloz, M. F., Amerika, W. E., Šimek, A. A. M., De Jeu, M. T., Steinberg, J. P., Takamiya, K., Hoebeek, F. E., Linden, D. J., Huganir, R. L., & De Zeeuw, C. I. (2011). Reevaluating the Role of LTD in Cerebellar Motor Learning. *Neuron*, *70*(1), 43–50. https://doi.org/10.1016/j.neuron.2011.02.044

Schonewille, M., Girasole, A. E., Rostaing, P., Mailhes-Hamon, C., Ayon, A., Nelson, A. B., Triller, A., Casado, M., De Zeeuw, C. I., & Bouvier, G. (2021). NMDARs in granule cells contribute to parallel fiber–Purkinje cell synaptic plasticity and motor learning. *Proceedings of the National Academy of Sciences*, *118*(37), 1–9. https://doi.org/10.1073/pnas.2102635118

Scott, T. G. (1963). A unique pattern of localization within the cerebellum [34]. *Nature*, *200*(4908), 793. https://doi.org/10.1038/200793a0

Serapide, M. F., Pantó, M. R., Parenti, R., Zappalá, A., & Cicirata, F. (2001). Multiple zonal projections of the basilar pontine nuclei to the cerebellar cortex of the rat. *Journal of Comparative Neurology*, *430*(4), 471–484. https://doi.org/10.1002/1096-9861(20010219)430:4<471::AID-CNE1044>3.0.CO;2-G

Shambes, G. M., Gibson, J. M., & Welker, W. (1978). Fractured Somatotopy in Granule Cell Tactile Areas of Rat Cerebellar Hemispheres Revealed by Micromapping; pp. 94–105. *Brain, Behavior and Evolution*, *15*(2), 94–105. https://doi.org/10.1159/000123774

Shidara, M., Kawano, K., Gomi, H., & Kawato, M. (1993). Inverse-dynamics model eye movement control by Purkinj (1993). Inverse-dynamics model eye movement control by Purkinje cells in the cerebellum. Nature, 365(6441), 50–52. http://doi.org/10.1038/365050a0e cells. *Nature*, *365*(6441), 50–52. http://dx.doi.org/10.1038/365050a0

Shinoda, Y., Kakei, S., Futami, T., & Wannier, T. (1993). Thalamocortical Organization in the Cerebello-thalamo-cortical System. *Cerebral Cortex*, *3*(5), 421–429. https://doi.org/10.1093/cercor/3.5.421

Shinoda, Y., Sugihara, I., Wu, H.-S., & Sugiuchi, Y. (2000). The entire trajectory of single climbing and mossy fibers in the cerebellar nuclei and cortex. In *Progress in Brain Research* (Vol. 124, pp. 173–186). https://doi.org/10.1016/S0079-6123(00)24015-6

Shinoda, Y., Sugiuchi, Y., Futami, T., & Izawa, R. (1992). Axon collaterals of mossy fibers from the pontine nucleus in the cerebellar dentate nucleus. *Journal of Neurophysiology*, *67*(3), 547–560. https://doi.org/10.1152/jn.1992.67.3.547

Sillitoe, R. V., Chung, S.-H., Fritschy, J.-M., Hoy, M., & Hawkes, R. (2008). Golgi Cell Dendrites Are Restricted by Purkinje Cell Stripe Boundaries in the Adult Mouse Cerebellar Cortex. *Journal of Neuroscience*, *28*(11), 2820–2826. https://doi.org/10.1523/JNEUROSCI.4145-07.2008

Silver, R. A., Lübke, J., Sakmann, B., & Feldmeyer, D. (2003). High-Probability Uniquantal Transmission at Excitatory Synapses in Barrel Cortex. *Science*, *302*(5652), 1981–1984. https://doi.org/10.1126/science.1087160

Simat, M., Parpan, F., & Fritschy, J.-M. (2007). Heterogeneity of glycinergic and gabaergic interneurons in the granule cell layer of mouse cerebellum. *The Journal of Comparative Neurology*, *500*(1), 71–83. https://doi.org/10.1002/cne.21142

Simões de Souza, F. M., & De Schutter, E. (2011). Robustness effect of gap junctions between Golgi cells on cerebellar cortex oscillations. *Neural Systems & Circuits*, *1*(1), 7. https://doi.org/10.1186/2042-1001-1-7

Soares, C., Trotter, D., Longtin, A., Béïque, J.-C., & Naud, R. (2019). Parsing Out the Variability of Transmission at Central Synapses Using Optical Quantal Analysis. *Frontiers in Synaptic Neuroscience*, *11*(August). https://doi.org/10.3389/fnsyn.2019.00022

Soler-Llavina, G. J., & Sabatini, B. L. (2006). Synapse-specific plasticity and compartmentalized signaling in cerebellar stellate cells. *Nature Neuroscience*, *9*(6), 798–806. https://doi.org/10.1038/nn1698

Song, S. H., & Augustine, G. J. (2015). Synapsin Isoforms and Synaptic Vesicle Trafficking. *Molecules and Cells*, *38*(11), 936–940. https://doi.org/10.14348/molcells.2015.0233

Sotelo, C. (2015). Molecular Layer Interneurons of the Cerebellum: Developmental and Morphological Aspects. *The Cerebellum*, *14*(5), 534–556. https://doi.org/10.1007/s12311-015-0648-x

Sotelo, C., & Llinás, R. (1972). SPECIALIZED MEMBRANE JUNCTIONS BETWEEN NEURONS IN THE VERTEBRATE CEREBELLAR CORTEX. *Journal of Cell Biology*, *53*(2), 271–289. https://doi.org/10.1083/jcb.53.2.271

Sotelo, C., Llinas, R., & Baker, R. (1974). Structural study of inferior olivary nucleus of the cat: morphological correlates of electrotonic coupling. *Journal of Neurophysiology*, *37*(3), 541–559. https://doi.org/10.1152/jn.1974.37.3.541

Spaeth, L., Bahuguna, J., Gagneux, T., Dorgans, K., Sugihara, I., Poulain, B., Battaglia, D., & Isope, P. (2022). Cerebellar connectivity maps embody individual adaptive behavior in mice. *Nature Communications*, *13*(1), 580. https://doi.org/10.1038/s41467-022-27984-8

Spaeth, L., & Isope, P. (2022). What Can We Learn from Synaptic Connectivity Maps about Cerebellar Internal Models? *The Cerebellum*, *0123456789*. https://doi.org/10.1007/s12311-022-01392-6

Südhof, T. C. (2002). Synaptotagmins: Why So Many? *Journal of Biological Chemistry*, *277*(10), 7629–7632. https://doi.org/10.1074/jbc.R100052200

Sugihara, I., & Shinoda, Y. (2004). Molecular, topographic, and functional organization of the cerebellar cortex: a study with combined aldolase C and olivocerebellar labeling. *The Journal of Neuroscience : The Official Journal of the Society for Neuroscience*, *24*(40), 8771–8785. https://doi.org/10.1523/JNEUROSCI.1961-04.2004

Sultan, F., & Bower, J. M. (1998). Quantitative golgi study of the rat cerebellar molecular layer interneurons using principal component analysis. *Journal of Comparative Neurology*, *393*(3), 353–373. https://doi.org/10.1002/(SICI)1096-9861(19980413)393:3<353::AID-CNE7>3.0.CO;2-0

Suvrathan, A., Payne, H. L., & Raymond, J. L. (2016). Timing Rules for Synaptic Plasticity Matched to Behavioral Function. *Neuron*, *92*(5), 959–967. https://doi.org/10.1016/j.neuron.2016.10.022

Szapiro, G., & Barbour, B. (2007). Multiple climbing fibers signal to molecular layer interneurons exclusively via glutamate spillover. *Nature Neuroscience*, *10*(6), 735–742. https://doi.org/10.1038/nn1907

Tabuchi, T., Umetani, T., & Yamadori, T. (1989). Corticonuclear and corticovestibular projections from the uvula in the albino rat: differential projections from sublobuli of the uvula. *Brain Research*, *492*(1–2), 176–186. https://doi.org/10.1016/0006-8993(89)90900-1

Takács, J., & Hámori, J. (1994). Developmental dynamics of Purkinje cells and dendritic spines in rat cerebellar cortex. *Journal of Neuroscience Research*, *38*(5), 515–530. https://doi.org/10.1002/jnr.490380505

Takagi, M., Tamargo, R., & Zee, D. S. (2003). Effects of lesions of the cerebellar oculomotor vermis on eye movements in primate: Binocular control. *Progress in Brain Research*, *142*, 19–33. https://doi.org/10.1016/S0079-6123(03)42004-9

Tang, Y., An, L., Yuan, Y., Pei, Q., Wang, Q., & Liu, J. K. (2021). Modulation of the dynamics of cerebellar Purkinje cells through the interaction of excitatory and inhibitory feedforward pathways. *PLOS Computational Biology*, *17*(2), e1008670. https://doi.org/10.1371/journal.pcbi.1008670

Tauffer, L., & Kumar, A. (2021). Short-Term Synaptic Plasticity Makes Neurons Sensitive to the Distribution of Presynaptic Population Firing Rates. *Eneuro*, *8*(2), ENEURO.0297-20.2021. https://doi.org/10.1523/ENEURO.0297-20.2021

Thanawala, M. S., & Regehr, W. G. (2013). Presynaptic Calcium Influx Controls Neurotransmitter Release in Part by Regulating the Effective Size of the Readily Releasable Pool. *Journal of Neuroscience*, *33*(11), 4625–4633. https://doi.org/10.1523/JNEUROSCI.4031-12.2013

Tsien, R. Y. (2005). Building and breeding molecules to spy on cells and tumors. *FEBS Letters*, *579*(4), 927–932. https://doi.org/10.1016/j.febslet.2004.11.025

Turecek, J., Jackman, S. L., & Regehr, W. G. (2016). Synaptic Specializations Support Frequency-Independent Purkinje Cell Output from the Cerebellar Cortex. *Cell Reports*, *17*(12), 3256–3268. https://doi.org/10.1016/j.celrep.2016.11.081

Turecek, J., & Regehr, W. G. (2018). Synaptotagmin 7 Mediates Both Facilitation and Asynchronous Release at Granule Cell Synapses. *The Journal of Neuroscience*, *38*(13), 3240–3251. https://doi.org/10.1523/JNEUROSCI.3207-17.2018

Uusisaari, M., & Knöpfel, T. (2008). GABAergic synaptic communication in the GABAergic and non-GABAergic cells in the deep cerebellar nuclei. *Neuroscience*, *156*(3), 537–549. https://doi.org/10.1016/j.neuroscience.2008.07.060

Uusisaari, M., Obata, K., & Knöpfel, T. (2007). Morphological and Electrophysiological Properties of GABAergic and Non-GABAergic Cells in the Deep Cerebellar Nuclei. *Journal of Neurophysiology*, *97*(1), 901–911. https://doi.org/10.1152/jn.00974.2006

Vaaga, C. E., Brown, S. T., & Raman, I. M. (2020). Cerebellar modulation of synaptic input to freezing-related neurons in the periaqueductal gray. *ELife*, *9*, 1–28. https://doi.org/10.7554/eLife.54302

Vaden, J. H., Banumurthy, G., Gusarevich, E. S., Overstreet-Wadiche, L., & Wadiche, J. I. (2019). The readily-releasable pool dynamically regulates multivesicular release. *ELife*, *8*, 1–27. https://doi.org/10.7554/eLife.47434

Valera, A. M., Binda, F., Pawlowski, S. A., Dupont, J.-L., Casella, J.-F., Rothstein, J. D., Poulain, B., & Isope, P. (2016). Stereotyped spatial patterns of functional synaptic connectivity in the cerebellar cortex. *ELife*, *5*(e09862), e09862. https://doi.org/10.7554/eLife.09862

Valera, A. M., Doussau, F., Poulain, B., Barbour, B., & Isope, P. (2012). Adaptation of Granule Cell to Purkinje Cell Synapses to High-Frequency Transmission. *Journal of Neuroscience*, *32*(9), 3267–3280. https://doi.org/10.1523/JNEUROSCI.3175-11.2012

van Beugen, B. J., Nagaraja, R. Y., & Hansel, C. (2006). Climbing Fiber-Evoked Endocannabinoid Signaling Heterosynaptically Suppresses Presynaptic Cerebellar Long-Term Potentiation. *Journal of Neuroscience*, *26*(32), 8289–8294. https://doi.org/10.1523/JNEUROSCI.0805-06.2006

van der Want, J. J. L., Wiklund, L., Guegan, M., Ruigrok, T., & Voogd, J. (1989). Anterograde tracing of the rat olivocerebellar system with phaseolus vulgaris leucoagglutinin (PHA-L). Demonstration of climbing fiber collateral innervation of the cerebellar nuclei. *The Journal of Comparative Neurology*, *288*(1), 1–18. https://doi.org/10.1002/cne.902880102

van Woerden, G. M., Hoebeek, F. E., Gao, Z., Nagaraja, R. Y., Hoogenraad, C. C., Kushner, S. A., Hansel, C., De Zeeuw, C. I., & Elgersma, Y. (2009). βCaMKII controls the direction of plasticity at parallel fiber–Purkinje cell synapses. *Nature Neuroscience*, *12*(7), 823–825. https://doi.org/10.1038/nn.2329

Vervaeke, K., LÖrincz, A., Gleeson, P., Farinella, M., Nusser, Z., & Silver, R. A. (2010). Rapid Desynchronization of an Electrically Coupled Interneuron Network with Sparse Excitatory Synaptic Input. *Neuron*, *67*(3), 435–451. https://doi.org/10.1016/j.neuron.2010.06.028

Viet, N.-M., Wang, T., Tran-Anh, K., & Sugihara, I. (2021). Heterogeneity of intrinsic plasticity in cerebellar Purkinje cells linked with cortical molecular zones. *IScience*, *25*(1), 103705. https://doi.org/10.1016/j.isci.2021.103705

Voogd, J. (1967). Comparative Aspects of the Structure and Fibre Connexions of the Mammalian Cerebellum. *Progress in Brain Research*, *25*(C), 94–134. https://doi.org/10.1016/S0079-6123(08)60963-2

Voogd, J., & De Zeeuw, C. I. (2020). Cerebellum: What is in a Name? Historical Origins and First Use of This Anatomical Term. *Cerebellum*, *19*(4), 550–561. https://doi.org/10.1007/s12311-020-01133-7

Voogd, J., Epema, A. H., & Rubertone, J. A. (1991). Cerebello-vestibular connections of the anterior vermis. A retrograde tracer study in different mammals including primates. *Archives Italiennes de Biologie*, *129*(1), 3–19. https://doi.org/10.4449/aib.v129i1.844

VOOGD, J., GERRITS, N. M., & RUIGROK, T. J. H. (1996). Organization of the Vestibulocerebellum. *Annals of the New York Academy of Sciences*, *781*(1 Lipids and Sy), 553–579. https://doi.org/10.1111/j.1749-6632.1996.tb15728.x

Voogd, J., & Ruigrok, T. J. H. (2004). The organization of the corticonuclear and olivocerebellar climbing fiber projections to the rat cerebellar vermis: The congruence of projection zones and the zebrin pattern. *Journal of Neurocytology*, *33*(1), 5–21. https://doi.org/10.1023/B:NEUR.0000029645.72074.2b

Wagner, M. J., Kim, T. H., Kadmon, J., Nguyen, N. D., Ganguli, S., Schnitzer, M. J., & Luo, L. (2019). Shared Cortex-Cerebellum Dynamics in the Execution and Learning of a Motor Task. *Cell*, *177*(3), 669-682.e24. https://doi.org/10.1016/j.cell.2019.02.019

Wagner, M. J., Kim, T. H., Savall, J., Schnitzer, M. J., & Luo, L. (2017). Cerebellar granule cells encode the expectation of reward. *Nature*, *544*(7648), 96–100. https://doi.org/10.1038/nature21726

Walmsley, B., & Nicol, M. J. (1990). Location and morphology of dorsal spinocerebellar tract neurons that receive monosynaptic afferent input from ankle extensor muscles in cat hindlimb. *Journal of Neurophysiology*, *63*(2), 286–293. https://doi.org/10.1152/jn.1990.63.2.286

Walter, J. T., Alviña, K., Womack, M. D., Chevez, C., & Khodakhah, K. (2006). Decreases in the precision of Purkinje cell pacemaking cause cerebellar dysfunction and ataxia. *Nature Neuroscience*. https://doi.org/10.1038/nn1648

Wang, S. S.-H., Denk, W., & Häusser, M. (2000). Coincidence detection in single dendritic spines mediated by calcium release. *Nature Neuroscience*, *3*(12), 1266–1273. https://doi.org/10.1038/81792

Wang, X., Novello, M., Gao, Z., Ruigrok, T. J. H., & De Zeeuw, C. I. (2021). Input and output organization of the mesodiencephalic junction for cerebro-cerebellar communication. *Journal of Neuroscience Research*, *100*(2), 620–637. https://doi.org/10.1002/jnr.24993

Wang, Y. T., & Linden, D. J. (2000). Expression of Cerebellar Long-Term Depression Requires Postsynaptic Clathrin-Mediated Endocytosis. *Neuron*, *25*(3), 635–647. https://doi.org/10.1016/S0896-6273(00)81066-1

Wetmore, D. Z., Jirenhed, D.-A., Rasmussen, A., Johansson, F., Schnitzer, M. J., & Hesslow, G. (2014). Bidirectional Plasticity of Purkinje Cells Matches Temporal Features of Learning. *Journal of Neuroscience*, *34*(5), 1731–1737. https://doi.org/10.1523/JNEUROSCI.2883-13.2014

Wiksten, B. (1985). Retrograde HRP study of neurons in the cervical enlargement projecting to the cerebellum in the cat. *Experimental Brain Research*, *58*(1), 95–101. https://doi.org/10.1007/BF00238957

Witter, L., Rudolph, S., Pressler, R. T., Lahlaf, S. I., & Regehr, W. G. (2016). Purkinje Cell Collaterals Enable Output Signals from the Cerebellar Cortex to Feed Back to Purkinje Cells and Interneurons. *Neuron*, *91*(2), 312–319. https://doi.org/10.1016/j.neuron.2016.05.037

Wlklund, L., Toggenburger, G., & Cuénod, M. (1984). Selective retrograde labelling of the rat olivocerebellar climbing fiber system with d-[3h]aspartate. *Neuroscience*, *13*(2), 441–468. https://doi.org/10.1016/0306-4522(84)90242-2

Wolpert, D. M., Miall, R. C., & Kawato, M. (1998). Internal models in the cerebellum. *Trends in Cognitive Sciences*, *2*(9), 338–347.

Woolston, D. C., Kassel, J., & Gibson, J. M. (1981). Trigeminocerebellar mossy fiber branching to granule cell layer patches in the rat cerebellum. *Brain Research*, *209*(2), 255–269. https://doi.org/10.1016/0006-8993(81)90152-9

Wu, H. S., Sugihara, I., & Shinoda, Y. (1999). Projection patterns of single mossy fibers originating from the lateral reticular nucleus in the rat cerebellar cortex and nuclei. *Journal of Comparative Neurology*, *411*(1), 97–118. https://doi.org/10.1002/(SICI)1096-9861(19990816)411:1<97::AID-CNE8>3.0.CO;2-O

Wylie, D. R., De Zeeuw, C. I., Digiorgi, P. L., & Simpson, J. I. (1994). Projections of individual purkinje cells of identified zones in the flocculus to the vestibular and cerebellar nuclei in the rabbit. *The Journal of Comparative Neurology*, *349*(3), 428–447. https://doi.org/10.1002/cne.903490308

Xie, Z., Long, J., Liu, J., Chai, Z., Kang, X., & Wang, C. (2017). Molecular Mechanisms for the Coupling of Endocytosis to Exocytosis in Neurons. *Frontiers in Molecular Neuroscience*, *10*, 47. https://doi.org/10.3389/fnmol.2017.00047

Xu-Friedman, M. a, Harris, K. M., & Regehr, W. G. (2001). Three-Dimensional Comparison of Ultrastructural Characteristics at Depressing and Facilitating Synapses onto Cerebellar Purkinje Cells. *The Journal of Neuroscience*, *21*(17), 6666–6672. https://doi.org/10.1523/JNEUROSCI.21-17-06666.2001

Xu, J., Mashimo, T., & Südhof, T. C. (2007). Synaptotagmin-1, -2, and -9: Ca2+ Sensors for Fast Release that Specify Distinct Presynaptic Properties in Subsets of Neurons. *Neuron*, *54*(4), 567–581. https://doi.org/10.1016/j.neuron.2007.05.004

Yaginuma, H., & Matsushita, M. (1989). Spinocerebellar projections from the upper lumbar segments in the cat, as studied by anterograde transport of wheat germ agglutinin-horseradish peroxidase. *Journal of Comparative Neurology*, *281*(2), 298–319. https://doi.org/10.1002/cne.902810211

Yoon, T. Y., & Munson, M. (2018). SNARE complex assembly and disassembly. *Current Biology*, *28*(8), R397–R401. https://doi.org/10.1016/j.cub.2018.01.005

Yu, F., Jiang, Q. J., Sun, X. Y., & Zhang, R. W. (2015). A new case of complete primary cerebellar agenesis: Clinical and imaging findings in a living patient. *Brain*, *138*(6), e353. https://doi.org/10.1093/brain/awu239

Zeeuw, C. I., & Berrebi, A. S. (1995). Postsynaptic Targets of Purkinje Cell Terminals in the Cerebellar and Vestibular Nuclei of the Rat. *European Journal of Neuroscience*, *7*(11), 2322–2333. https://doi.org/10.1111/j.1460-9568.1995.tb00653.x

Zhang, W., & Linden, D. J. (2009). Neuromodulation at Single Presynaptic Boutons of Cerebellar Parallel Fibers Is Determined by Bouton Size and Basal Action Potential-Evoked Ca Transient Amplitude. *Journal of Neuroscience*, *29*(49), 15586–15594. https://doi.org/10.1523/JNEUROSCI.3793-09.2009

Zhang, W., & Linden, D. J. (2012). Calcium influx measured at single presynaptic boutons of cerebellar granule cell ascending axons and parallel fibers. *Cerebellum*. https://doi.org/10.1007/s12311-009-0151-3

Zhou, H., Lin, Z., Voges, K., Ju, C., Gao, Z., Bosman, L. W. J., Ruigrok, T. J., Hoebeek, F. E., De Zeeuw, C. I., & Schonewille, M. (2014). Cerebellar modules operate at different frequencies. *ELife*, *3*(e02536), e02536. https://doi.org/10.7554/eLife.02536

Zucker, R. S., & Regehr, W. G. (2002). Short-Term Synaptic Plasticity. In *Annual Review of Physiology* (Vol. 64, Issue 1). https://doi.org/10.1146/annurev.physiol.64.092501.114547

APPENDIX
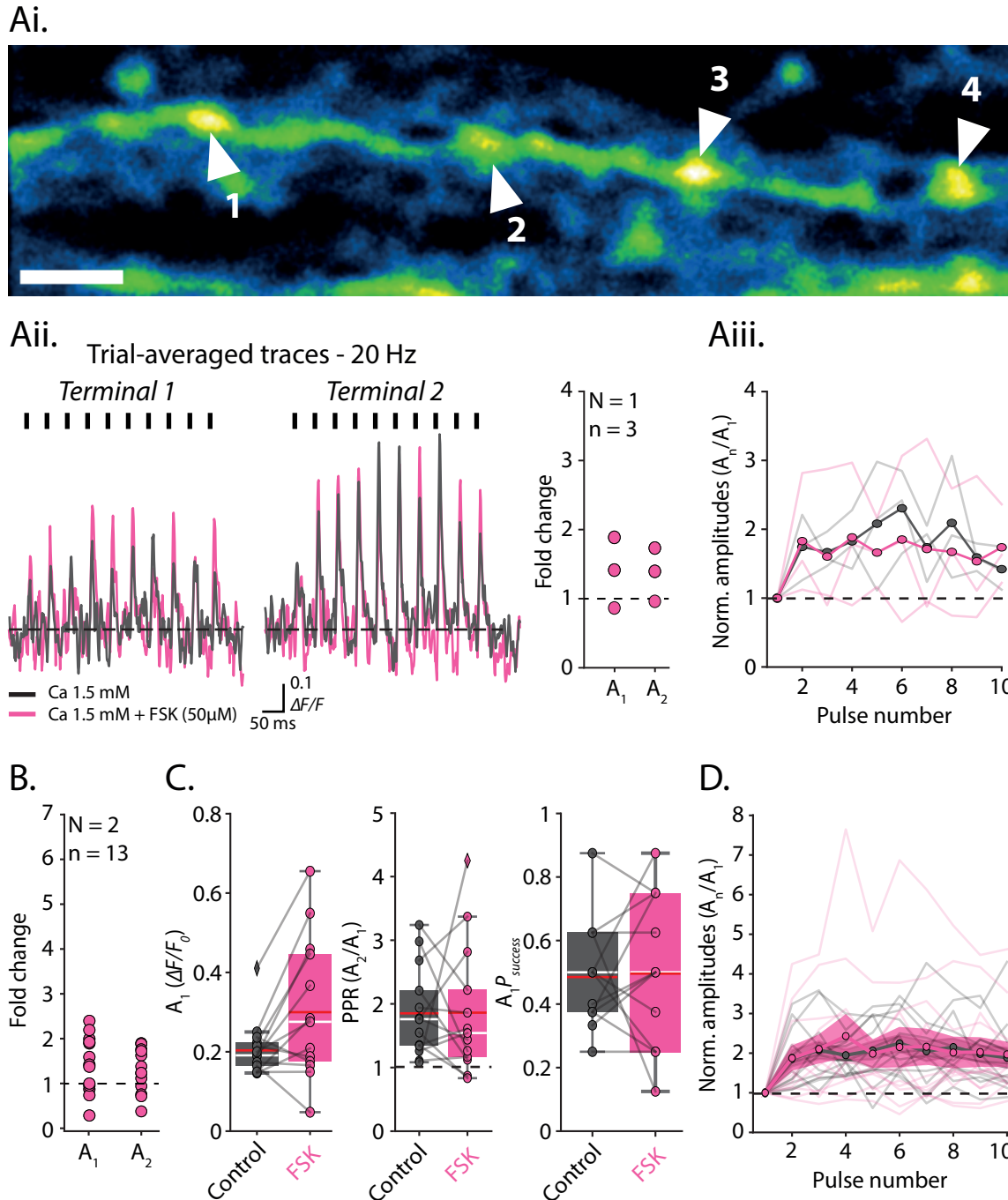
Figure Ann1 : Heterogeneous contribution of adenylyl cyclase on glutamate release between granule cell terminals under 1.5 mM extracellular Ca²⁺ concentration.

Ai) Two-photon imaging of 5 terminals along the same parallel fibre expressing SF-iGluSnFR.S72A. Scale bar: 2 µm.

Aii) Trial-averaged fluorescence traces from terminals 1 and 3 evoked by ten pulses at 20 Hz in control and FSK conditions and fold change of the first two amplitudes (A_1 and A_2). The fold change for A_1 and A_2 is calculated by the ratio $A_1FSK/A_1Control$ and $A_2FSK/A_2Control$.

Aiii) Normalized amplitudes of trial-averaged fluorescence traces from terminals 1 to 5 evoked by ten pulses at 20 Hz under control and FSK conditions. Means (colored lines and dots) ± SEM.

B) Same as fold change in Aii) for all terminals imaged.

C) Comparison of A_1, $A_1P_{success}$ and PPR beween control and FSK conditions. Means and medians are indicated by red and white bars (A_1: p = 7,9.10⁻², PPR: p = 6,3.10⁻¹, Wilcoxon signed-rank test with Bonferroni correction; $A_1P_{success}$: p = 1.0, paired Student t-test with Bonferroni correction).

D) Same as Aiii) for all terminals imaged.
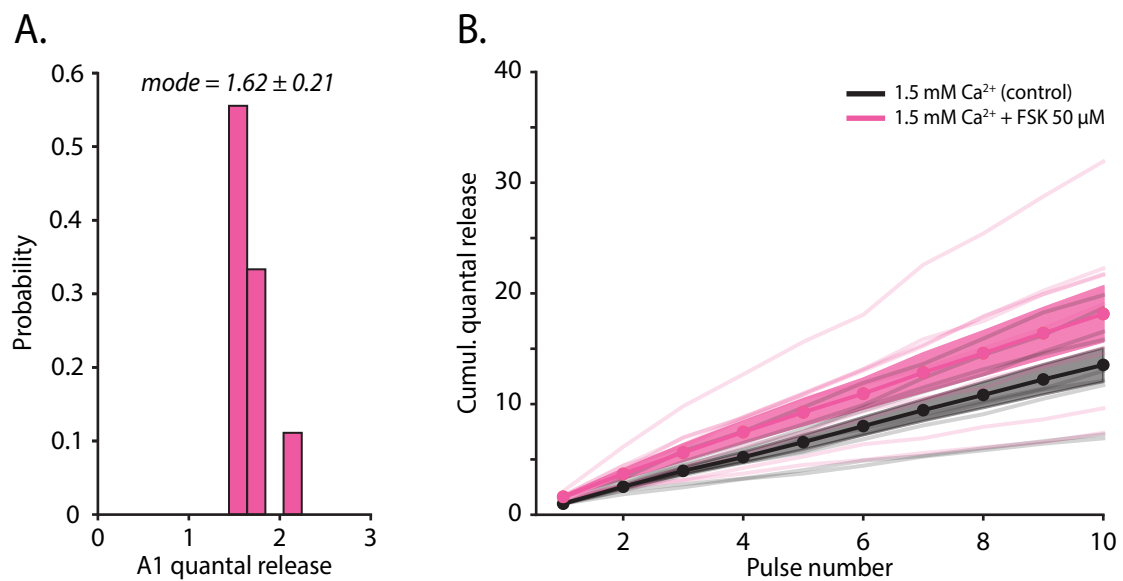
Figure Ann2 : Adenylyl cyclase slightly changes glutamate quantal release at GC terminals under 1.5 mM extracellular Ca²⁺.

A) Quantal release for the first transient with FSK. Quantal release is calculated by the ratio $A_1FSK/A_1Control$ from trial-averaged fluorescence traces.

B) Cumulative quantal release in control and FSK conditions over the burst of electrical pulses at 20 Hz. For FSK plot, amplitudes from transients under FSK condition are normalized by the amplitude of the first transient deprived of failures. For control plot, the cumulative sum of amplitudes normalized by the first one was applied.
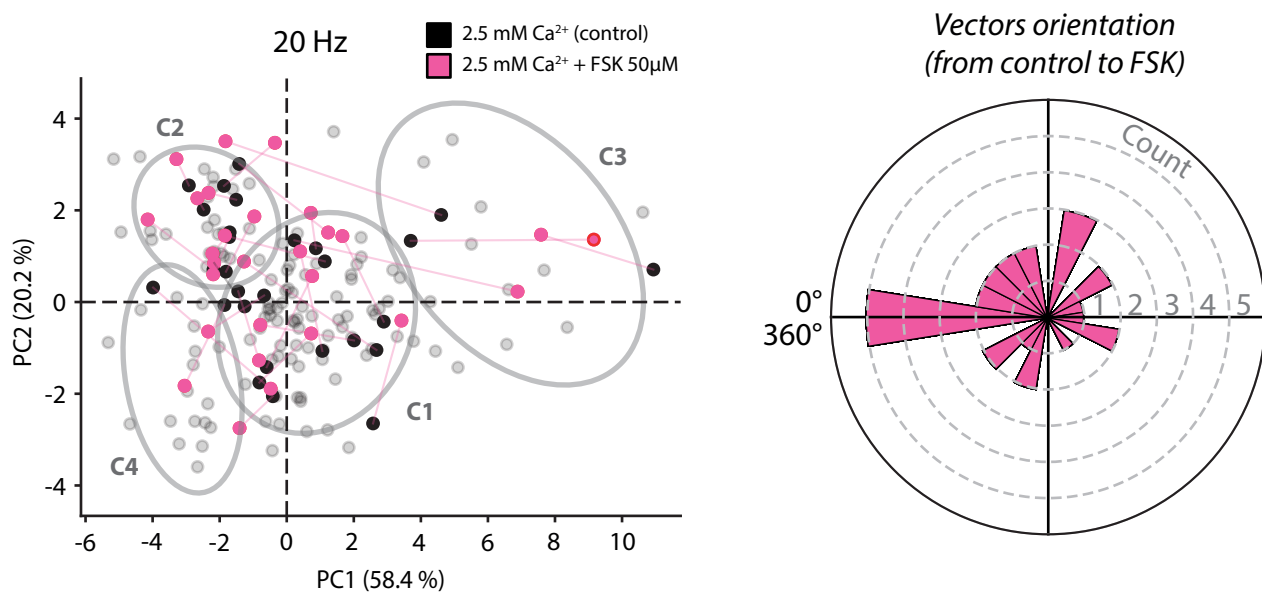
Figure Ann3 : The response of adenylyl cyclase activation contributes to short-term plasticity diversity under 2.5 mM extracellular Ca²⁺ concentration.

Spatial location on the PCA subspace (left) and vectors orientation (right) of terminals stimulated at 20 Hz under control and FSK conditions. Vectors from control to FSK are indicated by light-pink lines. On the polar plot, the origin of each vector represents the dots in control condition. The distribution of the angles of the vectors is given by the histogram.

Résumé détaillé de la thèse en français

Diversité fonctionnelle de la libération de glutamate aux boutons des cellules en grains du cervelet

Par Théo ROSSI

Sous la direction du Dr. Philippe ISOPE

Résumé détaillé de la thèse

I.   Contexte général et objectifs

Le cervelet joue un rôle majeur dans la coordination motrice, l'apprentissage moteur, le maintien de l'équilibre et le contrôle temporel des actions. Le cortex cérébelleux est composé de microcircuits neuronaux stéréotypés appelés modules. Ces modules traitent les informations sensorimotrices afin de prédire le retour sensoriel attendu d'une commande motrice nécessaire à l'ajustement de l'exécution du mouvement. Chaque module est composé de cellules de Purkinje (CP) adjacentes, seules sortie du cortex cérébelleux, projetant spécifiquement vers des régions des noyaux cérébelleux profonds. Les informations intégrées dans les noyaux cérébelleux profonds sont transmise aux structures effectrices du système moteur dans le tronc cérébral, la moelle épinière et le cortex cérébral via le thalamus. Les CPs intègrent les informations sensorimotrices corticales et spinales des fibres moussues (FM) via un relai par les cellules en grains (CG). Le long axone en T des CGs forme la fibre parallèle (FP) qui parcourt de longues distances et contacte les dendrites de plusieurs CPs, assurant ainsi une communication entre différents modules. Les FPs contactent également les interneurones de la couche moléculaire (ICM) impliqués dans l'inhibition antérograde des CPs.

Les informations sensorimotrices sont transmises au cortex cérébelleux sous la forme de salves de potentiels d'action à hautes fréquences (de quelques dizaines à quelques centaines de Hertz). Ces hautes fréquences déclenchent différentes formes de plasticité à court terme (PCT) présynaptiques qui ajustent la libération vésiculaire du glutamate et façonnent dynamiquement la force synaptique à l'échelle de la milliseconde. Dans le cas de la facilitation

à court terme (FCT), l'accumulation de calcium dans le bouton présynaptique au cours du train à haute fréquence augmente progressivement la probabilité de libération (P_r) du glutamate. Dans la dépression à court terme (DCT), la P_r augmente également mais la majorité des vésicules synaptiques sont libérées au début du train conduisant ainsi à une diminution progressive de la libération de glutamate. Ainsi, à l'échelle de la milliseconde, la FCT accroit la force synaptique et agit comme filtre passe-haut des informations tandis que la DCT produit l'effet inverse. FCT et DCT sont spécifiques d'un type d'information entrante aux synapses FM-CG et codent temporellement les évènements multisensoriels au niveau d'une seule CG.

L'équipe dans laquelle j'ai mené mon projet de thèse vise à comprendre **comment le cervelet encode temporellement les informations sensorimotrices pour assurer ses fonctions**. Des données récentes de l'équipe ont démontré deux points importants. Premièrement, les PCT des CGs sont diversifiées aux synapses excitatrices et inhibitrices et modulent dynamiquement la balance excitation/inhibition des CPs. Deuxièmement, une délétion de la Synapsine II, une protéine exprimée de manière hétérogène entre les boutons des CGs et impliquée dans le trafic des vésicules synaptiques, réduit la diversité de PCT aux synapses CG-ICM et altère le traitement temporel de l'information par les ICM. **L'objectif de mon projet de thèse a été de comprendre comment les propriétés de PCT varient le long des FPs et quels sont les mécanismes présynaptiques qui modulent ces propriétés**. Le projet s'articule autour des trois axes présentés dans la section suivante.

II.   Résultats

1. *Mise en place d'un protocole de microscopie biphotonique adapté à l'imagerie des PCT aux boutons présynaptiques individuels des fibres parallèles*

Etudier l'hétérogénéité de la PCT le long d'une même FP requiert un suivi rigoureux de la libération de glutamate aux boutons individuels. Les approches électrophysiologiques ne peuvent être utilisées car il faudrait enregistrer chaque CP qu'une FP croise (i.e. des dizaines de cellules), ce qui n'est pas réalisable avec les méthodes de patch-clamp en tranches aiguës de cervelet. La mise au point d'une méthode de microscopie biphotonique basée sur un nouveau senseur fluorescent du glutamate génétiquement encodé (iGluSnFR) a permis l'étude simultanée des propriétés de PCT à de multiples boutons issus d'une même CG. Alors que les mesures électrophysiologiques de glutamate sont influencées à la fois par la dynamique des récepteurs AMPA et par le filtrage dendritique, l'imagerie biphotonique de la

fixation du glutamate sur le iGluSnFR fournit une mesure directe du neurotransmetteur libéré par l'élément présynaptique. Dans le but d'exprimer iGluSnFR aux boutons des CGs, j'ai effectué des injections stéréotaxiques d'un virus adéno-associé contenant le gène du iGluSnFR dans la couche granulaire du cortex cérébelleux. La libération de glutamate évoquée par des stimulations électriques des FPs conduit à une augmentation du signal fluorescent du iGluSnFR proportionnellement à la quantité de neurotransmetteur libéré dans la fente synaptique. Compte tenu du fait que la PCT est déclenchée par les hautes fréquences, j'ai utilisé une version mutée du senseur (SF-iGluSnFR-S72A) possédant des cinétiques rapides (constante de temps de décroissance du signal autour de 7 ms). La faible affinité de ce variant pour le glutamate (constante de dissociation de 200 µM) limite la contamination des enregistrements par le glutamate extrasynaptique (i.e. non spécifique du bouton ciblé et dont la concentration est plus faible que dans la fente synaptique). **Ainsi, cette méthode d'imagerie biphotonique du SF-iGluSnFR-S72A est adaptée à l'étude de la libération de glutamate à haute fréquence à l'échelle unitaire des boutons des CGs.**

2. *Etude de l'hétérogénéité et de l'organisation des dynamiques de PCT aux boutons individuels d'une même fibre parallèle.*

L'étape suivante a été dédiée à l'étude de l'organisation des propriétés de PCT entre les boutons d'une même FP. En appliquant le protocole d'imagerie décrit précédemment, des stimulations électriques à hautes fréquences (20Hz–50Hz) des FPs ont montré que les profils de PCT sont hautement diversifiés entre les boutons : un profil stationnaire et trois profils différents de facilitation. Contrairement aux facilitations, les boutons à profil stationnaire sont caractérisés par une libération homogène de glutamate tout au long du train de stimulations, probablement issue de la libération d'une seule vésicule à chaque coup. Sachant qu'une même FP contacte plusieurs CPs et différents types d'interneurones inhibiteurs, une telle diversité dans la PCT suggère un lien entre les propriétés de libération vésiculaire et le type de cellule postsynaptique. J'ai vérifié cette hypothèse en identifiant les cellules postsynaptiques lors des expériences de microscopie biphotonique. Pour ce faire, j'ai exprimé SF-iGluSnFR-S72A dans les CGs de la lignée murine transgénique L7-tdTomato. Cette lignée exprime le fluorophore tdTomato spécifiquement dans les CPs afin de distinguer en temps réel ces cellules des autres types postsynaptiques (ICM, Golgi, Candelabre). Une superposition des marqueurs vert (SF-iGluSnFR-S72A) et rouge (tdTomato) indique une potentielle connexion entre le bouton de la FP et l'épine dendritique de la CP. Dans le cas échéant, la synapse est considérée comme étant établie avec une autre cible. Contrairement à mon

hypothèse, les profils de PCT sont hétérogènes entre les synapses CG-CP mais également entre les synapses CG-CP et CG-interneurone. Par conséquent, ces résultats indiquent qu'un profil donné de PCT n'est pas dépendant du type de cellule postynaptique. **Néanmoins, cette diversité suggère une hétérogénéité des mécanismes présynaptiques le long d'une même FP impliqués dans le contrôle de la libération du glutamate.**

3. Etude des mécanismes présynaptiques de la libération du glutamate impliqués dans la diversité de PCT.

Les boutons des CGs contiennent une constellation de protéines et de voies de signalisations impliquées dans la modulation de la libération de glutamate. Il est très bien connu qu'une élévation de la concentration calcique augmente la P_r en mobilisant une majorité de vésicules au début du train de potentiels d'action. Ceci fait basculer le profil de la synapse d'une FCT vers une DCT dans les mesures électrophysiologiques. Dans les expériences de SF-iGluSnFR-S72A, la P_r a été modifiée au sein du même bouton en variant la concentration de calcium extracellulaire. Conformément à nos attentes, la transition du bas (1.5mM) vers le haut (4mM) calcium conduit à une augmentation de la libération de glutamate. Etonnamment, cette élévation n'induit pas la transition FCT→DCT et montre que le bouton de la CG conserve un très fort soutien de la libération de glutamate (jusqu'à 40 fois plus de glutamate libéré au cours du train). De plus, la diversité de PCT est fortement réduite dans ces conditions de forte P_r. **Ces résultats suggèrent (1) que le haut calcium recrute des sites de libération de vésicules mobilisées uniquement lors de hautes fréquences pour soutenir la neurotransmission, (2) que le calcium est un facteur déterminant dans l'hétérogénéité de la PCT, et (3) une implication des récepteurs AMPA dont la mobilité et la désensibilisation sont connues pour affecter les mesures de PCT dans les méthodes d'électrophysiologie classiques.**

Par la suite, j'ai étudié l'implication de l'activation de l'adénylate cyclase présynaptique connue pour réguler les populations de vésicules synaptiques et déclencher des phénomènes de plasticité à long terme. Dans les expériences d'imagerie biphotonique à l'échelle du bouton unitaire, la forskoline a été utilisée pour activer l'adénylate cyclase qui mobilise la voie des protéines kinases A. Ces kinases peuvent agir sur la synapsine II dont la phosphorylation conduit à une disponibilité plus importante des vésicules synaptiques autour des sites de libération. Les résultats ont montré une grande hétérogénéité des effets de la forskoline d'un bouton à l'autre. Dans la plupart des boutons, la forskoline augmente la libération de glutamate conformément aux attentes. D'autres boutons ont montré une absence d'effet de la forskoline suggérant un état déjà potentialisé qui occlut l'induction d'une augmentation de la libération

de glutamate. Enfin, la forskoline a diminué la libération de glutamate dans une moindre population de boutons suggérant la mobilisation d'autres effecteurs moléculaires. Contrairement au haut calcium, l'activation de l'adénylate cyclase modifie le profil de PCT de manière hétérogène sans en impacter la diversité. De plus, pour la première fois, ces résultats mettent exclusivement en évidence les effets de l'adénylate cyclase présynaptique sur la libération de glutamate. Ces effets sont moindres par rapport à la forte contribution de l'adénylate cyclase postsynaptique sur la potentialisation de la transmission rapportée par les données électrophysiologiques de la littérature. **Ainsi, les résultats suggèrent que (1) d'un bouton à l'autre les voies de signalisation intracellulaires de l'adénylate cyclase sont hétérogènes, et (2) que ces voies régulent différemment la disponibilité des vésicules synaptiques pour moduler la diversité de PCT.**

III. Conclusion

A travers ce projet de thèse, j'ai montré que le SF-iGluSnFR-S72A combiné à la microscopie biphotonique est un outil efficace pour mesurer la PCT aux boutons individuels des CGs. La PCT est hétérogène le long d'une même FP et les profils de cette plasticité sont indépendants du type de cellule postsynaptique. Cette diversité est fortement contrôlée par l'homéostasie calcique présynaptique capable de mobiliser des sites de libération et des populations de vésicules spécifiques de la transmission à haute fréquence. De plus, l'activation de l'adénylate cyclase module le profil de PCT de manière hétérogène d'un bouton à l'autre sans impacter la diversité de la PCT. Enfin, les différences observées entre les mesures électrophysiologiques indirectes décrites dans la littérature et les mesures d'imagerie directe de la libération de glutamate que j'ai acquises révèlent une potentielle implication des récepteurs AMPA postsynaptiques dans la modulation du profil de PCT.

Mon travail apporte de nouvelles compréhensions et perspectives quant à l'organisation et la mécanistique des capacités d'encodage temporel de l'information dans le cervelet. Les FPs distribuent les informations sensorimotrices des FMs aux différentes cibles neuronales. La diversité de PCT le long d'une même FP suggère un contrôle hautement dynamique de la balance excitation/inhibition de la CP à travers une forte expansion des capacités d'encodage temporel des informations sensorimotrices. Un tel contrôle est fondamental pour façonner le message de sortie du cortex cérébelleux et ainsi assurer les fonctions du cervelet.

Théo ROSSI

Functional diversity of glutamate release at cerebellar granule cell boutons

Résumé en français

Le cortex cérébelleux est composé de modules qui traitent les informations sensorimotrices et coordonnent les mouvements. Les informations sont transmises au cortex cérébelleux par les fibres moussues (FM) et relayées par les cellules en grains (CG) jusqu'aux cellules de Purkinje (CP), la seule sortie du cortex cérébelleux. L'axone en T des CGs forme les fibres parallèles (FP) pouvant également inhiber les CP via les interneurones de la couche moléculaire (ICM) et assurer la communication entre les modules cérébelleux. Les informations entrantes sont transmises sous forme de salves d'activité à haute fréquence. Sur la voie FM-CG-(IML)-CP, les salves déclenchent la plasticité synaptique à court terme (PCT) qui façonne la force synaptique à l'échelle de la milliseconde. La PCT génère un codage temporel de l'information pour contrôler dynamiquement la balance excitation/inhibition des CPs. L'objectif de ma thèse est de comprendre comment les propriétés de PCT sont organisées et modulées au niveau des boutons unitaires des CGs le long de la FP pour fournir un codage temporel spécifique des informations sensorimotrices dans le cortex cérébelleux. J'ai développé une méthode d'imagerie biphotonique de pointe combinée à un rapporteur de glutamate fluorescent génétiquement encodé exprimé dans les CGs pour identifier la PCT au niveau de boutons uniques pendant des stimulations électriques à haute fréquence. J'ai démontré que les profils de PCT sont hétérogènes d'un bouton à l'autre et ne dépendent pas de la cible postsynaptique. De plus, une $[Ca^{2+}]$ élevée a révélé que les boutons libèrent une large gamme dynamique de vésicules synaptiques pour soutenir la libération de glutamate et normaliser la PCT. Enfin, l'activation d'une voie de signalisation présynaptique impliquée dans la régulation des populations de vésicules synaptiques a affecté de manière hétérogène la PCT entre les boutons sans en réduire la diversité. Ces résultats suggèrent que la diversité de PCT le long de la FP fournit des signatures temporelles pour que les CPs traitent différemment l'information entre les voies inhibitrice et excitatrice. Ma thèse apporte une nouvelle compréhension quant au traitement de l'information entre les modules permettant d'assurer les fonctions cérébelleuses.

Résumé en anglais

The cerebellar cortex is composed of modules that process sensorimotor information and coordinate movements. Information are conveyed to the cerebellar cortex through mossy fibers (MFs) and relayed by granule cells (GCs) up to Purkinje cells (PCs), the sole output of the cerebellar cortex. The T-shaped axon of GCs makes parallel fibers (PF) that also contact molecular layer interneurons (MLI) providing feed-forward inhibition onto PCs and enable communication between cerebellar modules. Incoming information are conveyed as high-frequency bursts. On the MF-GC-(MLI)-PC pathway, bursts of activity trigger short-term synaptic plasticity (STP) that shape synaptic strength in the millisecond range. STP generates temporal coding of information to dynamically control excitatory/inhibitory balance of PCs firing. The goal of my thesis is to understand how STP properties are organized and modulated at single GC boutons along the PF to provide specific temporal coding of sensorimotor information in the cerebellar cortex. I developed a state-of-the-art two-photon imaging method combined to a genetically-encoded fluorescent glutamate reporter expressed in GCs to monitor STP at single boutons during high-frequency electrical stimulations. I demonstrated that STP profiles are heterogeneous from bouton to bouton and do not depend on the postsynaptic target. Moreover, high $[Ca^{2+}]$ unveiled that boutons release a large dynamic range of synaptic vesicles to sustain glutamate release and standardize STP. Finally, activation of a presynaptic signaling pathway involved in regulation of synaptic vesicle pools heterogeneously affected STP between boutons without reducing the diversity. These results suggest that STP diversity along the PF provides temporal signatures for PCs to differentially process information between the feed-forward inhibition and the excitatory pathway. My thesis provides new understandings on information processing across modules to ensure cerebellar functions.